THE APPLICATION OF PRESSURISED CARBON DIOXIDE TO RECOVER ELECTROLYTE FROM LITHIUM-ION BATTERIES IN ELECTRIC VEHICLES

by

SHIVA JAGDISH JETHWA

A thesis submitted to the University of Birmingham for the degree of

DOCTOR OF PHILOSOPHY

Department of Chemical Engineering

College of Engineering and Physical Sciences

University of Birmingham

February 2024

Abstract

Electric vehicles (EVs) have experienced significant growth and market dominance over the past decade, contributing to a reduction in greenhouse gas emissions as they replace traditional internal combustion engine vehicles. However, the lithium-ion battery (LIB) technology powering these EVs degrades over time and eventually requires replacement. This has led to a growing accumulation of end-of-life LIB waste. Most commercial processes currently focus on recovering high-value materials from spent LIBs, often overlooking the recovery of organic materials, particularly the electrolyte component. This research thesis aims to address this gap by investigating the recovery of EV LIB electrolyte using pressurised carbon dioxide.

The initial study focused on the solubility of the primary solvent components of typical LIB electrolytes, namely, dimethyl carbonate (DMC), ethyl methyl carbonate (EMC), and ethylene carbonate (EC). Each was established in binary and quaternary (1:1:1 wt) systems in carbon dioxide under temperatures of 298.2, 313.2, and 328.2 K, and pressures ranging from 0.12-14.1 MPa. Within the constraints of the system parameters explored, the linear carbonates required mild pressure and high temperature conditions to promote their solubility, whereas EC required the elevation of pressure and low temperature conditions to enhance its dissolution in carbon dioxide. Additionally, both linear carbonates were found to act as co-solvents to the cyclic carbonate, promoting its solubility in carbon dioxide.

Findings from the phase equilibria studies were applied to a pressurised fluid extraction process. Pressurised carbon dioxide was used to extract an artificially created LIB electrolyte mixture (DMC, EMC, and EC) in a 1:1:1 mass ratio, weighing 1.5 g. Initial optimisations focused on extraction duration and dynamic flowrate, and the most optimal conditions were identified to occur between 90-210 minutes at 2.4-2.6 L/min. The combined effects of pressure and temperature were investigated, and both conditions were optimised and evaluated using response surface methodology (RSM). The optimal extraction yield for the artificial LIB electrolyte was 70.2%, achieved at conditions of 12.0 MPa and 328.2 K. Key findings concluded that linear carbonates respond more effectively to temperature enhancement, highlighting the importance of vapour pressure, while the cyclic component demonstrated a strong association with fluid density.

Final investigations explored the analysis, processing, and extraction of commercial EV LIB pouch cells using supercritical carbon dioxide and solvent extraction techniques. The research found that more than 60% of the electrolyte was trapped in the electrodes and separator components, and substantial electrolyte loss was experienced due to the volatility of the linear carbonate, posing a challenge for collection. The electrolyte component was characterised before and after extraction using GC-MS, NMR, and ICP-OES techniques. The supercritical carbon dioxide extraction was performed at 12.0 MPa and 328.2 K, at a flowrate of 6 g/min for 60 minutes of dynamic and 45 minutes of static operation. The extraction produced satisfactory results, recovering a predominantly linear carbonate mixture with maximum recovery yields of 47.6% and 44.4% from the anode and separator materials, respectively. For solvent extraction, acetone was used under an HPV temperature of 323.2 K and a pump flowrate of 6.5 L/min for 165 minutes. The process achieved a maximum electrolyte yield of 96.7% from the anode material and proved effective in recovering the lithium conducting salt.

Acknowledgements

I am sincerely thankful to my supervisor, Professor Gary Leeke. Your continuous support, encouragement, and guidance have been pivotal throughout this turbulent journey. This significant milestone would have been far from complete without your invaluable time and patience dedicated in guiding me through the complexities of this research.

I would like to thank Professor Paul Anderson for the insightful discussions and invaluable suggestions, particularly during the initial stages of the project.

A special thanks goes to my financial sponsors, The Faraday Institution and EPSRC. The support has been instrumental in the realisation of the project, and I express my sincere gratitude for their contributions. Appreciation goes out to the entire ReLiB team for their extensive support and provision of resources throughout the project; their collaborative efforts have constructively shaped the research.

I extend my utmost gratitude to Dr Guozhan Jiang; I am truly appreciative of the endless support and assistance provided throughout my research. If given a penny for every one of my questions, Guozhan would undoubtedly be a very rich individual!

I express my appreciation to Dr Sam Widijatmoko, a colleague but more importantly, a good friend, who engaged in countless discussions and generously shared insightful ideas.

A kind thank you to both Dr Luis Roman Ramirez and Dr Albert Lipson for their contributions towards our publications.

I would like to acknowledge the work carried out by the MEng students studying at the University of Birmingham – Aran Nguyen, Eve Nelson, Jimmy Wu, Lucy Phillipson, Mueen Ikhlaq, and Timothy Lee. Their dedicated work and interesting findings have supported this research.

A special acknowledgement is extended to the dedicated staff, IT team, and colleagues at the School of Chemical Engineering. Their camaraderie and support have made them not just colleagues but true friends.

I am profoundly fortunate to be surrounded by a network of treasured friends and family who have always provided me with endless support throughout this rollercoaster of a journey.

I cannot even begin to describe the perpetual support, motivation, and encouragement my parents have provided throughout my education, so thank you both. To my siblings, Kieran, Meera, and Rio, for what I perceived at the time as daily interruptions when writing up, on reflection, now stand as cherished moments in our memories.

For as long as I can remember, my father has instilled in my siblings and I, the belief that we can achieve anything we set our minds to with preparation, hard work, and dedication. This milestone truly feels like a testament to his inspiring words.

"One, remember to look up at the stars and not down at your feet. Two, never give up work. Work gives you meaning and purpose and life is empty without it. Three, if you are lucky enough to find love, remember it is there and don't throw it away".

Stephen Hawking (1942-2018)

Peer Reviewed Publications and Conference Proceedings

Published papers:

1. Vapor Equilibrium Data for the Binary Mixtures of Dimethyl Carbonate and Ethyl Methyl Carbonate in Compressed Carbon Dioxide. (2023)
   International Journal of Thermophysics. Impact Factor – 2.416
   doi.org/10.1007/s10765-023-03186-2

2. Roadmap for a sustainable circular economy in lithium-ion and future battery technologies - Electrolyte recovery and recycling (2023)
   Journal of Physics: Energy. Impact Factor – 6.9
   doi.org/10.1088/2515-7655/acaa57

Conferences:

1. Faraday Institution Conference, 2023 – Birmingham, UK

2. Batteries Event, 25th Edition, 2023 – Lyon, France

Table of Contents

List of Figures

List of Tables

Glossary of Terms

AARD	Average absolute relative deviation
ANOVA	Analysis of variance
BMS	Battery management system
BP	Boiling point
BPR	Back pressure regulator
CCD	Central Composite Design
CER	Constant extraction rate
CPA	Cubic Plus Association
DC	Diffusion controlled
DMC	Dimethyl carbonate
DOE	Design of Experiments
DOE-OSTI	Department of Energy - Office of Scientific and Technical Information
EC	Ethylene carbonate
ECR	Elliott Combining Rule
EMC	Ethyl methyl carbonate
EOL	End of life
EoS	Equation of State
ESW	Electrolyte stability window
EV	Electric vehicle
FER	Falling extraction rate
FKM	Fluorine kautschuk material (Fluroelastomer)
GC	Gas Chromatograph
FID	Flame Ionisation Detector
MS	Mass Spectrometry
TCD	Thermal Conductivity Detector
HEV	Hybrid electric vehicle
HF	Hydrogen fluoride
HPLC	High-Pressure Liquid Chromatography
HPV	High-pressure vessel
HRR	Heat release rate
IC-CD	Ion Chromatography-Conductivity Detection
ICE	Internal combustion engine
ICP-OES	Inductively Coupled Plasma – Optical Emission Spectroscopy
ID	Internal diameter
IEA	International Energy Agency
LCO	Lithium cobalt oxide
LFP	Lithium iron phosphate
LIB	Lithium-ion battery
LiF	Lithium fluoride
$LiPF_6$	Lithium hexafluorophosphate

LME	London Metal Exchange
LMO	Lithium manganese oxide
LOD	Limit of detection
LTO	Lithium titanate oxide
MP	Melting point
MPV	Minor pressure vessel
MST	Méndez-Santiago and Teja
NBR	Nitrile butadiene rubber
NCA	Lithium nickel cobalt aluminium oxide
NIST	National Institute of Standards and Technology
NMC	Lithium nickel manganese cobalt oxide
NMR	Nuclear Magnetic Resonance
OD	Outside diameter
OEM	Original equipment manufacturers
OFP	Organofluorophosphates
P&ID	Piping and instrumental diagram
PC	Propylene carbonate
PF_5	Phosphorus pentafluoride
PR	Peng Robinson
PTFE	Polytetrafluoroethylene
ReLiB	Recycling of Lithium-Ion Batteries
RF	Response factors
RGD	Rapid gas decompression
RSD	Relative standard deviation
RSM	Response surface methodology
SBCF	Subcritical fluid
$scCO_2$	Supercritical carbon dioxide
SCF	Supercritical fluid
SDS	Safety data sheets
SEI	Solid electrolyte interphase
SEM	Scanning Electron Microscopy
SFC	Supercritical Fluid Chromatography
SFE	Supercritical fluid extraction
SOC	State of charge
SOP	Standard operating procedure
SRK	Soave Redlich-Kwong
STP	Standard temperature and pressure
TGA	Thermogravimetric Analysis
UV	Ultraviolet
vdW	van der Waals
VLE	Vapour-liquid equilibrium
WHO	World Health Organisation

Nomenclature

a	Attraction parameter
a_0	Characteristic parameter in CPA
b	Repulsion parameter
c_1	Characteristic parameter in CPA
D	Diffusivity
F	Faraday constant
g	Radial distribution function
k_{ij}	Binary interaction parameter
M_r	Relative molecular mass
n	Number of moles
P	Pressure
P_c	Critical pressure
P_v	Vapour pressure
Q	Electric charge
R	Universal gas constant
T	Temperature
T_c	Critical temperature
T_r	Reduced temperature
V	Total volume
x	Total number of electrons
X_A	Fraction of molecules not bonded at site A
$\bar{x}$	Mean value
y	Vapour mole fraction
ρ	Density
μ	Dynamic viscosity
ν	Kinematic viscosity
η_{JT}	Joule-Thomson coefficient
ω	Acentric factor
ε	Relevant permittivity

List of Appendices

Chapter 1: Introduction and Objectives

1.1 Motivation

"We will not stop until every car on the road is electric."

famously quoted by Elon Musk, the Co-Founder & CEO of Tesla Inc., in 2011. Today, the electric vehicle (EV) market is thriving and more valuable than ever, with global sales increasing yearly. However, despite the rapid advancements to decarbonise personal vehicles, the process of recovering and recycling end-of-life lithium-ion batteries (LIBs) has not been developed with the same resolve and vigour. This issue must be addressed to ensure the sustainable growth of the EV market.

Lately, there has been increasing pressure from governments and organisations globally to impose new directives to promote greater recycling rates and reduce greenhouse emissions. Currently, only a small fraction of all LIBs are recycled, and the few that are, undergo recycling practices that exclusively focus on recovering valuable metals.

Supercritical carbon dioxide has proven to be an effective extraction medium, proficient in recovering organic, solvent-free extracts. Naturally, carbon dioxide is the preferred choice due to its mild critical temperature and pressure requirements, low toxicity, non-flammability, and abundance. Widely validated across various industrial sectors such as food, pharmaceutical, and waste treatment, this green technology is an alternative to conventional liquid extraction methods for recovering LIB waste [1, 2].

Supercritical carbon dioxide exhibits a high density and solvating power, through its gas-like viscosity and high diffusivity, allowing a more effective permeation of solid matrices than conventional liquid extraction techniques [3].

1.2 Background

In 2023, the International Energy Agency (IEA) reported that global sales of electric vehicles (EVs) exceeded 12 million units, accounting for more than 14% of all vehicle sales worldwide, see **Figure 1-1**. This represented an exponential growth of over 35% from the previous year. With the support of existing policy measures and additional stimulus, there are now over 26 million EVs on the road [4, 5].

Lithium-ion technologies power the majority of EVs, known for their high energy density and voltage discharge capabilities in contrast to other battery chemistries. However, in the US, the EU, and Australia, the proportion of end-of-life (EOL) LIBs collected and recycled currently is only 3-5% [6], in comparison to other battery chemistries such as lead-acid, which have a recycling rate of close to 100% in the UK alone [7].

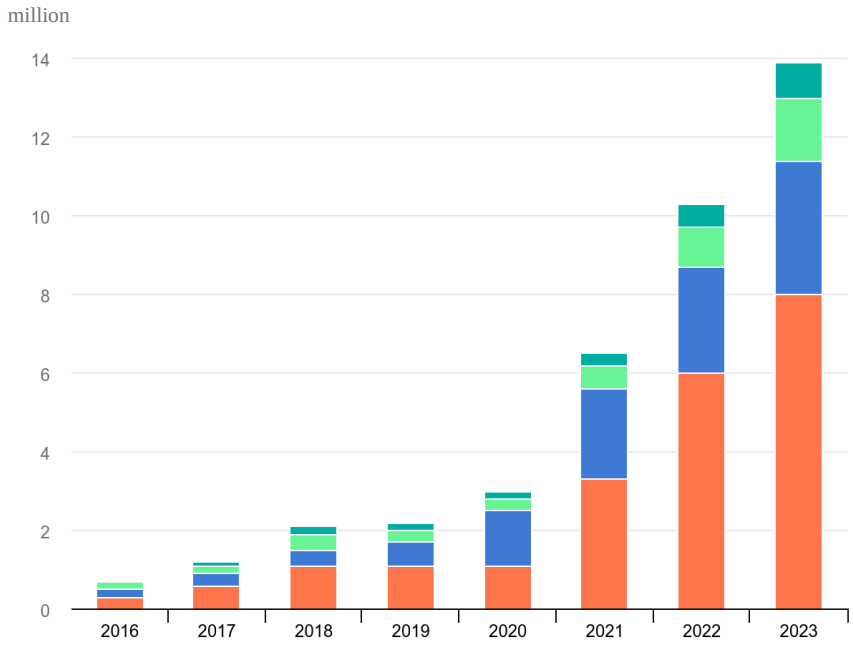

Figure 1-1: Global electric vehicle sales; (●) China, (●) Europe, (●) United States, (●) Other [5].

Of the small proportion of LIBs that are recycled, many are likely to undergo a process that will not necessarily recover all the raw materials within. Generally, four major recycling methods exist: (i) pyrometallurgical treatment, (ii) hydrometallurgical treatment, (iii) direct recycling, and (iv) a combination of all these processes [8-10].

These recycling techniques all share a common interest; they all primarily focus on raw components based exclusively on their economic value. Within the pyrometallurgical method the electrolyte and separator materials would be incinerated producing a vast array of toxic emissions, and in other techniques the electrolyte would be neutralised with chemicals, thus unrecoverable.

The economic incentives primarily focus on the supply and demand of raw materials required to manufacture a LIB, such as lithium. Reprocessing the end-of-life lithium could gradually reduce the strain on supply and the proportion of lithium required to be mined. As long as demand remains relatively constant, a greater overall supply would drive down the market price.

Materials from the battery device can be directly recycled in their raw form, but this generally requires specialised processes and equipment. Alternatively, the end-of-life battery devices can be used in second life applications, such as energy storage, where their lesser efficiency and charge capacity would be adequate [11].

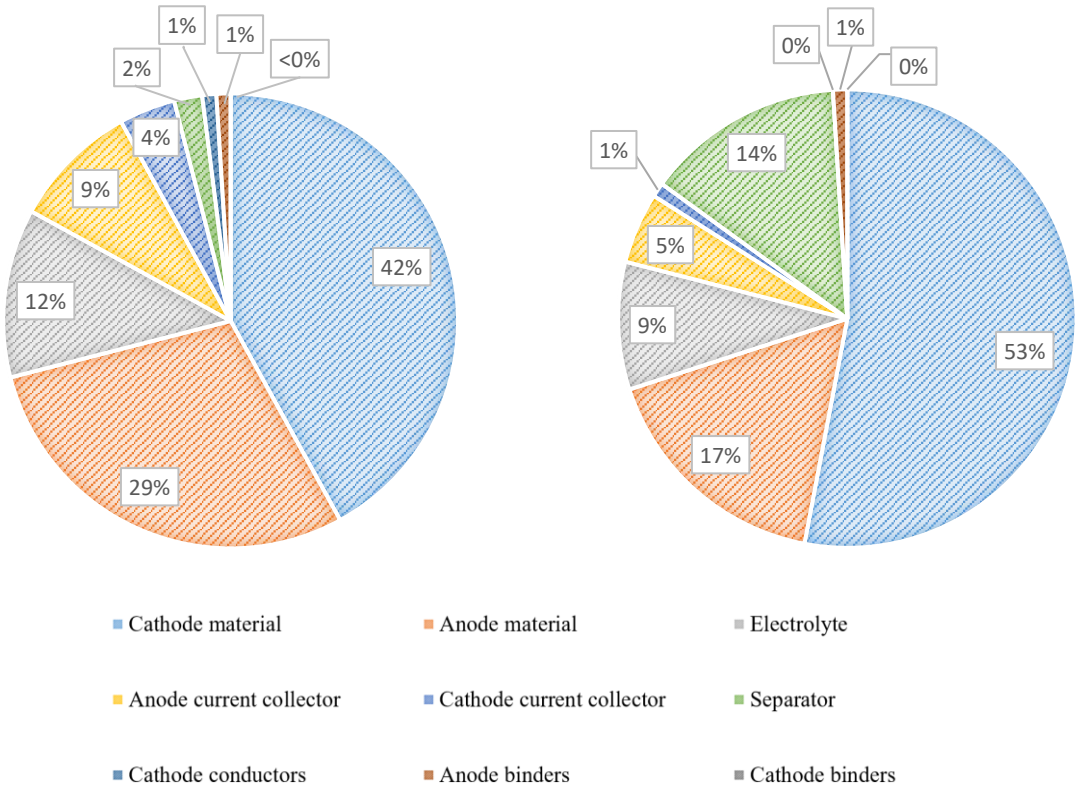

Figure 1-2:Typical cylindrical LIB by components. Mass composition (left), cost breakdown (right) [12].

The composition of the LIB electrolyte encompasses a lithium conducting salt dissolved in several solvent carbonates, along with a series of additives. By mass, the electrolyte component accounts for 10-15% of the total weight of the LIB [12], as seen in **Figure 1-2**. Compared to the electrodes (anode and cathode), which account for more than two-thirds of the total value of the LIB, the electrolyte is relatively inexpensive, equating to less than 10% of the total value [13].

However, due to increasing pressures from economic factors, social influences, and governmental reforms, the obligation to recycle the LIB electrolyte is now ever more paramount.

1.3 Aims and Objectives

The principal aim of this research is to assess and propose a viable and sustainable process for recovering the electrolyte component of lithium-ion batteries (LIBs) used in commercial electric vehicles (EVs) through the application of pressurised carbon dioxide extraction.

The following research objectives were introduced to reach the principal aim:

1. Determine the solubility behaviour of LIB electrolyte solvents in carbon dioxide under a range of temperature and pressure conditions.
2. Investigate the intermolecular interactions of components within a vapour-liquid equilibrium (VLE) quaternary system that resembles the composition of the LIB electrolyte solvent.
3. Optimise the pressurised carbon dioxide extraction process for the recovery of artificial LIB electrolyte.
4. Establish a standard protocol for the safe and efficient disassembly of commercial EV LIBs.
5. Apply the optimised pressurised carbon dioxide extraction technique to recover the electrolyte component from disassembled commercial EV LIBs.

1.4 Research Plan

To achieve the aim and objectives, the following key research phases were outlined and completed in the form of a research plan:

First Phase – Project Initiation

1. Literature review: A comprehensive literature review was conducted to investigate the factors involved in achieving the overall goal. This included fundamental knowledge of LIBs and their integration into EVs, supercritical fluids and their applications, and current LIB recovery techniques. These fields were examined and assessed to determine the current level of research.
2. Development and construction of a suitable experimental process: To determine the solubilities of the electrolyte component in carbon dioxide, a practical high-pressure rig with vapour sampling capabilities was developed. The high-pressure carbon dioxide extraction processes required a more intricate design to allow for collection of liquid electrolyte, and static and dynamic operation. Developing operational steps and awareness of safety protocols were crucial for both working rigs.
3. Throughout all experimental chapters, characterisation and quantification were a necessity. The literature review guided identifying the most suitable analytical methods, with gas chromatography being the foremost choice. Additionally, understanding each instrument's operation and safety procedures was imperative.

Second Phase – Solubility Studies

1. Binary system – The initial work of the solubility studies was to establish the solubility behaviours of typical LIB electrolyte components in pressurised carbon dioxide. Solubility data is imperative to determine the feasibility of the supercritical extraction process.

Each binary system was correlated using a range of Equation of State (EOS) and semi empirical models.

2. Multicomponent system – Building upon the binary solubility studies, a mixture resembling the composition of the LIB electrolyte solvent component was created. The quaternary system was established to understand each component's selectivity and the behaviour of intermolecular interactions in the solvation process.

Third Phase – Extraction of LIB Electrolyte Using Pressurised Carbon Dioxide

1. An artificial mixture of LIB electrolyte was created and recovered from a cotton wool matrix using pressurised carbon dioxide. A range of factors were explored, namely flowrate, extraction duration, temperature, and pressure. This allowed the optimisation and enhancement of the pressurised carbon dioxide extraction process.
2. A standard protocol for efficiently dissembling a commercial EV LIB had to be established.
3. Proceeding with the recovery of the artificial LIB electrolyte using pressurised carbon dioxide, the most effective operational conditions were adopted and utilised to recover the electrolyte component from a commercial EV LIB.

1.5 Thesis Structure

The research thesis is structured across seven chapters, detailed as follows:

Chapter 1: Introduction

Chapter 2: Literature Review

Chapter 3: Materials and Analytical Techniques

Chapter 4: Solubility Measurements of LIB Electrolyte Components in Carbon Dioxide

Chapter 5: Extraction of Artificial LIB Electrolyte Using Pressurised Carbon Dioxide

Chapter 6: Recovery and Characterisation of LIB Electrolyte from Electric Vehicles

Chapter 7: Conclusions and Recommendations for Future Work

Following the introduction, Chapter 2 presents a literature review of the key areas of achieving the goal. This includes LIB fundamentals and their integration into EVs, the LIB electrolyte component, supercritical fluids and their applications, and current LIB recovery techniques.

Chapter 3 covers the materials and analytical techniques employed throughout the research. In Chapter 4, the solubility measurements of LIB electrolyte components in carbon dioxide are determined and discussed. Chapter 5 presents the utilisation of the solubility data to extract an artificial LIB electrolyte using pressurised carbon dioxide. Chapter 6 focuses on the processing, recovery, and characterisation of commercial EV LIB material. Finally, Chapter 7 concludes the thesis by summarising the main findings and providing practical recommendations for future work.

References – Chapter 1

[1] C.A. Eckert, B.L. Knutson, P.G. Debenedetti. Supercritical fluids as solvents for chemical and materials processing. Nature. (1996).383(6598):313-318. Doi:10.1038/383313a0.

[2] E. Ibáñez, J.A. Mendiola, M. Castro-Puyana. Supercritical Fluid Extraction. In: B. Caballero, P.M. Finglas, F. Toldrá, editors. Encyclopedia of Food and Health. Oxford: Academic Press; (2016). p. 227-233.

[3] P. Ferguson, R. Cross, G. Schad. Chapter 8 - Application of SFC for the characterization of formulated drug products. In: M. Hicks, P. Ferguson, editors. Separation Science and Technology. 14: Academic Press; (2022). p. 221-255.

[4] E.C. Oskaras Alsauskas, Andrew Daou, Alexandre Gouy, Mathilde Huismans, Hyeji Kim, Jean-Baptiste Le Marois, Shane McDonagh, Apostolos Petropoulos and Jacob Teter. Global EV Outlook 2023 - Catching up with climate ambitions. International Energy Agency; 2023.

[5] E. Connelly. Electric car sales break new records with momentum expected to continue through 2023(2023). Available from: https://www.iea.org/data-and-statistics/charts/electric-car-sales-2016-2023.

[6] Z. Dobó, T. Dinh, T. Kulcsár. A review on recycling of spent lithium-ion batteries. Energy Reports. (2023).9:6362-6395. Doi:https://doi.org/10.1016/j.egyr.2023.05.264.

[7] A. Sonoc, J. Jeswiet. A Review of Lithium Supply and Demand and a Preliminary Investigation of a Room Temperature Method to Recycle Lithium Ion Batteries to Recover Lithium and Other Materials. Procedia CIRP. (2014).15:289-293. Doi:10.1016/j.procir.2014.06.006.

[8] C. Ekberg, M. Petranikova. Lithium Batteries Recycling. Lithium Process Chemistry Resources, Extraction, Batteries, and Recycling: Elsevier; (2015). p. 237-243.

[9] R. Sommerville, P. Zhu, M.A. Rajaeifar, O. Heidrich, V. Goodship, E. Kendrick. A qualitative assessment of lithium ion battery recycling processes. Resources, Conservation and Recycling. (2021).165:105219. Doi:https://doi.org/10.1016/j.resconrec.2020.105219.

[10] L. Gaines. Lithium-ion battery recycling processes: Research towards a sustainable course. Sustainable Materials and Technologies. (2018).17:e00068. Doi:https://doi.org/10.1016/j.susmat.2018.e00068.

[11] C. Xu, P. Behrens, P. Gasper, K. Smith, M. Hu, A. Tukker, et al. Electric vehicle batteries alone could satisfy short-term grid storage demand by as early as 2030. Nature Communications. (2023).14(1):119. Doi:10.1038/s41467-022-35393-0.

[12] D. Greenwood. Future Lithium Ion Batteries. The University of Warwick Advanced Propulsion Systems / WMG; 2016.

[13] E. Mossali, N. Picone, L. Gentilini, O. Rodrìguez, J.M. Pérez, M. Colledani. Lithium-ion batteries towards circular economy: A literature review of opportunities and issues of recycling treatments. Journal of Environmental Management. (2020).264:110500. Doi:https://doi.org/10.1016/j.jenvman.2020.110500.

Chapter 2: Literature Review

2.1 Lithium-ion Batteries (LIBs) and their Integration into Electric Vehicles (EV)

2.1.1 Introduction

Lithium-ion batteries (LIBs) have played a pivotal role in providing convenient and portable power for various devices, ranging from mobile phones and laptops to power tools. The widespread adoption of lithium-ion technology is attributed to its superior combination of high energy density, extensive cycle life, and continually decreasing manufacturing costs as observed in **Figure 2-1**. The growing demand for LIBs has been a key driver in cost reduction. Initially used predominantly in portable devices and electronics, the landscape changed in 2008 when Tesla introduced the first LIB-powered electric vehicle (EV). Since then, the market share for EVs has steadily increased, with today's demand for lithium supply being predominantly driven by the EV sector, surpassing that of any other consumer electronics [1, 2].

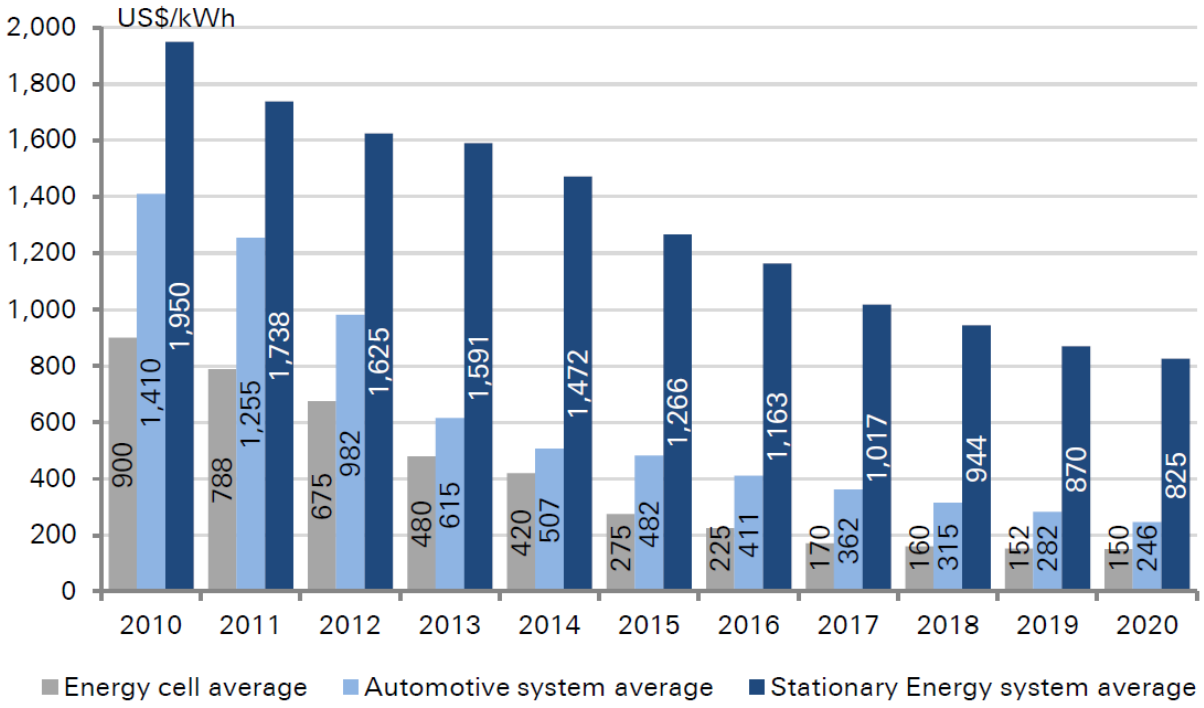

Figure 2-1: Declining price trend of lithium-ion batteries by application [3].

The groundbreaking lithium-ion battery technology was not the discovery of one individual but rather transpired through the collaborative efforts of numerous leading experts across different fields. One of the initial breakthroughs involved identifying a suitable cathode material that served as an efficient oxidising agent, remained stable when in contact with the electrolyte, and was relatively cost-effective to produce [4].

During the 1980s, John Goodenough and his team tested many oxide variations, finding it challenging as more lithium deposited into the positive electrode would result in a greater proportion of energy output. However, the downside of a cathode containing a large lithium-based composition occurred post-redox reaction, when the lithium-ion transfer would leave the cathode hollow, resulting in the electrode structure crumbling upon itself when reaching approximately 4 volts. The solution was found by incorporating a stable metal oxide of cobalt to create the lithium cobalt oxide (LCO) cathode. This technology and a graphite anode, gave rise to the first rechargeable LIB, later commercialised by Sony in 1991 [5].

In 2019, John B. Goodenough, M. Stanley Whittingham, and Akira Yoshino were honoured with the Nobel Prize in Chemistry for their significant contributions to the development of lithium-ion technology during the 1980s and 1990s [6].

2.1.2 LIB components and operation

In simple terms, a battery operates on the principle of converting chemical energy into electrical energy. A key distinction in the design of a LIB is the reversibility of the chemical reaction, enabling the battery to be recharged and discharged numerous times.

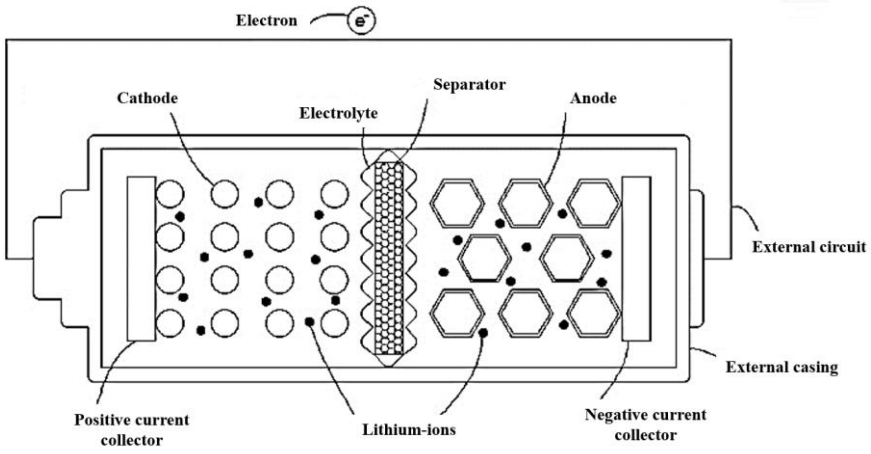

Figure 2-2: Simple illustration of the core components within a classic LIB design.

The battery casing encompasses five main constituents (as depicted in **Figure 2-2**): cathode, anode, separator, electrolyte and two current collectors. During battery discharge, the anode undergoes oxidation, releasing lithium ions that traverse the electrolyte and separator to reach the positive electrode, the cathode, where reduction occurs. Notably, electrons cannot pass through the electrolyte as lithium ions do; instead, they flow externally through the outer circuit. Both processes must occur simultaneously for the battery to function [7].

Electrochemical reactions can estimate the specific capacity of the electrodes within the LIB. For instance, consider the lithium cobalt oxide (LCO) battery, where two electrochemical redox reactions occur.

The first half-cell reaction initiated at the graphite anode undergoes oxidation and can intercalate reversibly with lithium to form LiC_6:

$$Li^+ + e^- + C_6 \leftrightarrow LiC_6 \quad \textbf{(2-1)}$$

The second transpires at the $LiCoO_2$ cathode (reduction reaction):

$$CoO_2 + Li^+ + e^- \leftrightarrow LiCoO_2 \quad \textbf{(2-2)}$$

The overall reaction is:

$$CoO_2 + LiC_6 \rightarrow LiCoO_2 + C_6 \quad \textbf{(2-3)}$$

Faraday's second law of electrolysis derives the following equation:

$$m = \frac{Q\ M}{n\ F} \quad \textbf{(2-4)}$$

By simple rearrangement, theoretical specific capacity ($C_{theoretical}$) is:

$$C_{theoretical} = \frac{xF}{nM} \quad \textbf{(2-5)}$$

Where, m is the mass of the substance (g), n is the number of moles of the active electrode material (mol), Q is the electrical charge (C), M is the molecular weight of the active electrode material (g/mol), F is Faraday's constant (F = 96485 C/mol) and x is the total number of electrons transferred within the reaction.

The specific theoretical capacity of both the graphite anode and the $LiCoO_2$ cathode can be estimated as follows:

Graphite anode:

$$C_{theoretical} = \frac{1\ x\ 96485\ C/mol}{6\ x\ 12\ g/mol}$$

$$= 372\ mAh/g$$

$LiCoO_2$ cathode:

$$C_{theoretical} = \frac{1\ x\ 96485\ C/mol}{1\ x\ 98\ g/mol}$$

$$= 274\ mAh/g$$

However, realistically speaking, the maximum achievable capacity for LIBs is nearer 140 mAh/g. This is due to a structural limitation where, after 50% of the lithium supply within the cathode structure has been extracted, a structural transformation is observed from the hexagonal to monoclinic phase. This transformation reduces the cathode's electrochemical capacity due to structural instability. To accurately gauge the specific capacity of a LIB, other vital internal battery components and the battery management system must also be considered [8-11].

Electrodes, solid conductors facilitating the movement of electrons and ions between the anode and cathode, are coated onto the surface of current collectors. An aluminium foil is commonly used as the cathode current collector; similarly, a copper foil is used as the anode current collector. Electrodes should exhibit properties such as high conductivity, thermal and chemical stability, and ease of fabrication.

Metal oxides, including lithium manganese oxide (LMO), lithium cobalt oxide (LCO) and lithium nickel manganese cobalt oxide (NMC), are frequently used to produce the cathode. These compositions greatly affect battery dynamics, influencing vital qualities such as cycle life, energy density, and economics, as the cathode typically accounts for at least 25% of the battery's overall cost [12, 13].

Carbon anodes remain the most dominant material in LIBs today due to their lattice structure, which can facilitate lithium ions' movement and temporary capture between electrodes, resulting in high cyclability. However, present and future materials also consist of metallic composites and silicon-based nanomaterials.

The electrolyte, which permits the transportation of lithium ions between electrodes, comes in various types, including aqueous solutions, conducting salts in solvents, and solid electrolytes. The following subchapter will focus exclusively on this component and give more insight. Suspended within the electrolyte is a thin insulation layer, the separator. Typically constructed from a microporous polymer, the separator allows the free movement of lithium ions between electrodes and prevents the electrodes from coming in contact with each other [14]. If the electrodes were to come into contact, the battery would short circuit, potentially resulting in a fire via the intermediary step, thermal runaway. Thus, before the temperature rapidly climbs enough to trigger thermal runaway, the separator acts almost like a fuse, melting and blocking the permeable pores, preventing the transportation of lithium ions and effectively shutting down all cell operations [11]. The microporous polymeric separator is typically manufactured from either polypropylene or polyethylene or, in some cases, a blend of the two. They promote high chemical stability and robust mechanical properties. The membrane can consist of a single, monolayer, or several layers, depending on the application. Other types of separators can also include nonwoven mats, composite membranes, and gel-polymer electrolyte membranes [15].

During the first charging cycle, it was discovered that a protection layer is formed upon the surfaces of both electrodes, the solid electrolyte interphase (SEI). The SEI layer was found to protect the electrolyte from further decomposition, as prolonged contact with electrons results in electrolyte decomposition and drying. Hence, the SEI acts as a barrier to the electrons, preventing their passage due to insulation properties but allowing the lithium ions to pass through. Formation of SEI occurs when lithium ions (approx 5% wt) react with the electrolyte at both electrode surfaces, creating a barrier formed from the decomposed electrolyte constituents. However, the flip side to forming the SEI layer is that it has been allegedly linked to being the dominant driver of cell ageing, directly responsible for lithium loss and electrolyte drying associated with calendric ageing [16, 17]. The working nature and formation mechanism is not yet completely understood as the layer is incredibly thin (10-100 nm) and highly sensitive to oxygen and water. Additionally, the SEI layer is formed from a structural species similar to the electrolyte, making it difficult to differentiate and characterise using most analytic techniques [18].

2.1.3 LIB chemistries

As stated, cell chemistries directly affect the operating properties; each chemistry is unique and requires a diverse set of materials and composition blends. The strengths and weaknesses of each chemistry enable some chemistries to be more suitable in certain applications than others; a comparison of different LIB chemistries is exhibited in **Figure 2-3**.

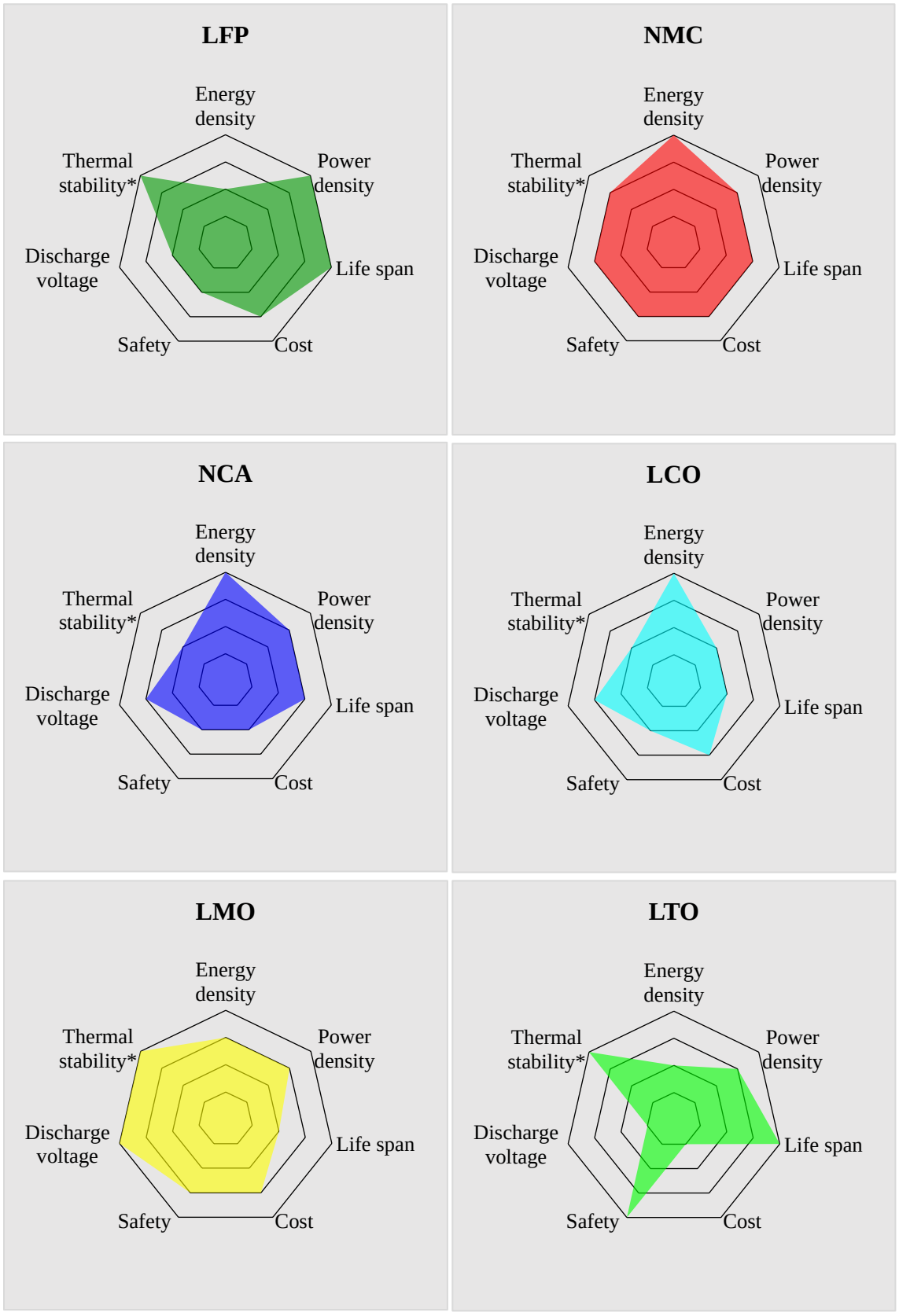

*Note: The thermal stability comparison is solely based upon the upper-temperature limit and does not evaluate data below 0°C.

Figure 2-3: Comparison of the characteristics of commercial LIB chemistries [19].

In 1996, the University of Texas identified phosphate as an effective cathode material. Lithium Iron Phosphate (LFP), $LiFePO_4$, has an olivine crystal structure, where phosphorus and iron form a layered, complex structure with a network of oxygen atoms packed throughout. Due to the strong bonds formed between oxygen and phosphorus atoms, LFP is considered to be incredibly safe. Additionally, the integration of iron creates stability within the chemistry, and since iron is abundant, it is relatively inexpensive compared to other chemistries. LFP can operate in a wide temperature range from -30 ℃ to 60 ℃, making it less susceptible to thermal runaway. However, it produces a low nominal voltage of approximately 3.3 volts, limiting the maximum energy density achievable [20, 21]. Despite this limitation, the long life of LFP makes it a suitable choice for energy storage systems, as well as other applications. In China, most commercial EV manufacturers prioritise safety and use LFP technology. BYD Company Ltd is a leading Chinese manufacturer that has implemented LFP chemistry into a wide range of automotive designs, including transit buses, taxis, mining vehicles, and consumer vehicles [3, 22].

Lithium Nickel Manganese Cobalt Oxide (NMC), $LiNiMnCoO_2$, is highly successful in many applications and is formed by combining nickel, manganese, and cobalt to create a layered crystal structure. The arrangement of alternating layers of transition metals forms octahedral sites; this structure can vary significantly depending on the "blend" of transition metals upon application. Combining these three elements creates a balanced formula that provides excellent attributes while offsetting any flaws in any one element. Nickel is known for its high energy density but comes at the cost of poor stability. However, combining nickel with manganese improves stability and reduces internal resistance [20]. Traditionally, all the transition metals were used equally in a 1:1:1 ratio, but cobalt is considerably more expensive than the other two elements. According to the London Metal Exchange (LME), the cost of one tonne of cobalt has

fluctuated between $25,000 and $80,000 in the last five years [23]. To decrease the overall cost of NMC, the blend ratio can be adjusted to reduce the proportion of cobalt used. NMC has many applications due to its high thermal stability and energy density. Numerous EV manufacturers have adopted this chemistry into their designs, including Nissan (Leaf), Mercedes (eCitaro), and BMW (i3) [21, 24].

The Lithium Nickel Cobalt Aluminium Oxide (NCA), $LiNiCoAlO_2$, chemistry has been available since 1999. It is known for its association with Tesla, as it is the only EV manufacturer to implement the chemistry into its design. A range of elements, including nickel, cobalt, and aluminium, are combined within the LIB to produce a layered crystal structure similar to NMC. The elements are arranged in alternating layers, allowing the lithium ions to occupy sites in between. NCA boasts high energy and power density with a relatively long lifespan. However, its safety and temperature stability fall short, as it suffers from thermal runaway at low temperatures close to 150℃. This issue is thought to be associated with adding aluminium to the blend. Additionally, the chemistry suffers from overwhelming capacity fade at high temperatures due to the severe ageing mechanism, SEI formation.

Similar to NMC, NCA also uses cobalt within the chemistry. Thus, different blends have been adopted to drive the overall cost of the LIB down. Tesla has been increasingly mindful of cost-saving and incorporates blending different compositions. From 2012 to 2018, Tesla successfully decreased the cobalt needed for their EVs by over 50 %. In 2012, production of the ‘Roadster’ required ~11 kg of cobalt, while the newer ‘Model 3’ needed only ~4.5 kg of cobalt in 2018 [20, 21, 25].

Lithium Manganese Oxide (LMO), $LiMn_2O_4$ was initially discovered to be a suitable cathode material in the early 1980s, but it took almost another 15 years to commercialise fully. LMO is

unlike the previous cathode materials covered. Its three-dimensional spinel lattice structure dramatically enhances the ion flow through the cathode, substantially improving the current control and reducing the internal resistance. LMO can function at a high nominal voltage of approximately 3.9 volts, so it's anticipated to have a high specific energy density. However, only close to half of the lithium ions can be removed from the oxide before the oxygen atoms oxidise the electrolyte or become depleted, affecting its energy density. Additionally, the chemistry suffers from poor cycling performance due to the manganese leaching out of the cathode during cycling. If the manganese becomes dissolved within the electrolyte, then over time, the impedance increases, and manganese will accumulate upon the anode SEI layer, possibly resulting in the formation of dendrites.

LMO does not depend on cobalt and nickel, which are used in other chemistries. The absence of these transition metals in this specific chemistry drives down the price, as manganese is relatively low-cost. However, due to the substandard energy density, lifespan, and specific capacity performance, the LMO chemistry is usually blended with other chemistries to improve the underlying weaknesses [20, 21].

Lithium Titanate Oxide (LTO), $Li_4Ti_5O_{12}$, has been known as a suitable replacement for graphite anodes since the 1980s. The arrangement of LTO resembles a spinel structure, similar to the LMO cathode chemistry, where the lithium ions occupy sites called “tunnels” within a three-dimensional lattice. The chemistry is often referred to as “zero strain” due to an insignificant volume change (<0.2%) when the transitions from lithiation to delithiation and vice versa occur. LTO has a specific energy density of roughly half of the graphite, standing at 175, and a low operating voltage compared to other LIB chemistries. However, LTO is one of the safest LIB anode chemistries available, making it popular in many portable medical apparatuses. LTO can be safely discharged in a wide range of temperatures (-30-55℃) and is

particularly effective at low temperatures, retaining 80% of its total charge capacity at a temperature of -30℃. Many applications use LTO due to its extended operational life cycle, with some LTO anodes sustaining tens of thousands of cycles. LTO can diminish the formation of the SEI layer around the anode and prevent the growth of dendrites, which reduces the internal resistance and capacity losses over time, prolonging the life of the LIB. Few EV manufacturers have implemented the technology into their design, but recognised brands include Honda (FIT) and Mitsubishi (i-MiEV). However, the prime applications of LTO LIBs are buses and railway appliances due to their high cycle life, ability to fast charge and achieve full depth of discharge after many thousands of cycles [21, 26, 27]. The German manufacturing giant Siemens has developed an electrified train with LTO chemistry and has sold the appliance in several locations across Europe. The specifications of the LIB within the electrified train are alleged to have a service life of 15 years and be capable of full capacity recharge in less than 12 minutes [28, 29].

Lithium Cobalt Oxide (LCO), $LiCO_2$, requires no introductions and is famously known as the first commercial LIB available. Its structure is similar to the NCA and NMC chemistry. It is formed from a layered crystal structure, establishing an octahedral structure with lithium and cobalt atoms surrounding the oxygen atom in a hexagonal symmetry. LCO has a high nominal and operating voltage, which enables a high theoretical specific capacity of 274 mAh/g. It has been used in many different appliances, but its market share is gradually declining due to its low stability and cycle life. LCO's cycle life is relatively low compared to other chemistries, and it does not retain stability at high temperatures, causing thermal runaway at temperatures near 200 ℃ [20, 21, 27]. Although the breaking point is centred around its economic viability, the high proportion of cobalt used in the overall cathode composition accounts for ≈ 60% of the total. In comparison, NMC, the chemistry incorporating the next highest proportion of cobalt,

has a content of 10-30% (depending on the blend). Cobalt is a highly expensive transition element and drives up the overall cost of EV battery packs, predominantly since EVs consist of many LIB cells. Despite this, some EV manufacturers, including Tesla (Roadster) and Smart (Fortwo), have opted for the LCO chemistry [21, 30].

2.1.4 LIB integration into EVs

Depending on the application, LIBs are manufactured in various shapes and sizes, primarily cylindrical, prismatic or pouch, each possessing unique properties despite nearly identical cell chemistry. Cell combinations can be varied, with a series arrangement increasing voltage and a parallel arrangement increasing current. Some applications, such as EVs, demand a much greater voltage and capacity since they operate between 200-800 V. In such a case, cells must be combined to satisfy the strain of demand. A single lithium-ion cell typically has a voltage between 2.5–4 Volts; for an EV, multiple cells are connected to meet the voltage requirements.

For example, in the BMW i3 EV, a cluster of 12 cells is combined to form a module. The module exists for practical reasons; they are low voltage (< 60 V) and inherently safer. The dimensions and weight are practicable, allowing operators to move the modules safely during EV manufacturing. The modules are protected via a metal frame and tough casing to shield the cells from external shocks, heat, and vibrations. Eight of these modules are then assembled to produce a pack. An EV battery pack can weigh several hundred kilograms and is fitted with a battery management system (BMS), which protects the pack by monitoring and regulating operational aspects, including voltage, state of charge, temperature, and cell health [11, 31, 32].

Unlike internal combustion engine (ICE) vehicles, EVs produce little or no sound as they do not rely on an internal combustion engine to propel the vehicle forward. Another advantage of EVs is their superior initial torque due to their simplified drive train, which makes them more

efficient when accelerating. In contrast, an ICE vehicle must divert the power through the transmission system and into the drivetrain, involving more components and incurring more significant losses. Nevertheless, consumers are still mindful of owning an EV due to major technology and social trade-offs, with insufficient infrastructure regarding recharge points, low driving range, and long recharge durations being the three leading concerns.

Despite a 250% increase in UK charging locations within the last three years, totalling over 50,000 units in 2023, it is still insufficient. As the use of EVs increases, the charging infrastructure needs to keep up. Additionally, some charging points may not support all types of vehicles, requiring adapters, and there is a risk of arriving at a charging point that may already be occupied [33].

Various factors, including the driving speed, driving style, load weight, driven terrain, and the use of energy-consuming applications such as air conditioning, influence the maximum driving range of an EV. Several factors will affect the time for an EV to charge, including battery size, its current state (empty or full), the maximum charging rate of the vehicle or charging point, and environmental factors [34].

Temperature is known to impact battery efficiency and reduce lifespan, especially within cold climate countries such as Canada and Alaska, both of which have been known to experience temperatures below -15℃. Typically, an EV's driving range will be diminished by 20-50% in extremely cold climates as internal resistances increase, inducing the formation of dendrites and excessive heat build-up. Similarly, in hot climates, complications arise; the surrounding temperature increases the internal battery core temperature. Thus, if there is no method of dissipation to cope with the influx in temperature, thermal runaway is likely to occur [35, 36].

2.1.5 Hazards of LIBs

A fundamental challenge that needs to be addressed is the safety concerns surrounding LIBs. It is widely known that many LIB chemistries are relatively toxic and can be prone to fire hazards in some conditions. Since LIBs have dominated the battery market, fires have become an increasingly significant issue due to the substantial upgrade in energy density, which was not achieved in the technologies before LIBs. Regarding energy density, Li-ion technology possesses three times the energy density of the nickel-metal hydride (Ni-MH) chemistry [37].

In the event of a battery fire, the severity depends on numerous factors, with size, number of batteries used per application, power rating, and the manufacturing materials being paramount. Thus, considering size and power rating, an EV would pose a greater risk than an e-cigarette or smartphone. Additionally, while fires are often associated with being the sole risk of LIB hazards, many overlook the silent killer, the toxic gases being produced and inhaled. Gases such as H_2, CH_4, CO, HF, and various other organic gases are produced from the combustion of a LIB.

When analysing the associated risk per device, investigations can be classified into three categories: electrical, mechanical, and environmental.

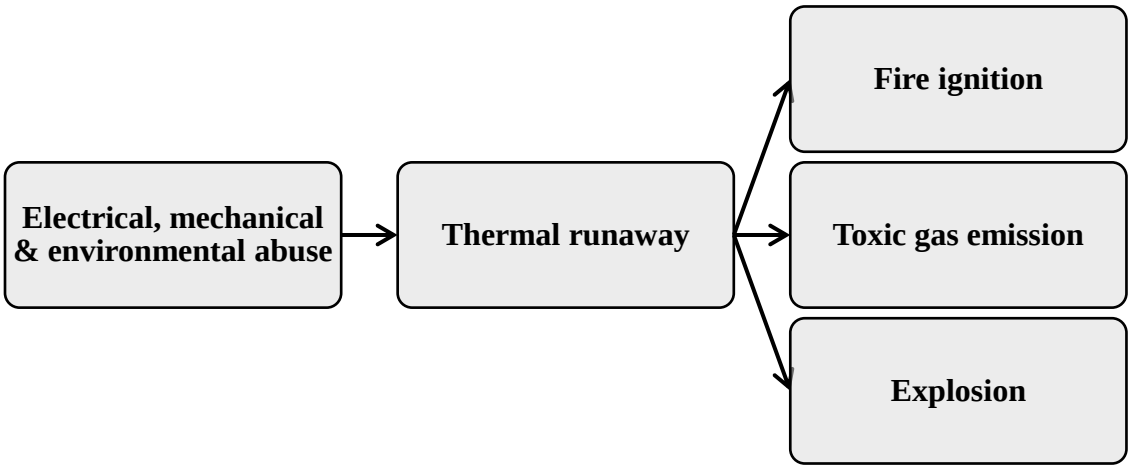

Figure 2-4: Mechanism of Lithium-ion battery failure as a consequence of abuse.

Electrical risks involve overcharging and internal circuit faults within the battery system; overcharging or charging the device at a higher power rating may severely degrade operating performance over time or render the device non-operational. Characteristics common with overcharging include intense heat generation and gas formation from electrolyte decomposition. However, if operating correctly, the BMS or power transmission control systems protect and mitigate many electrical risks.

Risks associated with mechanical issues primarily focus on appliances experiencing harsh impacts and collisions, which are expected in EV accidents. In the case of a severe collision, the battery is likely to become crushed or punctured, initiating a series of events. If the battery becomes crushed, electrolyte leakage may pose a fire risk due to the solvents' highly flammable properties. In an ideal outcome, reaching the melting point causes the pores within the separator to close, increasing internal resistance and inhibiting further battery operation [36, 38].

Penetration of the battery is regarded as one of the most aggressive forms of damage due to the combination of mechanical and electrical abuse arising simultaneously, particularly if the battery is punctured and exposed to air. To mitigate against the mechanical risks, the location

of the battery pack is generally reinforced with protective plates and extra reinforcement material, allowing it to retain its structure and avert deformation upon impact. Once pierced, an internal electrical shortage will occur, releasing electrical energy; the energy cannot be contained and is emitted as thermal energy until full discharge or critical temperature is attained. Researchers discovered that as much as 70% of the electrical energy can be discharged within the first 60 seconds, explaining the rapid temperature rise that follows [38].

2.2 LIB Electrolytes

2.2.1 Introduction

The electrolyte is a vital constituent in LIBs, often overlooked in operation and function. The electrolyte is responsible for the electrochemical performance, acting as a conducting medium that transfers lithium ions from the anode to the cathode and vice versa. Accounting for 10-15% of the total weight of a LIB, it wets into the porous electrodes and permeates the pore spaces within the separator membrane [39, 40].

Previously, LIBs incorporated aqueous electrolyte solutions. Although less flammable and toxic, the electrolyte stability window (ESW) was more constrained, limiting the maximum output to around 1.2 V. In contrast, non-aqueous electrolytes can achieve 4-5 V per cell, depending on the active components. Today, non-aqueous electrolytes are overwhelmingly the preferred choice in commercial LIBs, with other alternatives including polymer electrolytes, ionic liquids, and solid-state electrolytes [41].

This ionic conducting medium is essentially an electron insulator containing no free electrons; this prevents the electrons from flowing through the electrolyte; instead, the electric current moves through the current collectors and around the circuit. Anions assist the lithium ions as they traverse between each electrode. However, the electrolyte itself does not participate in the

redox reaction that occurs at each electrode. Once the lithium salts are dissolved within the electrolyte solution, the positively charged lithium cations pair up with negatively charged solvates. These charged particles move in opposing directions; the cations will move in the same direction as the electrical current flow, while the anions move in the opposite direction [42]. The composition of the electrolyte is divided into three fundamental components: the solvent, conducting salt and a wide array of additives.

2.2.2 Electrolyte solvents

Conventional electrolyte solvents consist of linear and cyclic carbonates, as illustrated in **Figure 2-5**. The most commonly used linear carbonates in commercial LIBs include dimethyl carbonate (DMC), ethyl methyl carbonate (EMC), and diethyl carbonate (DEC) [43].

Each organic carbonate demonstrates a range of chemical and physical properties; thus, a blend of multiple carbonates is combined to form a ratio close to 3:7 (v/v) consisting of cyclic and linear carbonates. This balance enhances the characteristics of the electrolyte and improves its operational efficiency [44].

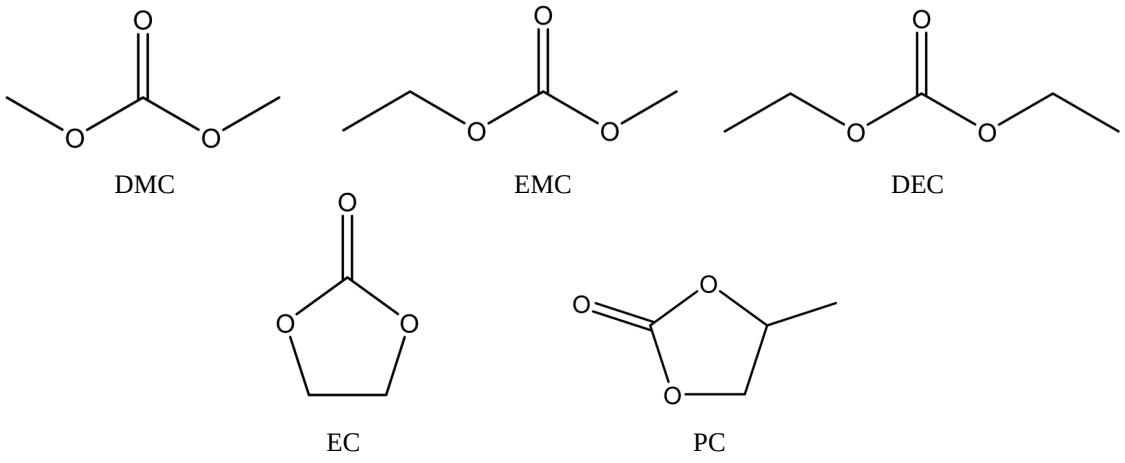

Figure 2-5: LIB electrolyte solvents; linear carbonates (top row), cyclic carbonates (bottom row).

DMC is a green solvent that readily biodegrades within the atmosphere. Today, the main line of formulation is through the oxidative carbonylation of methanol using oxygen. As a non-polar and aprotic alkyl carbonate, it exhibits good miscibility with water. Industrially, it is employed for various applications, from chemical transformation reagents to pharmaceutical applications. However, it has recently gained prominence as an electrolyte medium in LIBs [45, 46].

Like DMC, EMC is the simplest asymmetric ester and a key intermediate in organic synthesis. The synthesis of EMC traditionally involved the base catalysis transesterification of methyl chloroformate with ethanol, but due to environmental concerns, the transesterification of DMC with ethanol using a metal oxide catalyst is the synthesis route generally preferred. Driven by its industrial application in LIB electrolytes, its formulation is expected to reach upwards of 100,000 tonnes per year, a similar output as its equivalent, DMC [47-49].

Linear carbonates generally have a lower dielectric constant and are more volatile than their cyclic counterparts, partly due to their low flash points. Besides their structural differences, cyclic carbonates display significant chemical and thermal stability variations. The most widely applied cyclic carbonates within the electrolyte solvent blend are ethylene carbonate (EC) and propylene carbonate (PC).

Ethylene carbonate (EC) is a cyclic ester and is one of the most crucial components within the electrolyte solvent blend, exhibiting low toxicity and good solvating ability. In terms of electrolyte characteristics, it displays extensive cycle life and high chemical and electrochemical stability. Several methods exist to synthesise EC, but the leading process reacts ethylene oxide with carbon dioxide at high temperature and pressure conditions. Once heavily incorporated in the textile and cosmetic industry for its ability to dissolve a wide range of

polymers, polyester fibres, and resins. Its high dipole moment makes it suitable for high permeability applications, such as inks, dyes, lubricants, and electrolyte solvents [50-52].

However, EC's relatively high melting point and viscosity at low temperatures result in a low ionic conductivity. To address this, linear carbonates are combined to create a solution that can withstand a more comprehensive operating temperature range. Propylene carbonate, while offering a high dielectric constant and lower melting point than EC, cannot create an SEI layer with the graphite anodes [42]. Furthermore, PC tends to undergo co-intercalation, leading to the exfoliation of the graphite anode and structural deterioration. For this reason, PC is solely used in low concentrations, if at all [53].

2.2.3 Electrolyte conducting salts

The conducting salt is dissolved in a blend of solvents to create a solution that promotes ion mobility. On a volumetric basis, approximately 30-50% of the overall electrolyte composition consists of the conducting salt. Positively charged lithium cations are paired with approximately 3-4 anion solvate particles, allowing the lithium ions to be transported between electrodes during the charging/discharging cycle. Upon approaching the electrodes, the weak bonds between the ions are broken by the stronger charge strength of the electrodes, permitting the lithium ions to undergo oxidation and reduction.

Lithium hexafluorophosphate ($LiPF_6$) stands out as one of the most commercially successful conducting salts on the market, extensively employed in various LIB applications. Its structure comprises a central phosphate atom surrounded by six fluorine atoms, creating the anion that pairs with the lithium cation. $LiPF_6$ is a well-rounded conducting salt, demonstrating key attributes such as high ionic conductivity, a wide ESW, and the ability to passivate the

aluminium current collector. However, despite its distinguished operational performance, the conducting salt has several underlying weaknesses [42].

Firstly, the thermal stability of the conducting salt is exceptionally poor and is usually the limiting factor of the operational temperature in most LIBs. An equilibrium exists (**Equation 2-6**) between $LiPF_6$, phosphorus pentafluoride (PF_5), and lithium fluoride (LiF). As the temperature increases, $LiPF_6$ becomes progressively more unstable, and the equilibrium shifts towards the decomposition products.

$$LiPF_6 \rightleftharpoons LiF + PF_5 \qquad \textbf{(2-6)}$$

However, the main issue arises when the conducting salt comes into contact with moisture, as $LiPF_6$ undergoes hydrolysis, forming a range of highly toxic compounds, including hydrogen fluoride (HF). HF can react with internal components (both active and inactive) in the LIB, leading to functional deterioration.

Alternative commercially available conducting salts include lithium tetrafluoroborate ($LiBF_6$), lithium fluoroalkylphosphate (LiFAP), and lithium bis(oxalato)borate (LiBOB). $LiBF_6$ closely resembles the $LiPF_6$ compound, surpassing it in terms of thermal stability and safety, and the impact from moisture is less severe. Unfortunately, the ionic conductivity of this conducting salt is lesser than $LiPF_6$ due to its poor dissociation within the carbonates. This is the case with many lithium conducting salts, thus the replacement of $LiPF_6$ commercially is challenging.

2.2.4 Electrolyte additives

Although the electrolyte proves effective during operation, the solution remains relatively poor regarding safety. Flammable and toxic properties are exhibited due to the relatively low flashpoint and the vast range of decomposition products formed. Manufacturers are ultimately

under pressure to establish a fine balance between maintaining the operational performance of the electrolyte, preserving a degree of safety, and remaining receptive towards environmental factors.

LIB manufacturers will generally use very similar electrolyte materials; however, the precise ratio and addition of additives diverge upon application and are implemented to balance the imperfections of the solvents and the conducting salts. Accounting for less than 10% of the mass fraction of the electrolyte, additives can significantly enhance vital characteristics and critical areas such as the formation of the SEI layer, improved thermal stability, and prevention of overcharging [41, 54].

However, it is essential to consider that additives may enhance one or more LIB characteristic areas but may hinder another attribute as a result. For example, one additive may significantly improve the range of temperatures a LIB can operate between but negatively impact the overall ionic conductivity [42]. Several commercial additives and their associated function within current LIBs have been tabulated in **Table 2-1**.

Table 2-1: LIB electrolyte additives [41, 42, 54, 55].

Focus of Enhancement	Additive
Increase the SEI stability and reduce gas generation	Vinylene carbonate (VC), vinyl ethylene carbonate (VEC), allyl ethyl carbonate, vinyl acetate, divinyl adipate, acrylic acid nitrile, 2-vinyl pyridine, maleic anhydride, methyl cinnamate and vinyl-containing silane-based compounds
Cathode protection agent, 1) Scavenge moisture and acidic impurities. 2) Combines the metal ions into a protection surface layer.	Butylamine, N,N-dicyclohexylcarbodiimide, N,N-diethylamino trimethylsilane and lithium bis(oxalto)-borate (LiBOB)
Stabilising the conducting salt	Tris(2,2,2-trifluoroethyl) phosphite (TTFP), 1-methyl-2-pyrrolidinone, fluorinated carbamate and hexamethyl-phosphoramide
Fire retardant	Trimethyl phosphate (TMP), triethyl phosphate (TEP), tris(2,2,2-trifluoroethyl) phosphate, triphenyl phosphate (TPP)

	hexamethoxycyclotriphosphazene and methyl nonafluorobutyl ether (MFE)
Improve wettability	Cyclohexane and trialkyl phosphate
Viscosity diluter	Phosphorus pentoxide
Improve thermal stability	Methyl difluoroacetate (MFA)
Overcharging protection	Cyclohexyl benzene (CHB), tetracyanoethylene, tetramethyl phenylenediamine, dihydrophenazine, lithium fluorododecaborates and diphosphate
Corrosion resistant	Adiponitrile

2.2.5 The optimal design of electrolytes

To achieve effective battery operation, the design of electrolytes must strive to meet the following requirements:

1) High ionic conductivity: This allows the lithium ions to move freely between the electrodes during the charging and discharging cycle. High ionic conductivity promotes ion mobility by decreasing the resistance acting on the ions as they travel through the electrolyte material [42].
2) Superior solvation: The lithium salt should readily dissolve within the solvent mixture, ensuring the solution contains enough charge carriers for favourable ionic conduction. Solvation is directly dependent on the dielectric constant; a large dielectric constant increases the dissociation of the conducting salt, while a smaller dielectric constant promotes ion pair formation [41].
3) Flexible electrochemical stability window (ESW): Both solvents and salts must withstand a wide range of operating voltages while remaining relatively stable. Failure to operate within the ESW risks electrolyte degradation.

4) Viscosity: This is an unusually significant property for the solvents. It is favourable to retain a low viscosity to promote high ion mobility. However, solvents that exhibit a high dielectric constant invoke high viscosity, limiting the rate at which lithium ions can be transported within the electrolyte. Likewise, solvents exhibiting a low dielectric constant suffer in ion mobility but promote the ideal viscosity conditions required [56].
5) Wettability: This measures how effectively a liquid maintains contact and distributes itself over a solid surface. High wettability is desirable when referring to the interaction between the electrolyte, separator, and electrodes. Wettability can affect the separator and cell resistance; the separator's retention ability to absorb the electrolytes also profoundly impacts the internal resistance [57, 58].
6) Thermal stability: The electrolyte should be capable of operating at a range of temperatures whilst remaining stable. The melting and boiling points of the electrolyte constituents should be below and above the LIBs' operating temperature, respectively, ensuring the solution remains in the liquid state [43].
7) Chemically passive and environmentally safe: The electrolyte constituents should not spur a chemical reaction and should remain relatively inert when in contact with all LIB components (both active and inactive). The electrolyte should strive to be environmentally friendly, containing little to no toxic substances. Additionally, to keep the operation safe and low risk, the electrolyte solution should ideally have a high flash point and be non-flammable [41].
8) Economics: The electrolyte components should be relatively abundant and inexpensive. Additionally, the manufacturing and processing costs should follow the same trend.

2.2.6 Electrolyte degradation and ageing

Ageing is a phenomenon that undoubtedly leads to the demise of the LIB's operational ability. As countless charging/discharging cycles occur, the battery performance deteriorates. The capacity can no longer hold a charge equivalent to the original, resulting from the irreversible chemical and physical alterations that occur with extensive operation. Several factors affect ageing, but focusing purely on the electrolyte, the foremost includes solvent and conducting salt decomposition. A limited number of decomposition reactions are fully understood, and many ageing processes still require further research to determine the impact and range of products formed.

Solvent decomposition is understood to occur via two main pathways; the first is the most dominant process, whereby the cyclic carbonates undergo polymerisation. The second pathway involves the transesterification of a linear carbonate [44].

The principal cyclic carbonate, EC, undergoes a polymerisation reaction on the negative electrode surface, occurring when a Lewis acid, transesterification catalyst, or base initiates the reaction [59]. As a result, the cyclic carbonate is transformed into a copolymer and ejects a carbon dioxide molecule that incites gas generation, causing the volume to swell. However, this is an alternative type of battery degradation. Transesterification is the second major decomposition process. The pathway involves the linear carbonate, EMC, which undergoes the process in the presence of an acid or base catalyst to form DEC. However, film-forming additives are commonly added to suppress the transesterification reaction [44].

Over time, the liquid electrolyte is depleted due to electrolyte solvent degradation. This effectively leads to the electrodes drying out, promoting contact loss between the electrolyte and active materials and severely reducing the capacity of the LIB [17].

As mentioned previously, $LiPF_6$ is thermally unstable and in constant equilibrium with its decomposition products, largely influenced by the temperature effects and the moisture present. When exposed to moisture, a spontaneous chain reaction is triggered. The steps below outline the $LiPF_6$ hydrolysis process:

$$LiPF_6 \rightleftharpoons Li^+ + PF_5^- \quad \textbf{(2-7)}$$

$$LiPF_6 \rightleftharpoons LiF + PF_5 \quad \textbf{(2-8)}$$

$$PF_5 + H_2O \longrightarrow POF_3 + 2HF \quad \textbf{(2-9)}$$

$$POF_3 + H_2O \longrightarrow POF_2(OH) + HF \quad \textbf{(2-10)}$$

$$POF_2(OH) + H_2O \longrightarrow POF(OH)_2 + HF \quad \textbf{(2-11)}$$

Due to the high hygroscopicity of $LiPF_6$ and the decomposition products, the reaction proceeds to take place until all the water molecules have been fully expended; commercial-grade battery electrolyte typically consists of approximately 25 ppm of water moisture [60]. In the pure dry form (<10 ppm moisture), $LiPF_6$ is thermally stable within temperatures less than ~107℃, but once dissolved within the solvent solution, the intermolecular interactions result in progressive cell fading at temperatures surpassing 55℃, and when exposed to an abundance of water moisture, this temperature is further reduced [61].

The damaging effect of moisture is supported by research conducted by *Grützke et al.* [62], which explores commercial LIB electrolyte's thermal ageing and hydrolysis mechanisms. The electrolyte of a used LIB from a reclaimed hybrid electric vehicle (HEV) was investigated. The LIB was opened under three unique conditions, adapted to simulate electrolyte exposure to different environments. The conditions consisted of: i) inside a glove box (simulating an inert environment), ii) exposure to air for 5 minutes, and iii) exposure to air for 45 minutes. Both experiments that involved exposure to air were carried out to simulate the leakage of electrolyte

from an HEV battery pack and present the associated dangers. The electrolyte from each condition was then analysed to explore the changes in composition. The research results found the decomposition products, including acids, to be more complex in LIBs opened in the presence of air and humidity. When exposed to these conditions, the $LiPF_6$ underwent hydrolysis to a further extent and at a faster rate than the electrolyte exposed to inert conditions. It is also important to remember the influence of temperature as a variable affects the decomposition rate ahead of the moisture content due to the significant changes in kinetics driven by the temperature. Additionally, the authors suggested that due to the abundance and strength of the acids formed within the $LiPF_6$ reaction mechanism, it would be wise for emergency responders to have on hand acid-binding formulas in the case of an EV accident [60, 62].

Currently, the main challenge concerning the safety of LIBs lies in dealing with the aged components of the electrolyte solution, as many corrosive substances are formed via the solvent and salt decomposition pathways. Numerous researchers have devoted their efforts to exploring these substances and their associated short-term and long-term effects.

Henschel et al. [44] conducted an analytical study on the electrolyte degradation on various field-tested EV LIBs from leading manufacturers. The research characterised 19 different LIB electrolytes from 5 global original equipment manufacturers (OEM) using analysis techniques that included ion chromatography-conductivity detection (IC-CD), gas chromatography-flame ionisation detector (GC-FID), and gas chromatography-mass spectrometry (GC-MS). As the water content is a crucial parameter for prompting degradation, a Karl-Fischer titration was performed on four electrolyte samples. The titration results indicated a concentration between the range of 113-995 ppm of water moisture, much more significant than when LIBs were originally manufactured.

When analysing the DMC/EMC based solvent blend, DEC was found to have been produced in 15 of the 19 samples, supporting the notion that when solvents undergo transesterification, DEC is formed as a result. Other sample species identified included carbonate oligomers generated from the solvent decomposition. This includes dimethyl-2,5-dioxahexane dicarboxylate (DMDOHC), ethylmethyl-2,5-dioxahexane dicarboxylate (EMDOHC), and diethyl-2,5-doxahexane dicarboxylate (DEDOHC). These oligomers are believed to be detrimental to the LIB performance and essentially increase the internal resistance by altering the viscosity and ionic conductivity of the electrolyte.

Salt decomposition products were principally based upon the hydrolysis mechanism occurring with the dominant conducting salt, $LiPF_6$. The hydrolysis reaction generated many acid/non-acidic organo(fluoro)phosphates (OFPs). On average, there were 35 species in each sample, and in total, there were 18 acidic and 20 non-acidic unique samples identified.

Limited information regarding the toxicity effects of substances produced due to LIB electrolyte ageing is available. However, a few components that have been managed to be characterised have been identified to be highly dangerous and resemble structures similar to nerve agents used in chemical warfare. Three decomposition products of PF_6, namely dimethyl fluorophosphates (DMFP), ethyl methyl fluorophosphates (EMFP), and diethyl fluorophosphates (DEFP), all substances fall under category 1 within “The Globally Harmonized System of Classification and Labelling of Chemicals” (GHS), which classifies them as extremely hazardous by the World Health Organisation (WHO) [44].

The initial stage of recycling LIBs typically involves shredding battery material. Following the research into thermal ageing and the hydrolysis mechanisms of commercial LIB electrolytes, Grützke *et al.* [63] evaluated the severity of aged NMC LIB material. This material was

shredded, deposited in storage containers, and studied over a period of 20 months. The shredded material was placed in tinplate and polypropylene containers; however, the tinplate cans exhibited corrosion after several days. This is thought to be a result of the residual charge of the active material or the redox reactions between the tinplate surface, metal, and electrolyte in the shredded LIB material. Both DMFP and DEFP were identified and quantified in the study. As data concerning toxicity exposure to humans is difficult to obtain, findings were based on lethal concentrations when exposed to mice. Over a duration of 10 minutes, lethal dosages to mice are 290 $\mathrm{mg\,m^{-13}}$ of DMFP and 500 $\mathrm{mg\,m^{-13}}$ of DEFP via inhalation. This effectively suggests that the simultaneous release of both components from 290 and 500 kg of shredded material, respectively, under conditions of high temperature (150℃), would ultimately be fatal. Thus, to conclude, it should be noted that even though a biological comparison cannot be formed between mice and humans, the hazardous components formed as a consequence of the decomposition and ageing processes should not be ignored. For this reason, the storage of LIB material should be kept in well-ventilated spaces, and human exposure must be minimal [63].

2.3 Supercritical Fluids

2.3.1 Introduction

The critical phenomenon is that upon exceeding its critical point, a fluid will no longer act solely within the liquid or gas state but will exhibit characteristics of both, creating a single phase. In 1822, the French physicist Baron Charles Cagniard de la Tour conducted an experiment based on the acoustics generated from the splashing of a flint ball within a liquid housed in a digester. The splashing was audible at room temperature as the spherical ball tumbled through the liquid-vapour interface. However, as the digester was progressively heated, the distinctive splashing acoustic faded upon surpassing a set temperature. The experiment was repeated with various liquids, revealing that each fluid had a unique critical temperature, ultimately discovering the supercritical fluid phase [64].

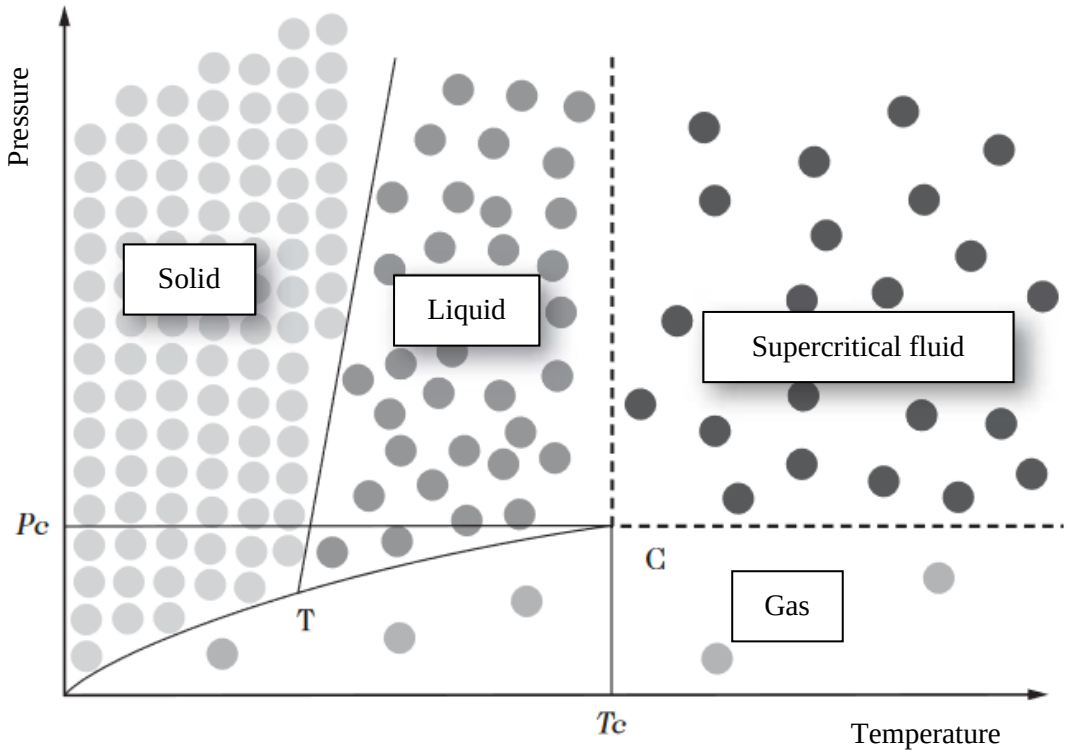

Figure 2-6: P-T phase diagram of a pure component (adapted from A.Taleb) [65].

2.3.2 Phase behaviour of a pure component

The P-T phase diagram (presented in **Figure 2-6**) [65] highlights three phases: solid, liquid, and gas, each partitioned by a significant transition curve corresponding to a change of state. Physicochemical transformations initiate the transition between each phase through the alteration of density. Thermodynamic equilibrium occurs at the location of the triple point (T). Here, all three phases of the single-component fluid coexist, and the transition lines (sublimation, liquefaction, and vaporisation) intersect at this point. Advancing past the sublimation curve lies the evaporation curve, shifting the liquid phase to gas. The curve begins at the triple point and culminates at the critical point (C) [65].

The supercritical fluid phase is attained when the single-component fluid exceeds the critical temperature (T_c) and pressure (P_c) parameters. The distinction between vapour and liquid ceases to exist upon surpassing the critical isotherm $T = T_c$ and the critical isobar $P = P_c$. In basic terms, a supercritical fluid can be observed as a highly pressurised gas with liquid-like density and tremendous transport properties, exhibiting low viscosity and high diffusivity [66]. As a result of the high compressibility of supercritical fluids (SCF), the density and solvating power can be fine-tuned as required through subtle adjustments in their pressure and temperature parameters [67]. In this supercritical phase, elevated pressure fluctuations will not revert the phase back into a liquid state, nor will a higher temperature deviation reverse the phase into a gaseous form [66].

Table 2-2: Physical and transport properties of fluids [68].

Property	Gas*	SCF ($\geq T_c, P_c$)	Liquid*
Density ρ (kg/m^{-3})	0.6-2	200-500	600-1600
Dynamic viscosity μ (mPa)	0.01-0.3	0.01-0.03	0.2-0.3
Kinematic viscosity ν $(= \mu/\rho)$ $(10^6\ m^2\ s^{-1})$	5-500	0.02-0.1	0.1-5
Diffusivity D $(10^6\ m^2\ s^{-1})$	10-40	0.07	0.0002-0.002

*At ambient conditions

The effectiveness of supercritical fluid extraction (SFE) is grounded in the physical properties of the solvent and solute(s) combination. **Table 2-2** compares the physical and transport properties of each fluid. Specifically, the density and thermal parameters of the pure solvent directly impact the loading capacity and solvent regeneration. At the same time, the chemical potential and transport properties provide the driving force and regulate the mass transfer rates.

In industry, fluids selected for supercritical applications are primarily centred around the cost and energy demands required to promote the pressure and temperature to the supercritical state. However, due to the associated safety concerns, not all fluids are equally fit for purpose. For example, ammonia is relatively inexpensive and exhibits a mild critical point; however, due to the toxic and corrosive properties associated with the fluid (presented in **Table 2-3**), it is not regularly applied. Likewise, the hydrocarbons ethane and methane require relatively low critical conditions to establish the supercritical phase, making them reasonably inexpensive within applications. However, each is highly flammable and would require additional safeguards for safe operation [69].

Lately, there has been a significant emphasis on using environmentally benign and non-toxic solvents within industrial processes. Both water and carbon dioxide promote safe properties, highlighting non-toxic, non-flammable, non-carcinogenic, and relatively inert characteristics. Hence, both are often referred to as “green solvents” [70].

Table 2-3: Critical parameters for established supercritical fluid solvents [66, 71].

Solvent	Molecular Formula	Critical Temperature (℃)	Critical Pressure (Bar)	Hazardous Classification
Ammonia	NH_3	132.5	113.5	C, A, E
Benzene	C_6H_6	289.0	48.9	F, I, H
Carbon dioxide	CO_2	31.1	73.8	
Ethane	C_2H_6	32.2	48.9	F
Methane	CH_4	-82.6	45.9	F
Methanol	CH_3OH	240.5	79.9	F, A, H
Nitrous oxide	N_2O	36.5	72.3	O
Water	H_2O	374.2	221.2	

A-Acute toxic, C-Corrosive, E-Environmental hazard, F-Flammable, H-Health hazard, I-Irritant, O-Oxidiser.

2.3.3 Supercritical carbon dioxide

Carbon dioxide is the most commonly used supercritical fluid (SCF) across various industries; the first application of the solvent dates back to the 1950s. It is widely available and considered one of the most inexpensive solvents, second only to water, on an economic scale. The critical parameters required to promote carbon dioxide to its supercritical conditions are 31.1℃ and 73.8 bar (as tabulated in **Table 2-3**). These are relatively mild and thus demand less energy to promote the fluid to its critical state.

However, during the late 1960s, the solvation power of carbon dioxide was thought to rival the strength of alkanes and ketones. As early models established the solvent strength upon the relationship between the Hildebrandt solubility (δ) and the square root of the critical pressure $\left[P_c^{1/2}\right]$, being directly proportional. Due to this, the solubility parameter of carbon dioxide was overpredicted by up to 100%, leading to claims for replacing traditional organic solvents with the fluid [72]. Today, carbon dioxide is the preferred option based on the clean nature of the fluid, unlike many organic solvents.

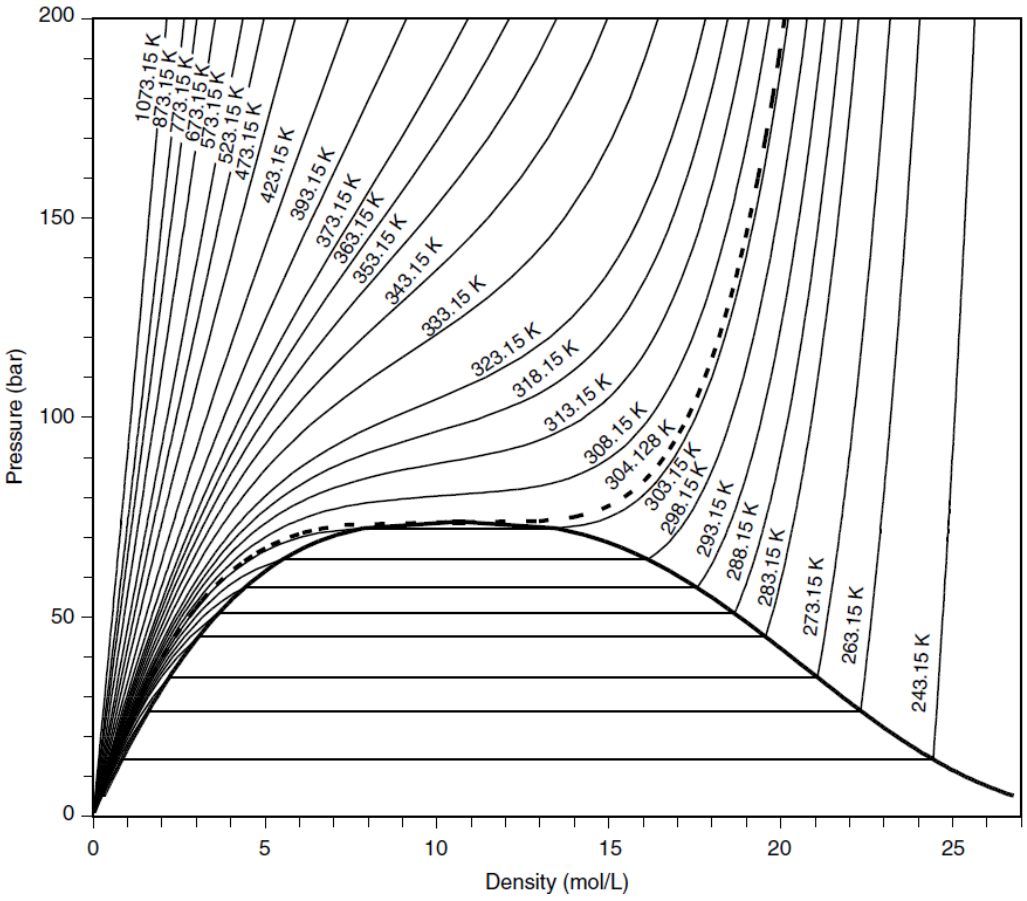

Figure 2-7: Density variation of carbon dioxide with temperature and pressure [73].

The dashed line defines the density at the critical temperature, and the bold line represents the saturated liquid line (left) and the saturated vapour line (right). As **Figure 2-7** shows, large density fluctuations are introduced beyond the critical points of temperature and pressure, with slight deviations made to the pressure at a constant temperature.

Compressibility, β, is defined by:

$$\beta = -\frac{1}{V_m}.\left(\frac{\partial V_m}{\partial p}\right)_T = \frac{1}{\rho}.\left(\frac{\partial \rho}{\partial p}\right)_T \qquad \textbf{(2-12)}$$

When at the critical point, the compressibility value is high and tends to infinity.

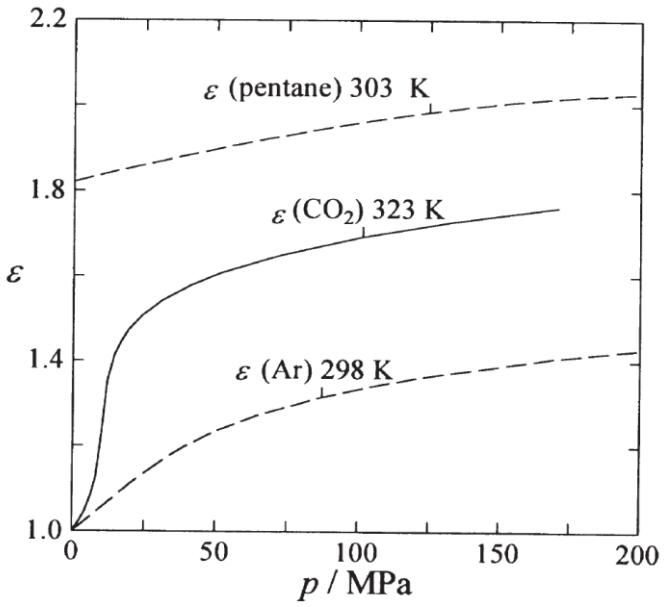

Figure 2-8: Relevant permittivities (ε) of pure carbon dioxide, argon and pentane as a function of pressure [66].

"Like dissolves like", a famous phrase coined by chemists, is often used when referring to the solubility interaction between solvents and solutes [74]. In terms of polarity, carbon dioxide is non-polar, primarily due to the zero dipole moment and low dielectric constant of the molecule [75].

Carbon dioxide molecules do not have a fixed electrical dipole moment; hence, the polarisation is limited to the contributions of the electrons and the nuclei. Typical solvation effects experienced are partially insignificant, and the intermolecular interactions are primarily composed of van der Waals forces and higher electrostatic attractions, such as the quadrupolar interactions. Exhibiting a rather small relative permittivity (as presented in **Figure 2-8**), carbon dioxide exhibits a dielectric constant (ε) of below 1.8 even at high pressures (200 MPa), where its density corresponds to that of liquids.

As a consequence, the solvent capabilities of supercritical carbon dioxide are rather specific, with the extraction capabilities being increasingly more effective for substances with a

low/medium molecular mass and that are non-polar. It is important to note that relative permittivity alone cannot determine solvent power; other factors, such as molecular interactions, solvation, and structural effects, must also be considered [66].

Subcritical carbon dioxide, also known as liquid carbon dioxide, is a technique also applied in extraction processes. Operation at the subcritical state is considered less harsh than the SCF state, whereby the pressure and temperature parameters are slightly lesser than that of the critical point. Thus, the physical properties, such as viscosity and surface tension, are greater than supercritical carbon dioxide, ultimately reducing the solvation ability. Although the subcritical technique has been applied within some extraction processes where the constituents are too delicate and would denature under the harsh conditions of supercritical carbon dioxide, typical processes include the extraction of carotenoids from microalgae/seaweeds and cannabinoids from cannabis [76].

2.3.4 Solubility

The association between phase equilibria and solubility in SCFs has been investigated using equations of state (EOS), statistical mechanical models, and solution thermodynamics. However, the application of these models is limited and requires extensive physicochemical data [69]. Mass transfer depends on the solubility of the solute within the SCF, with the solubility parameter varying for each solute compound and the applied operating conditions.

Solute behaviour within dense gases is based upon four main constraints, according to King and Friedrich (1990) [69]:

1) Miscibility pressure. This refers to the pressure or corresponding density in which the solute first begins to dissolve within the SCF. The miscibility pressure is obtained by solving the interaction between the total interaction parameter (χ) and the critical interaction parameter (χ_c) as a function of pressure or by graphical methods. The pressure value obtained is practical as a starting extraction position.

2) Maximum solubility pressure is the pressure at which the solute is most soluble within the SCF. Giddings' equation can predict the maximum solubility, whereby the solution is obtained when solubility and solute parameters are equivalent.

3) The fractionation pressure range defines the range of pressures between the miscibility pressure and the maximum solubility pressure, where the solubility of the solute ranges from zero to its maximum value. In this range, the solubility of one component will exceed the solubility of other components through the variation of pressure.

4) The physical properties of the solute, a critically important parameter is its melting point, as solutes tend to be increasingly more soluble in an SCF in their liquid form. Thus, in a selective extraction involving numerous solutes with different melting points and vapour pressures, the extraction temperature of the process will be vital in obtaining the selected solute(s).

Correlating SCF solubility with the molecular structure under the temperature and pressure parameters can be evaluated using King and Friedrich's reduced solubility parameter (Δ), as follows:

$$\Delta = \delta_1 / \delta_2 \quad \textbf{(2-13)}$$

Where δ_1 is defined as the solubility parameter of the solvent and δ_2 is the solubility parameter of the solute. The solubility parameter of fluid can be calculated according to Giddings et al.[77], as follows:

$$\delta_1 = 1.25\, {P_c}^{0.5}(\rho/\rho_{liq}) \quad \textbf{(2-14)}$$

Where P_c is the critical pressure, ρ is the density of the supercritical fluid and ρ_{liq} is the density of liquid gas. The solubility parameter of the solvent is correlated to the molecular structure using the following equation:

$$\delta_2 = \left(\frac{\Delta\varepsilon}{\Delta\nu}\right)^{0.5} \quad \textbf{(2-15)}$$

Where $\Delta\varepsilon$ is the vaporisation energy (at a given temperature) and $\Delta\nu$ is the corresponding molar volume, which is resolved by imputing the corresponding molecular weight and density values [69].

2.3.5 Supercritical fluid extraction

The supercritical fluid extraction (SFE) technique is a separation process used to extract and isolate substances through the application of supercritical fluids. One of the first commercial-scale applications of the SFE process was used to decaffeinate coffee beans [68]. In most cases, the SFE process comprises two main steps. First is the extraction from the sample, followed by a process involving the separation of the solvent and extractant. **Figure 2-9** presents a simple schematic outlining the SFE process.

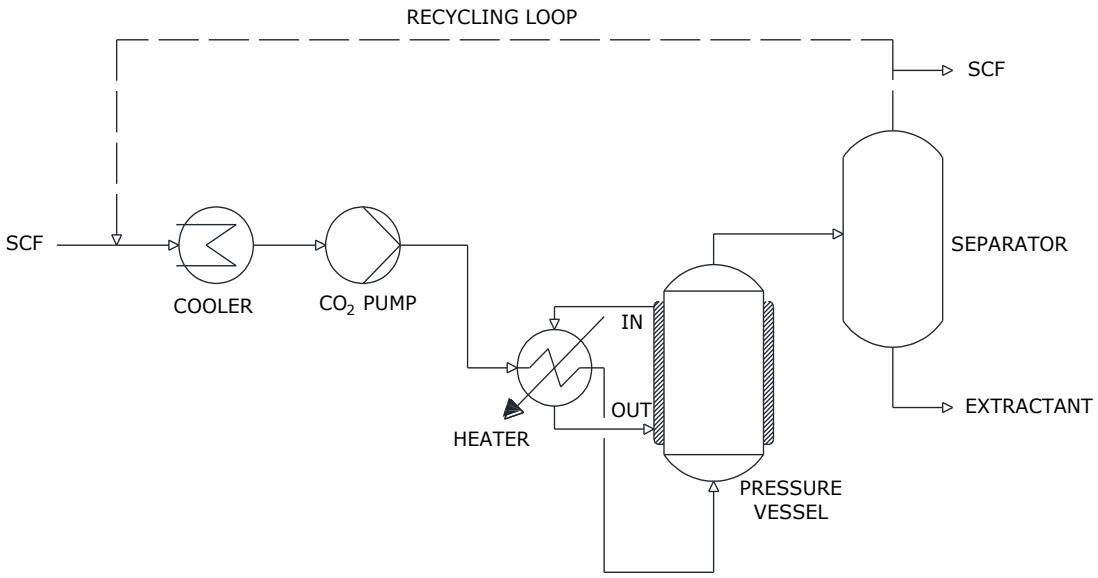

Figure 2-9: Schematic of a basic supercritical fluid extraction process.

Assuming that the SCF employed in this process is carbon dioxide, the initial step involves cooling it down to change its phase from gas to liquid, allowing it to be pumped. Once pressurised, it then contacts the sample, allowing solutes to be extracted via mass transfer effects. The bulk fluid containing the solute must then be separated; this is achieved through pressure reduction, resulting in the separation of phases and the precipitation of the solute.

This allows carbon dioxide to be diverted out of the process or, in some cases, recycled back into the feed stream. If a co-solvent is required, a mixer can be implemented to form a mixture of solvent and co-solvent or the co-solvent can be directly pumped into the vessel.

Fine-tuning the operating conditions is significantly important when optimising the extraction quality of the process. Generally, both parameters, temperature and pressure, drive substantial solubility fluctuations within SCFs. An increase in supercritical pressure promotes the density of the SCF medium; as the density increases, the fluid becomes more soluble, and the solubility increases.

Shifts within the temperature parameter are somewhat more delicate, an isobaric increase in temperature effectively decreases the density of the SCF; thus, the solubility of the solute falls. However, an enhancement of temperature at constant density promotes the solute vapour pressure, thus improving the solubility of the component within the solvent [78].

The effects of solvent flow rates depend on the type of sample being extracted. When the solubility/elution step primarily controls the extraction rate, the sample tends to have a high concentration of weakly bound analytes within the matrix. In this scenario, higher flow rates correspond to greater extraction rates. Additionally, static operation is less effective than dynamic over the same time interval. However, suppose the extraction rate is primarily driven by the rate of the initial desorption/kinetic step. In that case, the sample will tend to have a low concentration of strongly bound analytes within the matrix. For such samples, the solvent flow rate will have little or no effect on the extraction rate, assuming the sample void volume is adequately swept during operation. For this scenario, static operation is just as effective as dynamic [79].

In some processes, optimising the operating conditions alone is insufficient to achieve high-quality extractions. Practices to enhance the SCF solubility may involve adding co-solvents or a polar modifier to the solvent-solute mixture. The solvent strength of carbon dioxide is poor when extracting polar molecules; hence, a polar modifier may be added to produce a binary solvent mixture, improving the extraction yield and reducing the duration of the extraction process.

Several limitations associated with the SFE process can raise questions regarding its feasibility. As mentioned, carbon dioxide is the most applicable SCF and is non-polar; thus, extraction of the polar substances is increasingly difficult without the addition of a suitable polar modifier. Additionally, from an economic standpoint, the SFE process requires a complex equipment arrangement, and the operating conditions involve significantly high pressures. Thus, the capital investments and operating costs needed for the setup and operation are substantial.

However, depending on the process, the advantages collectively outweigh the expenses. Today, SFE is applied to many unique applications across various sectors, including food and beverages, pharmaceuticals, energy, and more. **Table 2-4** outlines a few of these applications and their associated operating conditions.

Table 2-4: Applications incorporating SCFs.

Industrial Sector	Application	Critical Fluid (Sc = supercritical, Sb = subcritical)	Pressure (bar)	Temperature (K)	Co-Solvent Applied	Extraction Method	Reference
Energy	Coal liquefaction	Sc (C_6H_6/ C_7H_7/C_5H_5N)	200	573-723	N/A		[80]
	Deasphalting of petroleum	Sb C_5H_{12}	35	333	N/A	Dynamic	[80]
Chemical	Coffee decaffeination	ScCO_2	250	363	N/A	Static	[81]
	Hops extract (humulus lupulus L)	SbCO_2	50-60	293-298	N/A	Static/dynamic	[82]
	Hops extract (humulus lupulus L)	ScCO_2	150-400	313-323	N/A	Static/dynamic	[82]
	Extraction of nicotine and solanesol from tobacco leaves	ScCO_2 / SbCO_2	80–250	298–333	N/A		[83]
	Dry cleaning	SbCO_2	50	291-295	N/A		[84]
	Polyethylene formation	ScC_2H_4	1200-3000	423-573	Oxygen / organic peroxides	Dynamic	[71]
	Fabric dyeing	ScCO_2 (H_2O saturated)	225–278	373–389	Dichlorotriazine dye		[85]

	Impregnation of wood	$ScCO_2$	150	313-333	Protection solvent	Static	[85]
Food and beverage	Roasted peanuts (Arachis hypogaea) extracts	$ScCO_2$	96	323	N/A		[86]
	Cumin flavouring extraction	$ScCO_2$	550	373	N/A	Static/dynamic	[86]
	Extracting orange oil	$ScCO_2$	131	308	N/A	Dynamic	[86]
	Cheddar cheese, fat (lipid) removal	$ScCO_2$	200	313	N/A		[86]
	Parmesan, fat (lipid) removal	$ScCO_2$	350	308	N/A		[86]
	Triglycerides from soybean flakes	$ScCO_2$	200-400	373	N/A	Static/dynamic	[85]
Waste	Recycling carbon fibre	Sb/ScH_2O	40-270	523-673	Potassium hydroxide	Static	[87]
	Decomposition of polyethylene terephthalate (PET)	$ScCH_3OH$	98	573-603	N/A		[88]
	Extraction of palladium and silver from waste printed circuit boards powder	$ScCO_2$	100-400	313-343	Acetone		[89]
	Splitting of industrial emulsions	SbC_3H_8	40	313–353	N/A	Dynamic	[85]
	Decomposition of rubber tyres	ScC_7H_8	35-55	573	N/A	Static	[90]

The rapid integration of supercritical fluids (SCFs) into various industrial processes has proven highly successful, primarily due to their significant solvating properties and environmentally friendly nature. Research has continued to push the capabilities of SCF technology in a wide array of practices, from separation techniques such as chromatography to recycling carbon fibre. A few of the leading applications of SCFs other than the SFE are expanded upon below:

Supercritical fluid-assisted drying – Conventional air drying naturally works based on drawing moisture to the surface of a substance through diffusion, when reaching the surface, the moisture is dissipated when contacting air. In comparison, supercritical fluid-assisted drying promotes an exchange using an extraction medium instead of heated air. Unlike conventional drying, surface tension effects are not a problem when drying highly porous materials, whereas under conventional drying, the water is removed from the liquid phase, allowing the solid structure to collapse. Application within the industry is commonly applied to produce a range of aerogels, e.g. polymers and biopolymers [85].

Supercritical fluid chromatography (SFC) – Many variations of chromatography exist (liquid, gas, ion exchange, etc.). However, all are still classified as analytical techniques for separating chemical compounds into their constituent elements. SCF draws together the advantages of high-pressure liquid chromatography (HPLC) and gas chromatography (GC), promoting an advantageous mobile phase as a result of its low viscosity, medium diffusivity and high density (closer to liquid state). Regarding analytical polarity, HPLC has the most comprehensive range; however, it is restricted to operating in distinct elution modes. SFC, in comparison, can operate in mutually compatible modes, allowing it to adopt conditions that target non-polar analytes before interchanging to polar elution modes. Hence, SFC can cover the widest analyte polarity range within a singular run [91].

2.4 LIB Recycling Techniques

2.4.1 Introduction

Despite the growing trend of recycling LIBs, many commercial recycling processes disregard the recovery of low-value components within the cell. The primary objective of many recycling processes is to maximise profitability, and this is often achieved by placing significant emphasis on the recovery of high-value electrode materials, including cobalt, manganese, nickel, and lithium. Consequently, the organic components, such as the separator and electrolyte, are frequently overlooked in these processes.

2.4.2 Commercial processes to recycle LIBs

The leading LIB recycling technologies implemented in large-scale operations use a combination of pre-treatment and processing methods. There are three main recycling techniques: pyrometallurgy, hydrometallurgy, and direct recycling. Each of these processes can be combined and adapted depending on factors like throughput, characteristics of the available LIB material, and the quantity and value of the recoverable materials [92].

One of the first prerequisites in most recycling techniques is to discharge the batteries before processing; this reduces the risk of fire and explosion and offers greater protection for the employees. In lab-scale processes, LIBs can simply be discharged through electrical means; however, this task is laborious and impractical in large commercial processes where many LIBs require processing. Thus, inert conditions are adopted, or the LIBs are cryogenically frozen when they are to be disassembled or shredded, preventing the lithium-ions from reacting with air. Another pre-treatment technique employed to pacify the hazardous reaction is to submerge the LIBs in a brine solution (usually sodium chloride), discharging the battery. However, upon

different battery models and chemistries, the discharge rate will vary, and some cells are adversely impacted by the brine's corrosive nature [93].

Mechanical treatment is a multifaceted process encompassing two key aspects: disintegration and separation. In the disintegration phase, components undergo crushing, milling, and shredding to process materials, effectively reducing particle sizes to under a few millimetres. Then, separation techniques are employed to extract valuable materials from the ground mixture. These methods leverage characteristics such as physical properties, conductivity, and magnetic ability to segregate components. Mechanical treatment methods primarily focus on recovering valuable metals and black mass.

Hydrometallurgical processes are typically integrated with mechanical steps to facilitate the breakdown of materials into a more accessible size and effectively separate components. Furthermore, a thermal pre-treatment step is employed to aid the separation of the active cathode material from the organic binder, resulting in the thermal decomposition of both binder and organic solvent. In contrast to pyrometallurgical treatment, hydrometallurgy proves more advantageous in lithium extraction, yielding lithium in a purer state. Much like mechanical treatment, hydrometallurgy emphasises the recovery of metals and high-purity lithium. Core processes employed for material recovery encompass leaching, solvent extraction, precipitation, and ion exchange [94-96].

The leaching process is widely employed to selectively target the active electrode materials and dissolve the metals in an acidic solution. A pre-treatment step involving reductive agents, such as hydrogen peroxide, sodium bisulphite, or sodium thiosulphate, is added to promote the dissolution through the reduction of the transition metal ions, for example, Ni^{3+} to Ni^{2+} and Co^{3+} to Co^{2+}. Next, the transition metals are leached by introducing an inorganic or organic

acid. Several commonly used acids include hydrogen chloride, sulphuric acid, nitric acid, citric acid, and malic acid [93]. The reaction initiated during the leaching process can be represented by **Equation 2-16** [94], which illustrates the interaction between the leaching medium (sulphuric acid), reductive agent (hydrogen peroxide) and the active material, $LiCoO_2$ in this case:

$$2LiCoO_2 + 3H_2O_2 + 3H_2SO_4 = 2CoSO_4 + Li_2SO_4 + 6H_2O + 2O_2 \qquad \textbf{(2-16)}$$

Once the leaching process has been executed, the resulting solution containing the extracted metals undergoes further processing through various techniques to refine and separate the mixture of metals. Some commonly employed methods include precipitation, solvent extraction, and electrowinning [93, 97]. These post-leaching techniques are critical for obtaining high-purity metals and preparing them for subsequent stages of the recycling process. Direct recycling involves separating the active anode and cathode materials using physical and mechanical methods. Whereas the hydrometallurgy process uses liquid solutions to leach and separate materials. One advantage of the direct recycling method is that it retains the crystal morphology of the cathode. However, strong acids dissolve the active cathode material into its constituent ions in the hydrometallurgical process. The choice between these methods depends on factors such as the desired purity of recovered materials [95].

The pyrometallurgical technique is independent and does not require physical or mechanical pre-treatment steps, as the furnaces are specifically designed to accommodate large volumes of batteries. This design feature allows LIBs to be loaded directly into the furnace for processing. The technique adopts elevated temperatures to recover valuable metals and purify them through physical and chemical transformations. It is important to note that the primary focus of this

technique is on the metals contained in the LIBs, while the remaining organic matter and polymer components are incinerated. Furthermore, not all recovered metals are obtained in their raw elemental form; for instance, copper, cobalt, and nickel are recovered in alloy form. Additionally, certain metals such as lithium, manganese, and aluminium are collected from the slag generated during the process. To further enhance these metals' purity, a hydrometallurgical recovery technique and a refining step would be required [94, 98].

2.4.3 LIB electrolyte recovery

As observed in the leading commercial processes to recycle LIBs, there is little emphasis on the electrolyte component. Three prominent techniques have emerged as leading contenders to address the growing demand for efficient and environmentally friendly methods to reclaim and reuse electrolytes: vacuum extraction, solvent extraction, and supercritical fluid extraction. Each method brings its unique set of advantages and challenges to the forefront, contributing to the evolving landscape of LIB electrolyte recovery.

Vacuum distillation is a separation method utilising the deviation between boiling points of components in a mixture. The technique is highly effective; besides preventing contact with the atmosphere, it exhibits higher evaporation rates, and substance sublimation occurs at lower temperatures. The process has been adopted in research by *Xu et al.* [99] and was found to be implemented commercially in a patent submitted by Duesenfeld (LIB recycler), both using the technique to recover LIB electrolyte solvents [100]. The simplified application of the process for EV LIBs is as follows. Battery packs are placed on an assembly line and broken into constituent modules; their metal/plastic outer casing is detached from the modules and sent for conventional recycling. The modules start by being discharged and are then shredded under vacuum conditions. A liquid electrolyte within the shredded material is then separated by evaporating the solvent component; the volatile vapour can be condensed back to liquid form.

However, a limitation of this process is that the lithium conducting salt component cannot be recovered from this technique directly, and the required operating temperature to evaporate cyclic carbonates is likely to initiate the decomposition of the lithium conducting salt.

Solvent extraction was an early recovery process of electrolytes and was first mentioned by *Schmidt et al.* in 2003 [101], whereby the electrolyte solvent and conducting salt within the LIB device are dissolved within an organic solvent [102], typical solvents include 1,2-dimethoxyethane, dimethyl carbonate, ethyl acetate, and acetone, which are then recovered through reduced pressure distillation. This process route effectively leaves a solution composed of the organic carbonates and the conducting salt; however, the technique has some significant drawbacks. Firstly, the solvent boiling point at reduced pressure must be kept at a temperature of 80℃ or lower, as higher temperatures can induce the conducting salt to decompose [103]. Also, the organic solvent used to dissolve the electrolyte tends to leave traces of solvent residue [102].

The first application of the supercritical fluid extraction (SFE) technique for recycling LIBs was demonstrated in a 2003 patent by *S.E Sloop* [104]. The patent focused on recovering the electrolyte from energy storage devices. Details regarding the extraction conditions, extraction behaviour, and the battery material extracted were limited. However, the patent provided the initial recycling prospect. The first application to target the electrolyte component in LIBs was conducted by *Grützke et al*. [105] in 2014. This process used helium head pressure carbon dioxide, as this mixture can attain supercritical conditions without using a compressor. $LiPF_6$ was dissolved in a mixture of DMC, EMC, and EC (1:1:1) and soaked into a polyethylene fleece and glass fibre separator. Operational conditions of 120 bar and 40°C were employed; the static approach was adopted, but a stirrer was employed. Optimal recovery resulted in 73.5%, but a significant emphasis was placed on the material from which the electrolyte was extracted.

Additional tests investigated commercial 18650 type cells, artificially aged through cycling; these cells were also extracted, and several ageing components were identified in the electrolyte recovered. Conclusions suggested using pure carbon dioxide and a co-solvent to enhance the recovery.

Liu et al. (2014) [103] made significant advances in developing the technique. The author optimised the operating conditions of the SFE process using pure carbon dioxide to extract an electrolyte (DMC/EMC/EC, in 1:1:1 vol%) containing a $LiPF_6$ conducting salt (in 1 mol). The influence of extraction parameters was studied using a Box-Behnken design; operational conditions included pressure (15 to 35 MPa), temperature (40 and 50°C), and static extraction duration (45 – 75 minutes). The optimal extraction conditions were 23 MPa and 40°C, producing an extraction yield of 85%. The results showed that the extraction pressure was the main influencing factor among all the parameters studied.

Further research by *Grützke et al*. (2015) [106] explored a dynamic operation using liquid and supercritical carbon dioxide. Again, 18650 type cells were used for extraction, at operating conditions of liquid phase: 25°C and 60 bar; supercritical phase: 40°C and 300 bar. The experiment used a combination of static and dynamic configurations. Conclusions indicated that liquid carbon dioxide is more effective for extracting the linear carbonates (DMC and EMC) and exhibits a more significant overall extraction yield. However, the supercritical extraction condition was more suitable for the cyclic carbonate, EC. It was found that the application of co-solvents, in addition to liquid carbon dioxide, significantly influenced the extraction process. Using a combination of acetonitrile and propylene carbonate (3:1), extraction yields reached as high as 89%. Furthermore, the method enabled the recovery of $LiPF_6$ in high concentrations. The study concluded that this method was suitable for investigating LIB electrolytes in post-mortem or ageing batteries, as it could provide a

qualitative overview within a few minutes of extraction. This was also possible for apparently ‘dry’ cells, where the electrolyte is deeply penetrated in the solid battery material [16].

The second study by *Liu et al*. (2016) [102] built upon the previous optimisations of the operating conditions and implemented a dynamic configuration into the high-pressure extraction. The electrolyte composition was kept consistent and was again soaked into a polypropylene separator [103]. Operating conditions focused on pressures between 15 to 35 MPa, temperatures between 30 and 50°C, and dynamic extraction durations between 25 – 65 minutes. Findings were in line with research conducted by *Grützke et al*., and the author found the EC recovery to increase with an enhancement in pressure. Concluding that the extraction of the electrolyte carbonates is a polarity predominated process, and each component should be extracted with a solvent that reflects this polarity. Additionally, polarity plays a more critical role than supercritical fluid density.

Furthermore, several other research studies [107-111] have also emphasised the use of pressurised carbon dioxide in relation to LIB recycling. These studies focus on more intricate LIB recycling processes and further optimisation of the operating conditions in the SFE process.

References – Chapter 2

1. Stevens P. The battery decade: How energy storage could revolutionize industries in the next 10 years. 2019. https://www.cnbc.com/2019/12/30/battery-developments-in-the-last-decade-created-a-seismic-shift-that-will-play-out-in-the-next-10-years.html.

2. Voelcker J. 1.2 Billion Vehicles On World's Roads Now, 2 Billion By 2035: Report. 29 July 2014. 2014; https://www.greencarreports.com/news/1093560_1-2-billion-vehicles-on-worlds-roads-now-2-billion-by-2035-report.

3. Shawn Park HT, James Kan, Seung Hoon Han, Martin Dunwoodie, Caroline Kim, Vincent Ha. F.I.T.T. for investors - charging the car of tomorrow. *Deutsche Bank.* 2016: 7, 43.

4. Pistoia G. *Lithium-Ion Batteries: Advances and Applications.* Elsevier B.V.; 2014.

5. LeVine S. NOT ENOUGH FOR GOODENOUGH - The man who brought us the lithium-ion battery at the age of 57 has an idea for a new one at 92. 2015; https://qz.com/338767/the-man-who-brought-us-the-lithium-ion-battery-at-57-has-an-idea-for-a-new-one-at-92/.

6. Foundation N. Nobel Prize in Chemistry 2019: Lithium-ion batteries. October 9, 2019; https://www.sciencedaily.com/releases/2019/10/191009082508.htm.

7. R M Dell DAJR. *Understanding Batteries.* Royal Society Of Chemistry; 2001.

8. Zoski CG. *Handbook of Electrochemistry.* 1 ed.: Elsevier; 2007.

9. Claus Daniel DM, Jianlin Li, and David L. Wood. Cathode Materials Review. 2015: 30. https://aip.scitation.org/doi/pdf/10.1063/1.4878478.

10. Kent JA. *Handbook of Industrial Chemistry and Biotechnology.* Springer; 2012.

11. Deng D. Li-ion batteries: basics, progress, and challenges. *Energy Science & Engineering.* 2015; 3(5): 385-418. doi: 10.1002/ese3.95.

12. Desjardins J. The Cathode is the Key to Advancing Lithium-Ion Technology. *Visual Capitalist.* 2017. https://www.visualcapitalist.com/cathode-advancing-lithium-ion/.

13. Greenwood D. *Future Lithium Ion Batteries*. Advanced Propulsion Systems WMG. 2016. https://www.brighton.ac.uk/_pdf/research/cae/future-li-ion-batteries.pdf. [Accessed 21/01/23].

14. Stoebe T. *Components of Cells and Batteries*. https://depts.washington.edu/matseed/batteries/MSE/components.html

15. Deimede V, Elmasides C. Separators for Lithium-Ion Batteries: A Review on the Production Processes and Recent Developments. *Energy Technology.* 2015; 3(5): 453-460. doi: 10.1002/ente.201402215.

16. Nowak S, Winter M. The Role of Sub- and Supercritical CO2 as "Processing Solvent" for the Recycling and Sample Preparation of Lithium Ion Battery Electrolytes. *Molecules.* 2017; 22(3): 2-6. doi: 10.3390/molecules22030403.

17. Kupper C, Weißhar B, Rißmann S, Bessler WG. End-of-Life Prediction of a Lithium-Ion Battery Cell Based on Mechanistic Aging Models of the Graphite Electrode. *Journal of The Electrochemical Society.* 2018; 165(14): A3468-A3477. doi: 10.1149/2.0941814jes.

18. Lucht B. *Revealing the Illusive Interphase in Lithium Ion Batteries* U.S. Department of Energy, Office of Scientific and Technical Information, 2013, https://science.osti.gov/bes/Highlights/2013/BES-2013-01-d.

19. *Battery University. BU-205: Types of Lithium-ion*. https://batteryuniversity.com/learn/article/types_of_lithium_ion [Accessed 23/04/20].

20. Warner JT. The Cathodes. In: *Lithium-Ion Battery Chemistries*. Elsevier; 2019. p. 99-114.

21. Miao Y, Hynan P, von Jouanne A, Yokochi A. Current Li-Ion Battery Technologies in Electric Vehicles and Opportunities for Advancements. *Energies.* 2019; 12(6): 1-3, 5-11, 12-14. doi: 10.3390/en12061074.

22. BYD. *BYD Electric vehicles.* International Council on Clean Transportation; 2020. https://theicct.org/sites/default/files/BYD%20EV%20SEDEMA.pdf. [Accessed 6/05/20].

23. London Metal Exchange (LME). London Metal Exchange: LME Cobalt. 2020. https://www.lme.com/Metals/Minor-metals/Cobalt#tabIndex=2.

24. Mercedes-Benz. *Mercedes-Benz Buses: The new eCitaro.* 2020. https://www.mercedes-benz-bus.com/en_DE/models/ecitaro.html [Accessed 06/05/20].

25. Bower G. Tesla Panasonic Quietly Outmaneuver All Lithium Battery Manufacturers. 2018; https://insideevs.com/news/338268/tesla-panasonic-quietly-outmaneuver-all-lithium-battery-manufacturers/.

26. Warner JT. The Anodes. In: *Lithium-Ion Battery Chemistries*. 2019. p. 115-138.

27. Nitta N, Wu F, Lee JT, Yushin G. Li-ion battery materials: present and future. *Materials Today.* 2015; 18(5): 252-264. doi: 10.1016/j.mattod.2014.10.040.

28. Siemens Mobility receives first order for battery-powered trains [press release]. Siemens, 17th March 2020. https://press.siemens.com/global/en/pressrelease/siemens-mobility-receives-first-order-battery-powered-trains.

29. Hanley S. Siemens Mobility Will Supply 20 Battery Electric Trains To Baden-Württemberg. 2020. https://cleantechnica.com/2020/03/24/siemens-mobility-will-supply-20-battery-electric-trains-to-baden-wurttemberg/.

30. Alves Dias P. BD, Pavel C.,Arvanitidis N. *Cobalt: demand-supply balances in the transition to electric mobility*. EUR 29381 EN, Publications Office of the European Union, Joint Research Centre (JRC), Luxembourg, 2018, http://dx.doi.org/10.2760/97710.

31. SamsungSDI. *The Composition of EV Batteries: Cells? Modules? Packs? Let's Understand Properly!* Samsung SDI; 2020. https://www.samsungsdi.com/column/all/detail/54344.html.

32. Watzenig AT. *Automotive Battery Technology.* Springer; 2014.

33. Zapmap. *How many charge points are there in the UK 2020*. https://www.zap-map.com/statistics/ [Accessed 09/05/20].

34. Un-Noor F, Padmanaban S, Mihet-Popa L, Mollah M, Hossain E. A Comprehensive Study of Key Electric Vehicle (EV) Components, Technologies, Challenges, Impacts, and Future Direction of Development. *Energies*. 1217. 2017; 10(8): 56-59. https://doi/org/10.3390/en10081217.

35. *Electric Vehicles*. 9780160872204, Committee on Energy and Natural Resources,U.S. Government Printing Office, Washington, 2010, https://books.google.co.uk/books?id=CG5tXERrNfoC.

36. Sun P, Bisschop R, Niu H, Huang X. A Review of Battery Fires in Electric Vehicles. *Fire Technology.* 2020: 6-12. doi: 10.1007/s10694-019-00944-3.

37. Ribière P, Grugeon S, Morcrette M, Boyanov S, Laruelle S, Marlair G. Investigation on the fire-induced hazards of Li-ion battery cells by fire calorimetry. *Energy and Environmental Science.* 2012; 5(1): 5271-5280. doi: https://doi.org/10.1039/C1EE02218K.

38. Feng X, Ouyang M, Liu X, Lu L, Xia Y, He X. Thermal runaway mechanism of lithium ion battery for electric vehicles: A review. *Energy Storage Materials.* 2018; 10: 247-255. doi: 10.1016/j.ensm.2017.05.013.

39. Davoodabadi A, Li J, Zhou H, Wood DL, Singler TJ, Jin C. Effect of calendering and temperature on electrolyte wetting in lithium-ion battery electrodes. *Journal of Energy Storage.* 2019; 26: 101034. doi: https://doi.org/10.1016/j.est.2019.101034.

40. Zhao W, Ji Y, Zhang Z, Lin M, Wu Z, Zheng X, et al. Recent advances in the research of functional electrolyte additives for lithium-ion batteries. *Current Opinion in Electrochemistry.* 2017; 6(1): 84-91. doi: https://doi.org/10.1016/j.coelec.2017.10.012.

41. Kalhoff J, Eshetu GG, Bresser D, Passerini S. Safer Electrolytes for Lithium-Ion Batteries: State of the Art and Perspectives. *Chemsuschem.* 2015; 8(13): 2155-2158, 2160-2151, 2163-2165. doi: 10.1002/cssc.201500284.

42. Warner JT. In: *Lithium-Ion Battery Chemistries*. Elsevier; 2019. p. 141-152.

43. Li Q, Chen J, Fan L, Kong X, Lu Y. Progress in electrolytes for rechargeable Li-based batteries and beyond. *Green Energy & Environment.* 2016; 1(1): 18-42. doi: https://doi.org/10.1016/j.gee.2016.04.006.

44. Henschel J, Horsthemke F, Stenzel YP, Evertz M, Girod S, Lürenbaum C, et al. Lithium ion battery electrolyte degradation of field-tested electric vehicle battery cells – A comprehensive analytical study. *Journal of Power Sources.* 2020; 447: 2-7. doi: 10.1016/j.jpowsour.2019.227370.

45. Pyo S-H, Park JH, Chang T-S, Hatti-Kaul R. Dimethyl carbonate as a green chemical. *Current Opinion in Green and Sustainable Chemistry.* 2017; 5: 61-66. doi: https://doi.org/10.1016/j.cogsc.2017.03.012.

46. Tundo P, Selva M. The Chemistry of Dimethyl Carbonate. *Accounts of Chemical Research.* 2002; 35(9): 706-716. doi: 10.1021/ar010076f.

47. Rimondino GN, Vila JA, Malanca FE. Atmospheric oxidation of ethyl methyl carbonate: Kinetics and reaction mechanism. *Journal of Photochemistry and Photobiology A: Chemistry.* 2023; 444: 114994. doi: https://doi.org/10.1016/j.jphotochem.2023.114994.

48. Miao Y-N, Wang Y, Pan D-H, Song X-H, Xu S-Q, Gao L-J, et al. Zn-Co@N-Doped Carbon Derived from ZIFs for High-Efficiency Synthesis of Ethyl Methyl Carbonate: The Formation of ZnO and the Interaction between Co and Zn. *Catalysts*. 2019; 9(1) https://doi/org/10.3390/catal9010094.

49. Shen ZL, Jiang XZ, Zhao WJ. A New Catalytic Transesterification for the Synthesis of Ethyl Methyl Carbonate. *Catalysis Letters.* 2003; 91(1): 63-67. doi: 10.1023/B:CATL.0000006318.45345.da.

50. Lyubimov SE, Zvinchuk AA, Sokolovskaya MV, Davankov VA, Chowdhury B, Zhemchugov PV, et al. A simple synthesis of ethylene carbonate from carbon dioxide and 2-chloroethanol using silica gel as a catalyst. *Applied Catalysis A: General.* 2020; 592: 117433. doi: https://doi.org/10.1016/j.apcata.2020.117433.

51. Lyadov AS, Kochubeev AA, Markova EB, Khadzhiev SN. Ethylene carbonate production by cyclocondensation of ethylene glycol and urea in the presence of metal oxides and metal acetylacetonates. *Petroleum Chemistry.* 2016; 56(9): 852-856. doi: 10.1134/S0965544116090152.

52. Johnson PH. *Properties of ethylene carbonate and its use in electrochemical applications: a literature review*. 1985. https://www.osti.gov/biblio/5370794.

53. Mönnighoff X, Friesen A, Konersmann B, Horsthemke F, Grützke M, Winter M, et al. Supercritical carbon dioxide extraction of electrolyte from spent lithium ion batteries and its characterization by gas chromatography with chemical ionization. *Journal of Power Sources.* 2017; 352: 56-63. doi: 10.1016/j.jpowsour.2017.03.114.

54. Zhang SS. A review on electrolyte additives for lithium-ion batteries. *Journal of Power Sources.* 2006; 162(2): 1385-1388. doi: 10.1016/j.jpowsour.2006.07.074.

55. Olivas A, Gaxiola E, Cruz-Reyes J, Alvarez Amparán M, Valdez R. Transition-metal influence (Fe, Co, Ni, Cu) on the MoWS catalyst for biphenyl hydrogenation. *Fuel Processing Technology.* 2020; 204: 1-4. doi: 10.1016/j.fuproc.2020.106410.

56. Han S. Structure and dynamics in the lithium solvation shell of nonaqueous electrolytes. *Sci Rep*. [Preprint] PMC6447571. 2019; 9(1): 1. https://doi/org/10.1038/s41598-019-42050-y.

57. Masaki Yoshio RJB, Akiya Kozawa. *Lithium-Ion Batteries.* Springer; 2009.

58. Flamme B, Rodriguez Garcia G, Weil M, Haddad M, Phansavath P, Ratovelomanana-Vidal V, et al. Guidelines to design organic electrolytes for lithium-ion batteries: environmental impact, physicochemical and electrochemical properties. *Green Chemistry.* 2017; 19(8): 1828-1830. doi: 10.1039/c7gc00252a.

59. Lee J-C, Litt MH. Ring-Opening Polymerization of Ethylene Carbonate and Depolymerization of Poly(ethylene oxide-co-ethylene carbonate). *Macromolecules.* 2000; 33(5): 1618. doi: 10.1021/ma9914321.

60. Terborg L, Weber S, Blaske F, Passerini S, Winter M, Karst U, et al. Investigation of thermal aging and hydrolysis mechanisms in commercial lithium ion battery electrolyte. *Journal of Power Sources.* 2013; 242: 832-837. doi: 10.1016/j.jpowsour.2013.05.125.

61. Hui Yang GVZ, Philip N. Ross, Jr. . *Journal of Power Sources.* Thermal Stability of LiPF6 Salt and Li-ion Battery Electrolytes Containing LiPF6. 161. Berkeley, CA 94720: University of California 2006.

62. Grützke M, Kraft V, Hoffmann B, Klamor S, Diekmann J, Kwade A, et al. Aging investigations of a lithium-ion battery electrolyte from a field-tested hybrid electric vehicle. *Journal of Power Sources.* 2015; 273: 83-88. doi: 10.1016/j.jpowsour.2014.09.064.

63. Grutzke M, Kruger S, Kraft V, Vortmann B, Rothermel S, Winter M, et al. Investigation of the Storage Behavior of Shredded Lithium-Ion Batteries from Electric Vehicles for Recycling Purposes. *Chemsuschem.* 2015; 8(20): 3433-3438. doi: 10.1002/cssc.201500920.

64. Bertrand Berche MH, Ralph Kenna. *Critical phenomena:150 years since Cagniard de la Tour*. Nancy Universite; 2009 10.1590/S1806-11172009000200015 https://arxiv.org/pdf/0905.1886.pdf.

65. Taleb A. Supercritical Fluids. In: Bréchignac C, Houdy P, Lahmani M, (eds.) *Nanomaterials and Nanochemistry*. Berlin, Heidelberg: Springer Berlin Heidelberg; 2007. p. 473-474.

66. Kiran E, Debenedetti PG, Peters CJ. *Supercritical Fluids: Fundamentals and Applications.* Springer Netherlands; 2012.

67. Eckert CA, Knutson BL, Debenedetti PG. Supercritical fluids as solvents for chemical and materials processing. *Nature.* 1996; 383(6598): 313-318. doi: 10.1038/383313a0.

68. Pradip Munshi SB. Supercritical CO2: a twenty-first century solvent for the chemical industry. *Current Science.* 2009; 97: 63-72. doi: https://doi.org/10.1002/chin.201011250.

69. Dean JR. *Applications of Supercritical Fluids in Industrial Analysis.* Springer Netherlands; 2012.

70. Chaudhary A, Dwivedi A, Upadhyayula S. Chapter 28 - Supercritical fluids as green solvents. In: Kharisov B, Kharissova O, (eds.) *Handbook of Greener Synthesis of Nanomaterials and Compounds*. Elsevier; 2021. p. 891-916.

71. Laitinen A. Supercritical fluid extraction of organic compounds from solids and aqueous solutions. *VTT Publications.* 1999: 13-16, 19.

72. Beckman EJ. Supercritical and near-critical CO2 in green chemical synthesis and processing. *The Journal of Supercritical Fluids.* 2004; 28(2-3): 121-191. doi: 10.1016/s0896-8446(03)00029-9.

73. Gupta RB, Shim JJ. Solubility in Supercritical Carbon Dioxide. *CRC Press.* 2007. https://books.google.co.uk/books?id=qdXLBQAAQBAJ.

74. Peach J, Eastoe J. Supercritical carbon dioxide: a solvent like no other. *Beilstein J Org Chem.* 2014; 10: 1878-1895. doi: 10.3762/bjoc.10.196.

75. Poovathinthodiyil Raveendran YI, Scott L. Wallen. Polar Attributes of Supercritical Carbon Dioxide. *American Chemical Society.* 2004; 38.

76. Poojary MM, Barba FJ, Aliakbarian B, Donsì F, Pataro G, Dias DA, et al. Innovative Alternative Technologies to Extract Carotenoids from Microalgae and Seaweeds. *Marine Drugs.* 2016; 14(11): 17,18. https://www.mdpi.com/1660-3397/14/11/214.

77. Giddings JC, Myers MN, King JW. Dense Gas Chromatography at Pressures to 2000 Atmospheres. *Journal of Chromatographic Science.* 1969; 7(5): 276-283. doi: 10.1093/chromsci/7.5.276.

78. Hrnčič MK, Cör D, Verboten MT, Knez Ž. Application of supercritical and subcritical fluids in food processing. *Food Quality and Safety.* 2018; 2(2): 59-64. doi: 10.1093/fqsafe/fyy008.

79. Steven B. Hawthorne ABG, Vincent O. Schmitt, and David J. Miller. Effect of SFE Flow Rate on Extraction Rates: Classifying Sample Extraction Behavior. *Analytical Chemistry.* 1995; 67. doi: https://doi.org/10.1021/ac00111a034.

80. Ely JF, Baker JK, Standards USNBo. *A Review of Supercritical Fluid Extraction.* U.S. Department of Commerce, National Bureau of Standards; 1984.

81. Iolanda De Marco* SR, Raffaele Iannone. Supercritical Carbon Dioxide Decaffeination Process: a Life Cycle Assessment Study. 2017; 57: 3. https://www.aidic.it/cet/17/57/284.pdf.

82. Knez Hrncic M, Spaninger E, Kosir IJ, Knez Z, Bren U. Hop Compounds: Extraction Techniques, Chemical Analyses, Antioxidative, Antimicrobial, and Anticarcinogenic Effects. *Nutrients.* 2019; 11(2). doi: 10.3390/nu11020257.

83. Ruiz Rodriguez A, Bronze M, Ponte M. Supercritical fluid extraction of tobacco leaves: A preliminary study on the extraction of solanesol. *Journal of Supercritical Fluids - J SUPERCRIT FLUID.* 2008; 45: 171. doi: 10.1016/j.supflu.2007.10.011.

84. DeSimone JM, Tumas W. *Green Chemistry Using Liquid and Supercritical Carbon Dioxide.* Oxford University Press; 2003.

85. Brunner G. Applications of Supercritical Fluids. *Annual Review of Chemical and Biomolecular Engineering.* 2010; 1(1): 323,324,327,328,336. doi: 10.1146/annurev-chembioeng-073009-101311.

86. Capuzzo A, Maffei ME, Occhipinti A. Supercritical fluid extraction of plant flavors and fragrances. *Molecules.* 2013; 18(6): 7194-7238. doi: 10.3390/molecules18067194.

87. Piñero-Hernanz R, Dodds C, Hyde J, García-Serna J, Poliakoff M, Lester E, et al. Chemical recycling of carbon fibre reinforced composites in nearcritical and supercritical water. *Composites Part A: Applied Science and Manufacturing.* 2008; 39(3): 454-461. doi: 10.1016/j.compositesa.2008.01.001.

88. Idzumi Okajima TS. Plastic Recycling with Supercritical Fluids. *Institute of Electrical and Electronics Engineers.* 2001.

89. Liu K, Zhang Z, Zhang FS. Direct extraction of palladium and silver from waste printed circuit boards powder by supercritical fluids oxidation-extraction process. *J Hazard Mater.* 2016; 318: 216-223. doi: 10.1016/j.jhazmat.2016.07.005.

90. Inamullah Bhatti KQ, Adel Zaqoot. Supercritical Decomposition of Scrap Tires using Toluene. *Proceedings of the 7th IASME / WSEAS International Conference on heat transfer, thermal engineering and environment.* 2009.

91. Hofstetter RK, Hasan M, Eckert C, Link A. Supercritical fluid chromatography. *ChemTexts.* 2019; 5(3): 13. doi: 10.1007/s40828-019-0087-2.

92. Gaines L. Lithium-ion battery recycling processes: Research towards a sustainable course. *Sustainable Materials and Technologies.* 2018; 17: e00068. doi: https://doi.org/10.1016/j.susmat.2018.e00068.

93. Pinegar H, Smith YR. Recycling of End-of-Life Lithium-Ion Batteries, Part II: Laboratory-Scale Research Developments in Mechanical, Thermal, and Leaching Treatments. *Journal of Sustainable Metallurgy.* 2020; 6(1): 143-148. doi: 10.1007/s40831-020-00265-8.

94. Ekberg C, Petranikova M. Lithium Batteries Recycling. In: *Lithium Process Chemistry Resources, Extraction, Batteries, and Recycling*. Elsevier; 2015. p. 237-243.

95. Kaya M. State-of-the-art lithium-ion battery recycling technologies. *Circular Economy.* 2022; 1(2): 100015. doi: https://doi.org/10.1016/j.cec.2022.100015.

96. Saleem U, Joshi B, Bandyopadhyay S. Hydrometallurgical Routes to Close the Loop of Electric Vehicle (EV) Lithium-Ion Batteries (LIBs) Value Chain: A Review. *Journal of Sustainable Metallurgy.* 2023; 9(3): 950-971. doi: 10.1007/s40831-023-00718-w.

97. Chen X. A Review on Hydrometallurgy of Typical Lithium-ion Batteries. *Journal of Physics: Conference Series.* 2022; 2378(1): 012033. doi: 10.1088/1742-6596/2378/1/012033.

98. Makuza B, Tian Q, Guo X, Chattopadhyay K, Yu D. Pyrometallurgical options for recycling spent lithium-ion batteries: A comprehensive review. *Journal of Power Sources.* 2021; 491: 229622. doi: https://doi.org/10.1016/j.jpowsour.2021.229622.

99. Xu R, Lei S, Wang T, Yi C, Sun W, Yang Y. Lithium recovery and solvent reuse from electrolyte of spent lithium-ion battery. *Waste Manag.* 2023; 167: 135-140. doi: 10.1016/j.wasman.2023.05.034.

100. Christian Hanisch BW, Wolfgang Haselrieder, Martin Schoenitz. *Method of treating used batteries, especially rechargeable batteries and battery processing equipment* DE102015207843A1,2015.

101. Michael Schmidt RPH, Margret Wohlfahrt-Mehrens, Christian Vogler, Giesela Arnold. *Process for Recycling Negative-Electrode Materials from Spent Lithium Batteries.* 09/584,059,2003.

102. Yuanlong Liu DM, Yunkun Dai, Quanxin Ma, Rujuan Zheng, Changsong Dai. Analysis on Extraction Behaviour of Lithium-ion Battery Electrolyte Solvents in Supercritical CO2 by Gas Chromatography. *International Journal of Electrochemical Science.* 2016: 7594-7604. doi: 10.20964/2016.09.03.

103. Liu Y, Mu D, Zheng R, Dai C. Supercritical CO2 extraction of organic carbonate-based electrolytes of lithium-ion batteries. *RSC Advances.* 2014; 4(97): 54525-54531. doi: https://doi.org/10.1039/C4RA10530C.

104. Sloop SE. *System and method for removing an electrolyte from an energy storage or conversion device using a supercritical fluid.pdf.* 10/340,358,2007.

105. Grützke M, Kraft V, Weber W, Wendt C, Friesen A, Klamor S, et al. Supercritical carbon dioxide extraction of lithium-ion battery electrolytes. *The Journal of Supercritical Fluids.* 2014; 94: 216-222. doi: 10.1016/j.supflu.2014.07.014.

106. Grützke M, Mönnighoff X, Horsthemke F, Kraft V, Winter M, Nowak S. Extraction of lithium-ion battery electrolytes with liquid and supercritical carbon dioxide and

additional solvents. *RSC Advances.* 2015; 5(54): 43209-43217. doi: 10.1039/c5ra04451k.

107. Mu D, Liu Y, Li R, Ma Q, Dai C. Transcritical CO2 extraction of electrolytes for lithium-ion batteries: optimization of the recycling process and quality–quantity variation. *New Journal of Chemistry.* 2017; 41(15): 7177-7185. doi: 10.1039/c7nj00771j.

108. Liu Y, Mu D, Li R, Ma Q, Zheng R, Dai C. Purification and Characterization of Reclaimed Electrolytes from Spent Lithium-Ion Batteries. *The Journal of Physical Chemistry C.* 2017; 121(8): 4181-4187. doi: 10.1021/acs.jpcc.6b12970.

109. Sloop S, Crandon L, Allen M, Koetje K, Reed L, Gaines L, et al. A direct recycling case study from a lithium-ion battery recall. *Sustainable Materials and Technologies.* 2020; 25. doi: 10.1016/j.susmat.2020.e00152.

110. Zachmann N, Fox RV, Petranikova M, Ebin B. Implementation of a sub-and supercritical carbon dioxide process for the selective recycling of the electrolyte from spent Li-ion battery. *Journal of CO2 Utilization.* 2024; 81: 102703. doi: https://doi.org/10.1016/j.jcou.2024.102703.

111. Zachmann N, Petranikova M, Ebin B. Electrolyte recovery from spent Lithium-Ion batteries using a low temperature thermal treatment process. *Journal of Industrial and Engineering Chemistry.* 2023; 118: 351-361. doi: https://doi.org/10.1016/j.jiec.2022.11.020.

Chapter 3: Materials and Analytical Techniques

3.1 Introduction

The key components of LIB electrolyte are vastly different in terms of their physical and chemical properties. Precise techniques were adopted for the identification and quantification of the LIB material. This chapter aims to outline the materials used and the analytical principles employed in the entirety of the research undertaken. The structure of the chapter is broken down as follows; first, the *Chemical Compounds* are summarised in Section **3.2**, the procedure for *Chemical Storage and Disposal* is given in Section **3.3**, details of the *Calibration of Instrumentation* are described in Section **3.4,** and finally, in Section **3.5** the chapter is concluded with the *Analytical Methods* applied.

3.2 Chemical Compounds

A summary of all the chemical compounds used in the experimentation is outlined in **Table 3-1**. Chemical assay of liquid samples was determined via gas chromatography, ensuring the chemical purities corroborated with values given by their suppliers and no additional impurities or moisture were present. Once the purities were confirmed to be in line with suppliers, all chemicals were used without further purification.

Table 3-1: Chemical compounds.

Component name	Molecular formula	CAS	Supplier	Supplier Purity (wt%)	Calculated Purity (wt%)
Acetone	CH_3COCH_3	67-64-1	Fisher Scientific UK	>99.8	-
Carbon dioxide	CO_2	124-38-9	BOC UK	>99.8	-
Diethyl carbonate	$(C_2H_5O)_2CO$	105-58-8	Sigma-Aldrich	>99.0	99.7
Dimethyl carbonate	$(CH_3O)_2CO$	616-38-6	Sigma-Aldrich	>99.0	99.5
Ethyl methyl carbonate	$(C_2H_5O)CO(OCH_3)$	623-53-0	TCI	>98.0	99.2
Ethylene carbonate	$(CH_2O)_2CO$	96-49-1	Sigma-Aldrich	>98.0	-
Nonane	$CH_3(CH_2)_7CH_3$	111-84-2	Sigma-Aldrich	>99%	-

3.3 Chemical Storage and Disposal

The direction for the storage of chemicals carefully followed the specifications of the safety data sheets (SDS) as provided by their respective suppliers. As most chemicals were flammable, they all emphasised the key points: “Keep container tightly closed and store in a dry and well-ventilated place. Keep away from heat and sources of ignition”. The bottles of chemicals in the laboratory were stored in fireproof storage cabinets, isolated from sunlight and ignition sources. Analytical solutions were freshly made and promptly tested, and stock solutions were not kept for more than a month to avoid contamination and solution degradation.

LIB pouch material was segregated by their components: anode, cathode, separator, and electrolyte. The solid material was rolled up and stored in 1000 mL ultra-violet (UV) glass jars with leak proof lids. UV glass was selected to mitigate against any potential photochemical reactions that may occur with LIB components.

Electrolytes, both artificial and from the LIB pouch cell, were stored in 100 mL borosilicate glass jars with a parafilm layer between the body and screw cap. All material was stored in a refrigerator, kept at temperatures between 2-5℃. As several carbonates displayed volatile properties and low flash points, fridge storage was imperative to inhibit vaporisation and lower the vapour pressure. Before sample preparation, all samples were allowed to acclimatise for thirty minutes in the laboratory at room temperature (21°C).

Waste substances and LIB pouch cells were segregated and disposed of as instructed by the University of Birmingham’s Hazardous Waste Disposal policy [1]. The key waste categories are as follows; non-hazardous, halogenated solvent, non-halogenated solvent, and specialist hazardous waste disposal.

3.4 Calibration of Instrumentation

3.4.1 Micropipette

Aspirating and dispensing liquids were carried out with an air displacement micropipette, Gilson, model Pipetman, P1000, with a volume range precision of 100-1000 µL. A reverse pipetting technique was adopted as it is more useful towards liquids with a high vapour pressure, i.e., acetone, DMC, and EMC.

Clear polypropylene tips obtained from Gilson, model Diamond D1200, were used with the Gilson micropipette. As trace metal analysis was a vital part of the research, coloured tips were avoided as some manufacturers use dyes containing metal additives which could leach into samples.

The calibration of the micropipette was based on the practice outlined in *BS 8655-6:200* [2]; details of the calibration are given below [3].

1. Fit a new tip to the air displacement pipette, aspirate water from the reservoir container, and expel it to waste five times. This allows the humidity in the dead air volume to stabilise.
2. Add water to the weighing vessel to a depth of at least 3mm. Record the water temperature inside the weighing vessel and place it on the balance, then tare it.
3. Fill the micropipette with water from the reservoir, then dispense it into the weighing vessel using the conventional approach.
4. Record the new balance reading. Time taken for the complete cycle should be kept to a minimum – preferably less than 60 seconds.

5. Repeat the operation in *3* and *4* a further nine times. At the end of each cycle, note the balance reading. At the end of the tenth cycle, record the temperature in the weighing container and the total elapsed time.
6. Calculate the mass of water deposited for each cycle. Find the density of water at the standard reference temperature recorded.
7. Calculate the volume at the recorded temperature. Add each volume of water deposited for each cycle in step 6 and divide by 10 to obtain the mean volume.

3.4.2 Thermocouple

J-type thermocouples were installed across the experimental rigs and equipment to measure temperature; across the various locations, the temperature ranged between -5°C and 60°C. They were calibrated using a circulating water bath, recirculating glycol chiller, and an RS Pro RS51 wired digital thermometer capable of measuring temperature from -50°C to 250°C in denominations of 0.1°C. Each thermocouple was calibrated against the digital thermometer, ranging from -10°C to 70°C. The thermocouple calibrations have been recorded and are tabulated in **Table A.2-1** in Appendix **A2**.

3.4.3 Weighing scales

Three types of laboratory weighing scales were used to weigh all chemical and material substances accurately; the technical details of each are outlined below. The calibration of each scale was conducted externally.

- Mettler Toledo, model PJ 6000. Weighs up to 6000 g (accuracy ± 0.1 g).
- A&D Instruments, model EK-610i. Weighs up to 600 g (accuracy ± 0.01 g).
- Sartorius, model R160P. Weighs up to 162 g, (accuracy ± 0.01 mg).

3.5 Analytical Methods

3.5.1 Gas Chromatography – Thermal Conductivity Detector (GC-TCD)

The quantification of liquid samples was conducted using a gas chromatograph (GC), Thermo Fisher Scientific, model, Trace 1300 series, equipped with a thermal conductivity detector (TCD). A Rxi-35Sil MS (30 m x 0.25 mm x 0.5 μm) fused silica column was fitted in the GC-TCD. The carrier gas used was helium, with a purity of 99.996%, obtained from BOC. The operational set up of the GC-TCD was as follows; splitless injection mode, the oven temperature operated between 40°C – 200°C, the ramp rate was 10°C/min, and the temperature of the detector was kept at a constant operational temperature of 250°C. The full elution of all compounds injected was found to be satisfactory at a total run time of 18 minutes.

3.5.1.1 External standard calibration

An external standard calibration practice was adopted to quantify the solubility data in *Chapter 4: Solubility Measurements of LIB Electrolyte Components in Carbon Dioxide.* The selection was based upon the simplicity and reproducibility of the sample preparation and the sheer number of injections performed. This method involved preparing standard samples at various concentrations diluted in acetone over a fixed range. The raw gas chromatographic peak area was then plotted against the standard concentration, producing a calibration curve in a linear function. Unknown concentrations of each analyte were then determined from their respective peak area through comparison with the calibration curve [4]. The standard calibration curves for DMC, EMC, and EC are presented in **Figure 3-1**, **3-2**, and **3-3**, respectively.

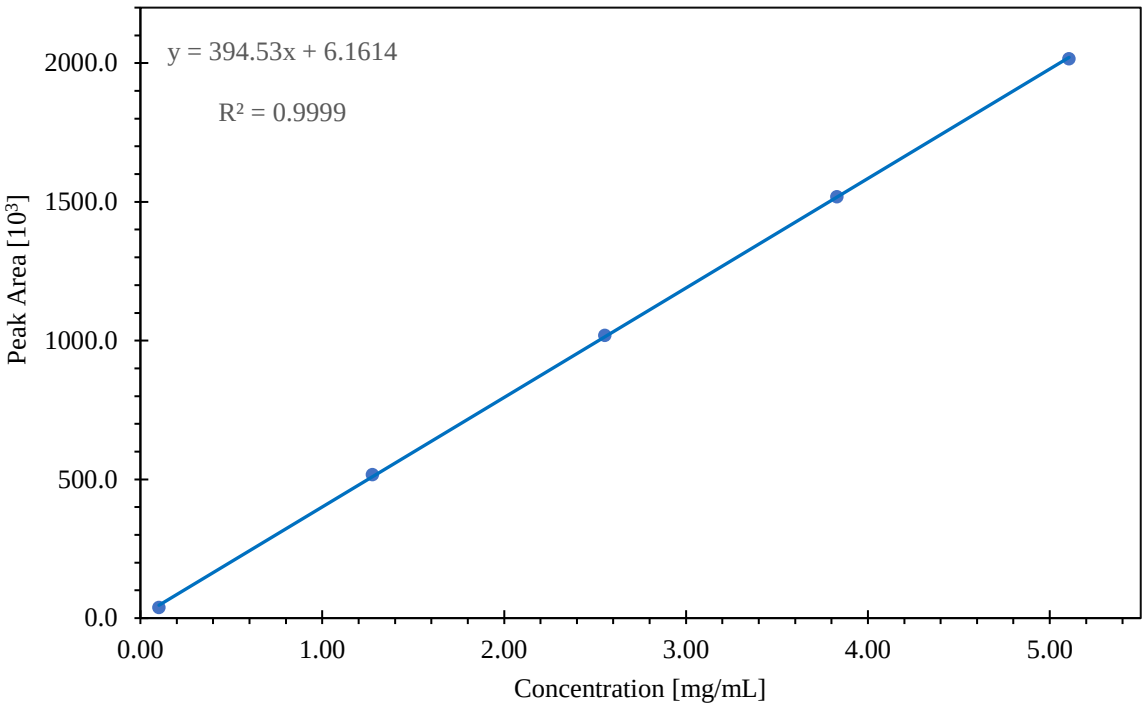

Figure 3-1: Standard GC-TCD calibration plot for dimethyl carbonate (DMC).

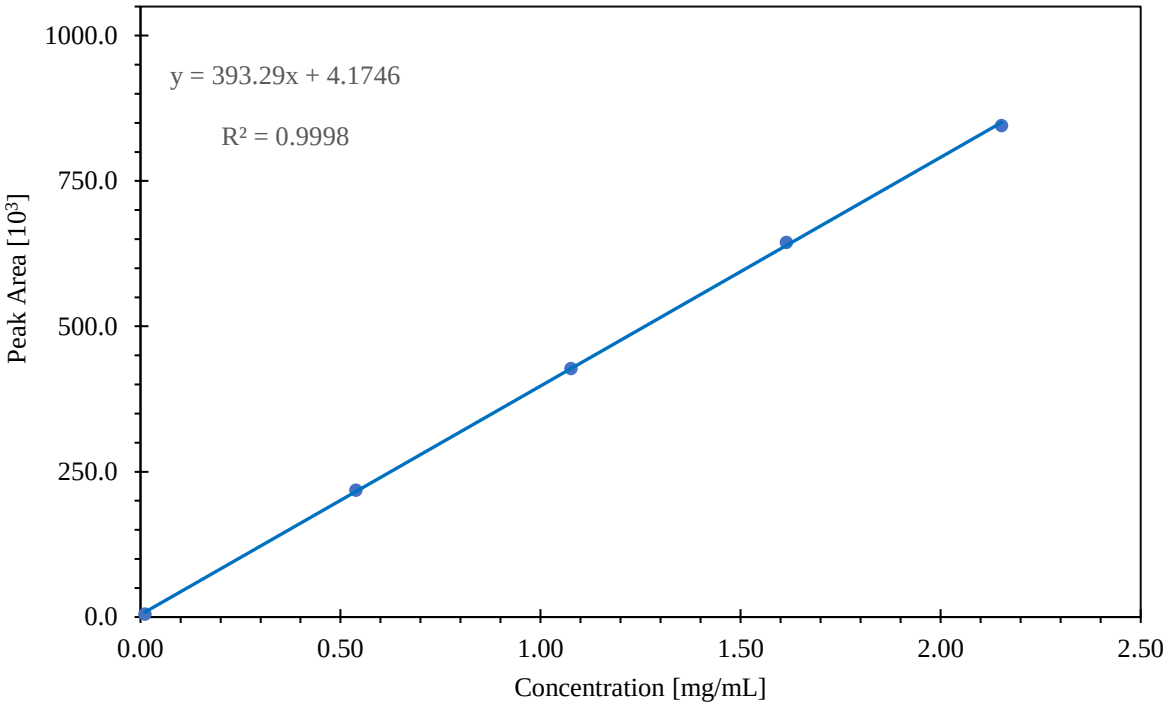

Figure 3-2: Standard GC-TCD calibration plot for ethyl-methyl carbonate (EMC).

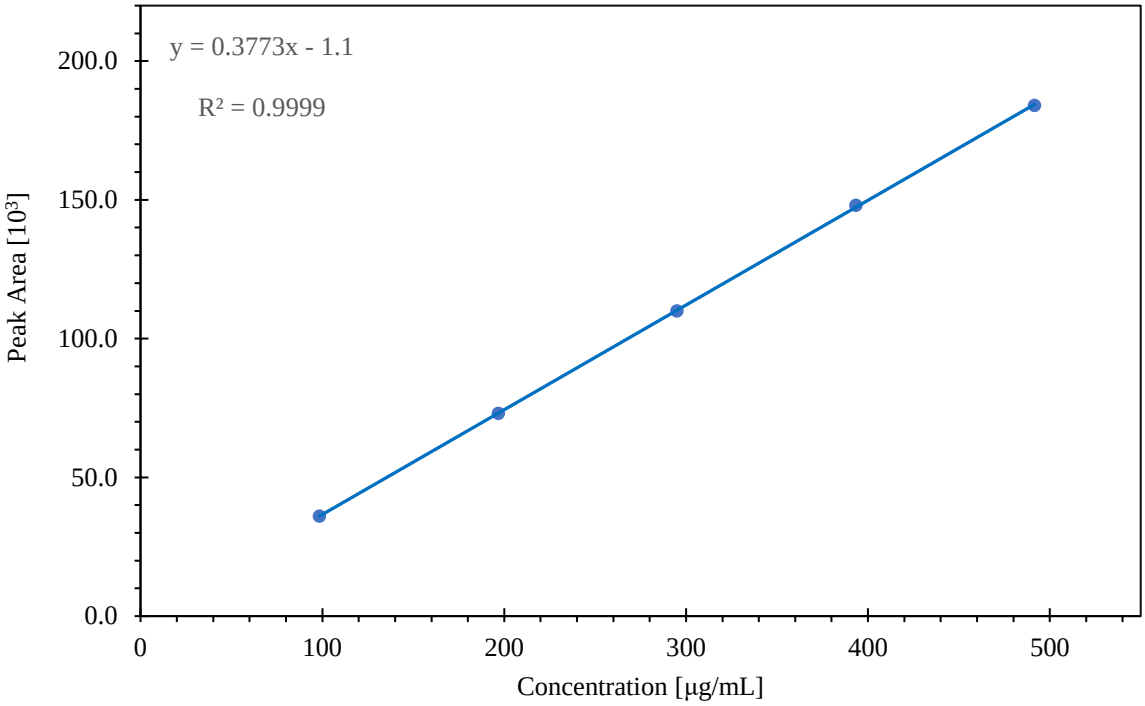

Figure 3-3: Standard GC-TCD calibration plot for ethylene carbonate (EC).

3.5.1.2 Internal standard calibration

Liquids samples in *Chapter 5: Extraction of Artificial LIB Electrolyte Using Pressurised Carbon Dioxide*, and *Chapter 6: Recovery and Characterisation of LIB Electrolyte from Electric Vehicles* were quantified with GC-TCD using an internal standard calibration technique; the method selection was introduced due to the variance in sample composition and preparation techniques. An internal standard is proven to compensate for variations in extraction efficiency, injection volume and detector drift [5].

The procedure involved preparing a solution with known mass quantities of analyte(s) and the internal standard. Standard response factors (RF) were then formed for each component, where A_X / A_{IS} represents the ratio of peak area response between the analyte, X, and internal standard,

IS. Similarly, w_X / w_{IS} represents the weight ratio between the analyte and internal standard. Unknown analyte quantities were determined using **Equations 3-1** and **3-2** [6].

$$\frac{RF_X}{RF_{IS}} = \frac{A_X}{A_{IS}} \frac{w_X}{w_{IS}} \quad \textbf{(3-1)}$$

$$Weight\ \%X = \left[\frac{(A_X\ RF_X\ )}{\sum_i (A_i\ RF_i)}\right] \times 100 \quad \textbf{(3-2)}$$

The internal standard, nonane, was deemed appropriate as it does not naturally occur in any of the samples tested. Nonane is extremely hydrophobic, and its boiling point fits within the range of the components analysed and does not interfere with sample response or retention in the column. **Figure 3-4** presents the chromatogram of the electrolyte solvents; DMC, EMC, DEC, and EC, with the nonane internal standard.

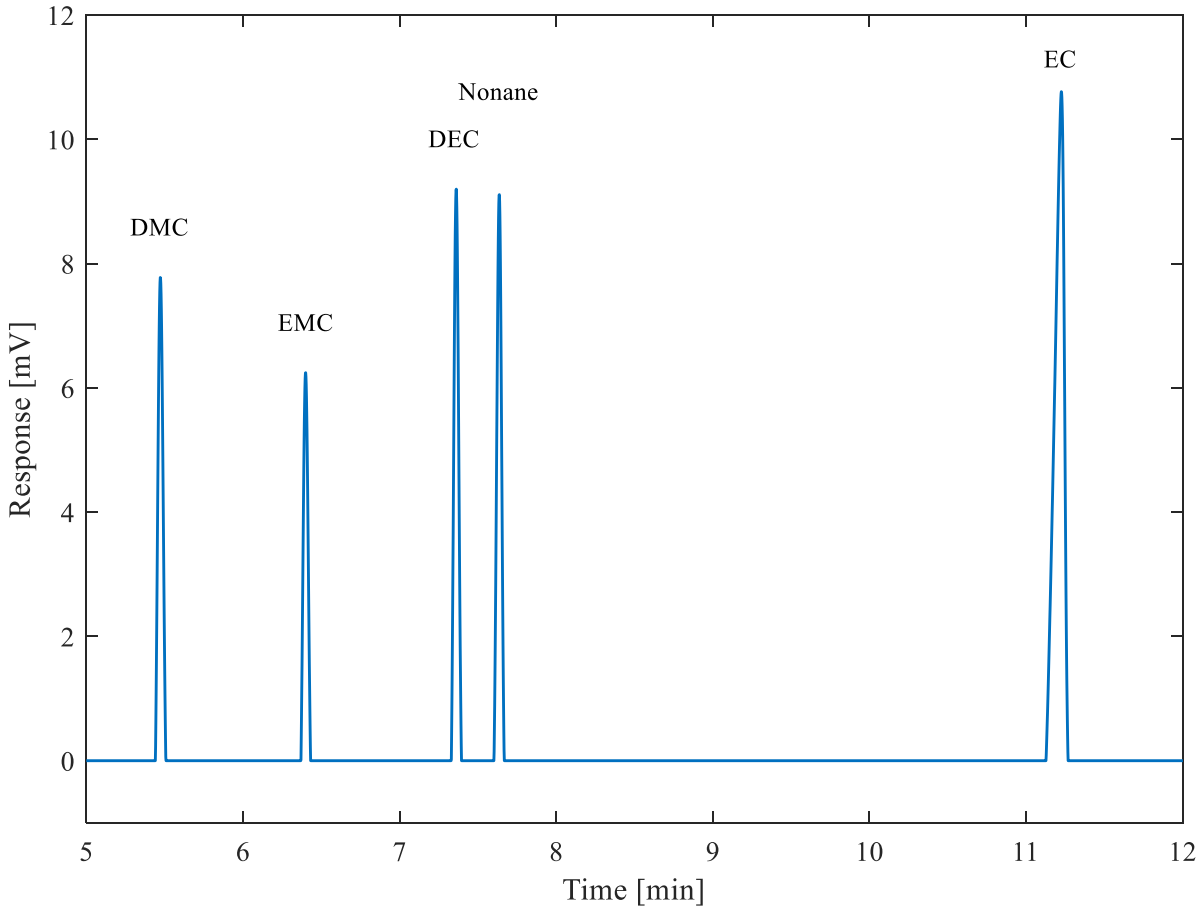

Figure 3-4: Standard GC-TCD chromatogram of samples; dimethyl carbonate (DMC), ethyl methyl carbonate (EMC), diethyl carbonate (DEC), ethylene carbonate (EC), and the internal standard (nonane).

3.5.2 Gas Chromatography – Mass Spectrometry (GC-MS)

Characterisation of analytes in liquid samples was performed using a GC, Thermo Fisher Scientific, model, Trace 1600 series with a mass spectrometer (MS), ISQ 7610. A Rxi-35Sil MS (30m x 0.25mm x 0.5 μm) fused silica column was fitted in the GC-MS, and liquid samples were auto injected using the AI 1610 liquid autosampler. The carrier gas used was helium, with a purity of 99.9992%, obtained from Air Products. The operational set up of the GC-MS was as follows; splitless injection mode, the oven temperature operated between 40°C – 270°C and the ramp rate was 8°C/min. During operation, the MS transfer line and ion source temperatures were kept at 200°C and 250°C, respectively.

Figure 3-5: Thermo Fisher Scientific, GC-MS.

3.5.3 Nuclear Magnetic Resonance (NMR) spectroscopy

Molecular structures in liquid samples were identified using ^{19}F and ^{31}P NMR spectroscopy. The measurements were taken with a Bruker NMR spectrometer, model AV400, operating at 400 MHz, coupled with Bruker 9.39 T Ultrashield magnet, and Bruker Avance NEO console. The samples were filtered and then added to deuterated dimethyl sulfoxide (DMSO-d_6) with a purity of 99.96% obtained from Eurisotop. Formation of a homogenous solution of both solvent and sample was established in Norell, standard series 500 MHz, 5 mm diameter glass NMR tubes. A field blank sample was initially performed to determine contaminants, analytical errors, or bias stemming from sample collection and analysis [7]. Both ^{19}F and ^{31}P NMR blank spectrums are provided in Appendix **A9**.

Figure 3-6: Bruker, NMR spectrometer.

3.5.4 Inductively Coupled Plasma – Optical Emission Spectroscopy (ICP-OES)

The identification and quantification of chemical elements in liquid samples were conducted using ICP-OES, Perkin Elmer, model Optima 8000. Supelco ICP multi-element standard solution IV contained 23 elemental concentrations (Ag, Al, B, Ba, Bi, Ca, Cd, Co, Cr, Cu, Fe, Ga, In, K, Li, Mg, Mn, Na, Ni, Pb, Sr, Tl, and Zn) diluted in nitric acid in a 1000 mg/L concentration. A copy of the certificate of analysis for the multi-element standard has been supplied in Appendix **A11**.

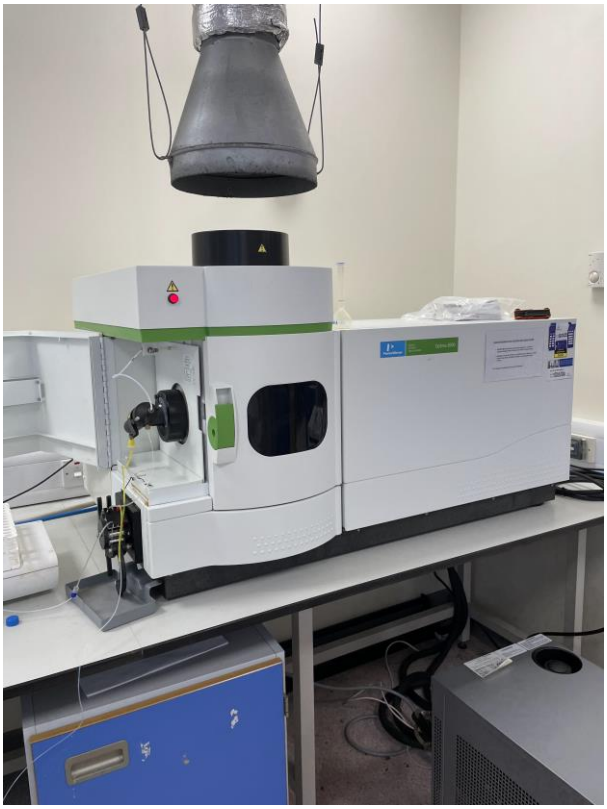

Figure 3-7: Perkin Elmer, ICP-OES.

The standard solution was further diluted with 3.5% (W/V) nitric acid, prepared from Nitric acid 70% (W/V) obtained from Fisher Scientific, and diluted in Milli-Q water. The concentrations used for the calibration curve were 0, 0.5, 1, 10 and 100 mg/L. Calibration curves for all the elements analysed have been presented in Appendix **A12**.

3.5.5 Thermogravimetric Analysis (TGA)

The thermal stability of samples was measured using a thermogravimetric analyser, Seiko Instruments Inc., model Exstar 6000, coupled with a TG/DTA6300. Nitrogen was used as the purge gas, and was maintained at a constant flowrate of 100 ml/min. A platinum crucible capable of withstanding high temperatures of up to 1200°C was used to hold the samples. The samples analysed were kept in the mass range of approximately 15 mg and heated from 50°C to 400°C at 10°C/min. The TGA temperature program applied to samples is displayed in **Figure 3-8**.

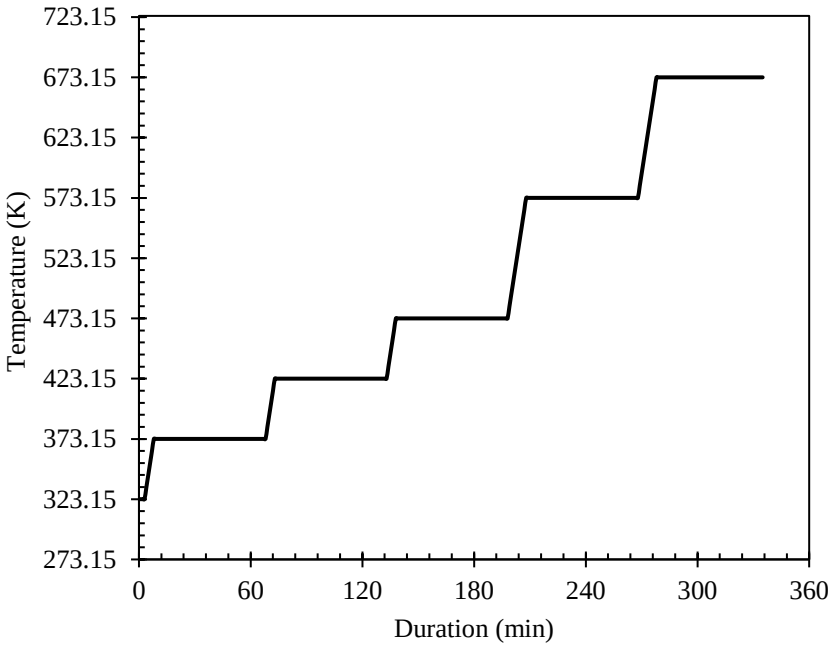

Figure 3-8: TGA temperature program.

3.5.6 Scanning Electron Microscopy (SEM)

The surface morphology of LIB components was assessed using a scanning electron microscope, Zeiss, model, EVO 15. The acceleration voltage was set at 20 kV, and reduced to 15 kV for non-conductive and beam sensitive specimens [8]. Samples were mounted to a double-sided carbon sticker and sputter coated with a 20 nm layer of gold at 50 mA using a Quantum Design Q150 T plus.

References – Chapter 3

1. *Hazardous Substances – Hazardous Waste Disposal. Chapter 1.* Birmingham: University of Birmingham 2005.

2. International Organization for Standardization. *ISO 8655-6:2022.* 2022.

3. John Blues DB, Mike Buckley. *The Calibration and Use of Piston Pipettes*. National Physical Laboratory. 2004. https://www.npl.co.uk/special-pages/guides/gpg69_piston.aspx?ext=. [Accessed 06/06/23].

4. Snow NH, Slack GC. Sample Preparation Techniques for Gas Chromatography. In: *Modern Practice of Gas Chromatography*. 2004. p. 545-604.

5. Burgard DR, Kuznicki JT. *Chemometrics Chemical and Sensory Data.* 1 ed.: CRC-Press; 1990.

6. Harold M. McNair, James M. Miller, Snow NH. Qualitative and quantitative analysis. In: *Basic Gas Chromatography*. Wiley; 2019. p. 139-155.

7. Raynie DE. The Vital Role of Blanks in Sample Preparation. *LCGC North America.* 2018; 36(8): 494–497. https://www.chromatographyonline.com/view/vital-role-blanks-sample-preparation.

8. Dusevich V. Choosing the Right Accelerating Voltage for SEM (An Introduction for Beginners). *Microscopy Today.* 2010; 18: 48-52. doi: 10.1017/S1551929510991190.

Chapter 4: Solubility Measurements of LIB Electrolyte Components in Carbon Dioxide

4.1 Introduction

Solubility, the relative ability of a solute to dissolve in a solvent to form a homogenous solution. Solubility is often regarded as the most important thermodynamic parameter affecting the efficacy of all supercritical processes. Factors such as rate, yield, design, and economy of the process are all directly affected by changes in solubility [1]. Commonly, experimental techniques determine the phase equilibria of high-pressure systems; today the experimental data can be correlated with the temperature, pressure, and equilibrium compositions using practical models [2].

This chapter outlines the design and operation of a static-analytical technique to obtain solubility data for LIB electrolyte solvents under a range of solvation strengths in carbon dioxide. The structure of the chapter is as follows: first, the *Objectives* of the solubility work performed are defined in Section **4.2**, the *Methodology* of the experimental practice is outlined in Section **4.3**, the *Calculations and Formulae* are given in Section **4.4**, the *Modelling Theory* is outlined in Section **4.5**, the experimental and modelling *Results and Discussion* are presented in Section **4.6**, and finally, the chapter is closed with a *Conclusion* in Section **4.7**.

4.2 Objectives

The main experimental objectives were twofold. Firstly, to assess the individual solubility of three alkyl carbonates: dimethyl carbonate, ethyl methyl carbonate, and ethylene carbonate. Each in a binary mixture with carbon dioxide under various temperature and pressure conditions. Secondly, to evaluate the change in solubility of a multi-component mixture. To achieve this, a quaternary system was established with carbon dioxide and a mixture of all three alkyl carbonates to mimic the electrolyte solvent blend in LIBs.

4.3 Methodology

4.3.1 Rig design

A working rig was designed and constructed to specifications suitable to obtain a range of low to high pressure vapour samples. The piping and instrumental diagram (P&ID) is illustrated in **Figure 4-1**. The main components of the rig consisted of a high-pressure vessel (HPV), a temperature control system, an air-driven liquid (carbon dioxide) pump and a vapour sampling loop.

Solubility measurements were performed in a static configuration, where the vapour – liquid equilibrium state was created in an autoclave manufactured by Baskerville Scientific, UK. The design features included three sapphire windows and a heating jacket. The design pressure of the reactor was rated at 33.1 MPa at a temperature of 403.15 K. Both vessel body and head (photographed in **Figure 4-2)** were cast from stainless steel 316, an alloy of steel containing an addition of molybdenum that provides a greater resistance against corrosion [3]. The nominal volume of the vessel is 500 ml, with an internal diameter (ID) of 60 mm, and an outside diameter (OD) of 127 mm.

The internal pressure was recorded using a transducer (Druck PTX 1400), connected to an indicator (Druck DPI) capable of displaying readings accurately up to ± 0.01 MPa. An additional series of three analogue manometers (Budenberg 966GP) were installed across the system, accurate to ± 0.5 MPa, each labelled PI 02, PI 03, and PI 04 in **Figure 4-1** [4]. The temperature of the vessel was recorded using a K-type thermocouple that fed into a transducer (TME electronics), providing readings accurate to ± 0.1 K.

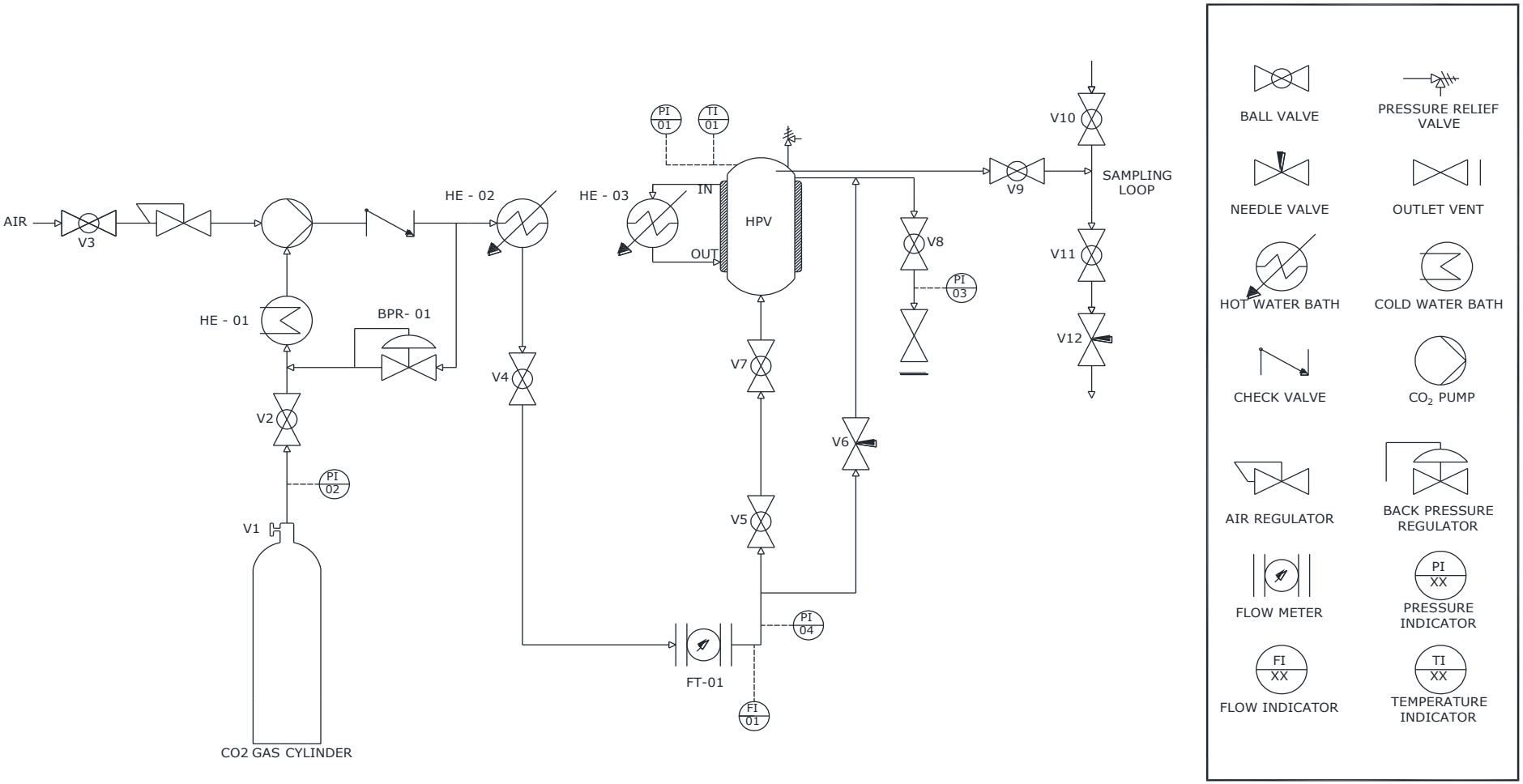

Figure 4-1: Schematic diagram of solubility experimental apparatus.

Figure 4-2: Photographs of Baskerville Scientific autoclave;
i) vessel head, ii) vessel body.

4.3.1.1 O-ring

Polymerisation processes have exposed certain relationships between supercritical carbon dioxide ($scCO_2$) effects and polymer microstructures. The prolonged contact of O-ring polymers with scCO2 causes plasticisation due to the high solubility and low diffusivity characteristics of scCO2, leading to a decrease in their polymer glass transition temperature [5].

During the early stages of the experiments, the reactor head was sealed to the body using O-rings made of nitrile butadiene rubber (NBR) and fluroelastomer (FKM). However, it was later discovered that these materials were incompatible. This was partly due to the nature of high-pressure carbon dioxide, which caused the NBR O-ring to become inferior due to the presence of plasticisers that could be extracted. Additionally, both the NBR and FKM materials were found to be non-resistant to DMC and EMC. Specifically, the FKM O-ring which was discovered to swell significantly in the presence of both components due to their low molecular weight and adverse reaction with their carbonate ester functional group.

The structural failures presented in **Figure 4-3** of both NBR and FKM O-rings resulted from their incompatibilities with chemical compounds and the mechanisms of rapid gas decompression (RGD). Post swelling, the material supersaturated with CO_2 released the dissolved gas rapidly, resulting in nucleation and the formation of internal gas bubbles. As the O-rings failed, the depressurisation rate increased, causing extensive physical damage resulting in surface blistering and shredding of the elastomer.

The selection of the O-ring was determined by the compatibility of polymers against various chemical function groups. The U.S. Department of Energy - Office of Scientific and Technical Information (DOE-OSTI) released a scientific report [5] outlining the compatibilities of various polymers in supercritical carbon dioxide. This report assisted in selecting a polytetrafluoroethylene (PTFE) O-ring machined to the reactor's specification [6]. The specifications of the PTFE O-ring: BS231, outer diameter (OD) – 73.33 mm, inner diameter (ID) – 66.27 mm, thickness – 3.53 mm.

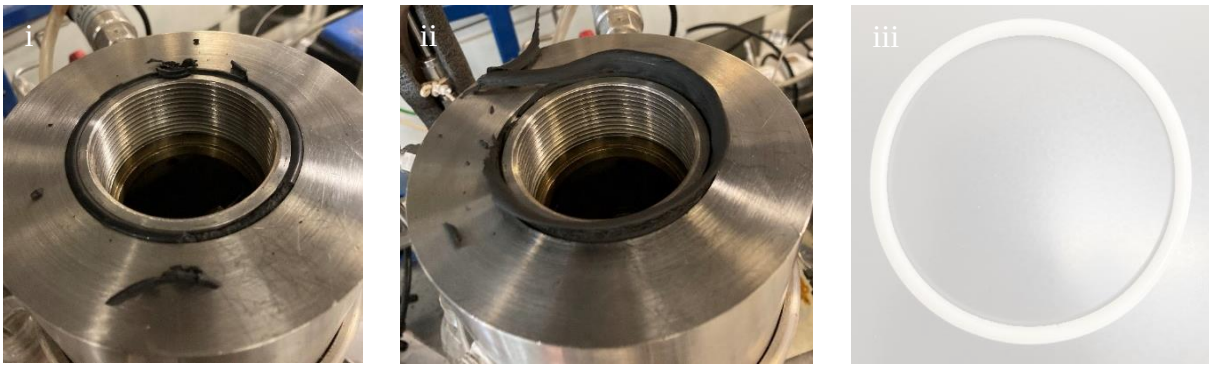

Figure 4-3: Photographs of O-rings; i) damaged NBR O-ring, ii) damaged FKM O-ring, iii) fitted PTFE O-ring.

4.3.1.2 Sampling loop

The complete arrangement of the sampling loop is presented in **Figure 4-1**. A thin stainless-steel capillary (Thames Restek UK), ID 100 μm, OD 1/32 in, and 0.2 m in length, captured vapour samples directly from the centre of the pressure vessel. The capillary extended from the high-pressure vessel (HPV) to the sampling loop via a connection with V9. Construction of the sampling loop was assembled using: 3 x Swagelok ball valves (SS-41GS1) and 315 mm of 1/16th in Swagelok steel tubing, wall thickness 0.02 in. A Hoke micro-metering valve (1315G2Y) (V12) connected to the ball valve (V11) ensured a controlled depressurisation of the collected vapour sample.

Before collecting the vapour samples, the internal volume of the sampling loop was accurately measured. The preliminary sampling loops' dead volume was estimated to be 0.081 mL based on the internal volume of the steel tubing; the valves were quoted to have virtually no dead space by the manufacturer and thus were not included within the basic calculation.

A more precise method for determining the internal volume of the sampling loop involved filling the entire sampling loop volume with dimethyl carbonate, and then flushing the internal volume with acetone repeatedly until DMC gave no detectable GC trace. The sample solution was then prepared to a volume of 10 mL before injecting the sample into the GC-TCD. Repeats were conducted after the sampling loop was washed with approximately 30 ml of acetone to remove any traces of DMC in the valves or lines of the piping.

An average sampling loop volume was calculated as 0.104 ± 0.009 mL, taken from a range of 10 samples, as presented in **Figure 4-4**. The relative standard deviation (RSD) in this value is 5.02 %.

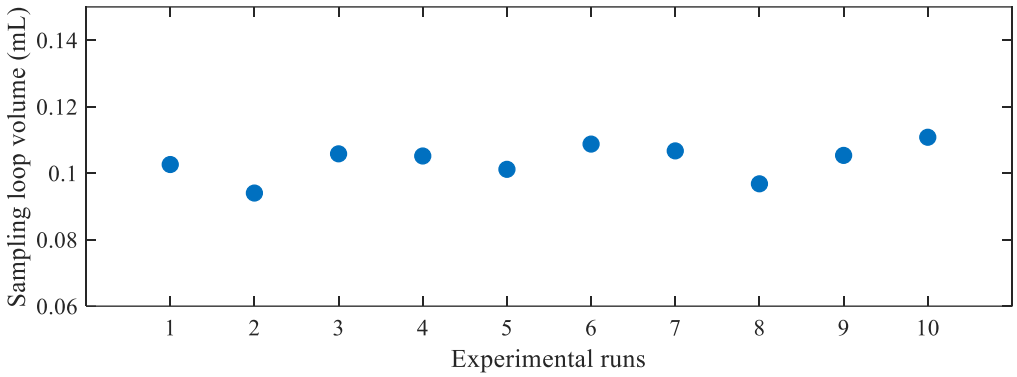

Figure 4-4: Experimental measurements to calculate the volume of the sampling loop.

4.3.2 Method

The solubility measurement technique is broken down into several notable stages:

4.3.2.1 Rig preparation

Prior to sample loading, the inside of the vessel was thoroughly cleaned using acetone to remove possible solute residue from the previous run. The inlet to the HPV would often flood post experiment with solute, thus the ball valve (V7) was disconnected from the inlet line and flushed with acetone and then with carbon dioxide. The identical practice was carried out in the sampling loop, all lines were disconnected, washed, and left to dry for approx.12 hours.

Prior to the experiment, the PTFE O-ring was visually inspected to verify the integrity of the seal and to ensure the previous experimental run had not damaged it.

4.3.2.2 Sample loading

Samples were given thirty minutes to acclimatise to room temperature before measuring. All samples (DMC, EMC, and EC) were measured gravimetrically. A 15 g sample was measured in a clean glass vial and then loaded into the HPV.

4.3.2.3 System pressurisation

Prior to pressurisation, the Baskerville heating jacket was preheated to the desired temperature via a hot water circulator (Polyscience model-9505) (HE-03), completing the step in advance prevented pressure fluctuations and allowed the system to stabilise more swiftly.

Referring to **Figure 4-1**. Liquid carbon dioxide was first introduced into the system via the gas cylinder inlet (V1), the carbon dioxide travelled through a series of coils sitting in a refrigerated immersion cooler (Grant C1G) (HE-01). The heat transfer fluid, glycol, was maintained at a temperature less than 5℃, to ensure the liquid state of carbon dioxide and protect the pump against cavitation. The steel tubing between the cold bath and the air driven liquid pump (PowerStar 4; Model: P464, Sprague) was kept as short as possible and insulated with polyethylene foam to minimise the vaporisation of carbon dioxide.

Pressurisation of the HPV was completed in two stages. First, the vessel was equalised to the internal pressure of the gas cylinder, at approx. 5.0 MPa, next compressed air was released (via V3) and the flowrate was fine-tuned through a regulator controlling the stroke rate of the liquid pump. The pressure of the HPV was controlled using a back pressure regulator (BPR), maintaining a defined pressure upstream of its own inlet and alleviating excess flow back into the recycle stream.

Before entering the HPV, carbon dioxide was passed through an arrangement of coils in a hot water bath (Tecam) (HE-02), pre-heating the flow to the desired temperature.

The mass flowrate of the carbon dioxide gas stream was directly measured prior to entering the vessel using a coriolis meter (Rheonik, D-85235), the sensor was linked to a digital transmitter (Rheonik, RHE08) capable of displaying and recording multiple feedback outputs.

4.3.2.4 Solvent sample contact

Once the internal HPV temperature and pressure conditions were stable, all inlet and outlet valves (V6, V7, V8, and V9) were closed to isolate the HPV. The contents were then permitted to reach equilibrium for a minimum of 8 hours allowing the vapour – liquid phases to equalise. This time interval was deemed sufficient, as GC-TCD analysis showed no significant solubility deviations beyond this interval. The determination of the duration required to establish vapour-liquid equilibrium is presented in Appendix **A3**.

4.3.2.5 Solute collection and depressurisation

The selected sampling method was an off-line quantification technique [2]. Once equilibrium had been established, the first step required any stagnant vapour residing in the dead volume of the tubing between the sampling loop and the reactor to be flushed. Three consecutive dummy samples were deemed sufficient. A minimum of three vapour samples were collected at each pressure and then analysed. The associated pressure drops were minimal, aided by the large volume of the HPV and the small dead volume of the sampling loop; the system pressure imbalance did not exceed 1.2 %. Each pressure drop experienced during sampling of the vapour phase has been recorded and is presented in Appendix **A4**.

Before a sample was released from the HPV, the internal temperature and pressure of the vessel were recorded. The ball valve (V9) was instantaneously opened and then closed to fill the sampling loop.

The ball valve (V11) and metering valve (V12) were sequentially opened, and the vapour sample was gradually bubbled into a test tube containing acetone. To ensure the solute condensed and was trapped in the acetone solution, the test tube was immersed in ice to keep the temperature of the acetone solution close to 0°C, considerably less than the boiling point of all components measured. As the boiling point of CO_2 is significantly lower than the temperature of the acetone solution, the small volume of gas simply escaped. Once the vapour sample had been completely expanded, a volume of acetone was flushed through the sampling loop and into the test tube via the ball valve (V10), dissolving the solute residue trapped in the lines of the tubing. Lastly, between each sample collection, the sampling loop was washed with an excess of acetone to remove any possible solute residue and then left to dry for twenty minutes before being evacuated and sealed.

4.3.2.6 Sample analysis

The sample solution was then standardised and diluted to a volume of 10 mL in acetone. The small nature of the vapour sample meant the solution did not require degassing before injecting an aliquot in the GC-TCD. The analyte responses were then compared to the external calibration standards plotted for each component (as presented in *Chapter 3: Materials and Analytical Techniques*), and a gravimetric quantity of solute was obtained.

4.4 Calculations and Formulae

The following equations were applied to obtain and process the experimental solubility and vapour equilibrium data in this chapter.

4.4.1 Vapour mole fraction

$$y_1 + y_2 = 1 \quad \textbf{(4-1)}$$

In vapour - liquid equilibrium, **Equation 4-1** holds true for a binary system where y_1 is the vapour mole fraction of component 1, and likewise, y_2 represents the vapour mole fraction of component 2 [7].

4.4.2 Sampling loop

$$V_{sample\ loop} = V_{solute} + V_{solvent} \quad \textbf{(4-2)}$$

The volumetric composition of a vapour sample is equivalent to the accumulation of the volume of the solute and the volume of the solvent, as expressed in **Equation 4-2**. Naturally, the sample loop contained air under standard conditions; under high pressures this is negligible as the air compresses, but for lower pressures it is more significant. Thus, the sampling loop was evacuated prior to collecting each sample.

The vapour equilibrium data was expressed in two principal forms, as a solubility and as a mole fraction.

4.4.3 Solubility of component

$$S_{solute} = \frac{m_{solute}}{m_{CO_2}} \quad \textbf{(4-3)}$$

$$= \frac{(\rho_{solute} * V_{solute})}{\left(\rho_{CO_2} * \left(V_{sample\ loop} - V_{solute}\right)\right)} \quad \textbf{(4-4)}$$

Where the solubility (S) (g/g) represents the mass (g) of the solute component dissolved in one gram of carbon dioxide, as presented in (**Equations 4-3** and **4-4**). Where m represents the mass, ρ the density and V the standard volume.

4.4.4 Moles of carbon dioxide

$$n_{CO_2} = \frac{\left(\rho_{CO_2} * \left(V_{sample\ loop} - V_{solute}\right)\right)}{M_{r\,CO_2}} \quad \textbf{(4-5)}$$

4.4.5 Mole fraction of carbon dioxide

$$y_{CO_2} = \frac{n_{CO_2}}{n_{total}} \quad \textbf{(4-6)}$$

$$= \frac{n_{CO_2}}{\frac{\left(\rho_{CO_2} * \left(V_{sample\ loop} - V_{solute}\right)\right)}{M_{r\,CO_2}} + n_{solute}} \quad \textbf{(4-7)}$$

The mole fraction of carbon dioxide (y_{CO_2}) is expressed as the ratio of moles of carbon dioxide (n_{CO_2}), to the total moles in the system (n_{total}), as outlined in **Equations 4-6** and **4-7**. Where M_r represents the molar mass (g/mol).

4.4.6 Sample standard deviation

Standard deviation measurements were formulated from a range of solubility and mass fraction data, the results were presented in tabular form, and in figures as error bars.

$$StDEV = \sqrt{\frac{1}{n-1}\sum_{i=1}^{n}(x_i - \bar{x})^2} \quad \textbf{(4-8)}$$

Where, (x_1, x_2…, x_N) are the raw data points, $\bar{x}$ represents the mean value of the data points, and n is the number of data points [8].

4.4.7 Average absolute relative deviation (AARD)

Calculated similarly to the sample standard deviation, the average absolute relative deviation was applied to evaluate the robustness of the semi-empirical models against the experimental data.

$$AARD\ (\%) = \sqrt{\frac{100}{n}\sum_{i=1}^{n}\frac{|x^{exp} - x^{cal}|}{x^{exp}}} \quad \textbf{(4-9)}$$

Where, x^{exp} is the experimental data points, x^{cal} represents the modelled values, and n is the number of data points [9].

4.5 Modelling Theory

4.5.1 Introduction

Phase equilibrium studies conducted at high pressure are often time exhaustive and expensive. For this reason, the development of several thermodynamic models have been employed. These models aim to enhance our comprehension of each system and validate the experimental data's reliability. Thermodynamic models are often employed to predict various properties, such as enthalpy or phase equilibrium. These types of models can be extended to include equations of state (EoS), activity coefficient, empirical, or special system specific. Such models are capable of correlating and predicting phase behaviour, allowing the optimisation of solubility. Model selection depends on several factors, foremost being process species and composition, temperature, and pressure conditions, plus the availability of data [10, 11].

Simple cubic EoS models combined with various mixing rules have been used extensively to calculate solute solubility in supercritical carbon dioxide. Application of such models require the critical properties, acentric factor (to calculate the fugacity coefficient), sublimation vapour pressure and molar solute volume to obtain the solubility [12].

Empirical equations employ density-based models, only requiring pure supercritical carbon dioxide density and the operational temperature and pressure parameters. Semi empirical models are reliable as they also utilise experimental data making them considerably more accurate than models solely relying on theoretical equations. Their realistic and practical approach can be extended to multi component systems with unknown components [13, 14].

This section covers the mathematical expressions for the thermodynamic models selected for the computations: Peng-Robinson (PR), the Cubic Plus Association (CPA) and a pair of density-based models.

4.5.2 Peng Robinson

Experimental data for both CO_2 + DMC and CO_2 + EMC were correlated with the Peng-Robinson (PR) equation of state (EoS) [15] and van der Waals (vdW) one-fluid mixing rules. The PR model was developed through improving the predictive capacity of the Soave modified Redlich-Kwong (SRK) model, which preserves the desired simplicity of the cubic form whilst improving the reliability of the performance in the critical region and along the saturated liquid curve [16]. The limitations of EoS models are, however, well known, especially when modelling complex mixtures (e.g. polar and associating), though they are applicable across a wide range of temperatures and pressures, and have been used for decades across the chemical industry due to their robustness and simple mathematical form [17].

$$P = \frac{RT}{V-b} - \frac{a(T)}{V(V+b)+b(V-b)} \quad \textbf{(4-10)}$$

Equation 4-11 is the recently updated version of the generalised Soave α-function [18].

$$a(T) = 0.45724\frac{R^2{T_c}^2}{P_c}\left\{1+k\left[1-\left(\frac{T}{T_c}\right)^{0.5}\right]\right\}^2 \quad \textbf{(4-11)}$$

$$k = 0.3919 + 1.4996\omega - 0.2721\omega^2 + 0.1063\omega^3 \quad \textbf{(4-12)}$$

$$b = 0.07780\frac{RT_c}{P_c} \quad \textbf{(4-13)}$$

The mixing parameters are defined by the one-fluid mixing rules:

$$a_m = \sum_i \sum_j x_i x_j a_{ij} \quad \textbf{(4-14)}$$

$$b_m = \sum_i x_i b_i \quad \textbf{(4-15)}$$

Where

$$a_{ij} = \left(1 - k_{ij}\right) {a_i}^{0.5} {a_j}^{0.5} \quad \textbf{(4-16)}$$

In its cubic polynomial form, **Equation 4-10** can be written as:

$$Z^3 - (1 - B)Z^2 + (A - 3B^2 - 2B)Z - (AB - B^2 - B^3) = 0 \quad \textbf{(4-17)}$$

Where

$$A = \frac{aP}{R^2 T^2} \quad \textbf{(4-18)}$$

$$B = \frac{bP}{RT} \quad \textbf{(4-19)}$$

$$Z = \frac{PV}{RT} \quad \textbf{(4-20)}$$

Where P represents the pressure (MPa), R defines the molar gas constant (J $\mathrm{mol}^{-1}\mathrm{K}^{-1}$), P_c is the critical pressure (MPa), T is the absolute temperature (K), T_c is the critical temperature (K), V is the molar volume ($\mathrm{m}^3/\mathrm{mol}$), k_{ij} represents the binary interaction parameter, ω is the acentric factor. The parameters a and b are generally obtained from correlations of critical properties, where a is a measure of attractive force and is a function of temperature, and parameter b is a constant associated with the size of the molecules.

4.5.3 Cubic Plus Association model

The Cubic Plus Association (CPA) model [19] combines the simplicity of a cubic equation of state. Soave Redlich Kwong (SRK) EoS [20] is employed to define the "physical" interactions, plus an additional term is taken from Wertheim's perturbation theory to consider the polar and

association effects. In respect to volume, it is not cubic (due to the Wertheim term) and contains five pure compound parameters determined using vapour pressures and saturated liquid densities [19, 21].

Expression of the CPA EoS can be presented in terms of pressure, as a sum of the SRK EoS and the contribution of the association term given by Michelsen and Hendriks [22].

$$P = \frac{RT}{V_m - b} - \frac{\alpha(T)}{V_m(V_m + b)} - \frac{1}{2}\left(\frac{RT}{V_m}\right)\left(1 + \frac{1}{V_m}\frac{\partial \ln g}{\partial\left(\frac{1}{V_m}\right)}\right)\sum_i x_i \sum_{A_i}\left(1 - X_{A_i}\right) \quad \textbf{(4-21)}$$

Where $\alpha(T)$ is the temperature dependent SRK energy parameter, g is the hard sphere radial distribution function, A_i corresponds to the association site A on component, not bonded to other sites. X_{A_i} is the fraction of sites, type A on component i, not bonded to other sites [21, 23].

The association term representing the binding strength between site A on molecule i and site B on molecule j is given by:

$$\Delta^{A_iB_j} = g(V_m)^{ref}\left[\exp\left(\frac{\epsilon^{A_iB_j}}{RT}\right) - 1\right] b_{ij}\beta^{A_iB_j} \quad \textbf{(4-22)}$$

Where $\epsilon^{A_iB_j}$ signifies the association energy, $\beta^{A_iB_j}$ is the volume of interaction between site A of molecule i and site B of molecule j, respectively. The term $g(V_m)^{ref}$ represents the contact value of the radial distribution function for the reference hard sphere fluid system.

The simplified radial distribution function is given by:

$$g(V_m)^{ref} = \frac{1}{1 - 1.9\eta} \quad \textbf{(4-23)}$$

And

$$\eta = \left(\frac{1}{4\,V_m}\right) b \tag{4-24}$$

Where η is the reduced fluid density.

The energy parameter, a, for the SRK EoS term is defined using a Soave-type temperature dependency:

$$a = a_0 \left(1 + c_1\left(1 - \sqrt{T_r}\right)\right)^2 \tag{4-25}$$

Where T_r is the reduced temperature (T/T_c). CPA EoS utilises five pure component parameters: three for non-associating compounds (a_0, b, c_1) and two additional parameters for associating compounds ($\epsilon^{A_iB_j}, \beta^{A_iB_j}$). The five pure component parameters are normally obtained by fitting the model to experimental vapour pressures and saturated liquid densities of the pure component. The three pure component parameters for non-associating compounds alternatively may be collected using T_c, P_c, and ω [19, 21].

Extension of the CPA EoS to mixtures requires mixing and combining rules for a and b, here the vdW one-fluid mixing rules are applied, as defined in **Equations 4-14** – **4-16**. Though, between different associating molecules, i.e., $i \neq j$ (e.g., water – alcohol or water – glycol systems) combining rules are required for the association energy and volume parameters. Many types of combining rules have been established, but from various investigations two choices, the so-called CR-1 rule [24] and the so-called Elliott combining rule (ECR) [25] have been proven to be more successful.

CR1:

$$\epsilon^{A_iB_j} = \frac{\epsilon^{A_iB_i} + \epsilon^{A_jB_j}}{2} \quad \textbf{(4-26)}$$

$$\beta^{A_iB_j} = \sqrt{\beta^{A_iB_i}\beta^{A_jB_j}} \quad \textbf{(4-27)}$$

ECR:

$$\Delta^{A_iB_j} = \sqrt{\Delta^{A_iB_i}\Delta^{A_jB_j}} \quad \textbf{(4-28)}$$

Under the assumption that the term $\exp\frac{\epsilon^{AB}}{RT} \gg 1$, the ECR can be presented in equivalent forms that incorporates the cross-association energy and volume parameter, as presented below [21]:

$$\epsilon^{A_iB_j} = \frac{\epsilon^{A_iB_i} + \epsilon^{A_jB_j}}{2} \quad \textbf{(4-29)}$$

$$\beta^{A_iB_j} = \sqrt{\beta^{A_iB_i}\beta^{A_jB_j}}\frac{b_ib_j}{b_{ij}} \quad \textbf{(4-30)}$$

4.5.4 Semi-empirical methods

Density based semi-empirical methods were employed to assess and correlate the CO_2 + EC system using CO_2 densities obtained from the NIST database. Often, semi-empirical models are selected because they are relatively simple to utilise, as opposed to the EoS models. They are based on simple error minimisation and often apply the least-square method, they do not require solute properties, only knowledge of temperature, pressure, density of solvent (e.g. scCO_2), and solubility data. Three of the most common semi-empirical methods are those developed by *Chrastil* (1982) [26], *Méndez-Santiago and Teja* (1999) [27], and *Bartle et al*. (1991) [28-30] .

The *Chrastil* model [26] follows the assumption that the interaction between solvent and solute molecules form a solvent complex, creating an equilibrium between the pair. The theoretical model is displayed below, **Equation 4-31**.

$$\ln y = a_1 \ln \rho + \frac{b_1}{T} + c_1 \quad \textbf{(4-31)}$$

Where y is the mole fraction of solute in the solvent, ρ represents the density of the supercritical fluid (g/ml), T is the system temperature (K), a_1, b_1, and c_1 are all model constraints obtained by fitting the experimental data.

Inspired by the dilute solution theory, the MST model [27] was proposed by *Mendez-Santiago and Teja*, centred on the algorithm of Henry's law constant of solute in a supercritical fluid. The association between component solubility and the system parameters is presented in **Equation 4-32**.

$$T \ln yP = A_1 + A_2\rho + A_3 T \quad \textbf{(4-32)}$$

Where y is the mole fraction of solute in the solvent, ρ represents the density of the supercritical fluid (g/ml), T is the system temperature (K), P is the system pressure (MPa) and A_1, A_2, and A_3 are all constants [31].

4.6 Results and Discussion

4.6.1 Experimental binary vapour equilibrium systems

Mass transfer and separation methods are heavily dependent on the comprehension of vapour-liquid equilibrium data. The solubility behaviour of DMC, EMC, and EC was investigated in carbon dioxide as a binary and quaternary component system, as noted below:

- Carbon Dioxide – Dimethyl Carbonate
- Carbon Dioxide – Ethyl-Methyl Carbonate
- Carbon Dioxide – Ethylene Carbonate
- Carbon Dioxide – Dimethyl Carbonate – Ethyl-Methyl Carbonate – Ethylene Carbonate

A literature survey was conducted for each component in a binary system with carbon dioxide. **Table 4-1** compiles the author and the parameters of their experiment, respectively. A literature review revealed that the CO_2 + EMC and CO_2 + EC binary systems have not been extensively explored, and the vapour phase data for each system has not been published, to our knowledge.

Each binary vapour equilibrium system was measured under the isotherms of 298.2 K, 313.2 K, and 328.2 K, ranging from 0.12 - 14.1 MPa. Each set of temperature and pressure conditions were deliberately chosen both below and above the critical point of carbon dioxide (7.38 MPa, 304.18 K) to evoke both the subcritical and supercritical states of carbon dioxide. The higher temperature limits were specifically selected to elevate the vapour pressure of components in carbon dioxide, thereby augmenting their solubility.

Table 4-1: Literature data for the binary systems of; CO_2 + DMC, CO_2 + EMC and CO_2 + EC.

	Author	Year	Temperature Range (K)	Method to Attain Equilibrium	Pressure Range (MPa) V – Vapour Phase L – Liquid Phase
DMC	F. Blanchard et al. [32].	2003	283.00 - 316.00	-	Atmospheric (L)
	S. Camy et al. [33].	2003	322.65 - 373.55	Magnetic Stirrer	1.33 – 12.75 (VL)
	J. Im et al. [34].	2004	310.27 - 340.27	Recirculation	0.83 – 10.00 (VL)
	C. Lu et al. [35].	2008	273.00 - 293.00	Stirrer	0.66 – 4.19 (VL)
	X. Gui et al. [36].	2010	280.70 - 327.66	Magnetic Stirrer	0.074 – 5.48 (L)
	Y. Hou et al. [37] .	2010	308.15 - 337.45	-	6.16 - 10.45 (L)
	R. Ciccolini et al. [38].	2010	310.20 - 373.60	Magnetic Stirrer	1.11 – 9.65 (L)
	M. Lee et al. [39].	2012	293.15 - 333.15	Recirculation	0.19 – 9.45 (VL)
	C. Li et al. [40].	2013	333.00 - 393.00	Magnetic Stirrer	3.98 -13.75 (VL)
	M. Anouti et al. [41].	2012	283.15 - 353.15	-	Atmospheric (L)
EMC	M Anouti et al. [41].	2012	283.15 – 353.15	-	Atmospheric (L)
EC	F Blanchard et al. [32].	2003	313.00 – 333.00	-	Atmospheric (L)
	M Anouti et al. [41].	2012	291.15 – 353.15	-	Atmospheric (L)

The experimental data for each system, CO_2 + DMC, CO_2 + EMC and CO_2 + EC is presented in **Tables 4-2**, **4-3**, and **4-4**, respectively. Where, the mole fraction of carbon dioxide in the vapour phase is denoted as y_{CO_2}, the solubility of each solute in carbon dioxide is represented as S, and the respective standard deviation (SD) value proceeds each parameter. Note, the pressurised carbon dioxide density values were obtained from the National Institute of Standards and Technology (NIST) chemistry web-book.

Table 4-2: Experimental vapour mole fraction and solubility of the binary system, CO_2 + DMC[a].

T (K)	P (MPa)	ρ_{CO_2} (g/ml)	S_{DMC} (g/g)	S_{DMC} SD	y_{CO_2}	y_{CO_2} SD
298.2	0.32	0.0058	0.0566	0.00373	0.9731	0.00172
	0.61	0.0112	0.0343	0.00341	0.9835	0.00161
	1.5	0.0289	0.0210	0.00343	0.9899	0.00164
	2.6	0.0539	0.0128	0.00284	0.9938	0.00137
	3.8	0.0870	0.0087	0.00081	0.9958	0.00039
	5.0	0.1313	0.0087	0.00094	0.9958	0.00046
	6.1	0.1995	0.0045	0.00077	0.9961	0.00037
313.2	0.42	0.0072	0.1010	0.01081	0.9530	0.00481
	0.75	0.0131	0.0475	0.00442	0.9773	0.00207
	2.0	0.0371	0.0250	0.00624	0.9880	0.00173
	4.1	0.0865	0.0124	0.00276	0.9940	0.00133
	6.2	0.1577	0.0105	0.00344	0.9949	0.00166
	8.0	0.2779	0.0202	0.00143	0.9926	0.00069
328.2	0.41	0.0067	0.1689	0.01809	0.9239	0.00754
	1.3	0.0220	0.0683	0.00879	0.9677	0.00402
	3.5	0.0654	0.0349	0.00180	0.9833	0.00085
	5.1	0.1041	0.0273	0.00144	0.9868	0.00069
	7.1	0.1667	0.0315	0.00260	0.9848	0.00123
	8.7	0.2385	0.0324	0.00166	0.9844	0.00078
	10.6	0.3772	0.0467	0.00576	0.9777	0.00268

n = 3. [a]Standard uncertainties are u(T) = 0.1 K, u(P) = 0.01 MPa, u(S_{DMC}) = 0.02, u(y_{CO_2}) = 0.008

Table 4-3: Experimental vapour mole fraction and solubility of the binary system, CO_2 + EMC[a].

T (K)	P (MPa)	ρ_{CO_2} (g/ml)	S_{EMC} (g/g)	S_{EMC} SD	y_{CO_2}	y_{CO_2} SD
298.2	0.13	0.0023	0.0373	0.00412	0.9845	0.00169
	0.63	0.0116	0.0180	0.00338	0.9925	0.00141
	1.0	0.0187	0.0042	0.00254	0.9966	0.00058
	1.8	0.0353	0.0023	0.00032	0.9975	0.00034
	3.5	0.0779	0.0028	0.00142	0.9981	0.00053
	5.7	0.1686	0.0023	0.00061	0.9985	0.00039
	7.8	0.7711	0.0016	0.00033	0.9989	0.00046
313.2	0.41	0.0071	0.0550	0.00417	0.9773	0.00168
	0.74	0.0129	0.0244	0.00304	0.9898	0.00126
	2.1	0.0392	0.0114	0.00242	0.9952	0.00101
	3.3	0.0660	0.0055	0.00019	0.9977	0.00008
	5.2	0.1196	0.0032	0.00104	0.9987	0.00044
	7.3	0.2170	0.0098	0.00035	0.9959	0.00015
328.2	0.17	0.0028	0.1364	0.01111	0.9478	0.00419
	0.98	0.0164	0.0446	0.00624	0.9811	0.00254
	2.8	0.0506	0.0172	0.00680	0.9928	0.00162
	5.5	0.1150	0.0137	0.00551	0.9943	0.00231
	8.1	0.2082	0.0294	0.00167	0.9877	0.00056
	9.6	0.2947	0.0453	0.00364	0.9812	0.00148

n = 3. [a]Standard uncertainties are u(T) = 0.1 K, u(P) = 0.01 MPa, u(S_{EMC}) = 0.01, u(y_{CO_2}) = 0.005

Table 4-4: Experimental vapour mole fraction and solubility of the binary system, CO_2 + EC[a].

T (K)	P (MPa)	ρ_{CO_2} (g/ml)	S_{EC} (g/g)	S_{EC} SD	y_{CO_2}	y_{CO_2} SD
313.2	1.2	0.0214	0.00000	0.00000	1.0000	0.00000
	3.1	0.0612	0.00000	0.00000	1.0000	0.00000
	5.3	0.1230	0.00000	0.00000	1.0000	0.00000
	8.1	0.2898	0.00129	0.00023	0.9994	0.00012
	10.2	0.6426	0.00299	0.00061	0.9985	0.00030
	12.2	0.7234	0.00491	0.00056	0.9976	0.00028
328.2	3.0	0.0547	0.00000	0.00000	1.0000	0.00000
	5.2	0.1067	0.00000	0.00000	1.0000	0.00000
	7.9	0.1992	0.00275	0.00038	0.9986	0.00019
	9.7	0.3020	0.00345	0.00049	0.9983	0.00024
	11.7	0.4796	0.00402	0.00030	0.9980	0.00015
	14.1	0.6224	0.00498	0.00072	0.9975	0.00036

n = 3. [a]Standard uncertainties are u(T) = 0.1 K, u(P) = 0.01 MPa, u(S_{EC}) = 0.0008, u(y_{CO_2}) = 0.0004. Note – values expressed at 0.00000 denote an undetectable gas chromatography reading.

The magnitude of the variability in each data set was assessed for all systems. In the DMC binary system, the largest standard deviation value was identified in the isotherm, 328.2 K, at a pressure of 0.41 MPa (presented in **Table 4-2**). Comparison of the mole fraction of carbon dioxide to the standard deviation (0.9239 ± 0.00754) produced a relative standard deviation (RSD) of 0.816%. Similarly, the maximum source of variability in the EMC system was located in the isotherm, 328.2 K, at a pressure of 0.17 MPa (presented in **Table 4-3**). The corresponding mass fraction of carbon dioxide and standard deviation (0.9478 ± 0.00419) resulted in an RSD value of 0.442%.

The identified points where the greatest RSD arise in both aliphatic systems is not surprising as both values correlate to the highest points of solubilities in their binary data set, thus the points of more variability.

The solubility isotherms for DMC, EMC, and EC as a function of pressure have been illustrated below in **Figures 4-5**, **4-7**, and **4-8**, respectively. Both DMC and EMC systems are observed to each exhibit high solubilities in carbon dioxide at low pressure isothermally, resulting in a decrease in vapour phase densities and an increase in densities in the liquid phase. Isobarically, a high solubility of both components in carbon dioxide is experienced as the absolute temperature rises. This is due to the increase in solute vapour pressure and reduction of densities in the vapour phase [42].

Deviation in the EC data set was assessed, the largest standard deviation in the data was identified in the isotherm, 328.2 K, at 14.1 MPa (presented in **Table 4-4**). The mole fraction of carbon dioxide, and corresponding standard deviation (0.9975 ± 0.00036), equated to an RSD of 0.072%. Comparably, the solubility and respective standard deviation of EC at the same point, 328.2 K and 14.1 MPa, are 0.00498 ± 0.00072, equating to an RSD of 14.5%. EC displays a considerably smaller solubility in carbon dioxide than DMC and EMC and can be observed to be insoluble at pressures below 5.3 MPa. As a result, the systematic and random errors are magnified proportionally.

King and Catchpole (1993) identified three possible sources of errors occurring when obtaining phase equilibria data [43]:

1. Failure to achieve equilibrium.
2. Entrainment of droplets or particles.
3. Purity of feedstock and extract.

It is possible that during sampling, entrainment of the solute occurs in the vapour phase, resulting in overpredictions of the solubility. Quantification of the phase composition is a crucial factor in determining the proportion of solute present in the vapour. Sampling can be classified into two main methods: on-line and off-line quantification. The on-line technique allows for direct sampling as the chemical analysis system is connected directly to the sampling loop, allowing a prompt and practical analysis of the response via computer software. As for the off-line method, the sample is removed from the solvent trap and requires further processing steps, such as diluting, concentrating, or the substitution of solvent type, before analysis by various chemical analyses.

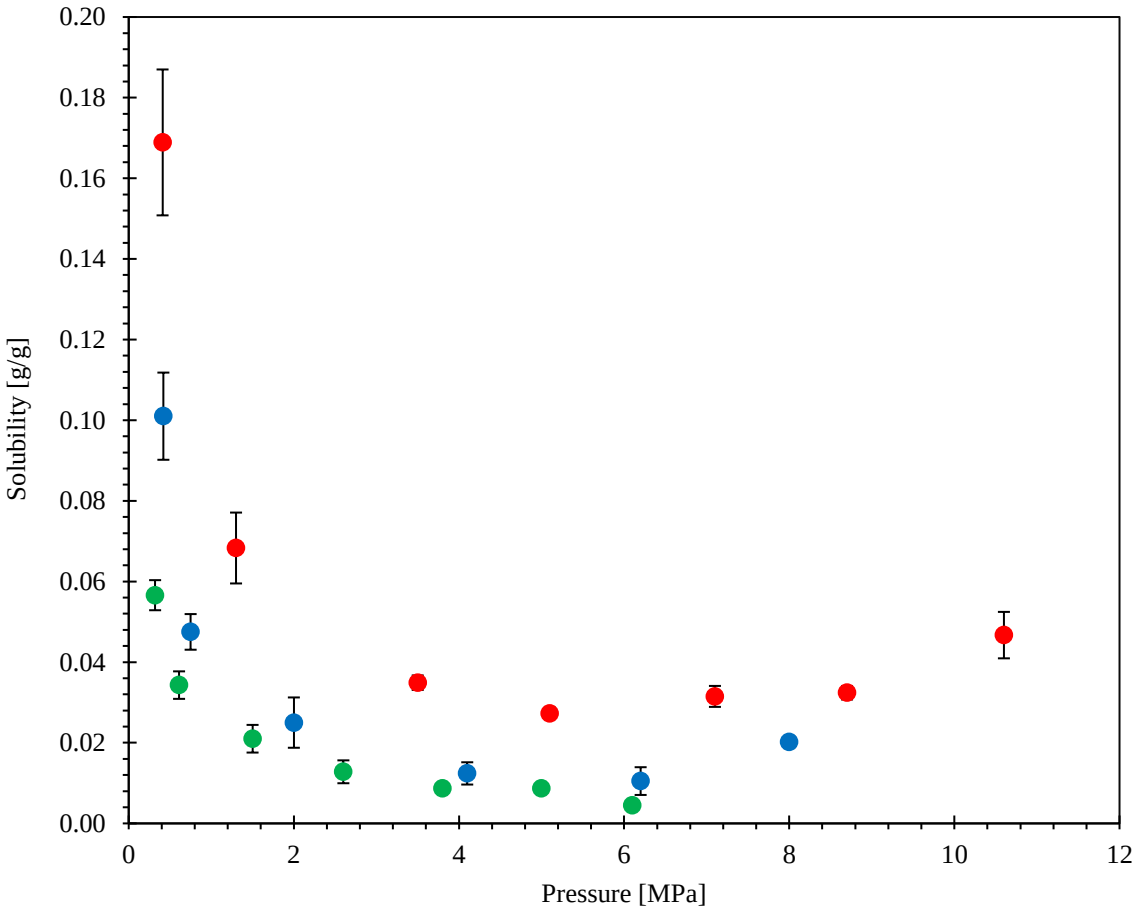

Figure 4-5: Solubility of dimethyl carbonate in carbon dioxide as a function of pressure. Experimental data (●) 298.2 K, (●) 313.2 K, (●) 328.2 K.
(Refer to **Table 4-2** for experimental data points).

Application of the off-line analytical technique and operating a manual injection set up for the GC carries drawbacks, both are often time consuming and may introduce errors in the processing and handling steps [2].

The experimental data collected for the DMC system was compared with the available literature data, as presented in **Figure 4-6**.

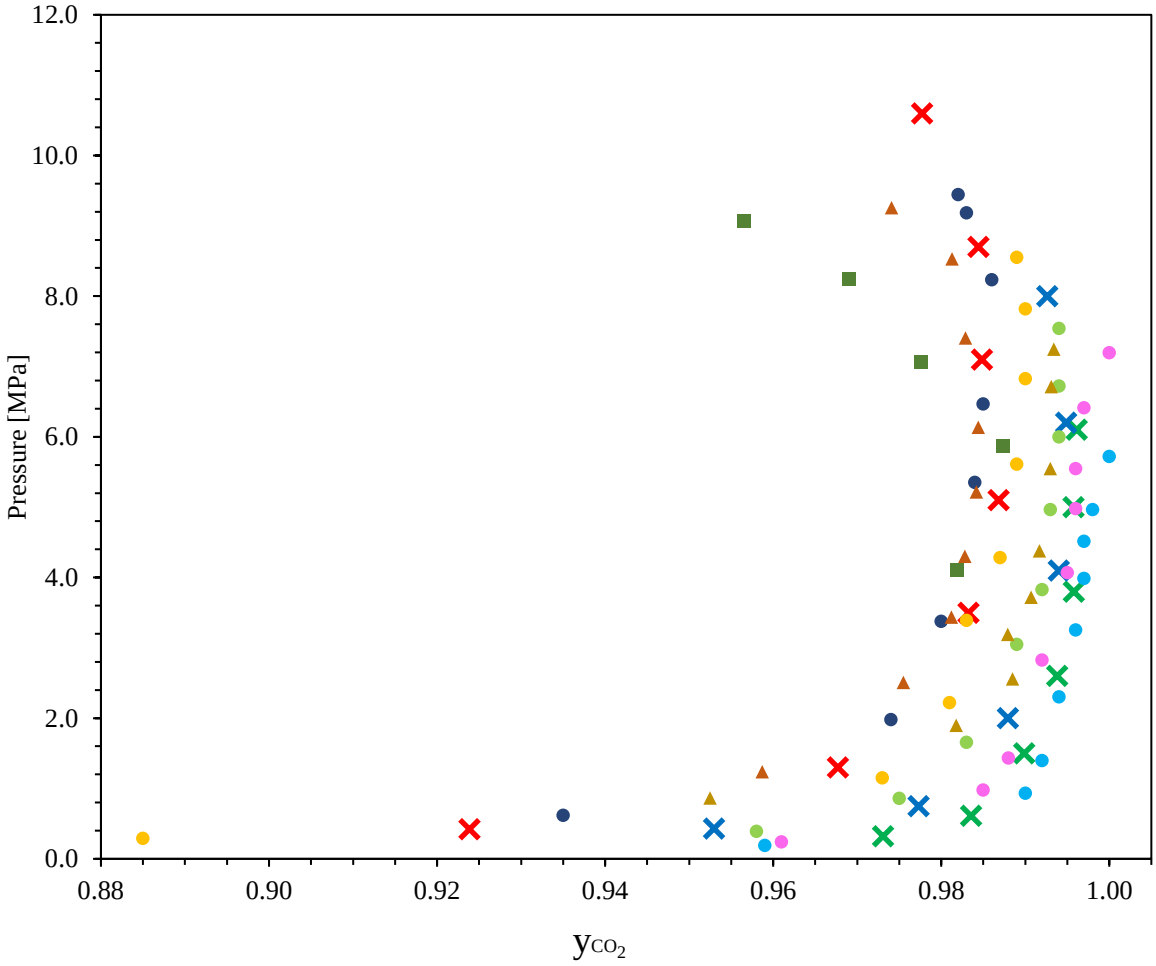

Figure 4-6: Vapour equilibrium of dimethyl carbonate and carbon dioxide in a binary system. Experimental data (✕) 298.2 K, (✕) 313.2, (✕) 328.2. Lee et al., (●) 293.15, (●) 303.15, (●)313.15, (●) 323.15, (●) 333.15. Im et al., (▲) 310.27, (▲) 330.3. Li et al. (■) 333.15. *[34, 39, 44]*. (Refer to **Table 4-2** for experimental data points).

Literature data was taken from several authors across a range of isotherms; *Lee et al.* (293.15 K, 303.15 K, 313.15 K, 323.15 K and 333.15 K), *Im et al.* (310.27 K and 330.3 K) and *Li et al.* (333.0 K) [34, 39, 44].

The literature data collected for comparative studies adopted two types of methods to achieve vapour-liquid equilibrium, both *Im et al.* and *Lee et al.* adopted a circulating-type apparatus, whilst *Li et al.* implemented a high-pressure cell with a magnetic stirrer. In comparison with the static setup adopted, both experimental practices conducted by *Im et al.* and *Lee et al.* expedited the phase homogeneity. However, in the current research this limitation was alleviated by increasing the duration to reach vapour–liquid equilibrium [42].

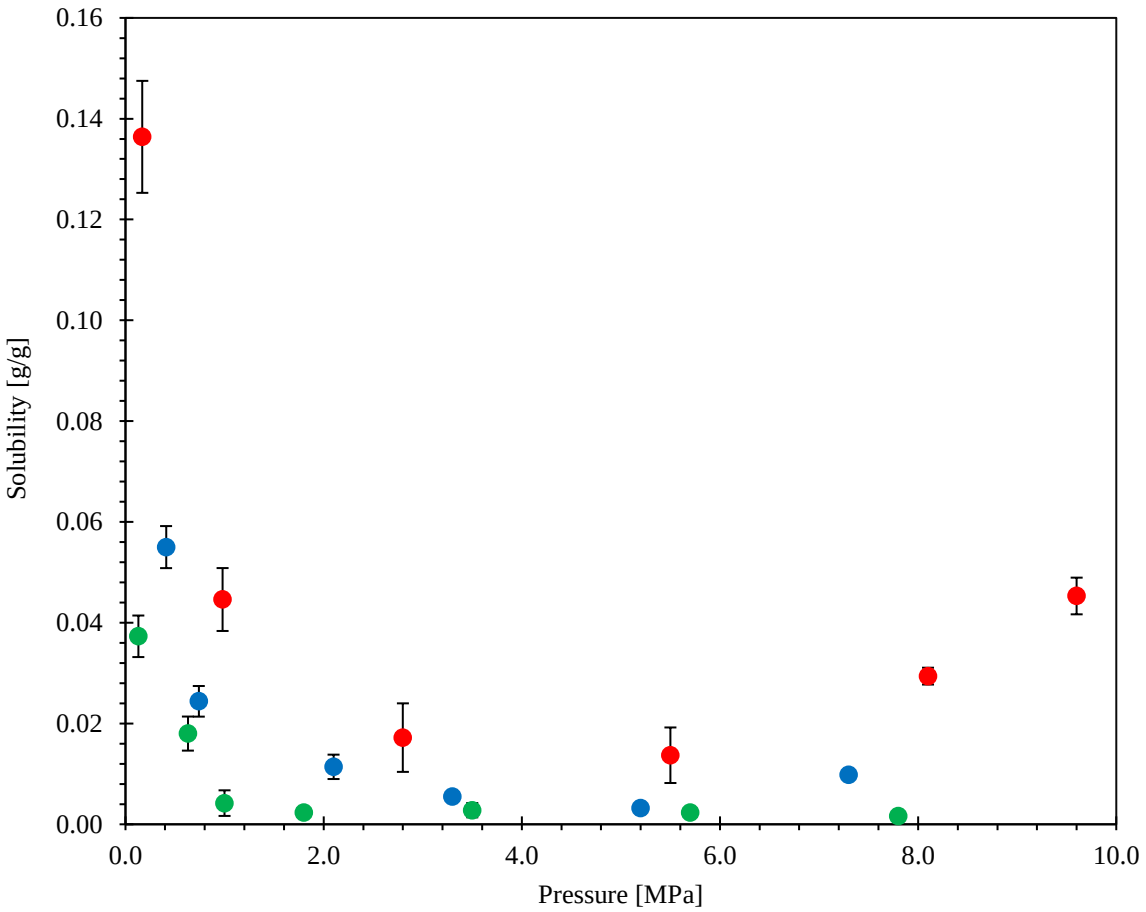

Figure 4-7: Solubility of ethyl-methyl carbonate in carbon dioxide as a function of pressure. Experimental data (●) 298.2 K, (●) 313.2 K, (●) 328.2 K.
(Refer to **Table 4-3** for experimental data points).

As observed in **Figure 4-6**, an exact comparison could not be established between the experimental and literature data at temperatures of 298.2 K and 328.2 K. However, the experimental data at 298.2 K visually fit within the isotherms of 293.15 K and 303.15 K from *Lee et al.*, denoting good agreement. Similarly, the experimental data at 328.2 K holds a close fit to both datasets obtained from *Lee et al.* (333.15 K) and *Im et al.* (330.3 K).

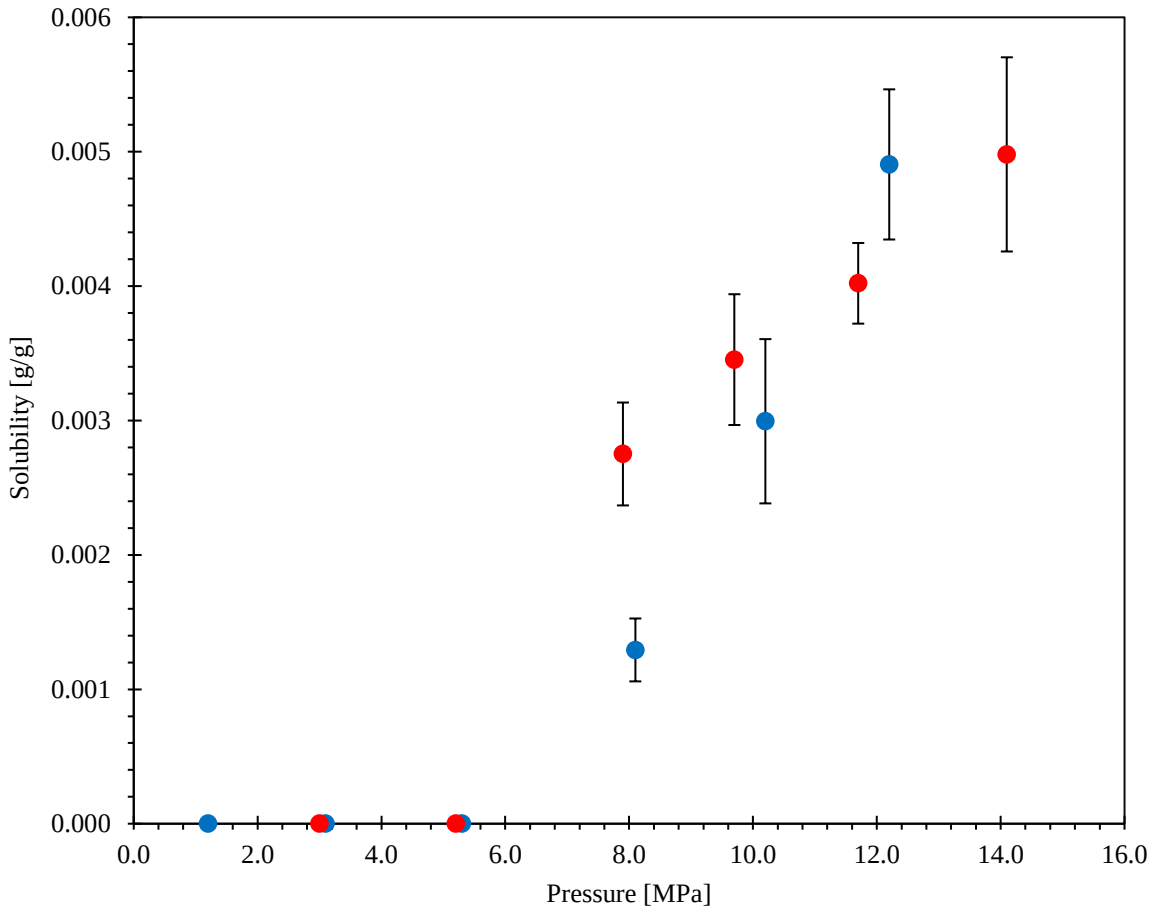

Figure 4-8: Solubility of ethylene carbonate in carbon dioxide as a function of pressure.
Experimental data (●) 313.2 K, (●) 328.2 K.
(Refer to **Table 4-4** for experimental data points).

Carbon dioxide exhibits an environmentally benign nature attributed to its extremely stable triatomic molecular bonds. It displays a weak quadrupole moment due to the small dipole across the carbon and oxygen atoms.

The bonding is composed of a pair of sigma and pi bonds, and like any C-O bond it is polarised such that the carbon atom carries a partial positive charge, whereas the oxygen atom carries a partial negative charge. Both dipoles act in opposite directions and cancel out, hence the molecule is classified as non-polar [1, 45]. It is important to consider the influence of the physical properties, and the impact on the solubilities of each component in carbon dioxide.

The interactions between non-bonded molecules exist as repulsive and attractive forces. Attractive interactions arise as a result of three different types of forces described by London, Keesom and Debye, and are commonly known as dispersion, orientation and induction effects, respectively [46].

Dispersion effects arise from the asymmetric distribution of electrons in a molecule, the unequal sharing of electrons causes intermittent polarisation. Orientation forces arise between molecules with permanent dipoles; the electrostatic attraction aligns the two permanent dipoles, thus creating an orientation effect. This interaction is considered the strongest amongst all intermolecular van der Waals forces of interactions, though their intensity is generally hampered by an increase in temperature *[47]*. Induction effects arise from the interaction between a permanent-induced dipole; though a molecule may not possess a permanent dipole, it may be polarised under the influence of neighbouring molecules that possess a permanent dipole *[48]*.

The dipole moment in a molecule may significantly affect the solubility behaviour of a component in a solvent. **Figure 4-9** models the partial charge distribution in each molecule, i) DMC, ii) EMC, and iii) EC. As observed, the DMC molecule exhibits a strong dipole moment across the double bond between the carbon and oxygen atoms, the low electron density is represented in a dark blue shade, conversely the high electron density is highlighted in red. Similarly, in the EMC molecule a distortion in electron density exists between the double bond between the carbon and oxygen atoms, as observed in DMC. However, EMC is an asymmetric molecule, thus stronger partial charge distributions are experienced in the surrounding C-O bonds. In comparison, EC exhibits a significantly stronger dipole moment than both DMC and EMC, the unusual asymmetric structure creates a disparity in the electron density as one side of the molecule contains several polar oxygen atoms, whereas the opposite orientation possesses none [49].

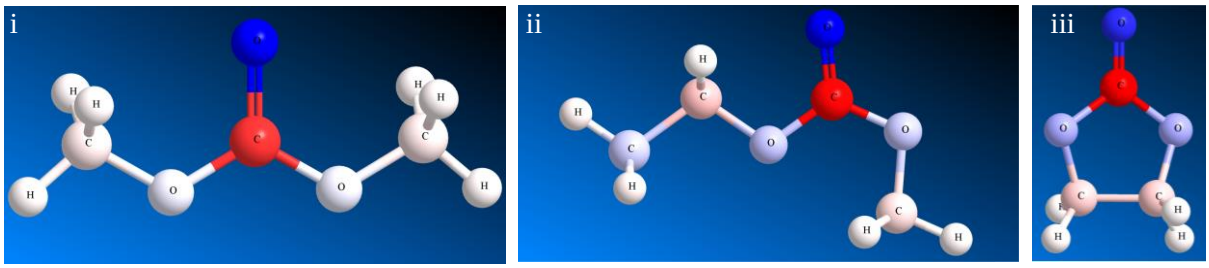

Figure 4-9: 3D molecular structures exhibiting the partial charge distributions of; i) dimethyl carbonate, ii) ethyl methyl carbonate, iii) ethylene carbonate.

Dobbs et al. [1987] reported the effects of orientation forces are relatively insignificant for components with a dipole moment below 5 D [50, 51]. The dipole moment of DMC was found to be 0.88 D [52], and the corresponding value for EMC was 0.89 D [53]. It is unsurprising that both values are alike since the geometric structure of both molecules are almost identical. The low dipole values suggest that both linear carbonates would not have undergone induction effects.

In comparison, the cyclic compound EC has a reported dipole moment of 4.81 D and a moderate hydrogen bond capability [54]. EC exhibits a hydrogen bond force (δ_H) of 5.1 $MPa^{0.5}$ and is likely to form hydrogen bonds with other EC molecules, resulting in a reduced interaction with carbon dioxide and explaining the reduced solubility behaviour [55-57]. Both DMC and EMC were experimentally proven to be more soluble than EC in carbon dioxide; this is a similar observation reported by *M. Anouti et al*., when evaluating the solubility of eight pure electrolyte solvents in carbon dioxide in the liquid phase where it was established that carbon dioxide is more readily soluble in acyclic molecules than cyclic [41].

The solubility experimental data presented in **Figures 4-5** and **4-7** from both linear carbonates indicate that the EMC is less soluble in carbon dioxide than DMC, this may be attributed to the differential in molecular size between both molecules. The molar refractivity of DMC and EMC were calculated as 19.0 and 23.7 cm^3/mol, respectively. The molar refractivity corresponds to the actual volume of molecules in one mole of a substance and hence can be compared to the volumetric properties calculated from density measurements [58].

Vaporisation denotes the phase transition of a substance into the vapour phase. During this physical transition, the increase in internal energy is associated with overcoming the intermolecular forces rather than raising the kinetic energy of the molecules (and therefore the system's temperature). In a pure component, vapour pressure denotes the pressure characteristic of a vapour in equilibrium with its liquid or solid form at any given temperature. It essentially gauges a compounds tendency to bond with itself; compound's that possess strong intermolecular forces exhibit lower vapour pressures, indicating a reduced propensity to escape into the vapour phase. Conversely, compounds with weaker bonding generally manifest higher vapour pressures [59, 60]. Referring to **Table 4-5**, a substantial deviation exists between the vapour pressures of the linear and cyclic components. At a temperature of 298 K in a closed

system, EC demonstrates a vapour pressure of 5.2 Pa [61]. In contrast, DMC and EMC display vapour pressures more than 750 times greater.

The vapour pressure of a component significantly influences its solubility. A higher vapour pressure signifies a greater propensity for vaporisation, thereby enhancing solubility, as Raoult's law describes.

4.6.2 Modelled binary vapour equilibrium systems

The modelling theory (outlined in section **4.5**) has been correlated against the experimental binary vapour equilibrium data to augment the results and evaluate the reliability of the experimental practice. EoS models required the incorporation of pure component parameters, as tabulated in **Table 4-5**.

Table 4-5: Physiochemical properties of compounds.

Component name	Skeletal structure	M_r	T_b	T_F	P_v	P_C	T_C	ω	Ref.
CO_2		44.009	194.69	-	-	7.375	304.13	0.225	[62]
DMC	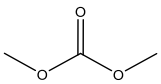	90.079	363.11	288.15	8.0[b]	4.835	557.38	0.385	[63, 64a, 65b]
EMC	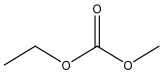	104.106	381.05	296.15	3.9[b]	3.839	560.75	0.429*	[64a, 65b, 66]
EC		88.063	517.50	423.15	0.0052	8.975	806.00	0.258	[61c, 67]

* Estimated from: $\omega = -(1/f^1)\left(\mathrm{Ln}\left(\frac{p_c}{1.01315}\right) + f^0\right)$, where f^0 and f^1 are Ambrose-Walton parameters for vapour pressure estimation, and p_c is the critical pressure (MPa) [68]. Where; M_r represents the molar mass (g/mol), T_b is the normal boiling point (K), T_F is the flash point (K), P_v represents the vapour pressure (kPa) at 298 K, P_C is the critical pressure (MPa), T_C is the critical temperature (K) and ω is the acentric factor.

Experimental data for the DMC (CO_2 + DMC) and EMC (CO_2 + EMC) binary systems have been modelled using the PR EoS, in addition the DMC binary system was modelled using the CPA EoS. The author wishes to acknowledge Dr Luis R. Ramirez for his support and work on the CPA EoS model.

The application of the PR EoS in modelling the phase behaviour of DMC (CO_2 + DMC) and EMC (CO_2 + EMC) binary systems was based on several key factors. Firstly, the PR EoS has found extensive application across various industrial fields and is known for its computational efficiency owing to its mathematical simplicity. This model has exhibited reliability across a broad spectrum of temperatures and pressures, pertinent to each system under investigation. For non-polar and slightly polar components like DMC and EMC, it has shown efficacy in providing accurate predictions of vapour pressure [69].

However, it's important to note that the PR EoS does not account for polar-polar interactions or hydrogen bonding, thereby constraining its accuracy in modelling the phase equilibria of polar components. To explore the potential impact of association effects, the Cubic-Plus-Association (CPA) model was introduced. One limitation of the CPA model is its requirement for extensive variables for application. Unfortunately, the EMC (CO_2 + EMC) binary system could not be modelled due to the unavailability of the pure component parameters. The model necessitated experimental data, specifically EMC's saturated liquid density and vapour pressure, which could not be obtained.

The data points obtained from the PR EoS model have been presented in **Table 4-6**.

Table 4-6: Modelled vapour mole fraction in the binary systems, CO_2 + DMC, and CO_2 + EMC using the PR (EOS).

CO_2 + DMC					**CO_2 + EMC**			
T (K)	**P (MPa)**	**y_{CO_2}**	**%ΔP**	**$\%\Delta y_{CO_2}$**	**P (MPa)**	**y_{CO_2}**	**%ΔP**	**$\%\Delta y_{CO_2}$**
298.2	0.33	0.9820	1.873	0.915	0.13	0.9742	2.174	1.046
	0.61	0.9901	0.284	0.671	0.65	0.9946	2.831	0.212
	1.5	0.9956	0.998	0.576	1.0	0.9964	1.984	0.020
	2.6	0.9972	0.283	0.342	1.8	0.9977	0.982	0.020
	3.8	0.9979	0.240	0.211	3.5	0.9986	0.355	0.050
	5.0	0.9983	0.736	0.251	5.7	0.9991	0.356	0.060
	6.1	0.9990	0.680	0.291	-	-	-	-
313.2	0.43	0.9705	2.548	1.836	0.44	0.9830	5.434	0.583
	0.74	0.9823	1.086	0.512	0.73	0.9892	1.454	0.061
	2.0	0.9925	1.516	0.455	2.1	0.9954	1.336	0.020
	4.1	0.9952	0.791	0.121	3.3	0.9965	1.031	0.120
	6.2	0.9955	0.473	0.060	5.2	0.9969	0.732	0.180
	8.0	0.9941	0.000	0.151	7.3	0.9964	0.104	0.050
328.2	0.40	0.9380	2.829	1.526	0.15	0.9014	12.709	4.896
	1.3	0.9785	2.211	1.116	1.0	0.9834	1.613	0.234
	3.5	0.9896	1.293	0.641	2.8	0.9922	0.554	0.060
	5.1	0.9910	0.696	0.426	5.5	0.9937	0.495	0.060
	7.2	0.9906	0.909	0.589	8.2	0.9918	0.840	0.415
	8.7	0.9882	0.478	0.386	9.6	0.9869	0.360	0.581

Percent relative deviations for pressure ($\%\Delta P$) and CO_2 vapour mole fraction ($\%\Delta y_{CO_2}$) were computed from **Equations 4-33** and **4-34**, respectively.

$$\%\Delta P = \left|\frac{(P_{exp} - P_{PR})}{P_{exp}}\right| \times 100 \quad \textbf{(4-33)}$$

$$\%\Delta y_{CO_2} = \left|\frac{(y_{CO_2 exp} - y_{CO_2,PR})}{y_{CO_2 exp}}\right| \times 100 \quad \textbf{(4-34)}$$

Initial efforts to correlate the experimental data with both EoS models were driven by optimising the binary interaction parameter (k_{ij}), and thereby minimising **Equation 4-35**, the objective function (f).

$$f = \sum_{i=1}^{N}\left[\left(\frac{P_i^{exp} - P_i^{calc}}{P_i^{exp}}\right)^2 + \left(y_{CO_2,i}^{exp} - y_{CO_2,i}^{calc}\right)^2\right] \quad \textbf{(4-35)}$$

Where P_i^{exp} and P_i^{calc} are the experimental and modelled system pressures, respectively. Similarly, $y_{CO_2,i}^{exp} - y_{CO_2,i}^{calc}$ are the experimental and modelled mole fractions of carbon dioxide, respectively. However, in the absence of the liquid phase data the outcome of the binary interaction parameter is highly dependent on the initial estimation. Thus, if the starting estimate input into the program were 0, it would soon converge to 0; likewise, if the starting value given were -0.02 the algorithm would converge to -0.02, and so on. This was the case for both systems, DMC and EMC. For this reason, the binary interaction parameter could not be optimised as per the experimental results. It was set at -0.024 for both systems by evaluating previous literature from *Im et al.* and *Tsivintzelis et al.* [34, 70]. The phase diagrams of the DMC and EMC binary systems are each illustrated in Figures **4-10** and **4-11**, respectively.

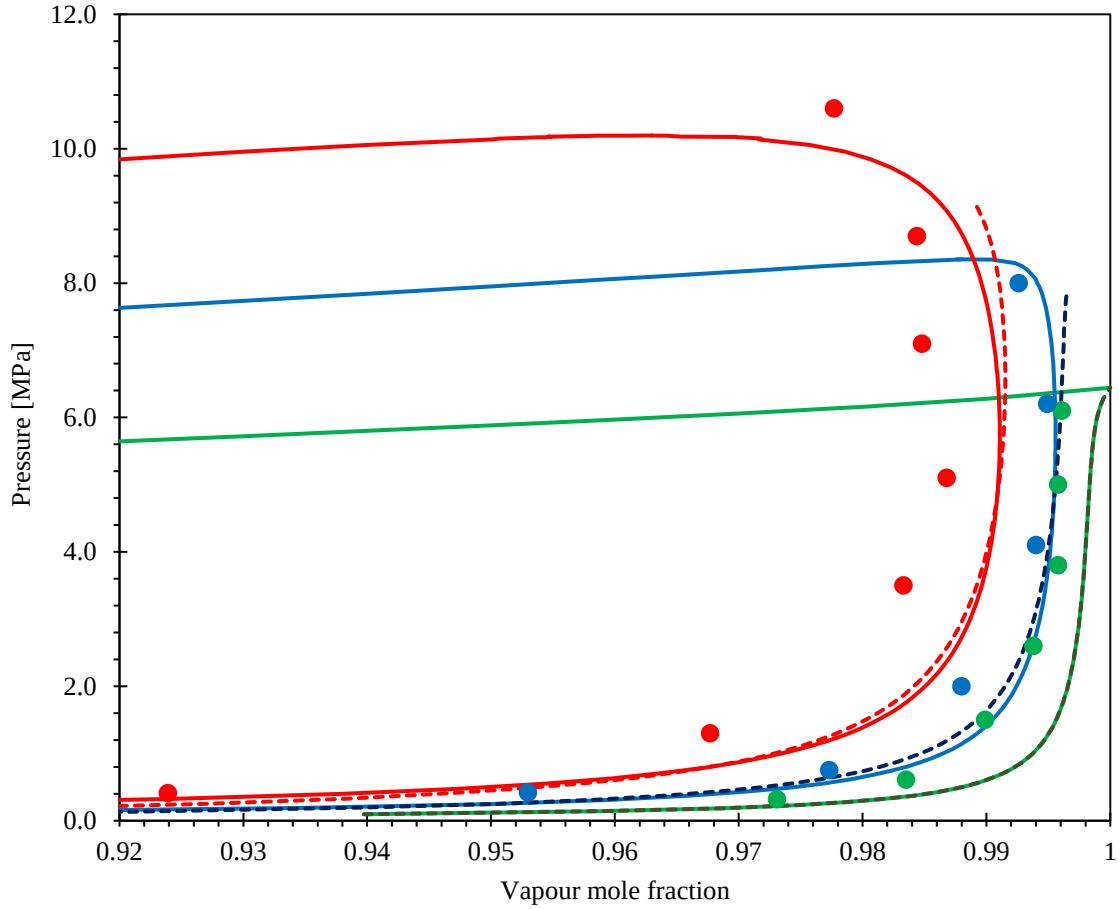

Figure 4-10: Phase diagram of the dimethyl carbonate and carbon dioxide binary system. Experimental data (●) 298.2 K, (●) 313.2 K, (●) 328.2 K, (—) PR EoS, (---) CPA EoS. (Refer to **Tables 4-2** and **4-6** for experimental and model data points, respectively).

The association between the experimental results and data computed using both EoS models strongly correlated with the DMC system. Both models generated similar responses, though the CPA EoS model produced a marginally better fit, as presented in **Figure 4-10**. At isotherms of 313.2 K and 328.2 K, along the dew point curve between pressures of 1.0 - 5.0 MPa, it can be observed to fit the experimental data better than the PR EoS model. However, at pressures greater than 5.0 MPa it begins to underpredict the solubility of the DMC component and deviate against the general trend of the experimental data.

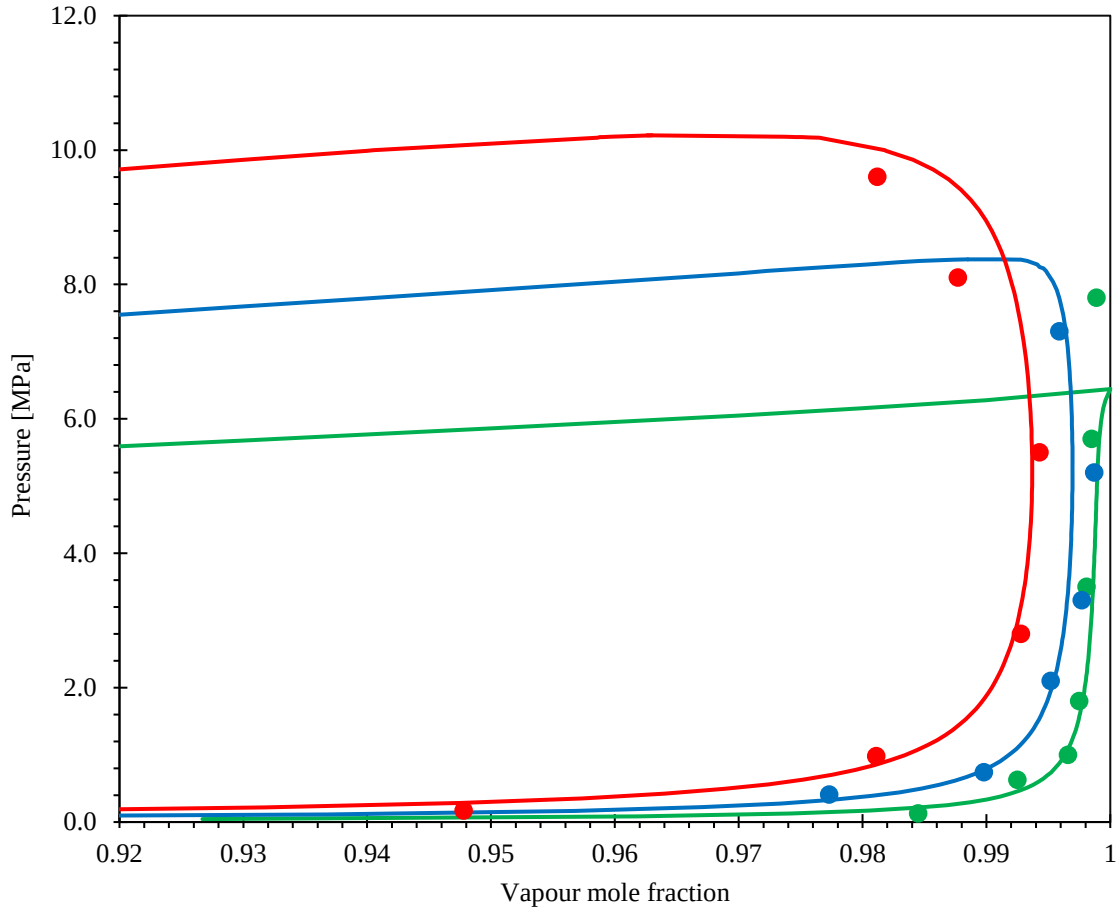

Figure 4-11: Phase diagram of the ethyl-methyl carbonate and carbon dioxide binary system. Experimental data (●) 298.2 K, (●) 313.2 K, (●) 328.2 K, (─) PR EoS. (Refer to **Tables 4-3**and **4-6** for experimental and model data points, respectively).

Statistical deviation between the CPA EoS and experimental data for pressure and the mole fraction of carbon dioxide produced maximum AARD values of 1.01 % and 0.75 %, respectively. Conversely, the PR EoS generated maximum AARD values of 1.18 % and 0.88 % for the pressure and the corresponding mole fraction of carbon dioxide.

The PR EoS correlation was assessed with the experimental data obtained for the EMC binary system and confirmed an acceptable fit across all isotherms; the maximum AARD for the pressure and the mole fraction of carbon dioxide was calculated as 1.66 % and 1.02 %, respectively.

The critical mixture points for the DMC and EMC binary systems were computed in each isotherm using the EoS models, as presented in **Table 4-7**. Initially, for the DMC binary system, both EoS models behave alike and produced an identical critical point of 6.44 MPa under the isotherm at 298.2 K. However, the values began to deviate more significantly as the temperature rose. Both sets of critical points at each isotherm for the DMC and EMC binary systems were nearly identical when modelled using the PR EoS. This may result from the comparable physical properties of each component (refer to **Table 4-5**), as models are under the constraints of these parameters; thus, the output is equally similar.

Table 4-7: Critical mixture points for DMC + CO_2 and EMC + CO_2 binary systems, modelled using PR and CPA.

Component	Temperature (K)	PR (MPa)	CPA (MPa)	Relative Deviation (%)
DMC	298.2	6.44	6.44	0.00
	313.2	8.36	8.30	0.72
	328.2	10.20	9.50	6.87
EMC	298.2	6.44	-	-
	313.2	8.37	-	-
	328.2	10.22	-	-

All the vapour data collected generally lies in the constraints of the critical mixture points, but a few nonconformities exist that should be treated cautiously. The first point in the DMC binary system lies in the isotherm 328.2 K, at 10.6 MPa, as presented in **Figure 4-10**, though the PR EoS model can be observed to retain a close fit to this experimental point displaying confidence in the data set. The second point in the EMC system lies in the isotherm 298.2 K, at 7.8 MPa, as given in **Figure 4-11**. This point may be erroneous as it is located well beyond the critical mixture point when the PR EoS model clearly indicates the pure liquid phase of EMC.

Ultimately, as both values lie outside the critical mixture points, each should be treated cautiously.

The validation of the ethylene carbonate (CO_2 - EC) binary system was assessed using semi empirical equations (as discussed in section **4.5.4**). Due to the limited availability of experimental data dealing with SCF-solid systems, there has been considerable interest in mathematical models for accurately predicting the phase behaviour of such systems as an alternative to EoS equations. The latter often necessitate extensive physical properties that are not always available [71]. The selection of semi-empirical density models was motivated by ECs high melting point and low vapour pressure.

Numerous semi-empirical equations exist, posing a challenge in determining the most suitable model for solubility calculations. To address this, two widely employed equations, the Chrastil and Méndez-Santiago and Teja (MST) models, were introduced to correlate the experimental data with carbon dioxide densities obtained from the NIST web-book. The comparison between experimental and semi-empirical models have been presented in **Table 4-8** and **Figure 4-12**, respectively.

Table 4-8: Modelled vapour mole fraction in the binary systems, CO_2 + EC using semi empirical models.

T (K)	P (MPa)	Chrastil			Méndez-Santiago and Teja		
		y_{CO_2}	y_{EC}	$\%y_{EC}$	y_{CO_2}	y_{EC}	$\%y_{EC}$
313.2	1.2	-	-	-	-	-	-
	3.1	-	-	-	-	-	-
	5.3	-	-	-	-	-	-
	8.1	0.9994	0.0006	0.0004	0.9992	0.0008	23.08
	10.2	0.9986	0.0014	6.304	0.9981	0.0019	19.51
	12.2	0.9985	0.0015	61.04	0.9980	0.0020	24.62
328.2	3.0	-	-	-	-	-	-
	5.2	-	-	-	-	-	-
	7.9	0.9987	0.0013	1.919	0.9986	0.0014	0.02783
	9.7	0.9983	0.0017	1.215	0.9985	0.0015	16.56
	11.7	0.9978	0.0022	8.213	0.9980	0.0020	0.0291
	14.1	0.9976	0.0024	2.027	0.9975	0.0025	0.3663

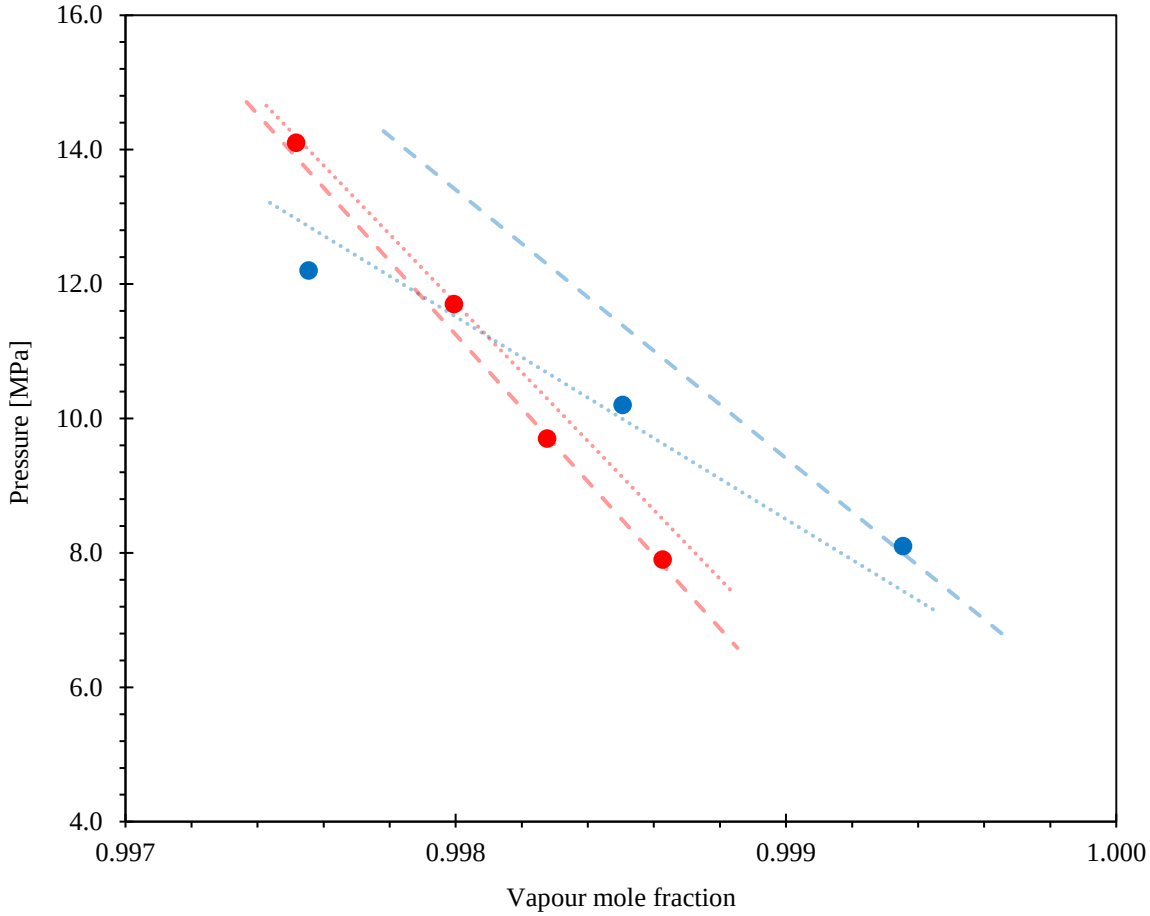

Figure 4-12: Phase diagram of the ethylene carbonate and carbon dioxide binary system. Experimental data (●) 313.2 K, (●) 328.2 K, (---) Chrastil model, (⋯) Méndez-Santiago and Teja model. (Refer to **Tables 4-4** and **4-8** for experimental and model data points, respectively).

As presented in **Figure 4-12**, EC displays a relatively low solubility in carbon dioxide, ranging from 1.29 – 4.98 g/kg across both isotherms. As the pressure of carbon dioxide rises, the solubility of EC becomes more favourable due to density effects. The intermolecular interactions between the solute and solvent are improved as the density of carbon dioxide increases, enhancing the solvent strength and thus the dissolution of ethylene carbonate.

Temperature effects on the solubility are not as straight forward and can be complex. An increase in temperature creates an opposing effect and decreases the density of the solvent, reducing the solvation power. Simultaneously, a rise in temperature will promote the vapour

pressure, increasing the solubility of the solute. **Figure 4-12** shows a cross-over point between both isotherms, 313.2 K and 328.2 K, at approximately 11 MPa. Below the cross over point the EC solubility is enhanced with an increase in temperature.

Inversely, above this cross over point the solubility decreases with a temperature influx, and at high pressures the density of carbon dioxide has a greater effect. Ultimately, high pressure and low temperature results in greater solubility. The model parameters for each semi empirical equation have been tabulated in **Table 4-9**.

Table 4-9: Model parameters of Chrastil and Méndez-Santiago and Teja semi empirical models.

Model	Parameters		AARD (%)
Chrastil	a_1	-0.000955	14.48
	b_1	7.239	
	c_1	-0.0249	
Méndez-Santiago and Teja	A_1	-5160.78	12.70
	A_2	909.28	
	A_3	10.65	

Both semi empirical models displayed a linear relationship with the experimental data. The MST model provided a slightly better fit than the Chrastil model, producing an AARD value of 12.7%.

4.6.3 Experimental quaternary vapour equilibrium system

Over 43,000 VLE data sets have been performed and recorded as of 2023 [72], and the vast majority of the data collected are from binary systems, with substantially less data available for tertiary and multicomponent systems. Multicomponent systems can be challenging to model, especially when considering systems that contain combinations of polar, non-polar, electrolytes, and supercritical components. According to *Novak et al.* [73], measuring a 10-component system at atmospheric pressure in 10 mol% steps would theoretically consume approximately 37 years [74]. Additionally, for tertiary and higher component systems, adequate graphical depictions of the behaviour of the system are problematic, and accurate computation, though sufficient for many systems, is still in development stages [75].

There have been limited publications on multicomponent systems for these carbonate ester components; both authors *Blanchard et al*. and *Dougassa et al.* have created several tertiary systems: CO_2 + DMC + EC, CO_2 + EMC + EC, and DMC + PC + EC, where PC is propylene carbonate. Measurement of the systems were conducted in the liquid phase at temperatures of 275-353 K, and under atmospheric pressure [32, 76].

To develop the understanding of the selectivity of each component and the behaviour of intermolecular interactions in the solvation process, a quaternary system was established under pressures of 2.1 – 10.0 MPa, at isotherms of 298.2 K, 313.2 K, and 328.2 K. Each electrolyte component (DMC, EMC, and EC) was prepared gravimetrically in a 1:1:1 ratio to form a homogenous solution replicating the electrolyte solvent mixture employed in LIBs. The vapour equilibrium data for the quaternary system, CO_2 + DMC + EMC + EC, and the selectivity results are tabulated in **Table 4-10**.

Table 4-10: Experimental vapour mole fraction and selectivity of the quaternary system, CO_2 + DMC + EMC + EC[a].

T (K)	P (MPa)	y_{DMC}	$y_{DMC\ SD}$	y_{EMC}	$y_{EMC\ SD}$	y_{EC}	$y_{EC\ SD}$	y_{CO_2}	S_{total} (g/g)	Selectivity (α)		
										y_{DMC}/y_{EMC}	y_{EMC}/y_{EC}	y_{EC}/y_{DMC}
298.2	2.1	0.0069	0.00118	0.0026	0.00056	0.00000	0.00000	0.9905	0.0204	2.59	-	-
	6.4	0.0031	0.00087	0.0016	0.00042	0.00041	0.00016	0.9949	0.0109	1.98	3.81	0.13
	8.3	0.0021	0.00034	0.0014	0.00022	0.00243	0.00044	0.9941	0.00966	1.56	0.56	1.15
313.2	2.9	0.0084	0.00319	0.0045	0.00095	0.00000	0.00000	0.9872	0.0282	1.87	-	-
	5.0	0.0075	0.00152	0.0044	0.00050	0.00000	0.00000	0.9882	0.0246	1.70	-	0.00
	10.0	0.0076	0.0110	0.0054	0.00068	0.00199	0.00042	0.9850	0.0288	1.40	2.72	0.26
328.2	4.6	0.0127	0.00430	0.0059	0.00229	0.00000	0.00000	0.9814	0.0360	2.17	-	-
	6.2	0.0190	0.00396	0.0126	0.00130	0.00032	0.00029	0.9681	0.0675	1.50	39.73	0.02
	9.4	0.0211	0.00489	0.0191	0.00289	0.00194	0.00033	0.9579	0.0868	1.10	9.84	0.09

n = 3. [a]Standard uncertainties are u(T) = 0.1 K, u(P) = 0.01 MPa, u(y_{DMC}) = 0.005, u(y_{EMC}) = 0.003, u(y_{EC}) = 0.0005. Note – values expressed at 0.00000 denote an undetectable gas chromatography reading.

The overall trend exhibited in the quaternary system reflects similarities in the solubility behaviour, as experienced by the linear carbonates in the binary systems. The overall solubility of components in carbon dioxide becomes increasingly more soluble with enhancements in temperature and pressure, as tabulated in **Table 4-10**. As the system pressure increases, the density of the solvent rises and the interactions between solvent-solute tend to become more favourable. The increase in temperature may reduce the solvation effect, however, this effect is negated and is dominated by the enhancement of the solutes vapour pressure, thus promoting the overall solubility.

Extraction and separation of the alkyl components using carbon dioxide can be optimised by analysing the solubility data and the influence of the operating conditions on selectivity. The solubility selectivity (α) is the ratio of the respective mole fractions of two or more components in the solvent stream. Selectivity of DMC and EC in the quaternary system as functions of pressure, under each isotherm 298.2 K, 313.2 K, and 328.2 K are presented in **Figures 4-13** and **4-14**, respectively.

In the quaternary system DMC is the most dominant solute in carbon dioxide, as observed in **Table 4-10**. In the binary system arrangements, DMC was identified as the most soluble component in carbon dioxide, thus the result is unsurprising. Comparison of the binary and quaternary systems indicate the solubility of DMC to largely remain constant, though under most pressures it can be noticed to exhibit solubilities less than that observed in the binary system. This phenomenon, whereby the solubility is diminished in multi-component systems containing $scCO_2$ compared to their equivalent binary system has been reported by several studies [77-80]. As observed in **Figure 4-13**, at all isotherms, EMC has an inverse effect on the selectivity of DMC.

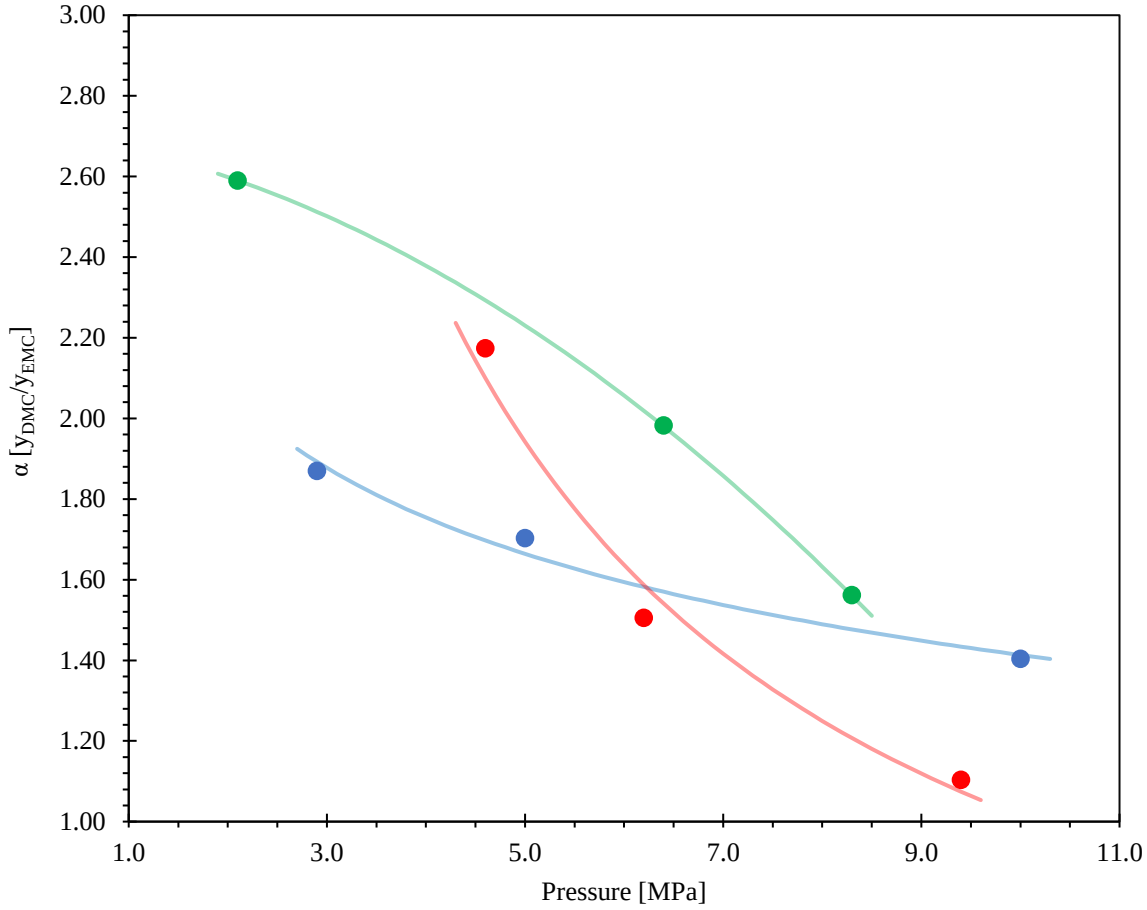

Figure 4-13: Selectivity isotherm of dimethyl carbonate (DMC/EMC) in quaternary mixture (CO_2 + DMC + EMC + EC) as a function of pressure; (●) 298.2 K, (●) 313.2 K, (●) 328.2 K. (Refer to **Table 4-10** for experimental data points).

Furthermore, the presence of other carbonates with lesser vapour pressures likely contributed to the decrease in the vapour pressure of the DMC component. As a result, the solubility of DMC was adversely affected by the presence of EMC, and this effect became more significant with an elevation in system pressure.

It is important to remember carbon dioxide is a largely nonpolar molecule, and the equilibrium behaviour is governed predominantly by physical interactions. As observed in the binary system, EC exhibited a considerably lower solubility than the linear carbonates.

This is because it experienced a weaker interaction with the carbon dioxide molecules due to its high polarity. However, EC was found to be considerably more soluble in the quaternary system than its binary system, and at high pressures, it was found to be several times more soluble. The addition of DMC and EMC acts as a co-solvent, significantly enhancing the solvating power of (supercritical) carbon dioxide and improving the interactions between the carbon dioxide and EC molecules.

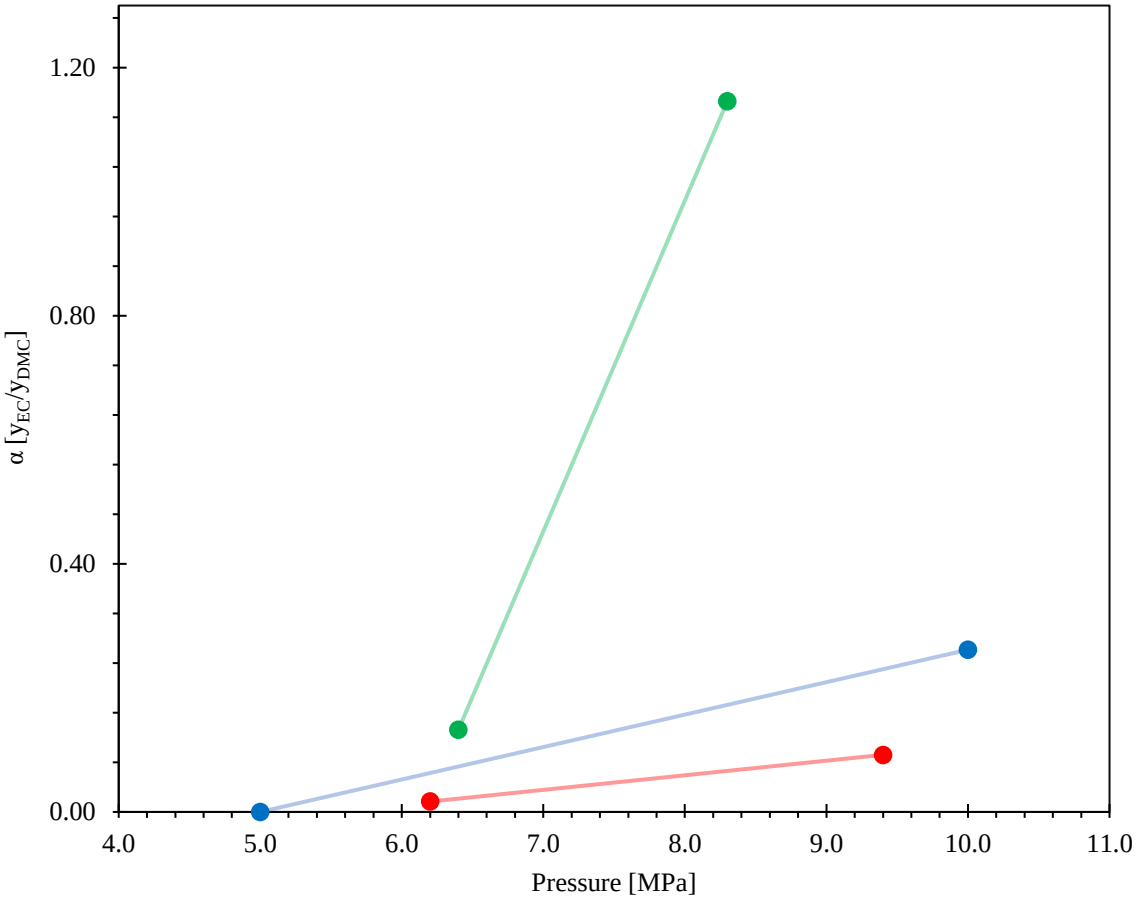

Figure 4-14: Selectivity isotherm of ethylene carbonate (EC/DMC) in quaternary mixture (CO_2 + DMC + EMC + EC) as a function of pressure; (●) 298.2 K, (●) 313.2 K, (●) 328.2 K. (Refer to **Table 4-10** for experimental data points).

There have been numerous studies investigating the influence of polar co-solvents on the solubility of polar solids in carbon dioxide and how a small addition of polar co-solvent can significantly improve the solubility, *Huang et al.* reported how the solubility of aspirin could be enhanced up to 5 times with acetone, and up to 14 times using either methanol or ethanol [81]. This can be observed in the two-point graph, **Figure 4-14**, the addition of DMC can be observed to greatly enhance the selectivity of EC under all isotherms.

The most significant enhancement in the solubility of EC was observed at higher carbon dioxide densities, thus, conditions of high system pressure. At the isotherm of 298.2 K when EC is in a solid state, the addition of DMC notably enhances its selectivity by more than 8 times. Regarding the influencing parameters, it seems that a rise in pressure favours the selectivity of EC, whereas an increase in temperature adversely affects it, significantly reducing the selectivity. Under these conditions, the mean intermolecular distance between components in the mixture would have been reduced, thereby amplifying the effects of variations in forces between similar and dissimilar molecules [50].

4.7 Conclusion

The objectives outlined in this chapter have been satisfied; an experimental rig was designed and constructed to obtain vapour equilibrium data for LIB electrolyte components in a binary and quaternary arrangement. Mixtures of carbon dioxide, with dimethyl carbonate, ethyl methyl carbonate, and ethylene carbonate, were all measured using a static-analytical technique and an off-line gas chromatography quantification method.

DMC exhibited the greatest solubility amongst all carbonates in binary and quaternary vapour-liquid equilibrium systems. Both DMC and EMC displayed significantly greater solubilities in carbon dioxide in comparison to the cyclic component, EC. These components' distinctive molecular structures and varying vapour pressures elucidated their solubility behaviour and the interactions experienced. The symmetrical structure of DMC rendered it considerably less polar, while EC, with its asymmetric arrangement, demonstrated a notably stronger dipole moment. The quaternary system generally reflected the solubility results of the components in each respective binary system. Though interestingly, both DMC and EMC were identified to act as co-solvents and greatly magnified the solubility of EC in the multicomponent system under all isotherms.

In conclusion, the acquired vapour equilibrium data validates the viability of extracting LIB electrolytes through the application of pressurised carbon dioxide. Although, the selection of system parameters is not straightforward. Both DMC and EMC demand low pressure and high temperature conditions to achieve a high solubility, whereas the EC component requires high pressure and low temperature to enhance its solubility. Consequently, the next chapter will explore a compromise amongst system conditions to optimise the extraction yield of an artificial electrolyte mixture.

References – Chapter 4

1. Gupta RB, Shim JJ. Solubility in Supercritical Carbon Dioxide. *CRC Press.* 2007. https://books.google.co.uk/books?id=qdXLBQAAQBAJ.

2. Hooi Sim Yeoh GHC, Norazinan Mohd Azahan, Russly Abdul Rahman, Thomas Shean Yaw Choong. Solubility Measurement Method and Mathematical Modeling in Supercritical Fluids. *Engineering Journal.* 2013; 17 (3): 68-69.

3. Aalco. *Stainless Steel - Austenitic - 1.4401 (316) Bar and Section*. https://www.aalco.co.uk/datasheets/Stainless-Steel-14401-316-Bar-and-Section_37.ashx [Accessed 16/04/22].

4. Matos RL. *Production of Curcumin Formulations by Supercritical Fluid-Assisted Coating and Coprecipitation Processes*. University of Birmingham; 2020.

5. Nalini Menon MW, Mark Anderson, Nathan Colgan. *Compatibility of polymers in super-critical carbon dioxide for power generation systems: High level findings for low temperatures and pressure conditions*. OSTI, California, 2019.

6. James Walker Ltd. *'O' Ring Guide*. https://www.jameswalker.biz/our-solutions/our-products/elastomers/o-rings [Accessed 21/04/22].

7. Jaubert J-N, Privat R. 3 - Low-Pressure Vapor–Liquid and Liquid–Liquid Equilibria of Binary Systems: Activity Coefficient Models. In: Jaubert J-N, Privat R, (eds.) *Thermodynamic Models for Chemical Processes*. Elsevier; 2021. p. 77-135.

8. Ross SM. Chapter 3 - Using Statistics to Summarize Data Sets. In: Ross SM, (ed.) *Introductory Statistics (Third Edition)*. Boston: Academic Press; 2010. p. 103.

9. Kai L. *Chemical, Biological and Environmental Engineering - Proceedings of the International Conference on Cbee 2009.* World Scientific Publishing Company; 2010.

10. Putra NR, Rizkiyah DN, Idham Z, Salleh LM, Machmudah S, Yunus MAC. Formulation and evaluation of a new semi-empirical model for solubility of plant extracts in supercritical carbon dioxide assisted by ethanol as co-solvent. *Chemical Engineering Communications.* 2020; 208(9): 1326-1334. doi: 10.1080/00986445.2020.1771324.

11. Tillman DA, Duong DNB, Harding NS. Chapter 7 - Modeling and Fuel Blending. In: Tillman DA, Duong DNB, Harding NS, (eds.) *Solid Fuel Blending*. Boston: Butterworth-Heinemann; 2012. p. 271-293.

12. Belghait A, Si-Moussa C, Laidi M, Hanini S. Semi-empirical correlation of solid solute solubility in supercritical carbon dioxide: Comparative study and proposition of a novel density-based model. *Comptes Rendus Chimie.* 2018; 21(5): 494-513. doi: https://doi.org/10.1016/j.crci.2018.02.006.

13. Alwi RS, Garlapati C. A new semi empirical model for the solubility of dyestuffs in supercritical carbon dioxide. *Chemical Papers.* 2021; 75(6): 2585-2595. doi: 10.1007/s11696-020-01482-x.

14. Sim Yeoh H, Hean Chong G, Mohd Azahan N, Abdul Rahman R, Yaw Choong TS. Solubility Measurement Method and Mathematical Modeling in Supercritical Fluids. *Engineering Journal.* 2013; 17(3): 67-78. doi: 10.4186/ej.2013.17.3.67.

15. Peng D-Y, Robinson DB. A New Two-Constant Equation of State. *Industrial & Engineering Chemistry Fundamentals.* 1976; 15(1): 59-64. doi: 10.1021/i160057a011.

16. Lopez-Echeverry JS, Reif-Acherman S, Araujo-Lopez E. Peng-Robinson equation of state: 40 years through cubics. *Fluid Phase Equilibria.* 2017; 447: 39-71. doi: https://doi.org/10.1016/j.fluid.2017.05.007.

17. Román-Ramírez LA, Leeke GA. Evaluation of the Peng–Robinson and the Cubic-Plus-Association Equations of State in Modeling VLE of Carboxylic Acids with Water. *International Journal of Thermophysics.* 2020; 41(5): 61. doi: 10.1007/s10765-020-02643-6.

18. Pina-Martinez A, Privat R, Jaubert J-N, Peng D-Y. Updated versions of the generalized Soave α-function suitable for the Redlich-Kwong and Peng-Robinson equations of state. *Fluid Phase Equilibria.* 2019; 485: 264-269. doi: https://doi.org/10.1016/j.fluid.2018.12.007.

19. Kontogeorgis GM, Voutsas EC, Yakoumis IV, Tassios DP. An Equation of State for Associating Fluids. *Industrial & Engineering Chemistry Research.* 1996; 35(11): 4310-4318. doi: 10.1021/ie9600203.

20. Soave G. Equilibrium constants from a modified Redlich-Kwong equation of state. *Chemical Engineering Science.* 1972; 27(6): 1197-1203. doi: https://doi.org/10.1016/0009-2509(72)80096-4.

21. Kontogeorgis GM, Michelsen ML, Folas GK, Derawi S, von Solms N, Stenby EH. Ten Years with the CPA (Cubic-Plus-Association) Equation of State. Part 1. Pure Compounds and Self-Associating Systems. *Industrial & Engineering Chemistry Research.* 2006; 45(14): 4855-4868. doi: 10.1021/ie051305v.

22. Michelsen ML, Hendriks EM. Physical properties from association models. *Fluid Phase Equilibria.* 2001; 180(1): 165-174. doi: https://doi.org/10.1016/S0378-3812(01)00344-2.

23. Herslund PJ, Thomsen K, Abildskov J, von Solms N. Application of the cubic-plus-association (CPA) equation of state to model the fluid phase behaviour of binary mixtures of water and tetrahydrofuran. *Fluid Phase Equilibria.* 2013; 356: 209-222. doi: https://doi.org/10.1016/j.fluid.2013.07.036.

24. Voutsas EC, Yakoumis IV, Tassios DP. Prediction of phase equilibria in water/alcohol/alkane systems. *Fluid Phase Equilibria.* 1999; 158-160: 151-163. doi: https://doi.org/10.1016/S0378-3812(99)00131-4.

25. Suresh SJ, Elliott JR, Jr. Multiphase equilibrium analysis via a generalized equation of state for associating mixtures. *Industrial & Engineering Chemistry Research.* 1992; 31(12): 2783-2794. doi: 10.1021/ie00012a025.

26. Chrastil J. Solubility of solids and liquids in supercritical gases. *The Journal of Physical Chemistry.* 1982; 86(15): 3016-3021. doi: 10.1021/j100212a041.

27. Méndez-Santiago J, Teja AS. The solubility of solids in supercritical fluids. *Fluid Phase Equilibria.* 1999; 158-160: 501-510. doi: https://doi.org/10.1016/S0378-3812(99)00154-5.

28. Bian X, Du Z, Tang Y. An improved density-based model for the solubility of some compounds in supercritical carbon dioxide. *Thermochimica Acta.* 2011; 519(1): 16-21. doi: https://doi.org/10.1016/j.tca.2011.02.023.

29. Sparks DL, Hernandez R, Estévez LA. Evaluation of density-based models for the solubility of solids in supercritical carbon dioxide and formulation of a new model. *Chemical Engineering Science.* 2008; 63(17): 4292-4301. doi: https://doi.org/10.1016/j.ces.2008.05.031.

30. Bartle KD, Clifford AA, Jafar SA, Shilstone GF. Solubilities of Solids and Liquids of Low Volatility in Supercritical Carbon Dioxide. *Journal of Physical and Chemical Reference Data.* 1991; 20(4): 713-756. doi: 10.1063/1.555893.

31. Yan J, Du S, Du H, Zhang H, Jiao A, Li H, et al. Comparison of Four Density-Based Semi-Empirical Models for the Solubility of Azo Disperse Dyes in Supercritical Carbon Dioxide. *Processes.* 2022; 10(10): 1960. https://www.mdpi.com/2227-9717/10/10/1960.

32. Blanchard F, Carré B, Bonhomme F, Biensan P, Lemordant D. Solubility of carbon dioxide in alkylcarbonates and lactones. *Canadian Journal of Chemistry.* 2003; 81(5): 385-391. doi: 10.1139/v03-069.

33. Camy S, Pic JS, Badens E, Condoret JS. Fluid phase equilibria of the reacting mixture in the dimethyl carbonate synthesis from supercritical CO2. *The Journal of Supercritical Fluids.* 2003; 25(1): 19-32. doi: https://doi.org/10.1016/S0896-8446(02)00087-6.

34. Im J, Kim M, Lee J, Kim H. Vapor−Liquid Equilibria of Binary Carbon Dioxide + Alkyl Carbonate Mixture Systems. *Journal of Chemical and Engineering Data.* 2004; 49(2): 243-245. doi: https://doi.org/10.1021/je034089a.

35. Lu C, Tian Y, Xu W, Li D, Zhu R. High-pressure phase equilibrium for the binary systems of {carbon dioxide (1)+dimethyl carbonate (2)} and {carbon dioxide (1)+diethyl carbonate (2)} at temperatures of 273K, 283K, and 293K. *The Journal of Chemical Thermodynamics.* 2008; 40(2): 321-329. doi: https://doi.org/10.1016/j.jct.2007.05.017.

36. Gui X, Tang Z, Fei W. CO2 Capture with Physical Solvent Dimethyl Carbonate at High Pressures. *Journal of Chemical and Engineering Data.* 2010; 55(9): 3736-3741. doi: 10.1021/je1002708.

37. Hou Y, Chen X, Ren S, Song Z, Wu W. Phase Behavior, Densities, and Isothermal Compressibility of (Carbon Dioxide + Dimethyl Carbonate). *Journal of Chemical and Engineering Data.* 2010; 55(4): 1580-1587. doi: 10.1021/je900691n.

38. Ciccolini RP, Madlinger AC, Rogers SA, Tester JW. Vapor−Liquid Equilibrium Data and Predictive Correlations for the Carbon Dioxide−Dimethyl Carbonate Binary Mixture. *Journal of Chemical and Engineering Data.* 2010; 55(8): 2673-2681. doi: https://doi.org/10.1021/je900948n.

39. Lee MH, Yim J-H, Kang JW, Lim JS. Measurement of VLE data of carbon dioxide+dimethyl carbonate system for the direct synthesis of dimethyl carbonate using supercritical CO2 and methanol. *Fluid Phase Equilibria.* 2012; 318: 77-82. doi: https://doi.org/10.1016/j.fluid.2012.01.020.

40. Chen L, Zhu RJ, Fang Y, Yuan PF, Cao LQ, Tian YL. Vapor-Liquid Equilibrium Data for Carbon Dioxide plus Dimethyl Carbonate Binary System. *Acta Physico-Chimica Sinica.* 2013; 29(1): 11-16. doi: 10.3866/PKU.WHXB201210262.

41. Anouti M, Dougassa YR, Tessier C, El Ouatani L, Jacquemin J. Low pressure carbon dioxide solubility in pure electrolyte solvents for lithium-ion batteries as a function of temperature. Measurement and prediction. *The Journal of Chemical Thermodynamics.* 2012; 50: 71-79. doi: 10.1016/j.jct.2012.01.027.

42. Jethwa SJ, Román-Ramírez LA, Anderson PA, Leeke GA. Vapor Equilibrium Data for the Binary Mixtures of Dimethyl Carbonate and Ethyl Methyl Carbonate in Compressed Carbon Dioxide. *International Journal of Thermophysics.* 2023; 44(6): 86. doi: 10.1007/s10765-023-03186-2.

43. King MB, Catchpole O. Physico-chemical data required for the design of near-critical fluid extraction process. In: King MB, Bott TR, (eds.) *Extraction of Natural Products Using Near-Critical Solvents*. Dordrecht: Springer Netherlands; 1993. p. 184-231.

44. Chen Li, Zhu Rong-Jiao, Yuan Ping-Fang, Cao Li-Qian, Yi-Ling T. Vapor-Liquid Equilibrium Data for Carbon Dioxide+Dimethyl Carbonate Binary System. *Acta Physico-Chimica Sinica.* 2013; 29(01): 11-16. doi: https://doi.org/10.3866/pku.Whxb201210262.

45. North M. Chapter 1 - What is CO2? Thermodynamics, Basic Reactions and Physical Chemistry. In: Styring P, Quadrelli EA, Armstrong K, (eds.) *Carbon Dioxide Utilisation*. Amsterdam: Elsevier; 2015. p. 3-17.

46. Packham DE. *Handbook of Adhesion.* 2 ed. Chichester: Wiley; 2005.

47. Madan RD. *ISC Chemistry Book 1 for Class XI* S. Chand Publishing; 2021.

48. Arora A. *Introductory Organic Chemistry*. Discovery Publishing House Pvt. Limited; 2006.

49. Appendix C5 - Estimation of HSP from Correlations. In: Durkee JB, (ed.) *Cleaning with Solvents*. William Andrew Publishing; 2014. p. 599-613.

50. Leeke G, Gaspar F, Santos R. The Effect of Water on the Solubilities of Essential Oils in Dense CO2. *Journal of Essential Oil Research.* 2003; 15(3): 172-177. doi: 10.1080/10412905.2003.9712105.

51. Dobbs JM, Wong JM, Lahiere RJ, Johnston KP. Modification of supercritical fluid phase behavior using polar cosolvents. *Industrial & Engineering Chemistry Research.* 1987; 26(1): 56-65. doi: 10.1021/ie00061a011.

52. Xiong G, Kundu A, Fisher TS. *Thermal Effects in Supercapacitors.* Springer International Publishing; 2015.

53. Xu K. Nonaqueous Liquid Electrolytes for Lithium-Based Rechargeable Batteries. *Chemical Reviews.* 2004; 104(10): 4303-4418. doi: 10.1021/cr030203g.

54. Chernyak Y. Dielectric Constant, Dipole Moment, and Solubility Parameters of Some Cyclic Acid Esters. *Journal of Chemical and Engineering Data.* 2006; 51(2): 416-418. doi: 10.1021/je050341y.

55. Ismail N, Essalhi M, Rahmati M, Cui Z, Khayet M, Tavajohi N. Experimental and theoretical studies on the formation of pure β-phase polymorphs during fabrication of polyvinylidene fluoride membranes by cyclic carbonate solvents. *Green Chemistry.* 2021; 23(5): 2130-2147. doi: 10.1039/D1GC00122A.

56. Skeist I. *Handbook of Adhesives.* Springer US; 2012.

57. Eisenhart AE, Beck TL. Quantum Simulations of Hydrogen Bonding Effects in Glycerol Carbonate Electrolyte Solutions. *The Journal of Physical Chemistry B.* 2021; 125(8): 2157-2166. doi: 10.1021/acs.jpcb.0c10942.

58. Pacák P, Kodejš Z. Molar volumes and refractivities of highly concentrated solutions of ammonium and potassium thiocyanates in water and dimethylsulphoxide. *Canadian Journal of Chemistry.* 1988; 66(9): 2244-2249. doi: 10.1139/v88-356.

59. Wallace JM, Hobbs PV. 3 - Atmospheric Thermodynamics. In: Wallace JM, Hobbs PV, (eds.) *Atmospheric Science (Second Edition)*. San Diego: Academic Press; 2006. p. 63-111.

60. Voutsas E. Chapter 11 - Estimation of the Volatilization of Organic Chemicals from Soil. In: Letcher TM, (ed.) *Thermodynamics, Solubility and Environmental Issues*. Amsterdam: Elsevier; 2007. p. 205-227.

61. Pokorný V, Štejfa V, Fulem M, Červinka C, Růžička K. Vapor Pressures and Thermophysical Properties of Ethylene Carbonate, Propylene Carbonate, γ-

Valerolactone, and γ-Butyrolactone. *Journal of Chemical and Engineering Data.* 2017; 62(12): 4174-4186. doi: 10.1021/acs.jced.7b00578.

62. National Library of Medicine. Compound Summary for CID 280, Carbon dioxide. 2022. https://pubchem.ncbi.nlm.nih.gov/compound/Carbon-dioxide.

63. Yaws CL. Critical Properties and Acentric Factor - Organic Compounds. Yaws' Critical Property Data for Chemical Engineers and Chemists. Knovel. N/A. https://app.knovel.com/hotlink/toc/id:kpYCPDCECD/yaws-critical-property/yaws-critical-property (2012).

64. Ma J. *Battery Technologies: Materials and Components.* Weinheim: Wiley-VCH; 2021.

65. Hess S, Wohlfahrt-Mehrens M, Wachtler M. Flammability of Li-Ion Battery Electrolytes: Flash Point and Self-Extinguishing Time Measurements. *Journal of The Electrochemical Society.* 2015; 162(2): A3084. doi: 10.1149/2.0121502jes.

66. Zhang X, Zuo J, Jian C. Experimental Isobaric Vapor−Liquid Equilibrium for Binary Systems of Ethyl Methyl Carbonate + Methanol, + Ethanol, + Dimethyl Carbonate, or + Diethyl Carbonate at 101.3 kPa. *Journal of Chemical and Engineering Data.* 2010; 55(11): 4896-4902. doi: https://doi.org/10.1021/je100494z.

67. Yaws CL. *Thermophysical Properties of Chemicals and Hydrocarbons.* Elsevier Science; 2014.

68. Poling BE, Prausnitz JM, O'Connell JP. *Properties of Gases and Liquids.* 5th ed. New York: McGraw-Hill Education; 2001.

69. Zhao W, Ge Y, Zhang X, Sun X, Xiang S. A generalized alpha function of Peng-Robison equation of state for non-polar, weakly polar and polar compounds. *Chinese Journal of Chemical Engineering.* 2023; 58: 234-243. doi: https://doi.org/10.1016/j.cjche.2022.10.019.

70. Tsivintzelis I, Musko NE, Baiker A, Grunwaldt J-D, Kontogeorgis GM. Experimental determination and modeling of the phase behavior for the direct synthesis of dimethyl carbonate from methanol and carbon dioxide. *The Journal of Supercritical Fluids.* 2013; 84: 155-163. doi: 10.1016/j.supflu.2013.09.020.

71. Letcher TM. *Development and Applications in Solubility.* RSC Pub.; 2007.

72. Dortmund Data Bank. www.ddbst.com (2023).

73. Novák JP, Matouš J, Pick Ji. *Liquid-liquid equilibria.* Amsterdam: Elsevier 1987.

74. Gorak A, Sorensen E. *Distillation: Fundamentals and Principles.* Elsevier Science; 2014.

75. Muhlbauer AL, Raal JD. *Phase Equilibria: Measurement & Computation.* CRC Press; 2023.

76. Dougassa YR, Tessier C, El Ouatani L, Anouti M, Jacquemin J. Low pressure carbon dioxide solubility in lithium-ion batteries based electrolytes as a function of temperature. Measurement and prediction. *The Journal of Chemical Thermodynamics.* 2013; 61: 32-44. doi: 10.1016/j.jct.2012.12.025.

77. Li J-l, Jin J-s, Zhang Z-t, Pei X-m. Equilibrium solubilities of a p-toluenesulfonamide and sulfanilamide mixture in supercritical carbon dioxide with and without ethanol. *The Journal of Supercritical Fluids.* 2010; 52(1): 11-17. doi: https://doi.org/10.1016/j.supflu.2009.11.011.

78. Asghari-Khiavi M, Yamini Y, Farajzadeh MA. Solubilities of two steroid drugs and their mixtures in supercritical carbon dioxide. *The Journal of Supercritical Fluids.* 2004; 30(2): 111-117. doi: https://doi.org/10.1016/j.supflu.2003.07.002.

79. Huang Z, Feng M, Guo Y, Su J, Teng L, Liu T, et al. Ternary solubility of mixed cholesteryl esters in supercritical carbon dioxide. *Fluid Phase Equilibria.* 2008; 272(1): 8-17. doi: https://doi.org/10.1016/j.fluid.2008.07.012.

80. García-González J, Molina MaJ, Rodríguez F, Mirada F. Solubilities of hydroquinone and p-quinone in supercritical carbon dioxide. *Fluid Phase Equilibria.* 2002; 200(1): 31-39. doi: https://doi.org/10.1016/S0378-3812(02)00010-9.

81. Huang Z, Chiew YC, Lu W-D, Kawi S. Solubility of aspirin in supercritical carbon dioxide/alcohol mixtures. *Fluid Phase Equilibria.* 2005; 237(1): 9-15. doi: https://doi.org/10.1016/j.fluid.2005.08.004.

Chapter 5: Extraction of Artificial LIB Electrolyte Using Pressurised Carbon Dioxide

5.1 Introduction

The application of supercritical fluids (SCFs) and compressed gases for extraction and separation processes has been used extensively across various industrial sectors for many years. Some notable examples of these industries include pharmaceuticals, food, and textiles [1]. Among the SCFs, carbon dioxide is an excellent choice for supercritical fluid extraction (SFE) processes due to its favourable properties, such as non-toxicity, mild critical parameters, abundance, and non-flammability. Using carbon dioxide eliminates the need for organic solvents, traditionally used in Soxhlet extraction, and reduces the concerns related to their storage, disposal, and potential environmental impact [2, 3].

Recycling practices face significant risks and challenges when recovering and processing LIB electrolyte. The volatile nature of this component makes it highly flammable and presents a severe fire hazard due to the vaporisation effects. As a result, the recovery process becomes complicated, especially during the conventional disassembly and pretreatment steps in current recycling processes. This complexity reduces product recovery yields and requires inherently safer recycling practices [4].

In recent years, efforts towards recovering the LIB electrolyte have led to the development of three leading initiatives: liquid extraction, supercritical carbon dioxide extraction, and vacuum extraction [5-8].

This chapter is structured as follows: the *Aims and Objectives* are defined in Section **5.2**, the *Methodology* of the experimental practice is outlined in Section **5.3**, the *Calculations and Formulae* are given in Section **5.4**, the *Experimental Design* is outlined in Section **5.5**, the experimental *Results and Discussion* are presented in Section **5.6**, and finally, the chapter is closed with a *Conclusion* in Section **5.7**.

5.2 Aims and Objectives

This chapter investigates the process design and optimisation of the extraction and recovery of an artificially prepared mixture of LIB electrolyte using pressurised carbon dioxide.

The influence of each process parameter, pressure, temperature, flow rate, and duration, was evaluated to determine their optimal conditions to maximise the extraction yield. To achieve the overall aim, the following questions were addressed:

1. How do the pressure and temperature process conditions influence the overall extraction and recovery of an artificial LIB electrolyte?

2. Is Response Surface Methodology (RSM) an appropriate method to model and optimise the extraction yield of an artificially prepared LIB electrolyte using pressurised carbon dioxide accurately?

3. Given the differences in physical properties of each component within the LIB electrolyte composition, how does the composition of recovered components change with adjustments in the process conditions?

5.3 Methodology

5.3.1 Rig design

A high-pressure rig was designed and fabricated to facilitate high pressure extractions in static and dynamic configurations. **Figure 5-1** illustrates a PID of the rig design used for the experiments.

The extraction of artificial LIB electrolyte was performed in a pressure vessel manufactured by the Parr Instruments Company, USA, as shown in **Figure 5-2**. The design pressure of the reactor was rated at 34.5 MPa, at a temperature of 373.15 K. This vessel was equipped with two sapphire windows and an integrated heating jacket. The reactor's design specifications are as outlined: an internal diameter of 30 mm, an outer diameter of 85 mm, and a nominal volume of 25 mL.

The internal pressure of the vessel was measured using an Ashcroft analogue pressure gauge (PI-03) capable of indicating readings up to 40 MPa and displayed in increments of 1 MPa. The vessel's internal temperature (TI-01) was recorded using a K-type thermocouple inserted into the reactor through the head of the vessel. It was connected to an RS Pro RS51 wired digital thermometer capable of measuring and indicating temperatures from 223.15 K to 523.15 K in increments of 0.1 K. Additional pressure indicators were located across the system: an analogue pressure gauge was installed after the carbon dioxide cylinder (PI-01), and the system pressure was displayed before entering the reactor on the HPLC pump (PI-02).

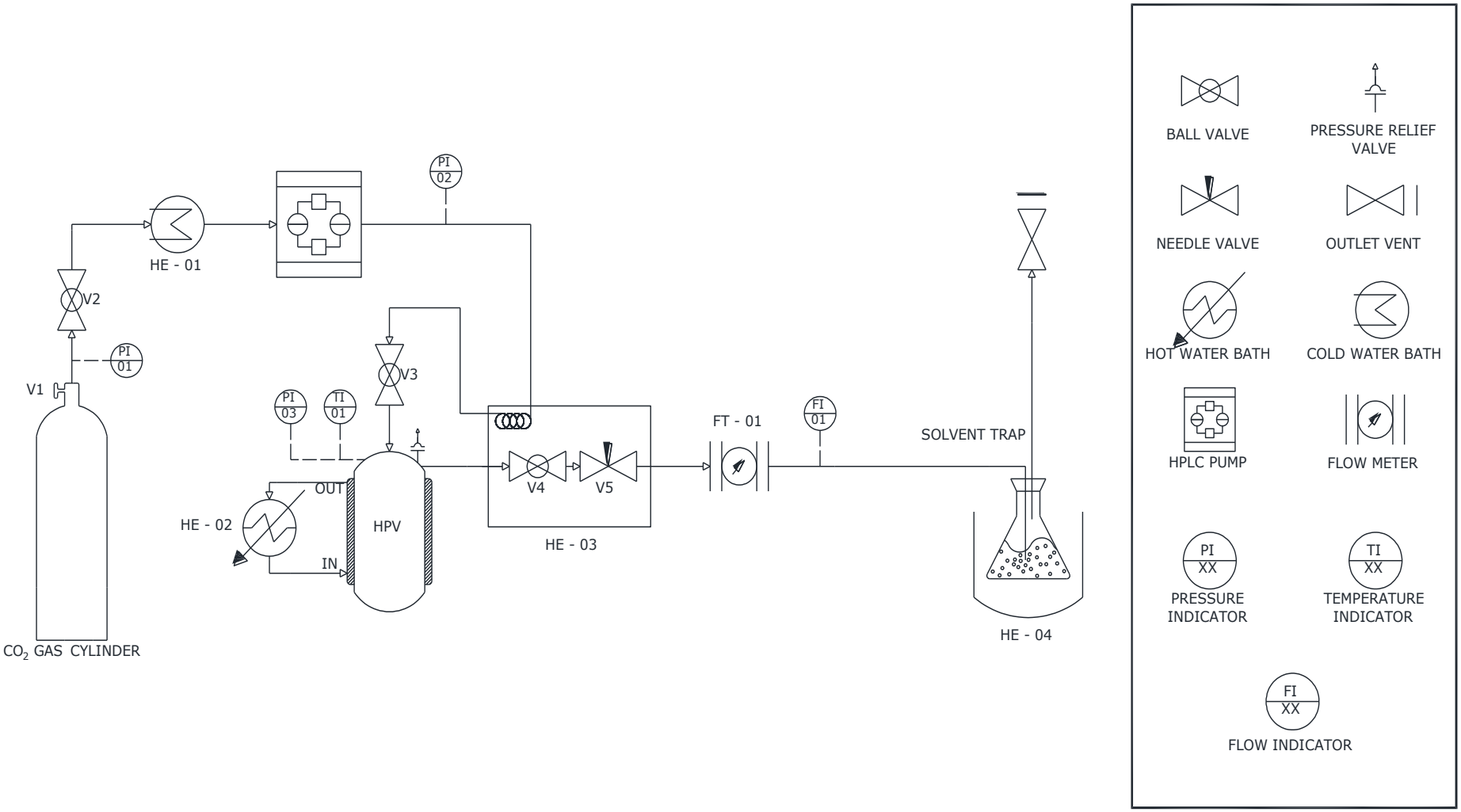

Figure 5-1: Schematic diagram of the pressurised carbon dioxide extraction system.

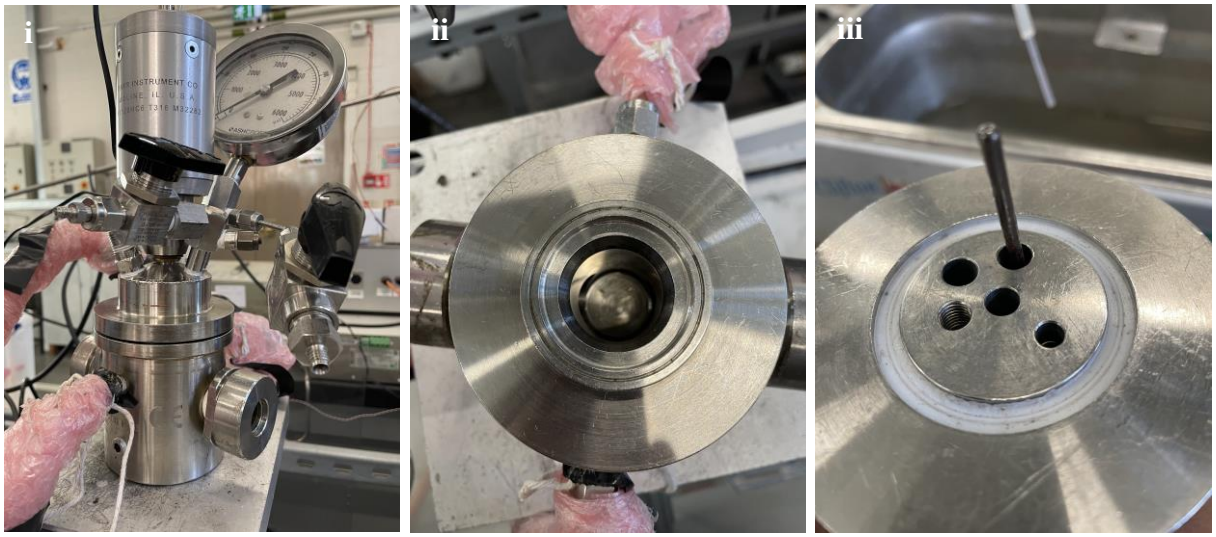

Figure 5-2: Photographs of the Parr Instrument Company autoclave; i) vessel body, ii) internal volume, iii) vessel head, PTFE O-ring, and K-type thermocouple.

5.3.1.1 Gas – liquid contactor

The design of the reactor has a limitation regarding the flow path of carbon dioxide. The inlet and outlet positions are both integrated into the head of the vessel. As a result, there is less contact between gas and liquid, thereby minimising the mass transfer effects. SFE processes typically require minimal mechanical contact arrangements due to the high penetrability of SCFs [9]. However, to enhance the interfacial contact area between carbon dioxide and the electrolyte components, a gas-liquid contactor was installed at the inlet of the vessel. This maximised fluid contact and expedited the extraction process. The gas-liquid contactor was constructed from stainless steel tubing with an internal diameter of $1/16^{th}$ inch and a wall thickness of 0.02 inches, sourced from Swagelok. Details of the design schematics are provided in **Figure 5-3**.

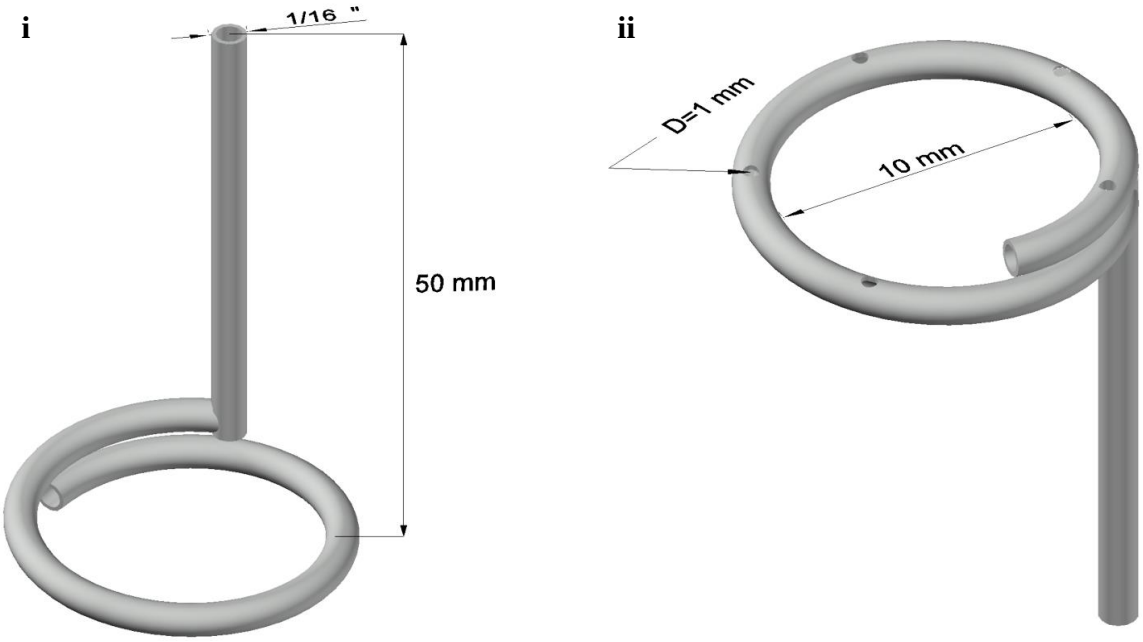

Figure 5-3: Gas – liquid contactor design; i) top orientation, ii) bottom orientation.

5.3.2 Method

The fundamental principles of the pressurised carbon dioxide extraction process generally remain consistent, regardless of the application. The basic apparatus for each system (as presented in **Figure 5-1**) includes a pump for pressurising carbon dioxide, a pressure cell to contain the sample, a device to control the pressure in the vessel, and a collection vessel [10]. Similar to the solubility studies (refer to *Chapter 4: Solubility Measurements of LIB Electrolyte Components in Carbon Dioxide*), the pressurised carbon dioxide extraction technique consists of several notable steps.

5.3.2.1 Rig preparation

Initial preparation steps were undertaken to ensure the quality and repeatability of the extraction process. Before loading the sample, the HPV was meticulously cleaned using acetone to eliminate any remnants of components from the previous run. Following this, the heat exchangers were pre-set to the desired operational conditions.

5.3.2.2 Sample loading

The artificial LIB electrolyte mixture was created on a gravimetric basis. Each carbonate (DMC, EMC, and EC) was weighed to create a homogenous mixture in a 1:1:1 mass ratio. The liquid mixture had a total weight of 1.5 g and was absorbed into a cotton wool matrix weighing approximately 0.5 g. The matrix and the mixture were both placed in a clear glass vial measuring 10 mL. The vial and contents were then inserted into the reactor (as photographed in **Figure 5-4**).

Figure 5-4: Glass sample holder containing electrolyte components absorbed in a cotton wool matrix.

5.3.2.3 System pressurisation

Before extraction, the HPV heating jacket was set to the desired temperature using a heating circulator bath (Thermo Haake, DC10-B3) (HE-02). Liquid carbon dioxide was introduced into the system via the gas cylinder (V1). The carbon dioxide travelled through a series of coiled tubing placed inside a refrigerated circulator bath (Grant, LTD6G) (HE-01), which was filled with a glycol heat transfer fluid and maintained at a temperature below 278.15 K to ensure the carbon dioxide remained largely in the liquid phase.

The system pressurisation was performed in two stages. First, the HPV was equalised to the pressure of the carbon dioxide gas cylinder. Then, the vessel was isolated from the carbon dioxide supply, and the HPLC pump (Cole-Parmer, Series III) was purged, to release any stagnant gas trapped within the lines between the HPV and the gas cylinder. This step maximised the carbon dioxide in the liquid phase, which was necessary to pressurise the carbon dioxide efficiently.

The unstirred thermostatic water bath (Clifton) (HE-03) was maintained at 303.15 K; this heat exchanger was imperative for the rig's operation. It is important to note that EC has a melting point of 309.6 K and exists as a solid at room temperature. In the absence of the heat exchanger, it was prone to freeze across the metering valve, causing a blockage [11].

Before entering the HPV, the pressurised carbon dioxide was heated to a temperature close to the vessel's heated jacket. More importantly, when leaving the vessel and passing across the metering valve, the carbon dioxide underwent flash and throttling expansion; this phenomenon caused the gas to supercool, freezing the valve. By utilising the Joule-Thomson coefficient and considering the maximum pressure deviation encountered, a calculated maximum temperature change of 77 K was determined. This value implies that a carbon dioxide stream initially at 298.2 K (lowest experimental temperature condition) would reach 221.2 K as it passed across the metering valve. Submerging the valve and coiled piping in the water bath proved instrumental in mitigating this adiabatic effect and kept the carbon dioxide in the vapour phase [12, 13].

5.3.2.4 Static and dynamic extraction

The extraction process incorporated both static and dynamic modes. In the static phase, the reactor was set to the desired pressure and temperature, and the HPV was then isolated via the ball valves V3 and V4. Once the specified extraction time had elapsed, the valves were opened, allowing the solvent and component mixture to be released.

During the dynamic extraction, a continuous stream of carbon dioxide was required throughout the entire extraction process. Similar to the static mode, pressure and temperature parameters were kept constant. To maintain a stable system pressure, the output flowrates of the HPLC pump and the metering valve (V5) were kept constant. The dynamic flowrate was measured using a variable area flow meter (Key Instruments), while the consumption of carbon dioxide was measured as a volume (STP) using a wet gas meter (Alexander Wright & Co.), which is accurate up to increments of ± 0.01 L. Both techniques included an initial stabilisation period of 2 minutes, during which the flowrate (for dynamic extraction), temperature, and pressure were closely monitored to ensure the stability of the system conditions.

5.3.2.5 Solute recovery

Several techniques were explored to maximise the collection and retention of the electrolyte components during the solute recovery stage. Initially, thermal trapping was considered due to its simplicity. In this method, the SFE effluent is depressurised into a cool vessel, causing the liquid to condense and the gas to escape. However, this method is limited to non-volatile organics since the high gas flowrate results in losses of even moderately volatile components. The alternative approaches more suitable for the quantitative recovery of volatile components are sorbent trapping and liquid solvent trapping.

Sorbent trapping is a highly effective sample collection method achieved by depressurising the SCF onto a sorbent trap. Once the analytes are trapped in the sorbent packing, they can be recovered by elution with a small volume of liquid solvent. The advantages of using this technique lie in the selectivity of recovery; the optimal sorbent packing material can selectively target analytes in the SCF, and the elution of analytes from the sorbent packing can be adjusted based on the components of interest [14].

While a high degree of selectivity was not a prerequisite, given that all the extracted components were intended for capture and recovery, the chosen method for this SFE process incorporated a combination of thermal trapping and entrapping the components in a liquid solvent. This approach represents the most commonly employed technique for analyte capture. The subsequent section expounds upon the procedural steps.

Once the extraction fluid passes across the metering valve (V5), the outlet pressure sharply declines, reducing the density of carbon dioxide and, consequentially, its dissolving power. The gas-liquid mixture is then bubbled into a conical flask (with a side arm) containing 150 mL of acetone. Significant differences in the boiling points between carbon dioxide and the electrolyte components ensure that each component condenses and remains in the liquid phase. The linear and cyclic carbonates are dissolved in the acetone solvent trap, whereas the carbon dioxide is simply released in its gaseous state.

However, it should be noted that solvent traps are not without losses. In this recovery process, the solvent trap was not entirely effective in trapping every component for the entire duration of the pressurised extraction. As a result, an investigation was conducted to determine the electrolyte component dissolution in the acetone solvent trap when influenced by temperature.

In this study, a gravimetric quantity of 1 g of each component (DMC, EMC, and EC) was dissolved in 150 mL of acetone, and three experiments were conducted at different temperatures: room temperature, ice regulated, and dry ice regulated.

The ice and dry ice regulated systems used water and acetone, as shown in **Figure 5-5**, and served as the heat transfer fluids, respectively, facilitating the heat exchange between the conical flask holding the acetone and the heat transfer fluid contained in a dewar flask.

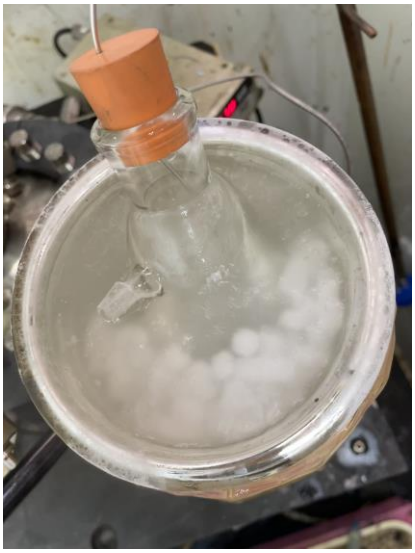

Figure 5-5: Acetone and dry ice regulated solvent trap, containing acetone and artificial electrolyte.

After weighing the conical flask and contents, carbon dioxide was introduced into the solution at a volumetric flow rate of 2.5 L/min for 60 minutes based on the optimal experimentation parameters. The temperature of the solution was measured 10 minutes after the initiation of carbon dioxide flow. After 60 minutes, an aliquot was injected into the GC-TCD, and the mass of the remaining electrolyte components was quantified using nonane as an internal standard. The total weight of the remaining solvent trap solution was repeatedly weighed until a constant value was achieved, indicating that most/all of the carbon dioxide had separated from the liquid solution.

To validate the experiment, it was repeated. The tabulated and graphical results of the thermal impact on the solvent trap and the retention of electrolyte components are presented in **Table 5-1** and **Figure 5-6**, accordingly. Where T represents the acetone solvent trap's temperature, measured 10 minutes after introducing a gas flow, and $\%m_{total}$ signifies the total mass loss of all components (DMC, EMC, EC, and acetone).

Table 5-1: The mass loss of electrolyte components (DMC, EMC, and EC) in an acetone solvent trap, expressed under several temperature conditions.

Solvent trap	T (K)	$\mathbf{m_{inital}}$ (g)	$\mathbf{m_{final}}$ (g)	Mass loss (%)			
				$\%\mathbf{m_{DMC}}$	$\%\mathbf{m_{EMC}}$	$\%\mathbf{m_{EC}}$	$\%\mathbf{m_{total}}$
Room temperature	279.45*	152.9	99.1	31.4	31.8	26.3	36.1
Ice-regulated	273.35	153.6	115.2	19.5	18.6	16.1	25.1
Dry ice-regulated	< 223.15**	152.8	137.6	6.9	6.6	5.4	8.3

n = 2. Standard uncertainties are u(T) = 0.1 K, u(m) = 0.01 g.
*The temperature of the solvent trap progressively fell and initially measured 295.25 K.
**The temperature measured in the dry ice configuration fell below the lower temperature limit (223.15 K) of the RS Pro S51 wired digital thermometer

The first law of thermodynamics in terms of enthalpy, states $dH = \delta q - VdP$, where dH represents the enthalpy of the system, δq represents the heat absorbed by the system, V is the volume, and dP is the change in pressure [15]. Since enthalpy is proportional to the temperature of the system, the temperature governs the internal energy of the system.

Therefore, when the electrolyte components enter the solvent trap, their enthalpy is drastically reduced as heat energy is absorbed by the system. As the temperature of the extraction products decreases, the loss of enthalpy initiates a phase transition of the volatile components, either from vapour to liquid or through sublimation if there is a significant temperature deviation [16].

As observed in **Table 5-1**, there is a significant reduction in the mass loss of the solvent trap when using dry ice to reduce the overall temperature. Based upon gravimetric measurements, the overall loss of components in the solvent trap (including acetone) after 60 minutes of passing carbon dioxide through it was 36%, 25%, and 8% under room temperature, ice regulated, and dry ice regulated conditions, respectively.

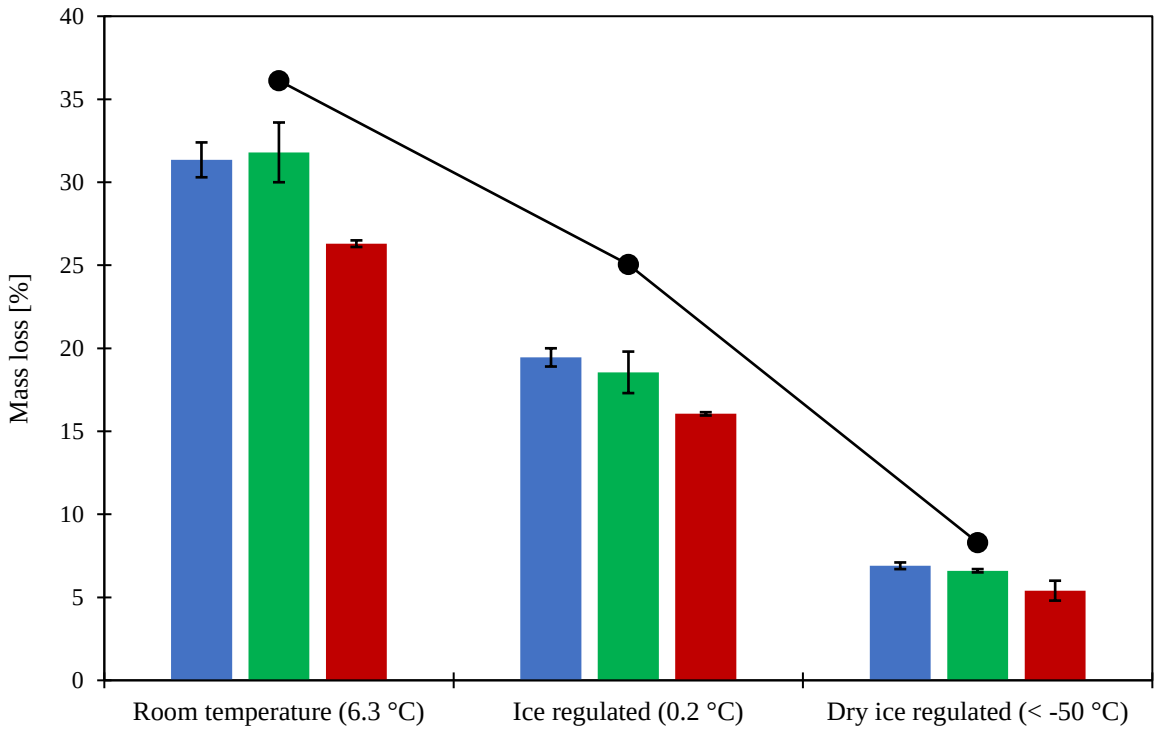

Figure 5-6: The mass loss of artificial electrolyte (DMC, EMC, and EC) in a solvent trap, expressed under several temperatures; DMC, EMC, EC, −●− Total mass loss. (Refer to **Table 5-1** for the experimental data points).

The results presented in **Figure 5-6** show the mass lost by each component under varying thermal conditions. The results are consistent with the predicted trends and reflect the vapour pressure behaviour of the components. The use of dry ice is an effective method to reduce the vaporisation of all components when carbon dioxide is introduced into the solvent trap. The difference in mass losses of the artificial electrolyte components exposed to room temperature and dry ice regulated conditions is almost five times greater.

After analysing the results, the dry ice solvent trap configuration was selected to capture and recover the electrolyte components for further extraction processes. To compensate for any discrepancies in the weight of each component, the recovery yield was adjusted accordingly to account for any potential losses caused by vaporisation.

5.4 Calculation and Formulae

The following equations were applied to obtain and process the experimental results of extracting the artificial LIB electrolyte using pressurised carbon dioxide.

5.4.1 Overall mass balance

$$Input - Output + \text{Generation} - \text{Consumption} = \text{Accumulation} \quad \textbf{(5-1)}$$

The general form of the mass balance is as stated above. Though, as the pressurised carbon dioxide extraction process is in the absence of a chemical reaction and is under the assumption of steady state, the overall mass balance simplifies to:

$$Input = Output \quad \textbf{(5-2)}$$

An overall mass balance was created to quantify the overall mass transfer in the boundaries of the system.

$$F + e = S + Ef \quad \textbf{(5-3)}$$

Where F is the solvent feed (g), e is the extractant (electrolyte components) (g), S represents the solute (g), and Ef is the effluent stream (g).

5.4.2 Extraction and recovery yields

Overall product extraction and recovery yield were calculated using **Equations 5-4** and **5-5**, respectively.

$$Extraction\ yield\ (\%) = \frac{E_{loaded} - E_{unextracted}}{E_{loaded}} \times 100 \quad \textbf{(5-4)}$$

$$Recovery\ yield\ (\%) = \frac{E_{recovered}}{E_{loaded}} \times 100 \quad \textbf{(5-5)}$$

Where E_{loaded} represents the loaded artificial electrolyte initially placed into the reactor (g), $E_{unextracted}$ is the unextracted artificial electrolyte still remaining in the reactor when extraction run is completed (g), $E_{recovered}$ represents the components gravimetrically quantified from the solvent trap, using GC-TCD (g).

5.4.3 Recovery process losses

Mass deviation in components loaded and recovered in the extraction system were calculated using:

$$Recovery\ losses\ (\%) = \frac{E_{loaded} - (E_{unrecovered} + E_{recovered})}{E_{loaded}} \times 100 \qquad \textbf{(5-6)}$$

The majority of the components were recovered and duly accounted for. Nevertheless, there were minimal unavoidable losses; this included solute trapped in the pipework, solute residue adhering to the internal walls of the pressure vessel, and primarily, the solute not captured by the solvent trap (escaping with the effluent). However, the impact was compensated as discussed in subsection **5.3.2.5**, *Solute recovery*.

5.4.4 Joule-Thomason effect

Temperature reduction across the metering valve (V5) resulted from the throttling process; this phenomenon is named the Joule-Thomson effect. The Joule-Thomson coefficient (μ) is the ratio of temperature change with pressure drop under constant enthalpy.

$$\mu = \left(\frac{\partial T}{\partial P}\right)_H \quad \textbf{(5-7)}$$

Where μ is the Joule-Thomson coefficient (K/Pa), T and P represent the temperature (K) and pressure of the gas (Pa) , respectively, and H is the enthalpy of the gas (KJ).

5.4.5 Solubility

$$S_{solute} = \frac{m_{solute}}{m_{CO_2}} \quad \textbf{(5-8)}$$

The solubility (S) (g/g) represents the concentration of a solute in equilibrium with the pure fluid at given conditions, as depicted in **Equation 5-8**.

5.4.6 Sample standard deviation

For further details, refer to *Chapter 4*, sub-section **4.4.6**.

5.5 Experimental Design

The Design of Experiments (DOE) represents a systematic scientific approach aimed at optimising processes, aiding product development, and fundamentally facilitating informed decision-making. This methodical technique involves conducting a series of experiments aimed specifically at elucidating the cause-and-effect relationships between input variables (known as factors) and output variables (responses). DOE enables the concurrent manipulation of multiple input factors, allowing for a comprehensive analysis of their effects on the desired output(s) [17]. Traditionally, in the absence of a DOE method, multiple experiments would be conducted to test the influence of one factor at a time. However, this sequential approach proves highly inefficient in terms of both time and cost. Moreover, it restricts the ability to simultaneously interpret the influence of two or more input variables [18].

The response surface methodology (RSM), first introduced by Box and Wilson in 1951 [19], encompasses a collection of mathematical and statistical approaches used to construct and analyse models through an empirical approach.

The experimental approach and analysis in RSM are founded on the premise that a response η is a function of a series of design variables x_n. This function can be approximated within a specific region of the variables, $x's$ using a polynomial model [20].

Mathematically, the representation of the response as a function of the design variables may be expressed as

$$\eta = f(x_1, x_2 \dots x_k) + \varepsilon \qquad \textbf{(5-9)}$$

Here, the true form of the true response function f, often remains unknown and exhibits complexity; the response η is contingent upon independent variables, $x_1, x_2, x_3 \ldots x_k$.

The experimental error, denoted by ε, accounts for the measurement errors associated with the response and other unaccounted variations or deviations not encompassed by f.

As the actual form of the true response function f is unknown, it necessitates an approximation. The practical implementation of RSM relies on establishing an appropriate approximation. Typically, a low-order polynomial in some small area of the independent variable space is satisfactory. The vast majority of models employ a polynomial of first order or second order; the first order model is expressed as [21, 22].

$$\eta = \beta_0 + \beta_1 x_1 + \cdots + \beta_k x_k \quad \textbf{(5-10)}$$

However, considering the curvature in the response surface requires the utilisation of a higher degree polynomial to effectively account for interactions. In such cases, a second order model typically would be required. The prevalent second order designs employed for this purpose include the Central Composite Design (CCD) and the Box-Behnken design. Both have been extensively applied in applications for optimising supercritical extraction processes [23].

$$\eta = \beta_0 + \sum_{i=1}^{k} \beta_i x_i + \sum_{i=1}^{k} \beta_{ii} {x_i}^2 + \sum_{\substack{i=1 \\ i<j}}^{k} \sum_{j=1}^{k} \beta_{ij} x_i x_j \quad \textbf{(5-11)}$$

These associated equations can be graphically depicted as response surfaces and can be employed to [24]:

1. Describe how the test variables influence the response.
2. Determine the interrelationships between the test variables.
3. Describe the combined relationship between all the test variables and the response.

This research employed the Central Composite design to fit the experimental data into the second order model (**Equation 5-11**). The design was selected as it provides comprehensive coverage of the design space, enabling the estimation not only of linear effects but also the detection of potential curvature in the response surface, as discussed earlier. Implementing this model allows for a robust analysis while necessitating fewer experimental runs to assess the influence of the independent variables. The outcomes and optimisation of the model are presented in the subsequent section, **5.6** Results and Discussions.

5.6 Results and Discussion

5.6.1 The influence of extraction flowrate

The solvent extraction flowrate can significantly influence both the extraction yield of the solute and the duration of the extraction process. An initial investigation into the dynamic flowrate of carbon dioxide was conducted to optimise the extraction yield of the artificial electrolyte.

A gravimetric quantity of 0.5 g of each component (DMC, EMC, and EC) was mixed and absorbed into a cotton wool matrix; the glass vial and contents were then placed into the vessel. The extraction pressure, temperature, and duration were all maintained at 6.0 MPa, 313.2 K, and 30 minutes, for each run, respectively. Based on previous literature findings, a dynamic flowrate in the range of 0.5-5.0 L/min were explored [7, 25]. As a mass flowrate, this is equivalent to approx. 1-10 g/min. To maintain the consistency of the carbon dioxide flow passing over the extractant, the flowrate was regularly monitored using the rotameter (Key Instruments) and verified against the wet gas meter (Alexander Wright & Co.) every 7.5 minutes. Each data point was repeated to ensure the validity of the relationship. The findings of the optimisation of flowrate have been presented in **Table 5-2**, and the complete data set and repeats are tabulated in **Table A5-1** in Appendix **A5**.

Table 5-2: The influence of dynamic flowrate of carbon dioxide on the extraction yield of artificial LIB electrolyte. From 1.5 g of sample at conditions of 6.0 MPa and 313.2 K.

$\dot{Q}$ (L/min)	V (L)	Extracted mass (g)	Extraction yield (wt.%)	S (g/ml)
0.56	19.4	0.112	7.3	5.74
1.03	32.9	0.210	13.2	6.38
2.05	63.8	0.323	21.3	5.61
2.52	78.8	0.401	26.3	5.10
3.07	95.8	0.351	23.1	3.66
3.53	106.1	0.318	20.8	3.00
4.47	138.0	0.301	19.8	2.19

n = 2. Standard uncertainties are u($\dot{Q}$) = 0.01 L, u(m) = 0.01 mg. t = 30 minutes.

The artificial electrolyte extraction can be observed to initially demonstrate an almost linear increase with an escalating flowrate, as depicted in **Figure 5-7**. At lower carbon dioxide flowrates, the mass transfer resistance restricts the transport of electrolyte components into the bulk of the solvent, and the carbon dioxide leaves the pressure vessel unsaturated. As the flowrate increases, the mass transfer resistance decreases, leading to an observable peak in extraction yield (2.4-2.6 L/min). At this point, the exiting carbon dioxide from the pressure vessel exhibits maximum saturation with the artificial electrolyte, establishing an equilibrium state. However, higher flowrates adversely affect the extraction yield.

Past this optimal point, and elevation in flowrate begins to diminish the residence time of solvent inside the vessel, reducing the effective contact between carbon dioxide and the electrolyte components.

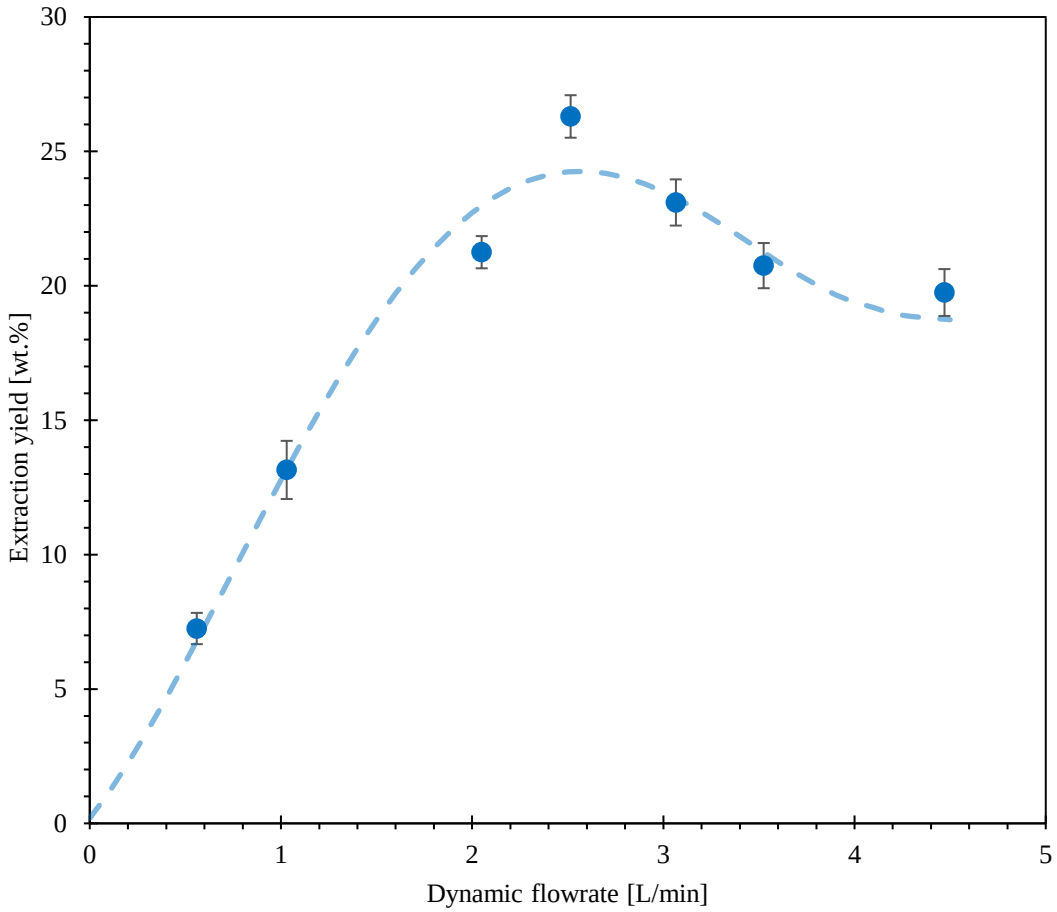

Figure 5-7: Influence of the dynamic flowrate of carbon dioxide on the extraction yield of artificial LIB electrolyte. (Refer to **Table 5-2** for experimental data points).

This deviation disrupts the system equilibrium, causing the carbon dioxide to exit the pressure vessel unsaturated despite the elevated mass transfer [26-28].

A maximum solubility of 0.00322 g/g of electrolyte components in carbon dioxide was achieved at conditions of 313.2 K and 6.0 MPa. This value was compared to the quaternary vapour-liquid equilibrium (VLE) solubility obtained in *Chapter 4*, which resulted in a value of 0.0246 g/g observed under conditions of 313.2 K and 5.0 MPa.

It is essential to note that the maximum solubility obtained from dynamic extractions should not exceed the VLE value, as this may suggest the entrainment of liquid electrolyte during the extraction process.

Based on the findings of this investigation, a constant flowrate of 2.5 L/min was implemented for all subsequent extractions conducted in this chapter.

5.6.2 The influence of extraction duration.

When determining an extraction process's optimal duration, efficiency and cost considerations are paramount. While solvent extraction using an organic solvent may span several hours, SFE can achieve completion in less than an hour. An incomplete extraction results from durations that are too short, while excessive durations lead to wastage of both solvent feed and time [28, 29].

Following the optimisation of the flowrate, a series of isothermal pressurised extractions were performed across a range of durations, spanning from 30 to 480 minutes. The optimised flowrate was maintained at a constant 2.5 L/min, and the vessel temperature was set to 313.2 K. Building upon the findings from *Chapter 4*, which demonstrated the significant influence of pressure on solubility, two pressure levels were evaluated over the allotted extraction durations. The first pressure was selected in the bounds of subcritical fluid (SBCF) conditions at 6.0 MPa, below the critical point of carbon dioxide (7.38 MPa). The second pressure, chosen in the SCF state, was 12.0 MPa. The parameters and results of the pressurised extraction are summarised in **Table 5-3**, where each run was repeated at least once.

Table 5-3: The influence of extraction duration on the extraction yield of artificial LIB electrolyte.

P (MPa)	t (min)	V (L)	e_{inital} (g)	e_{final} (g)	Extraction yield (wt. %)	S (mg/L)	$e_{unrecovered}$ (wt. %)		
							DMC	EMC	EC
6.0	30	78.6	1.514	1.044	31.0	5.98	34.7	18.4	46.9
	30	79.5	1.515	0.980	35.3	6.73	33.6	17.5	48.9
	60	154.6	1.535	0.724	52.8	5.25	23.0	13.4	63.6
	60	152.4	1.524	0.615	59.6*	5.96	20.0	12.4	67.6
	60	150.2	1.528	0.736	51.8	5.27	25.2	14.5	60.3
	120	303.5	1.514	0.517	65.8	3.29	11.2	7.2	81.6
	120	299.1	1.498	0.582	61.1	3.06	11.8	8.0	80.2
	240	607.7	1.513	0.446	70.5	1.76	0.3	0.2	99.5
	240	603.2	1.509	0.460	69.5	1.74	0.3	0.2	99.5
	360	917.3	1.509	0.368	75.6	1.24	0.1	0.3	99.6
	360	905.4	1.543	0.449	70.9	1.21	0.1	0.6	99.3
	480	1195	1.514	0.338	77.7	0.984	0.0	0.0	100.0
	480	1216	1.514	0.277	81.7	1.02	0.0	0.0	100.0
12.0	30	85.6	1.534	1.083	29.4	5.27	35.2	32.2	32.6
	30	87.4	1.512	1.054	30.3	5.24	33.3	29.3	37.4
	60	163.1	1.522	0.825	45.8	4.27	26.9	26.0	47.1
	60	165.7	1.512	0.890	41.1	3.75	29.2	25.8	45.0
	120	316.3	1.520	0.437	71.2	3.42	18.1	18.7	63.2
	120	311.1	1.515	0.500	67.0	3.26	19.4	19.2	61.4
	240	606.1	1.519	0.171	88.7	2.22	18.2	10.7	71.1
	240	614.3	1.536	0.241	84.3	2.11	15.6	9.4	75.0
	360	914.9	1.514	0.027	98.2	1.63	0.7	2.6	96.7
	360	918.6	1.504	0.016	98.9	1.62	0.9	1.8	97.3
	480	1227.5	1.547	0.001	99.9	1.26	0.0	0.0	100.0
	480	1202.3	1.519	0.003	99.8	1.26	0.0	0.0	100.0

n = 2. Standard uncertainties are u(P) = 1000 KPa, u(m) = 0.01 mg. $\dot{Q} = 2.5$ L/min
* Deviations in extraction yield of greater than 5% were repeated.

Where t represents the extraction duration (min), V signifies the volume of the solvent feed (L), $e_{initial}$ indicates the initial mass of artificial electrolyte in the vessel (g), e_{final} denotes the total mass of unrecovered artificial electrolyte, $e_{unrecovered}$ represents the mass fraction of unrecovered electrolyte component (wt. %), and S represents the solubility of all electrolyte components in carbon dioxide (mg/L).

The rate of extracting the component(s) is not a linear function of time. The representation of mass extraction as a function of time or mass of solvent permits the generation of an overall extraction curve. The study of these curves can assist in creating a mathematical model to describe the kinetics and physical behaviour of the solute dissolution from the matrix to the bulk solvent, which can be used to assess and enhance an extraction process.

Figure 5-8, the kinetics curve can be broken down into three primary stages. In the initial stage, known as the period of constant extraction rate (CER), the convective mass transfer between the electrolyte components and carbon dioxide results from the external mass transfer mechanism. This phase exhibits relative linearity, and the rate of solute extraction is the highest point attained in the process. The components recovered primarily originate from the proportion situated on the surface of the cotton wool matrix. Essentially, the influence of the CER stage correlates with the solvent flow passing over the matrix and the available solute on the surface. In the subsequent stage, termed falling extraction rate (FER), the readily available components located on the external surface of the cotton wool matrix have depleted. This becomes evident after the linear region of the graph, where the extraction rate begins to decline due to the reduction in effective mass transfer.

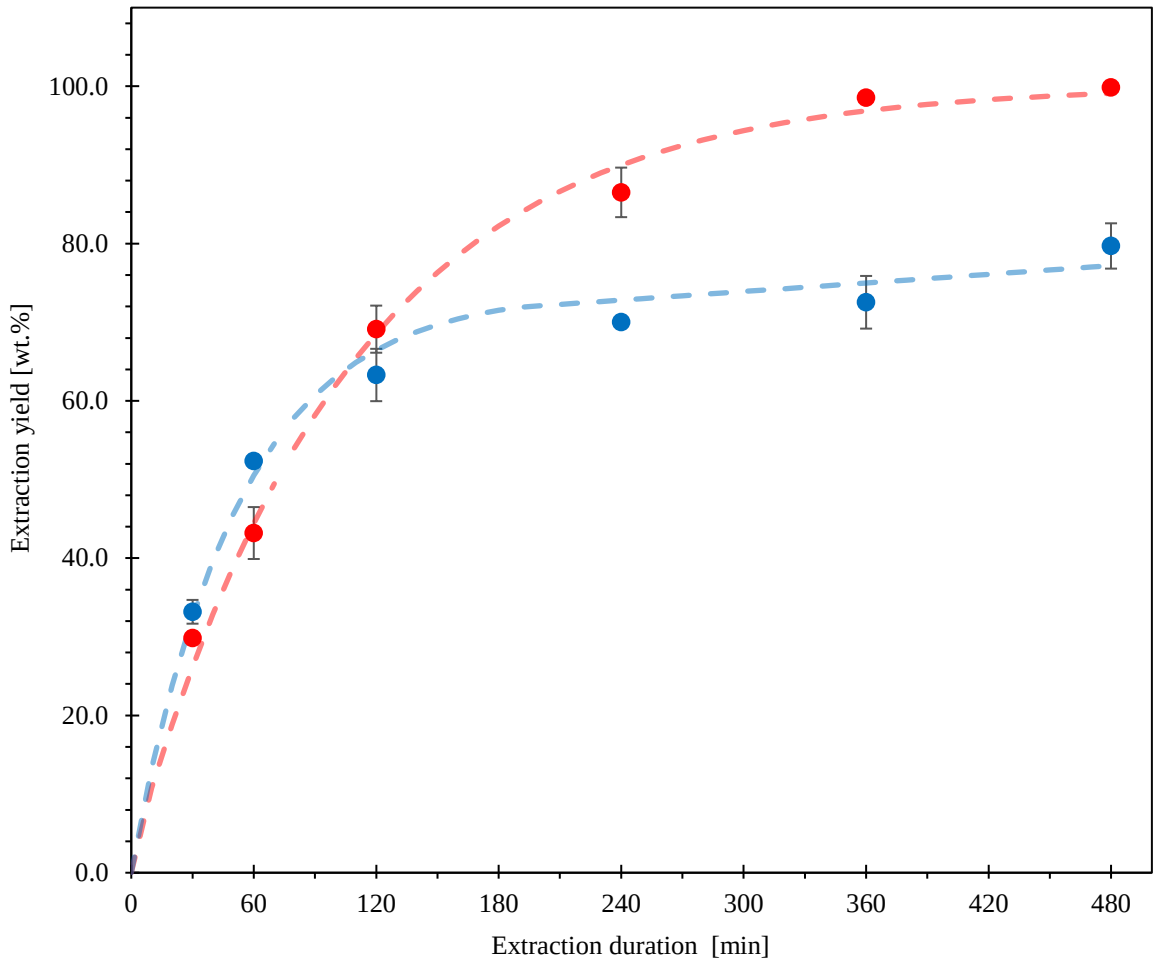

Figure 5-8: Influence of the extraction duration on the extraction yield of artificial LIB electrolyte. (●) Subcritical (313.2 K, 6.0 MPa), (●) Supercritical (313.2 K, 12.0 MPa). (Refer to **Table 5-3** for experimental data points).

In this phase, resistance to mass transfer occurs in both solid and fluid phases, with the extraction process relying significantly on diffusion and convection mechanisms.

In the final stage, termed diffusion controlled (DC), all the readily accessible electrolyte components have been exhausted, and the remaining components are trapped in the depths of the cotton wool matrix. The extraction rate becomes contingent on the diffusion of the solvent into the matrix's depth and its capacity to resurface for extraction.

This stage typically manifests in the last 2-3 hours of the extraction curve, as observed in **Figure 5-8**. During this phase, the time spent extracting the last remnants of the component is

highly inefficient; in most optimised processes, this step is typically avoided as it requires extensive solvent feed and time [23, 30].

Based on the experimental results concerning the impact of extraction duration on the yield of the artificial LIB electrolyte, the optimal extraction yield was identified to occur between 90-210 minutes. This duration prevents the extraction from transitioning into the uneconomical DC phase and maintains it primarily in the CER phase. The overall extraction process was conducted for 90 minutes, a duration determined to be sufficient for recovering the majority of the artificial LIB electrolyte while still allowing for the evaluation of the influence of pressure and temperature conditions. This extraction duration was implemented for all subsequent extractions discussed in this chapter.

To facilitate the diffusion of carbon dioxide into the depths of the matrix and enhance the recovery after the CER phase, a static extraction step was coupled with the dynamic extraction stage. Previous research conducted by *Liu et al*. determined that employing a combination of dynamic and static techniques was far more effective for extracting LIB electrolytes with pressurised carbon dioxide than solely employing static operations [23, 29]. The complete extraction comprised two 15-minute static extraction phases, where the vessel was isolated, and the contents were held for the full duration, alongside two 30-minute dynamic extractions, during which the vessel was swept with carbon dioxide.

5.6.3 Supercritical and subcritical fluid flow conditions

Figure 5-8 shows the initial extraction of electrolyte components using SBCF conditions at 313.2 K and 6.0 MPa and SCF conditions at 313.2 K and 12.0 MPa. Within the first 90 minutes of extraction, SBCF demonstrated a slight dominance over SCF and outperformed it. However, as the extraction duration progressed, a crossover point occurred at just under 2 hours, indicating the SCF to be more effective.

By the end of SFE process, occurring at just over 480-minutes, the extraction had almost reached completion, whilst the SBCF extraction had plateaued at this stage, indicating the occurrence of the diffusion controlled (DC) step and resistance in mass transfer to obtain the remaining extractant.

This disparity between flow conditions is further apparent in solubility, as presented in **Table 5-3**, where the overall solubility of the LIB electrolyte components in carbon dioxide is tabulated per extraction duration. In experiments up to 120 minutes, the solubility exhibited under SBCF conditions was notably higher than under SCF conditions. On average, the overall solubility of components under SBCF conditions across both experiments (60 and 120 minutes) was approximately 30% greater than under SCF conditions. However, as extraction dynamics shifted beyond the crossover point, SCF conditions demonstrated increased responsiveness, resulting in a higher overall solubility of the solutes in extractions beyond 120 minutes compared to SBCF conditions.

This observation aligns well with the quaternary vapour-liquid equilibrium (VLE) system established in *Chapter 4*. In the quaternary system, the total solubility (g/g) of electrolyte components in carbon dioxide was notably higher in SCF conditions than in SBCF conditions, as indicated in **Table 4-10**.

To elucidate the impact of flow conditions more distinctly, the mass fractions of the unrecovered electrolyte components were plotted against the extraction duration. **Figures 5-9** and **5-10** illustrate the results under pressures of 6.0 and 12.0 MPa, respectively.

A comparison of the figures, where the mass fractions of electrolyte components are plotted as a function of extraction duration, reveals the impact of extraction selectivity between SBCF and SCF conditions. In SCF conditions, components display relatively equal extraction rates within 60 minutes of extraction. Conversely, under SBCF conditions, there is a noticeable and prompt recovery of the linear carbonates, resulting in a considerable drift in the mass fractions of components.

This phenomenon was also observed by *Grützke et al.* [31]; GC-MS analysis of LIB electrolyte extracts from liquid carbon dioxide extraction revealed that the linear carbonates (DMC and EMC) were extracted with higher efficiency than EC.

The rapid recovery of linear carbonates is evident in SBCF conditions, as indicated by the near-zero mass fractions of DMC and EMC beyond 240 minutes. In contrast, compared to SCF conditions, achieving a similar extraction of linear carbonates required an additional 120 minutes.

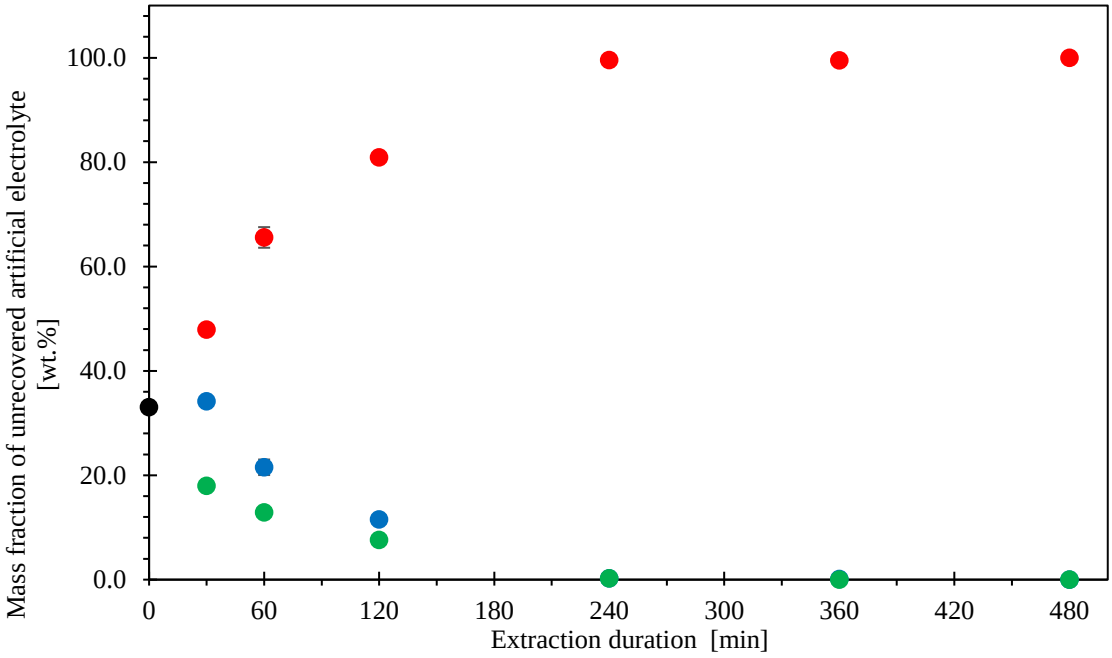

Figure 5-9: Mass fraction of unrecovered electrolyte components as a function of the extraction duration, at subcritical carbon dioxide conditions of 6.0 MPa and 313.2 K; (●) Initial composition, (●) DMC, (●) EMC, and (●) EC.
(Refer to **Table 5-3** for experimental data points).

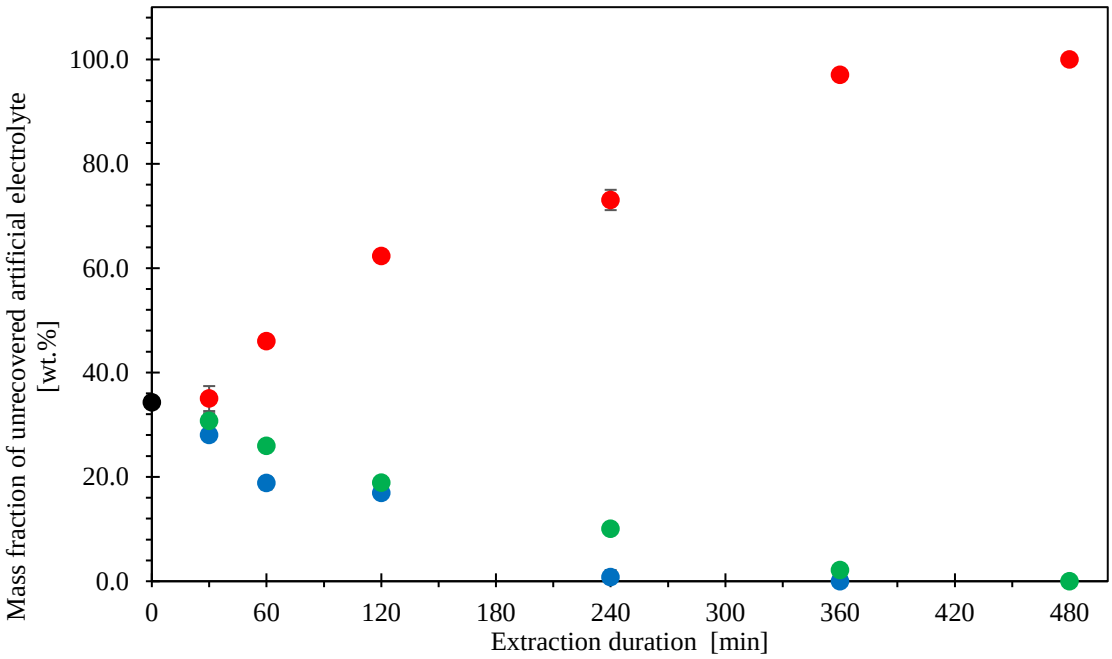

Figure 5-10: Mass fraction of unrecovered electrolyte components as a function of the extraction duration, at supercritical carbon dioxide conditions of 12.0 MPa and 313.2 K (●) Initial composition, (●) DMC, (●) EMC, and (●) EC.
(Refer to **Table 5-3** for experimental data points).

Furthermore, alterations in extraction pressure significantly impact vapour pressure. Lowering the system pressure increases the mean intermolecular distance between components, prompting molecules to transition from the liquid phase to the gas phase. Consequently, the linear carbonates become more prone to vaporisation, resulting in a higher extraction rate under SBCF conditions, as demonstrated in **Figure 5-9**.

The disparity in extraction yield between the SCF and the SBCF flows is observed in the artificial electrolyte extraction yield plot, as depicted in **Figure 5-8**. This divergence arises from the SBCF condition's inefficiency in effectively extracting the EC component. Notably, between 150 and 480 minutes of the extraction process, there is minimal variation in the extraction yield under the SBCF condition. In contrast, the SCF condition achieves a near-complete extraction of all components within 360 minutes. This difference indicates the inadequacy of SBCF in recovering the EC component within the observed extraction time frame.

The inability of the SBCF condition to effectively solubilise the EC has been previously discussed in *Chapter 4,* subsection **4.6.2**. The difference in solubility between both conditions can be attributed to density effects. The intermolecular interactions between solvent and solute are heightened as the density of carbon dioxide increases. At 313.2 K, the density of carbon dioxide at 6.0 MPa compared to 12.0 MPa is 149 and 718 kg/m^3, respectively [13]. This substantial density variation results in a more potent solvent strength, leading to a more significant dissolution of EC in SCF conditions. Moreover, under high pressure, carbon dioxide demonstrates a significantly higher diffusivity and lower viscosity, exceeding threefold. These physical properties grant the fluid greater penetrability, thus enabling SCF to diffuse into the matrix and recover the components more efficiently.

5.6.4 Design of Experiments (DOE) and Response Surface Methodology (RSM)

The DOE and RSM analyses were performed using Minitab Statistical Software, Version 21.1.0. For RSM, a full Central Composite Design was employed with 21 runs, including 4 replications of the centre point and 1 repetition of the four cube and axial points. The objective was twofold: firstly, to evaluate the relationship between factors and the response, and secondly, to optimise the response. Two independent variables, the pressure and temperature, were investigated across two levels. A visual representation of the design is presented in **Figure 5-11**. The dependent variable was the yield of artificial electrolyte extracted, expressed as a percentage. The experimental runs were performed in a randomised sequence to reduce the effects of systematic error.

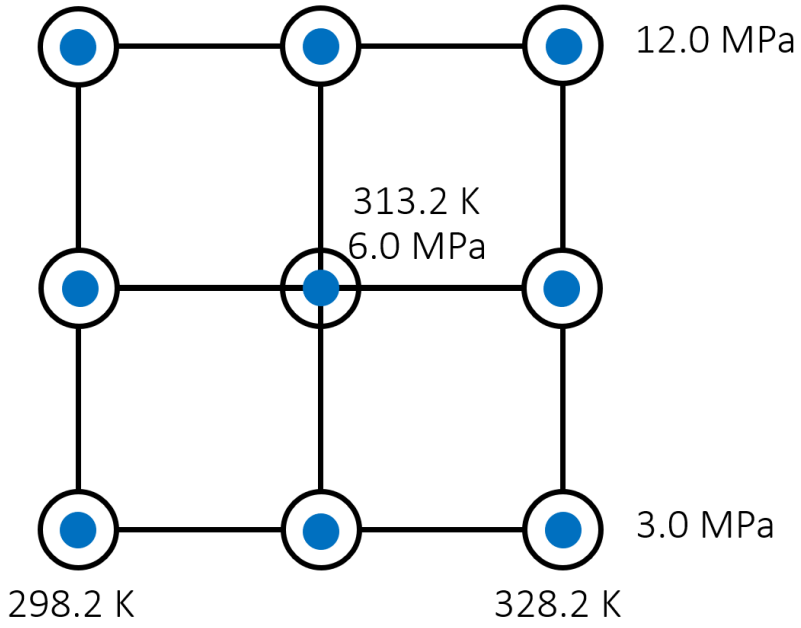

Figure 5-11: Experimental design for the extraction of artificial LIB electrolyte components using pressurised carbon dioxide.

The selected conditions were based on the findings from *Chapter 4*. As linear (DMC and EMC) and cyclic (EC) carbonates exhibited opposing solubility behaviours, a wide range of conditions were necessary to achieve high solubility. The pressure range was selected to encompass both subcritical and supercritical fluid phases of carbon dioxide, and the temperature range was maintained consistent with that explored in the solubility work.

The results of the Central Composite Design are tabulated in **Table 5-4**, with the subsequent experimental runs, independent variables (temperature and pressure), dependent variable (extraction yield of artificial electrolyte), and the standard deviation of experimental extraction yield at the corresponding operating conditions.

Table 5-4: Extraction yield of artificial LIB electrolyte (%) under the parameters of temperature (K) and pressure (MPa) as proposed by design of experiments.

Run	Temperature (K)	Pressure (MPa)	Experimental extraction yield (%)	SD
1	313.2	6.0	62.1	±0.8
2	313.2	12.0	56.4	±1.1
3	313.2	6.0	60.1	±0.8
4	328.2	12.0	70.2	±0.7
5	298.2	3.0	31.3	±1.4
6	313.2	3.0	32.3	±0.9
7	313.2	6.0	61.2	±0.8
8	328.2	6.0	65.6	±1.2
9	298.2	6.0	37.9	±0.5
10	298.2	12.0	46.1	±1.0
11	313.2	6.0	61.7	±0.8
12	313.2	6.0	60.9	±0.8
13	328.2	3.0	47.7	±1.2
14	298.2	3.0	29.4	±1.4
15	313.2	3.0	30.9	±0.9
16	298.2	12.0	44.6	±1.0
17	328.2	3.0	45.9	±1.2
18	328.2	12.0	69.3	±0.7
19	298.2	6.0	37.3	±0.5
20	313.2	12.0	54.9	±1.1
21	328.2	6.0	63.9	±1.2

The CCD enabled the response to be modelled by fitting a second order polynomial. The following regression equation expresses the quadratic model in terms of coded values:

$$Y = -1107 + 6.50\,T + 5.95\,P - 0.00944\,T^2 - 0.730\,P^2 + 0.0233\,TP \quad \textbf{(5-12)}$$

Where Y represents the extraction yield of artificial LIB electrolyte (wt. %), T is the temperature (K), P is the pressure (MPa), TP denotes the temperature-pressure interaction, and T^2, and P^2 represent their respective interactions.

The extraction yield of artificial LIB electrolyte was estimated using the quadratic regression model (**Equation 5-12**) and plotted linearly against the experimental values, as presented in **Figure 5-12**. The accuracy of the model's fit was determined by the percentage of variation in the response, R^2. *Jumbri et al.* [32] and *Hamzaoui et al.* [33], suggested a regression model with an R^2 value exceeding 0.9 indicates a strong correlation with experimental results [34]. Although a relatively strong correlation ($R^2 = 0.91$) of the responses was achieved, the CCD model could be improved to achieve a better fit within the quadratic polynomial model developed. The adjusted and predicted R-squared values were calculated as $R^2_{adj} = 0.88$ and $R^2_{pred} = 0.83$, respectively.

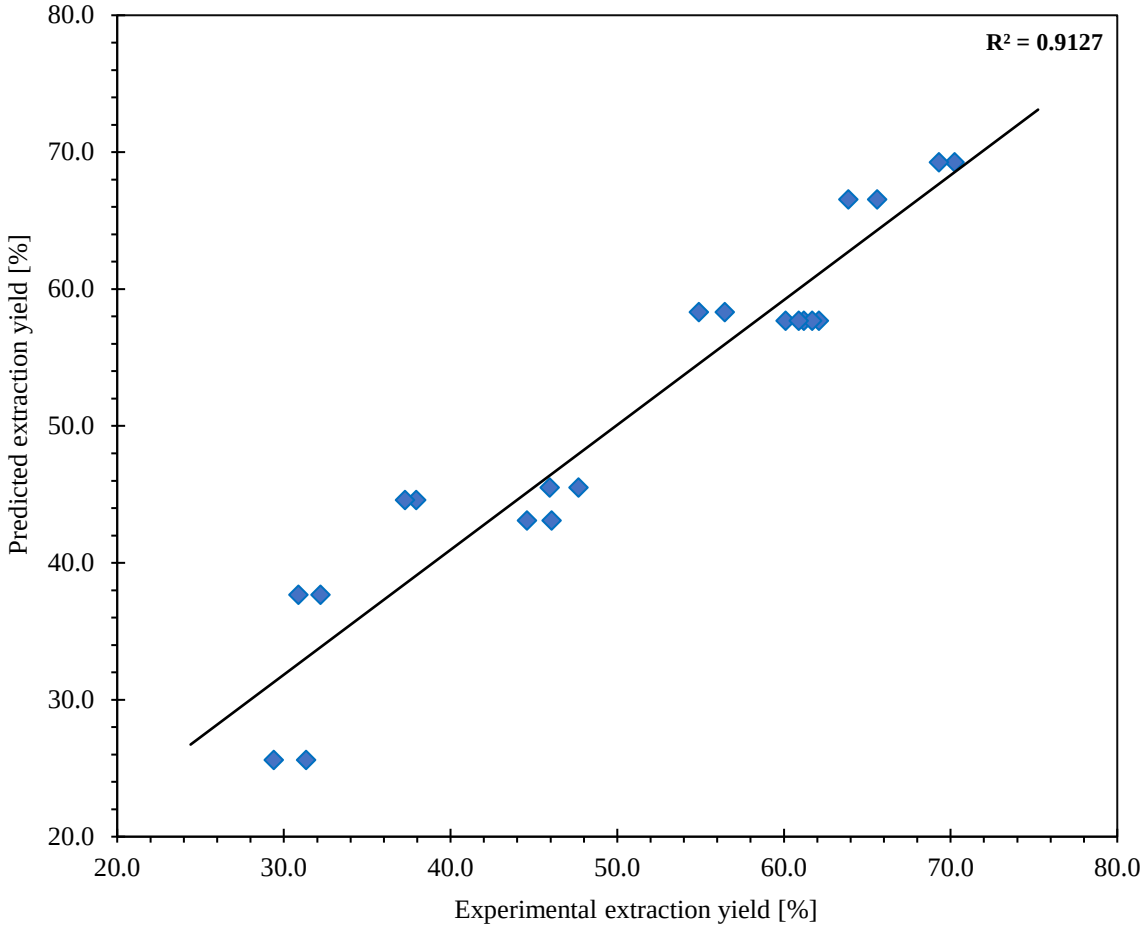

Figure 5-12: Experimental extraction yield of artificial LIB electrolyte (wt.%) against the predicted extraction yield of artificial LIB electrolyte (wt.%) using the CCD quadratic second order model.

To evaluate the fitness and predictive capabilities of the model, an experiment within the range of the model was performed at process conditions of 328.2 K and 9.0 MPa. The experimental extraction yield was 67.8%, and associated process conditions were fed into the quadratic polynomial model via the regression equation (**Equation 5-12**). This generated a predicted extraction yield of 74.5%. The deviation is significant and varies by 9.6% between the experimental and model extraction yields. This value indicates that the quadratic polynomial model requires a more extensive data set to improve its predictive capabilities.

The analysis of variance (ANOVA) was utilised to evaluate the quality of the fitted model for extraction of artificial LIB electrolyte and to identify which interactions are significant. The statistical difference was based on the total error with a confidence level of 95%. The results of the ANOVA are tabulated in **Table 5-5**.

The outcome of the ANOVA indicated that the significant factors ($P < 0.05$) influencing the yield of artificial LIB electrolyte exhibited notably low responses (P<0.001) in the model, far below the 0.05 threshold. This suggests a substantial impact on the response.

A high F and a small P value signify that the independent variables significantly impact the respective response variables [34]. Among the variables, the temperature parameter was demonstrated to have the most significant effect on all responses, followed by the pressure. The normal plot of effects and the Pareto chart of effects display the absolute values of the standardised effects. Each of these are presented in Appendix **A6**.

Table 5-5: Analysis of variance (ANOVA) for the CCD obtained from the DOE of the extraction of artificial LIB electrolyte, as presented in **Table 5-4**.

Source	DF	Adj SS	Adj MS	F-value	P-value
Model	5	3398.81	679.76	31.36	<0.001
Linear	2	2845.59	1422.79	65.64	<0.001
Temperature	1	1562.13	1562.13	72.07	<0.001
Pressure	1	1283.46	1283.46	59.21	<0.001
Square	2	930.74	465.37	21.47	<0.001
T · T	1	22.05	22.05	1.02	0.329
P · P	1	806.75	806.75	37.22	<0.001
2-way interaction	1	20.51	20.51	0.95	0.346
T · P	1	20.51	20.51	0.95	0.346
Error	15	325.14	21.68		
Lack-of-fit	3	314.06	104.69	113.38	0.000

Pure error	12	11.08	0.92
Total	20	3723.95	

5.6.5 Analysis of the artificial LIB electrolyte extraction yield using response surface analysis

The RSM results were analysed using three-dimensional surface plots. These diagrams better aid the visualisation of the combined influence of the process variables, namely pressure and temperature, on the extraction yield of artificial LIB electrolyte. The response surface optimisation plot and contour plot are presented in **Figures 5-13** and **5-14**, respectively.

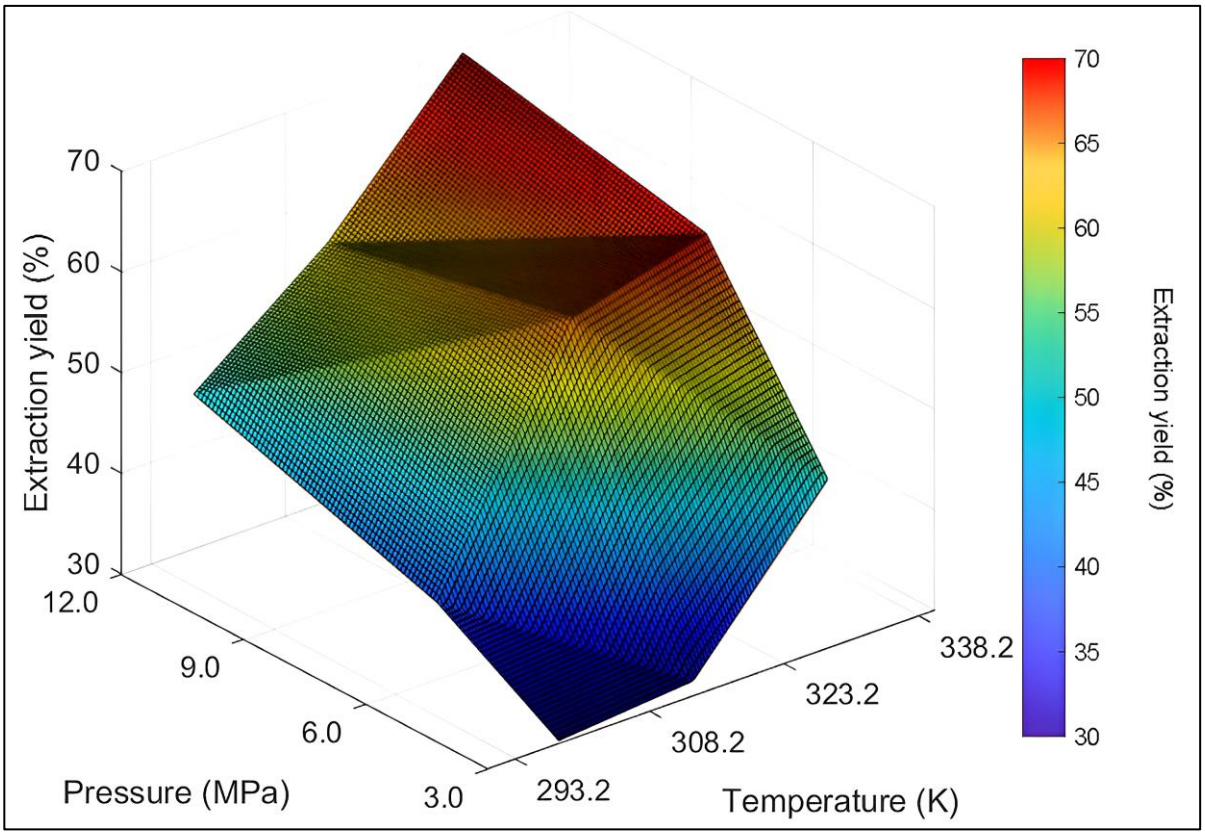

Figure 5-13: Surface response optimisation plot of the extraction of artificial LIB electrolyte (wt.%) as a function of pressure (3.0 - 12.0 MPa) and temperature (298.2 – 328.2 K) (Refer to **Table 5-4** for experimental data points).

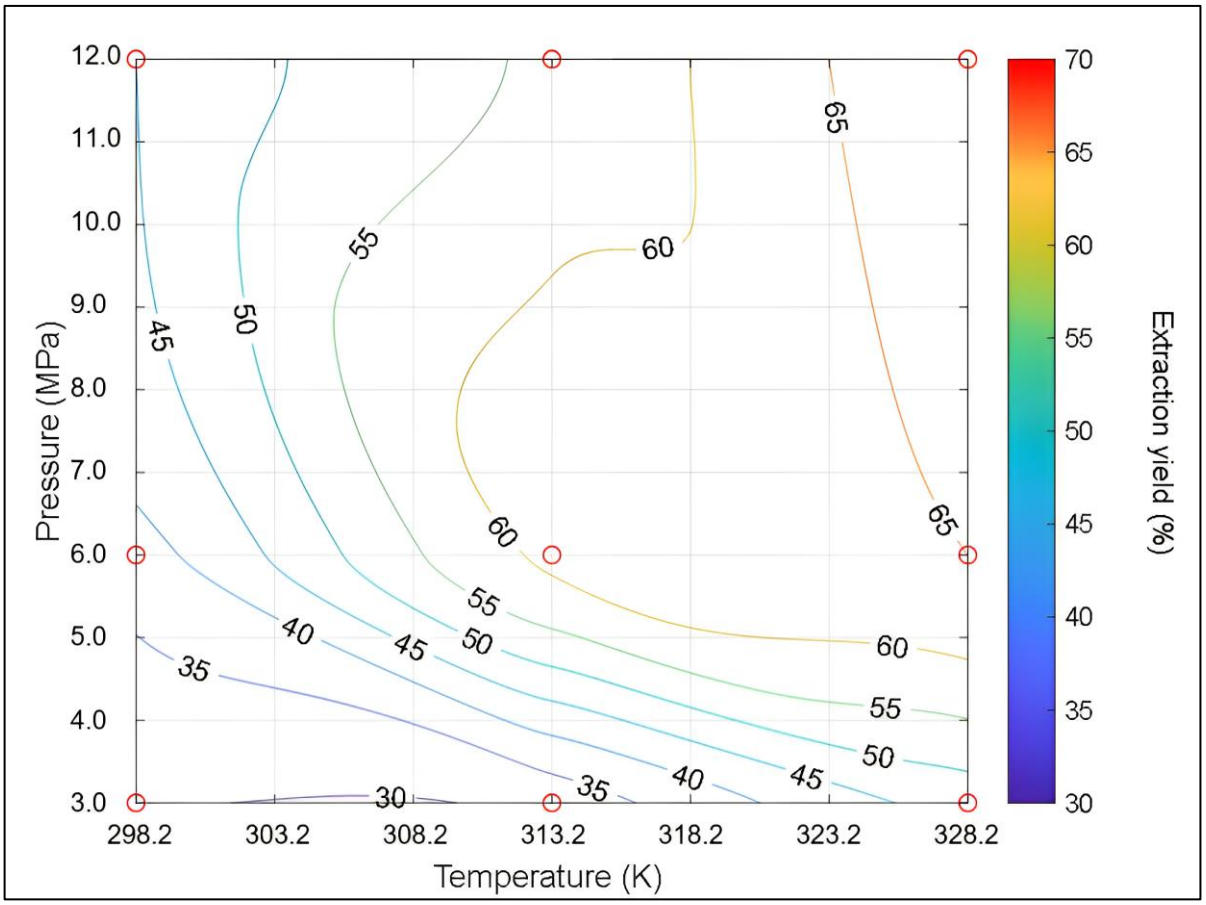

Figure 5-14: Contour plot of the extraction of artificial LIB electrolyte (wt.%) as a function of pressure (3.0 - 12.0 MPa) and temperature (298.2 – 328.2 K).
(Refer to **Table 5-4** for experimental data points).

The influence of the pressure and temperature parameters on the extraction yield of artificial electrolyte is clearly expressed in **Figures 5-13** and **5-14**. The observed trend indicates that as the pressure and temperature of the system increases, so does the extraction yield. The highest extraction yield obtained was 70.2 %, achieved at conditions of 328.2 K and 12.0 MPa.

After examining **Figure 5-13** more closely, a discrepancy in the correlation becomes apparent. Specifically, at 313.2 K and 6.0 MPa, the extraction yield exhibits a peak on the surface response plot that exceeds the correlation forecasted by the quadratic model.

A comparison was made between the experimental and model responses to explore the influence of a response point. At 313.2 K and 6.0 MPa, the percentage deviation averaged 8.5% across five points. Although this deviation was not the largest or the smallest among the response points, being the centre point of the CCD model amplified any deviation significantly. In conclusion, this response point clearly contributes to the observed weakness in the correlation, as previously discussed.

5.6.6 The influence and association of pressure and temperature

The application of pressurised carbon dioxide to extract LIB electrolyte has previously been investigated across a spectrum of parameters and arrangements in several studies [7, 25, 31, 35-40]. This research has integrated the phase equilibria studies with the pressurised carbon dioxide extraction process to understand the extraction behaviour of the artificial LIB electrolyte components. Many extraction parameters have been considered to optimise the solubility. The complexity of the extraction parameters' influence on the recovery yield is evident, notably the temperature and pressure.

The raw experimental data behind the response surface analysis and RSM is summarised in **Table 5-6**; the average mass loss of artificial electrolyte material amounted to 1.53% for the 24 extraction experiments performed. These findings align with the results presented in subsection 5.6.2, which explores the influence of extraction duration and compares extraction yields for individual components under SCF and SBCF conditions.

As observed (in **Table 5-6**), the three highest overall extraction yields occurred at carbon dioxide densities of 130, 149, and 505 g/L, resulting in average extraction yields of 64.8, 61.2, and 69.8 %, respectively.

The extractions conducted carbon dioxide densities of 130 and 149 g/L, were each performed at 6 MPa, under temperatures of 328.2 and 313.2 K, respectively. These conditions exceed the

critical temperature requirement but remain below the critical pressure, placing them in the SBCF condition. Both extraction scenarios demonstrate notable extraction of linear carbonates (DMC and EMC), as illustrated in **Figure 5-15**. However, each struggle to achieve the same level of EC extraction as observed in SCF conditions. The most optimal yield occurred under conditions of 328.2 K and 12 MPa (CO_2 fluid density – 505 g/L). This extraction achieved a balance in capturing both linear carbonates and the EC component.

In a similar extraction process conducted by *Mu et al.* [38], an RSM was performed, and the influential factors were ranked from the most to the least significant. The order attained as follows: pressure, temperature, and extraction time. However, it is important to note that their electrolyte mixture contained an additional electrolyte solvent component, propylene carbonate, a cyclic compound comparable to EC. Additionally, their process was performed between a temperature range of 28 – 36°C.

In contrast to the experimental temperature range of 25 – 55°C explored in this work, the higher adopted temperature range further enhanced the solubilities of both linear carbonates, as elaborated in *Chapter 4*, subsection **4.6.1**. This rise in solubilities is attributed to the increased vapour pressure of pure components and reduction of density in the vapour phase. The highlight of their study focused on the efficiency of SBCF extraction, as opposed to SCF extraction. The authors concluded that the effect polarity plays on the extraction is more significant than the SCF density [38].

Table 5-1: Extraction yield of artificial LIB electrolyte (wt.%) obtained under the parameters of temperature (K) and pressure (MPa).

T (K)	**P (MPa)**	**V (L)**	**ρ_{CO_2} (g/L)**	**e_{inital} (g)**	**e_{final} (g)**	**Extraction yield** (%)	**S (mg/L)**	**Mass recovery**						**Recovery yield** (%)
								DMC (g)	**DMC (%)**	**EMC (g)**	**EMC (%)**	**EC (g)**	**EC (%)**	
298.2	30	149	64.1	1.509	1.036	31.3	3.18	0.185	37.0	0.183	36.5	0.086	17.2	30.1
	30	151	64.1	1.513	1.068	29.4	2.94	0.159	31.8	0.166	33.3	0.116	23.2	29.2
	60	155	191	1.521	0.779	48.8*****	4.78	0.217	43.4	0.246	49.2	0.258	51.6	47.4
	60	153	191	1.516	0.941	37.9	3.76	0.168	33.7	0.226	45.2	0.172	34.5	37.4
	60	151	191	1.529	0.959	37.3	3.77	0.152	30.4	0.207	41.4	0.202	40.4	36.7
	120	166	846	1.528	1.004	34.3*****	3.15	0.133	26.6	0.174	34.8	0.189	37.9	32.5
	120	163	846	1.513	0.816	46.1	4.28	0.221	44.3	0.262	52.3	0.201	40.2	45.2
	120	164	846	1.525	0.845	44.6	4.14	0.191	38.2	0.233	46.6	0.231	46.2	43.0
313.2	30	151	58.9	1.522	1.032	32.2	3.26	0.192	38.5	0.183	36.7	0.092	18.5	30.7
	30	152	58.9	1.522	1.052	30.9	3.10	0.162	32.4	0.156	31.1	0.130	26.1	29.4
	60	154	149	1.516	0.575	62.1	6.10	0.404	80.7	0.386	77.1	0.136	27.2	61.0
	60	156	149	1.523	0.608	60.1	5.86	0.396	79.1	0.386	77.1	0.111	22.2	58.6
	60	152	149	1.512	0.586	61.2	6.08	0.420	84.1	0.410	82.0	0.085	16.9	60.5
	60	153	149	1.502	0.572	61.9	6.07	0.399	79.8	0.386	77.2	0.137	27.5	61.4
	60	152	149	1.526	0.597	60.9	6.12	0.368	73.7	0.351	70.3	0.152	30.4	57.1
	120	164	718	1.520	0.662	56.4	5.24	0.292	58.4	0.326	65.3	0.219	43.9	55.1
	120	160	718	1.539	0.694	54.9	5.28	0.315	62.9	0.301	60.2	0.190	38.1	52.4

328.2	30	147	54.7	1.520	0.644	57.6*****	5.97	0.348	69.6	0.332	66.4	0.176	35.2	56.3
	30	150	54.7	1.520	0.795	47.7	4.84	0.282	56.5	0.262	52.5	0.110	22.0	43.0
	30	149	54.7	1.511	0.817	45.9	4.66	0.314	62.8	0.295	58.9	0.074	14.7	45.2
	60	152	130	1.515	0.521	65.6	6.53	0.454	90.8	0.397	79.4	0.128	25.5	64.6
	60	153	130	1.533	0.554	63.9	6.39	0.418	83.5	0.444	88.8	0.085	17.0	61.7
	120	159	505	1.546	0.460	70.2	6.82	0.406	81.2	0.435	87.0	0.199	39.8	67.3
	120	158	505	1.517	0.466	69.3	6.66	0.400	79.9	0.401	80.2	0.234	46.8	68.2

$n \geq 2$. Standard uncertainties are u(P) = 1000 KPa, u(T) = 0.1 K, u(m) = 0.01 mg. $\dot{Q} = 2.5 \mathrm{L/min}$.
* Deviations in extraction yield of greater than 5% were repeated.

The research findings align with this observation, as **Figure 5-15** depicts. Under SBCF conditions, particularly at 313.2 K at 6.0 MPa, and 328.2 K at 6.0 MPa, the carbon dioxide densities were 149 and 130 g/L, respectively. These fluid densities, though not notably high in comparison to the maximum fluid density explored (846 g/L), exhibited significant extraction yields of the linear carbonates. This emphasises the point that extraction efficiency is not solely determined by the density of carbon dioxide.

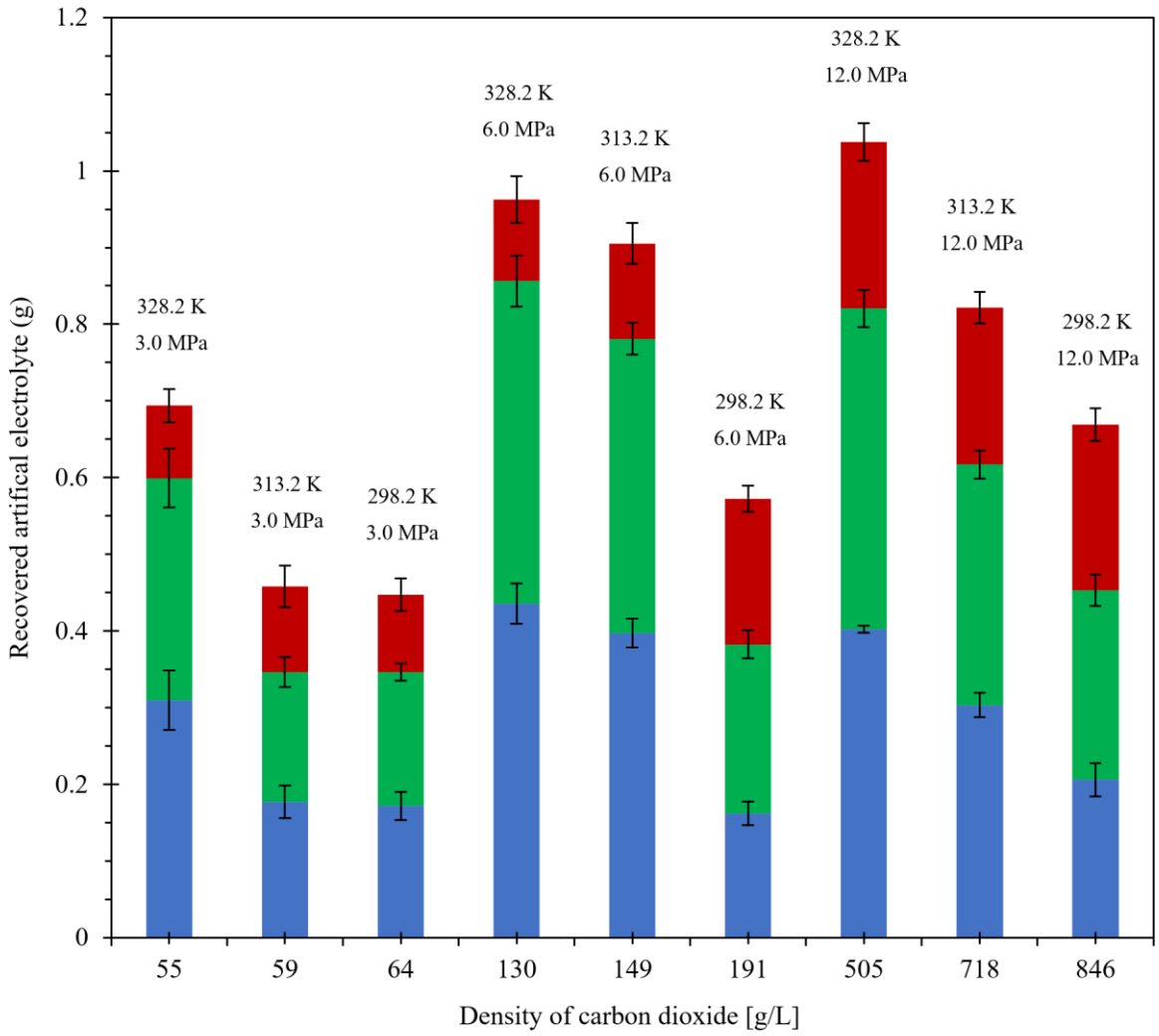

Figure 5-15: Influence of carbon dioxide density on the mass recovery of artificial LIB electrolyte components; DMC, EMC, EC.
(Refer to **Table 5-6** for the experimental data points).

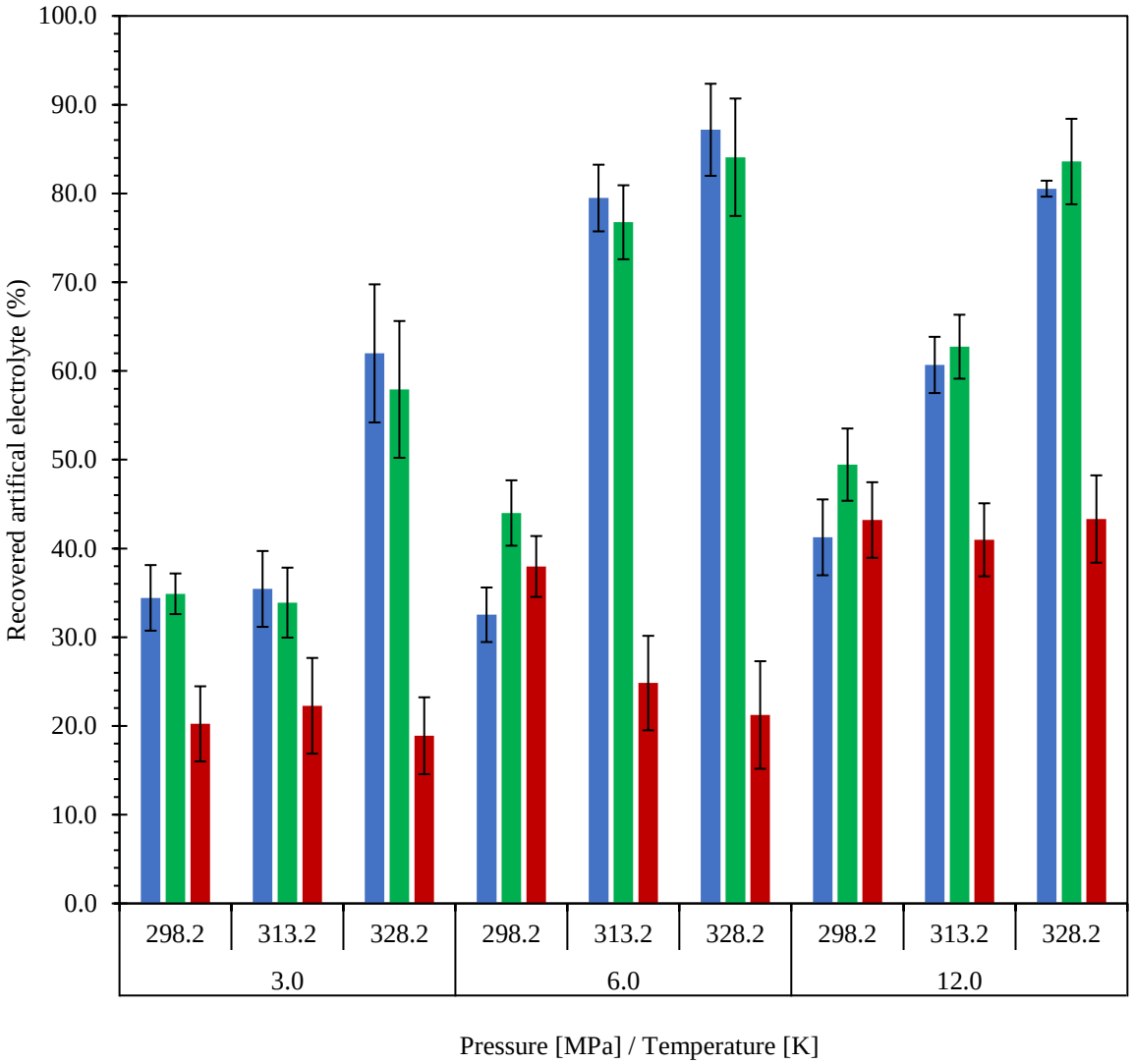

Figure 5-16: Influence of pressure and temperature on the mass recovery of artificial LIB electrolyte components; DMC, EMC, EC.
(Refer to **Table 5-6** for the experimental data points).

The impact of temperature is clearly observed in **Figure 5-16**. While fluid density does not consistently correlate with greater solubility and higher recovery of linear carbonates, the relationship with temperature is notably more evident. Across all pressure conditions, the cumulative recovery of linear carbonates was consistently higher. The most significant change occurred in the extractions conducted at 6 MPa, where the recovery yield of linear components at both 313.2 K and 328.2 K, compared to 298.2 K, is more than two-fold.

This substantial deviation in component recovery yield is primarily attributed to the increased vapour pressure of the linear carbonates. However, although carbon dioxide is considered a non-polar molecule, it has been suggested that alteration of pressure and temperature within scope could marginally influence the polarity of supercritical carbon dioxide. A decrease in pressure and an increase in temperature could potentially reduce the polarity of carbon dioxide molecules, thereby favouring the extraction process [25, 41].

However, the EC component demonstrates a strong correlation with the fluid density of carbon dioxide, as observed in **Figure 5-15**. Both extraction pressure and temperature correlate with fluid density; as pressure increases and temperature decreases, fluid density rises accordingly. The recovered EC component notably correlates with extraction pressure, particularly at densities of 191 g/mL and higher, where the three highest recovery masses of EC were obtained at a pressure of 12 MPa.

This association aligns with the findings from the binary system (CO2 + EC), *Chapter 4*, subsection **4.6.2**, where it was established that density effects enhance the solubility of EC. The relationship is also visibly depicted in **Figure 5-16**, where component recovery on a mass basis is delineated by pressure and temperature. Additional conclusions drawn from the solubility studies indicate that below the vapour mole fraction crossover point (approximately 11 MPa), temperature variation plays a more significant role, whilst above this point, the density effects become predominant. However, this correlation is not distinctly observable. However, the divergence in correlation might be attributed to the inclusion of linear carbonates, which were discovered to act as co-solvents, thereby enhancing the solubility of EC. This phenomenon was observed in *Chapter 4*, subsection **4.6.3**, the quaternary vapour equilibrium system, where EC exhibited a greater solubility under high fluid densities, thus, at high pressure and low temperature conditions, as illustrated in **Figure 4-14**.

5.7 Conclusion

This chapter aimed to investigate the extraction and recovery of artificially prepared LIB electrolyte using pressurised carbon dioxide. An experimental rig was designed and constructed to recover components using a combination of static and dynamic modes. The fundamentals were established, highlighting the pivotal role of solvent flow rate and extraction duration in attaining maximum and efficient recovery.

Several objectives were addressed to deliver the principal aim of the chapter. The central composite design (CCD) effectively optimised the extraction process to identify the most influential factors affecting extraction yield. The extractions were conducted at temperatures of 298.2, 313.2, and 328.2 K, and the system pressure was examined between 3.0-12.0 MPa. Both pressure and temperature were identified as crucial parameters in enhancing extraction conditions, with temperature emerging as the most significant factor. However, the obtained variation in the response ($R^2 = 0.91$) for the response surface methodology (RSM) was lower than anticipated. To improve this, future experiments should encompass a greater number of responses and explore a wider range of pressure conditions.

The remaining objectives were interrelated. Exploring pressure and temperature effects on the extraction was undertaken to understand their influence on overall yield and individual component recovery. Linear carbonates responded effectively to enhancements in temperature across all conducted pressures. SBCF conditions were overall favoured, and the optimal recovery of linear carbonates occurred at a mid-range pressure condition of 6.0 MPa, at 328.2 K. These findings suggest that fluid density is not the sole determinant controlling extraction efficiency.

Conversely, EC demonstrated a strong association with fluid density, as discussed in *Chapter 4*, subsection **4.6.2**. Under SBCF conditions, temperature often exhibited an adverse effect, whereas increased pressure consistently promoted EC recovery in all scenarios.

In conclusion, the optimal extraction yield of artificial LIB electrolyte was 70.2%, attained at a system pressure of 12.0 MPa and a temperature of 328.2 K.

The following chapter will leverage the insights and techniques acquired in the preceding work to investigate the processing and characterisation of commercial-grade LIB battery electrolyte material. This chapter focuses on establishing a standardised protocol for the safe and efficient disassembly of components from a commercial LIB pouch cell. The recovery of the electrolyte component from these materials will be conducted using the pressurised carbon dioxide technique demonstrated in this chapter, and as well as the solvent extraction method, another prominent LIB electrolyte recovery approach.

References – Chapter 5

1. Knez Ž, Markočič E, Leitgeb M, Primožič M, Knez Hrnčič M, Škerget M. Industrial applications of supercritical fluids: A review. *Energy*. 2014; 77: 235-243. doi: 10.1016/j.energy.2014.07.044.

2. Gupta RB, Shim JJ. Solubility in Supercritical Carbon Dioxide. *CRC Press.* 2007. https://books.google.co.uk/books?id=qdXLBQAAQBAJ.

3. Yang Y, Hu B. 21 - Bio-based chemicals from biorefining: lipid and wax conversion and utilization. In: Waldron K, (ed.) *Advances in Biorefineries*. Woodhead Publishing; 2014. p. 693-720.

4. Wei G, Liu Y, Jiao B, Chang N, Wu M, Liu G, et al. Direct recycling of spent Li-ion batteries: Challenges and opportunities toward practical applications. *iScience.* 2023; 26(9): 107676. doi: https://doi.org/10.1016/j.isci.2023.107676.

5. Sattar A, Greenwood D, Dowson M, Unadkat P. *Automotive Lithium ion Battery Recycling in the UK*. International Manufacturing Centre (WMG). 2020.

6. Neumann J, Petranikova M, Meeus M, Gamarra JD, Younesi R, Winter M, et al. Recycling of Lithium-Ion Batteries—Current State of the Art, Circular Economy, and Next Generation Recycling. *Advanced Energy Materials.* 2022; 12(17): 2102917. doi: https://doi.org/10.1002/aenm.202102917.

7. Liu Y, Mu D, Li R, Ma Q, Zheng R, Dai C. Purification and Characterization of Reclaimed Electrolytes from Spent Lithium-Ion Batteries. *The Journal of Physical Chemistry C.* 2017; 121(8): 4181-4187. doi: 10.1021/acs.jpcc.6b12970.

8. Michael Schmidt RPH, Margret Wohlfahrt-Mehrens, Christian Vogler, Giesela Arnold. *Process for Recycling Negative-Electrode Materials from Spent Lithium Batteries.* 09/584,059;6,511,639 ,2003.

9. Ghosh R. *Principles Of Bioseparations Engineering.* World Scientific Publishing Company; 2006.

10. Sapkale G, Patil SM, Surwase US, Bhatbhage PK. Supercritical Fluid Extraction. 2010.

11. Ma J. *Battery Technologies: Materials and Components.* Weinheim: Wiley-VCH; 2021.

12. Gao M, Wang L, Chen X, Wei X, Liang J, Li L. Joule-Thomson Effect on a CCS-Relevant (CO(2) + N(2)) System. *ACS Omega.* 2021; 6(14): 9857-9867. doi: 10.1021/acsomega.1c00554.

13. Linstrom PJ, Mallard WG. The NIST Chemistry WebBook: A Chemical Data Resource on the Internet. *Journal of Chemical and Engineering Data.* 2001; 46(5): 1059-1063. doi: 10.1021/je000236i.

14. Westwood SA. *Supercritical Fluid Extraction and its Use in Chromatographic Sample Preparation.* Springer Netherlands; 2012.

15. Dutta SK. *Metallurgical Thermodynamics Kinetics and Numericals.* New Delhi: S Chand & Co Ltd; 2012

16. Iwase M. Chapter 3.1 - First, Second, and Third Laws of Thermochemistry. In: Seetharaman S, (ed.) *Treatise on Process Metallurgy*. Boston: Elsevier; 2014. p. 399-493.

17. Telford JK. A brief introduction to design of experiments. *Johns Hopkins APL Technical Digest.* 2007; 27(3): 224-232.

18. Savic I, Gajic D, Stojiljkovic S, Savic I, Gennaro Sd. Modelling and Optimization of Methylene Blue Adsorption from Aqueous Solution Using Bentonite Clay. In: Klemeš JJ, Varbanov PS, Liew PY, (eds.) *Computer Aided Chemical Engineering*. 33. Elsevier; 2014. p. 1417-1422.

19. Box GEP, Wilson KB. On the Experimental Attainment of Optimum Conditions. *Journal of the Royal Statistical Society: Series B (Methodological).* 1951; 13(1): 1-38. doi: https://doi.org/10.1111/j.2517-6161.1951.tb00067.x.

20. Myers RH, Khuri AI, Carter WH. Response Surface Methodology: 1966-1988. *Technometrics.* 1989; 31(2): 137-157. doi: 10.2307/1268813.

21. Myers RH, Montgomery DC, Anderson-Cook CM. *Response Surface Methodology: Process and Product Optimization Using Designed Experiments.* Wiley; 2016.

22. Bradley N. *The Response Surface Methodology*. Indiana University 2007.

23. Manan ZA, Zahedi G, Mustapa AN. *Modeling, Simulation, and Optimization of Supercritical and Subcritical Fluid Extraction Processes.* Wiley; 2021.

24. Bahadar A, Khan MB, Asim MA, Jalwana K. Chapter 21 - Supercritical Fluid Extraction of Microalgae (Chlorella vulagaris) Biomass. In: Kim S-K, (ed.) *Handbook of Marine Microalgae*. Boston: Academic Press; 2015. p. 317-330.

25. Yuanlong Liu DM, Yunkun Dai, Quanxin Ma, Rujuan Zheng, Changsong Dai. Analysis on Extraction Behaviour of Lithium-ion Battery Electrolyte Solvents in Supercritical CO2 by Gas Chromatography. *International Journal of Electrochemical Science.* 2016: 7594-7604. doi: 10.20964/2016.09.03.

26. Kumoro AC, Hasan M. Supercritical Carbon Dioxide Extraction of Andrographolide from Andrographis paniculata: Effect of the Solvent Flow Rate, Pressure, and Temperature. *Chinese Journal of Chemical Engineering.* 2007; 15(6): 877-883. doi: https://doi.org/10.1016/S1004-9541(08)60018-X.

27. Idham Z, Zaini AS, Putra NR, Rusli NM, Mahat NS, Yian LN, et al. Effect of flow rate, particle size and modifier ratio on the supercritical fluid extraction of

anthocyanins from Hibiscus sabdariffa (L). *IOP Conference Series: Materials Science and Engineering.* 2020; 932(1): 012031. doi: 10.1088/1757-899X/932/1/012031.

28. Farías-Campomanes AM, Rostagno MA, Coaquira-Quispe JJ, Meireles MAA. Supercritical fluid extraction of polyphenols from lees: overall extraction curve, kinetic data and composition of the extracts. *Bioresources and Bioprocessing.* 2015; 2(1): 45. doi: 10.1186/s40643-015-0073-5.

29. Uwineza PA, Waśkiewicz A. Recent Advances in Supercritical Fluid Extraction of Natural Bioactive Compounds from Natural Plant Materials. *Molecules.* 2020; 25(17). doi: 10.3390/molecules25173847.

30. Cavalcanti RN, Meireles MAA. 2.07 - Fundamentals of Supercritical Fluid Extraction. In: Pawliszyn J, (ed.) *Comprehensive Sampling and Sample Preparation*. Oxford: Academic Press; 2012. p. 117-133.

31. Grützke M, Mönnighoff X, Horsthemke F, Kraft V, Winter M, Nowak S. Extraction of lithium-ion battery electrolytes with liquid and supercritical carbon dioxide and additional solvents. *RSC Advances.* 2015; 5(54): 43209-43217. doi: 10.1039/c5ra04451k.

32. Jumbri K, Al-Haniff Rozy MF, Ashari SE, Mohamad R, Basri M, Fard Masoumi HR. Optimisation and Characterisation of Lipase-Catalysed Synthesis of a Kojic Monooleate Ester in a Solvent-Free System by Response Surface Methodology. *PloS One.* 2015; 10(12): e0144664. doi: 10.1371/journal.pone.0144664.

33. Hamzaoui AH, Jamoussi BMN, Adel. Lithium recovery from highly concentrated solutions: Response surface methodology (RSM) process parameters optimization. *Hydrometallurgy.* 2008; 90(1): 1-7. doi: https://doi.org/10.1016/j.hydromet.2007.09.005.

34. Che Sulaiman IS, Basri M, Fard Masoumi HR, Chee WJ, Ashari SE, Ismail M. Effects of temperature, time, and solvent ratio on the extraction of phenolic compounds and the anti-radical activity of Clinacanthus nutans Lindau leaves by response surface methodology. *Chemistry Central Journal.* 2017; 11(1): 54. doi: 10.1186/s13065-017-0285-1.

35. Nowak S, Winter M. The Role of Sub- and Supercritical CO2 as "Processing Solvent" for the Recycling and Sample Preparation of Lithium Ion Battery Electrolytes. *Molecules.* 2017; 22(3): 2-6. doi: 10.3390/molecules22030403.

36. Mönnighoff X, Friesen A, Konersmann B, Horsthemke F, Grützke M, Winter M, et al. Supercritical carbon dioxide extraction of electrolyte from spent lithium ion batteries and its characterization by gas chromatography with chemical ionization. *Journal of Power Sources.* 2017; 352: 56-63. doi: 10.1016/j.jpowsour.2017.03.114.

37. Liu Y, Mu D, Zheng R, Dai C. Supercritical CO2 extraction of organic carbonate-based electrolytes of lithium-ion batteries. *RSC Advances.* 2014; 4(97): 54525-54531. doi: https://doi.org/10.1039/C4RA10530C.

38. Mu D, Liu Y, Li R, Ma Q, Dai C. Transcritical CO2 extraction of electrolytes for lithium-ion batteries: optimization of the recycling process and quality–quantity variation. *New Journal of Chemistry.* 2017; 41(15): 7177-7185. doi: 10.1039/c7nj00771j.

39. Grützke M, Kraft V, Weber W, Wendt C, Friesen A, Klamor S, et al. Supercritical carbon dioxide extraction of lithium-ion battery electrolytes. *The Journal of Supercritical Fluids.* 2014; 94: 216-222. doi: 10.1016/j.supflu.2014.07.014.

40. Sloop S, Crandon L, Allen M, Koetje K, Reed L, Gaines L, et al. A direct recycling case study from a lithium-ion battery recall. *Sustainable Materials and Technologies.* 2020; 25. doi: 10.1016/j.susmat.2020.e00152.

41. Yutaka I, Norio S, Masahiko A, Kunio A. Solvent Polarity Parameters of Supercritical Carbon Dioxide as Measured by Infrared Spectroscopy. *Bulletin of the Chemical Society of Japan.* 1991; 64(7): 2224-2229. doi: 10.1246/bcsj.64.2224.

Chapter 6: Recovery and Characterisation of LIB Electrolyte from Electric Vehicles

6.1 Introduction

The soaring demand for LIBs used in EVs translates into a considerable mountain of LIB waste. According to projections published by *McKinsey and Co*., more than 100 million EV batteries are expected to be retired globally in the next decade [1]. Current recycling processes are specifically tailored to recover and reprocess high-value LIB components, including Ni, Co, and Li, as well as less economically critical elements such as Al, Fe, Cu, and C [2, 3].

To promote recycling rates, governments and global organisations have intensified pressure on LIB manufacturers and recyclers by implementing directives and legislation. These initiatives aim to facilitate the transition from internal combustion engine (ICE) vehicles to EVs, thereby curbing emissions [4, 5].

The retrieval of LIB electrolytes has become an increasingly pertinent sustainability concern. However, a critical challenge for LIB recyclers is the lack of standardisation in the electrolyte composition. The diversity in electrolyte solvents and conducting salts poses a considerable obstacle to developing a universal applicable separation and refinement process [6, 7].

While previous experimental chapters primarily focused on the solvent component of LIB electrolytes, the presence of lithium conducting salt within the organic solvent mixture has added complexity to recovery efforts. This addition further complicates the recovery process. Coupled with a highly volatile nature and the ageing components in end-of-life (EOL) cells, the electrolyte component is susceptible to degradation mechanisms under certain conditions, resulting in the formation of hazardous components that contribute to environmental pollution and pose health risks [8].

This chapter will build upon the advancements and insights derived from *Chapter 5: Extraction of Artificial LIB Electrolyte Using Pressurised Carbon Dioxide*. Investigating the recovery and characterisation of commercial EV LIB pouch cell electrolyte and shedding light on the degradation components associated with EOL electrolytes.

The chapter is structured as follows: first, the *Aims and Objectives* are defined in Section **6.2**, the *Methodology* of the experimental practice is outlined in Section **6.3**, the *EV LIB Pouch Cell* processing and characterisation is outlined in Section **6.4**, the experimental *Results and Discussion* are presented in Section **6.5**, and finally, the chapter is closed with a *Conclusion* in Section **6.6**.

6.2 Objectives

This chapter encompassed two primary objectives. Firstly, it aimed to establish a standard protocol for efficiently dissembling a commercial EV LIB pouch cell. This protocol is designed to reduce the effects of solvent vaporisation and enhance the recovery yield while ensuring a safe working procedure by minimising the risks associated with the LIB pouch cell and disassembly process.

The second objective was to utilise the optimal conditions obtained from *Chapter 5*, which involved employing supercritical carbon dioxide to recover the electrolyte component from materials obtained after dismantling the LIB pouch cell. Furthermore, this chapter compares the supercritical fluid extraction (SFE) technique against solvent extraction, another prevalent method for recovering LIB electrolytes.

6.3 Methodology

6.3.1 Rig design

The principal experimental apparatus employed in this study has previously been detailed and depicted in *Chapter 4: Solubility Measurements of LIB Electrolyte Components in Carbon Dioxide*, sub-section **4.3**. However, for this research, the sampling loop utilised for the solubility studies was disconnected from the high-pressure vessel (HPV), and the rig was reconfigured to enable static and dynamic operations. For reference, a P&ID of the rig has been presented in **Figure 6-1**.

Several notable modifications were introduced in the rig's operation compared to the procedure detailed in *Chapter 4*. Firstly, a minor pressure vessel (MPV) was incorporated into the experimental practice. This MPV facilitated the separation of organic electrolyte components from carbon dioxide. The substantial pressure reduction from the HPV to the MPV decreased the solvation strength of carbon dioxide, trapping the liquid components inside the MPV whilst allowing the gaseous effluent to escape. Precise flow control in the MPV was regulated to maintain a pressure of 0.5 MPa using the micro-metering valve (V9) and back pressure regulator (BPR-02).

Another adaptation involved the inclusion of steel mesh filters at the HPV's base (illustrated in **Figure 6-2**) and its outlet. These filters were employed to capture solid particulates larger than 0.2 mm. Given that the anode sheets are composed of a graphite powder coating, they are susceptible to disintegration under stress. Hence, the filters were essential to prevent blockages in the tubing and valves.

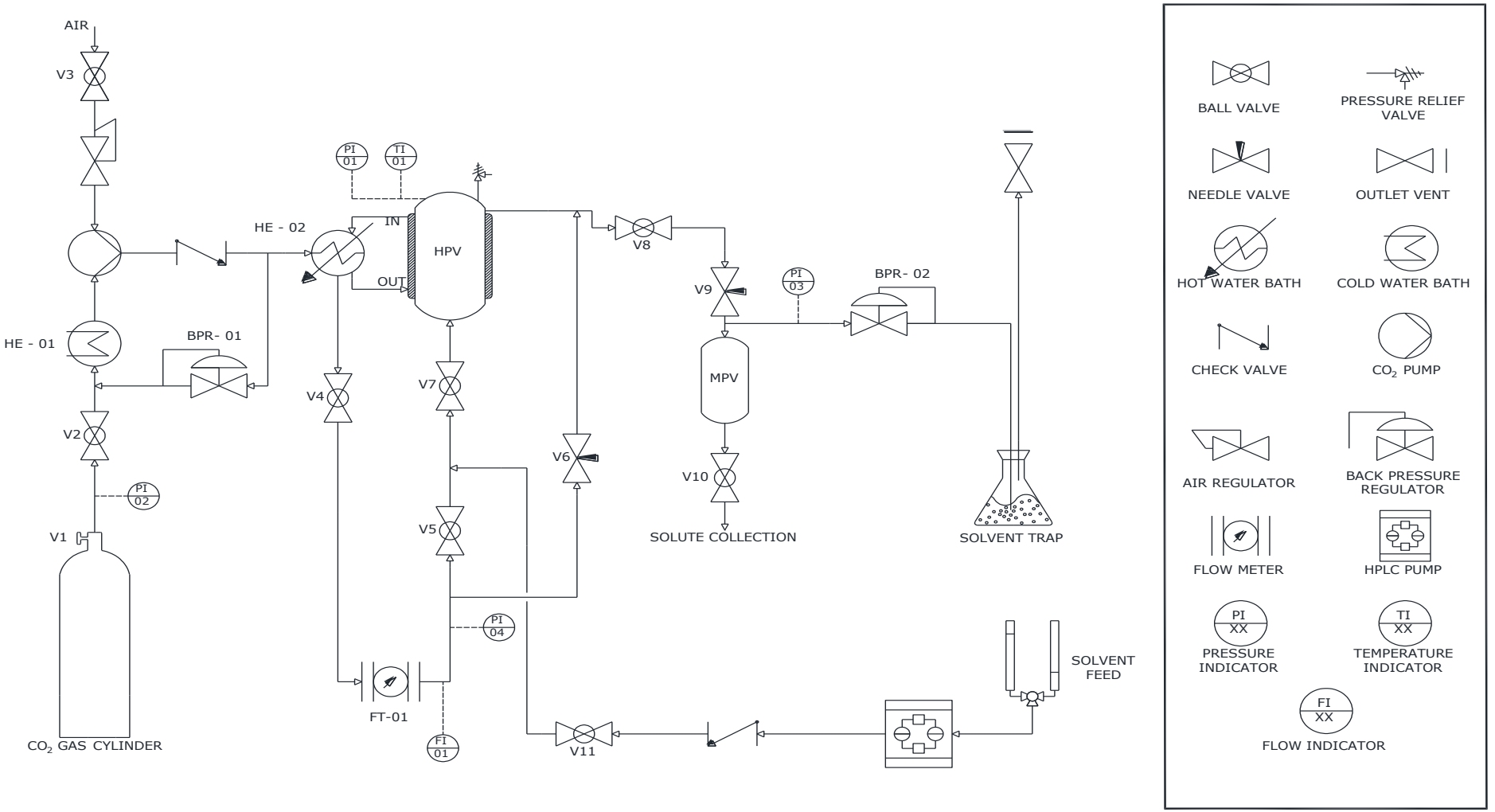

Figure 6-1: Schematic diagram of extraction experimental apparatus.

The final adjustment to the rig involved installing a solvent trap to separate the effluent from the extraction process before its discharge via the external vent. This addition was required due to the instability of the lithium conducting salt in the LIB electrolyte. When exposed to moisture, this salt is prone to react, initiating a degradation mechanism that yields hydrogen fluoride as one of its byproducts.

Figure 6-2: Photograph of HPV internal body, with steel mesh filter resting on base.

Hydrogen fluoride is well-recognised for its toxic and corrosive nature. Its colourless property poses a considerable challenge for gas detection [9]. Upon contact with water, it readily dissolves forming hydrofluoric acid, recognised for its high reactivity and its capability to react with a wide range of materials, including, glass, metals, concrete, and numerous organic solvents. To inhibit its effects, the hydrogen fluoride was neutralised and diluted in an aqueous solution of sodium carbonate to a concentration of less than 1%. The resulting acidic solution was then stored in a cool, dry, well-ventilated area and disposed of as per the guidelines on hazardous waste [9]. Stoichiometry calculations regarding the generation of hydrogen fluoride from the conducting salt and the subsequent neutralisation reaction have been outlined in *EV LIB Pouch Cell*, **6.4.4**.

6.3.2 Method

6.3.2.1 Supercritical carbon dioxide extraction

The SFE process using carbon dioxide involves several notable steps. Details of the *Rig preparation* and *System pressurisation* remain consistent with the method outlined in *Chapter 4*; for further insights, refer to subsection **4.3.2**.

Sheets of anode and separator material removed from the EV LIB pouch cell served as the source of electrolyte extraction. Each component was stored in a refrigerator at a temperature between 2-5°C to minimise vaporisation losses. Before the extraction process, each material was promptly weighed, tightly rolled up and placed in the HPV.

The operational conditions of the process reflected the optimal conditions obtained from *Chapter 5*, a system pressure of 12.0 MPa and a temperature of 328.2 K was adopted. The extraction process comprised three 15-minute static extraction phases, during which the HPV was isolated by closing the valves (V6, V7, and V8) connected directly to the vessel. This allowed the electrolyte trapped in the depths of the anode and separator material to diffuse more effectively.

Additionally, between the static phases, two dynamic extractions were performed. These involved sweeping the HPV with carbon dioxide at a dynamic flowrate of 6 g/min for a total of 60 minutes. This duration was determined based on the flow rate optimisations conducted in *Chapter 5*. The dynamic flowrate was fine-tuned using a Hoke micro-metering valve (1315G2Y) (V9), connected to both an isolation ball valve (V8) and the MPV. As the multicomponent flow passed through the MPV, the electrolyte components were separated and removed after each dynamic extraction phase. This step prevented product loss due to mass transfer effects and ensured a higher yield.

Post-experiment, the mixture was diluted in acetone, and the sample was quantified against an internal standard of nonane using GC-TCD.

6.3.2.2 Solvent extraction

The solvent extraction process was chosen to compare with the SFE technique. Acetone was selected as the extraction solvent because it is non-toxic and versatile. The dipole moment of acetone is 2.8 D, which is situated between the linear and cyclic electrolyte components, enabling it to dissolve both polar and non-polar components due to its chemical structure [10]. Moreover, its high volatility ensures an efficient separation between the solutes and the solvent [11].

The acetone was introduced into the system using an HPLC pump (Cole-Parmer, Series III), entering the rig before the ball valve (V7) and directly into the base of the HPV. The operational conditions of the extraction process incorporated an HPV temperature of 323.2 K. The process temperature was selected to increase the solubility of components in acetone, as it is well known that solubility generally increases with temperature. This observation has been exhibited in various solvent extraction processes incorporating acetone [12-14]. However, the temperature had to be regulated to prevent the vaporisation of acetone (BP – 329.45 K) [15] and to avert the degradation of the lithium conducting salt, which has been reported to occur at temperatures as low as 360 K in the presence of moisture [16]. For this reason, an analytical grade of acetone (≥99.8%) was used to limit the moisture introduced into the system.

The solvent flow was maintained at a constant flowrate of 6.5 mL/min for 165 minutes. Considering the nominal volume of the HPV is 500 mL, these operational parameters facilitated two complete wash cycles of the sample matrix based on the residence time of the process.

In contrast to the SFE process, the solvent and solute mixture accumulated in the MPV and were collected in a 1.5 L glass bottle via the ball valve (V10). An excess of boric acid (10 g) was added to the collection bottle pre-experiment to prevent the potential formation of an acidic solution and to neutralise the solution if required. The solution was then decanted into a 100 mL glass bottle and stored in the refrigerator. The quantification of the electrolyte solution was performed against an internal standard of nonane using GC-TCD.

6.4 EV LIB Pouch Cell

6.4.1 LIB pouch cell specification

In this section, the disassembly and analysis of Nissan Leaf Generation 1 pouch cells will be discussed. The new, unused pouch cells were acquired from the Faraday Institution through the Recycling of Lithium-Ion Batteries (ReLiB) project. **Table 6-1** highlights the specifications of the pouch cell.

Table 6-1: Nissan Leaf (gen 1) LIB pouch cell specification [17, 18].

Weight (g)	792.4
External dimensions L × W × H (mm)	256 x 215 x 7.1
Structure	Laminate type
Cell case material	Pouch – Aluminium
Cathode material	LMO ($LiMn_2O_4$) / NCA ($LiNiCoAlO_2$)
Cathode current collector material	Aluminium
Anode material	Graphite
Anode current collector material	Copper
Separator material	polypropylene

It is pertinent to note that the pouch cells (photograph displayed in **Figure 6-3**) were quality control rejected (QCR) as part of the manufacturer's quality control (QC) procedures. These cells were never integrated into a battery module and were supplied as individual cells discharged to 0 V [18].

6.4.2 LIB Pouch Cell disassembly

For the disassembly of the LIB pouch cell, a standard operating procedure (SOP) was followed. Comprehensive details regarding the disassembly procedure, associated risks, and mitigation are outlined below.

At the start of the disassembly process, the voltage of the LIB pouch cell was measured using a digital multimeter. This involved placing each probe against the two foil tabs located at the top end of the cell, as shown in **Figure 6-3**. This measurement aimed to ensure that the cell voltage was at 0 V before proceeding with the disassembly process. If the voltage measured were greater than 0 V, it would indicate the presence of residual charge within the cell, and therefore, for reasons of safety, no further processing would be taken.

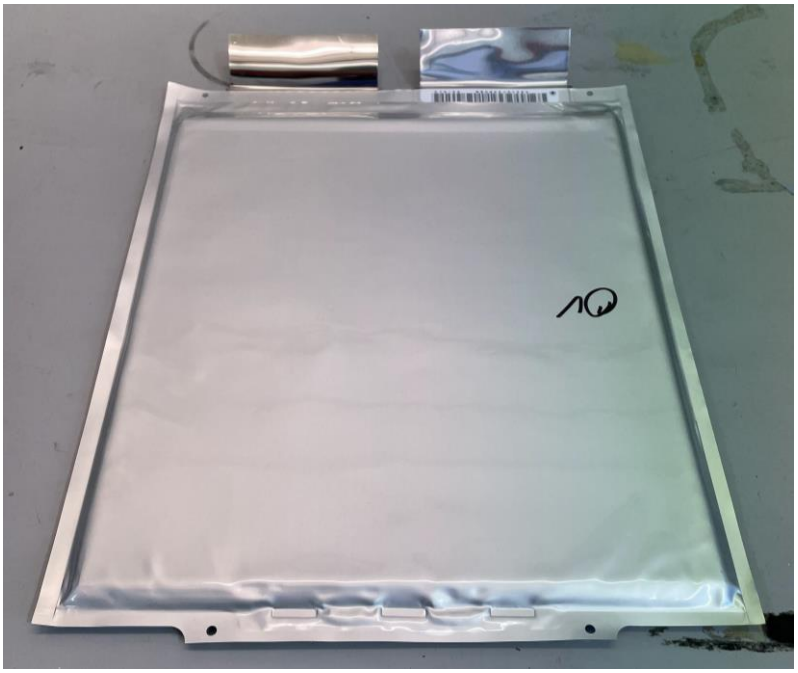

Figure 6-3: Photograph of Nissan Leaf (gen 1) EV LIB pouch cell.

The state of charge (SOC) and heat release rate (HRR) demonstrate a correlation. HRR refers to the rate at which energy is released during combustion. *Ribière et al.* conducted combustion tests on commercial LIB pouch cells and observed that cells with higher SOC exhibited a proportionally greater HRR. Elevated HRR levels can prompt an exothermic reaction leading to thermal runaway, posing a risk of fire and explosion [19].

Therefore, this disassembly process was conducted in a ducted fume cupboard to minimise the concentration of flammable carbonates in an enclosed space. The cell was placed on absorbent material, and an incision was carefully made 10 mm from the edge of the aluminium casing within an air pocket situated between the electrode stack and the pouch case. This incision was made using a pair of ceramic scissors and a scalpel. These non-conductive instruments were employed during the disassembly, as penetration of a cell with electrically conductive materials could induce an internal short circuit in the cell due to residual charge [20].

After cutting the three sides of the outer casing, it was pulled back, revealing the electrode stack and free liquid electrolyte. The electrode stack was then disconnected from the tabs and carefully separated layer by layer using plastic tweezers; the LIB components were then placed into three storage containers designated for the anode, cathode, and separator sheets. This meticulous separation method minimised the possibility of cross contamination between materials. Any excess electrolyte liquid on the electrodes' surface was drained, bottled, and stored. The complete disassembly of the LIB pouch cell and the containment of all materials took approximately 30 minutes to perform.

Further details regarding the storage of all LIB components are specified in *Chapter 3 – Materials and Analytical Techniques, Chemical Storage and Disposal,* **3.3**.

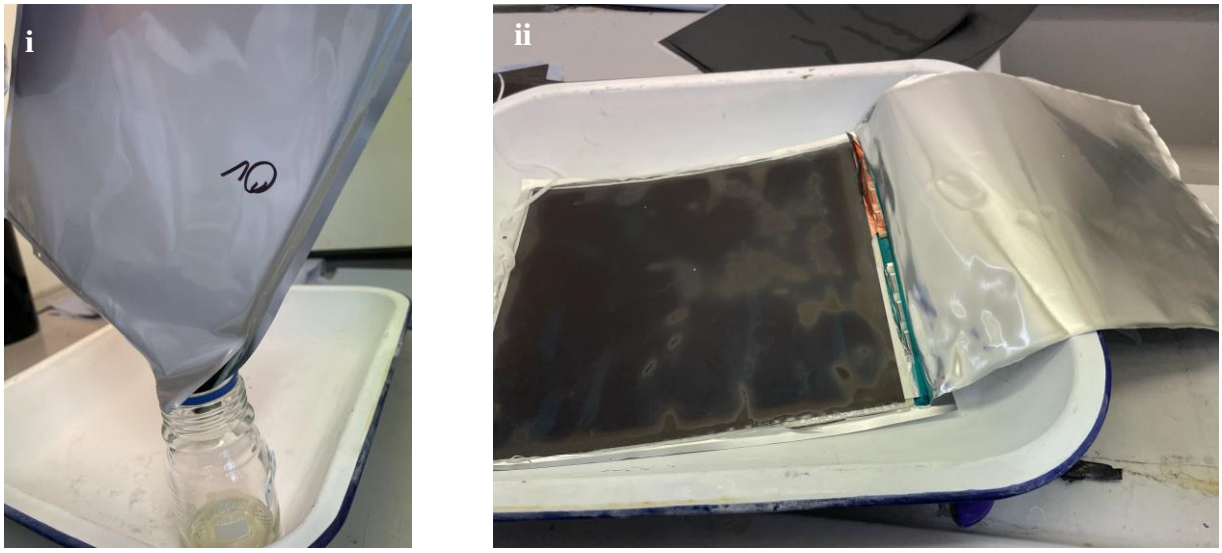

Figure 6-4: Photographs to depict the disassembly of a Nissan Leaf (gen 1) EV LIB pouch cell; i) Collection of liquid electrolyte components, ii) retraction of the aluminium casing, exposing the internal components.

6.4.3 LIB pouch cell mass breakdown

The quantification of the internal components from the disassembled LIB pouch cell was performed using a gravimetric approach. Each component was segregated, bottled, and weighed, serving as a critical step in assessing the mass breakdown of the individual components per cell. Furthermore, this method facilitated the quantification of the associated electrolyte content in each component. These initial measurements subsequently enabled the calculation of the recovery yield for each component subjected to the extraction processes.

A total of three pouch cells were dissembled and processed; each was assigned a unique reference code to ensure the traceability of the materials across the characterisation and quantification techniques employed. **Table 6-2** presents the mass breakdown of the LIB pouch cells according to their respective components.

Table 6-2: Mass breakdown of dissembled Nissan Leaf (gen 1) QCR pouch cell by components.

Reference code	m_{total}	$m_{cathode}$	m_{anode}	$m_{separator}$	$m_{electrolyte}$	m_{casing}	$m_{unrecovered}$
PC 0203	792.4	412.2	255.5	44.3	7.4	38.4	34.6
PC 2604	792.0	412.9	257.5	42.9	8.3	38.0	32.4
PC 1406	793.2	410.4	258.7	47.6	6.3	39.9	30.3

m_i denotes the mass of each component, measured in g. Standard uncertainty, u(m) = 0.01 g.

Where, m_{total} represents the total weight of the pouch cell before the disassembly, $m_{electrolyte}$ is the electrolyte in its free liquid form captured on the surface of the electrode stack, and $m_{unrecovered}$ represents the losses due to electrolyte vaporisation.

It is important to note that the electrodes and separator components are 'wetted', meaning that their overall mass, as presented in **Table 6-2**, includes a fraction of the electrolyte. Consequentially, these recorded values do not solely denote the pure form of these components. During the disassembly process, not all material could be preserved; some material was lost due to the volatility of the electrolytes. When the aluminium casing was cut open, exposing the internal components, a significant amount of electrolyte evaporated. This was particularly noticeable during the separation of the electrode sheets, as illustrated in **Figure 6-4 (ii)**, by noticeable differences in contrast and dark shades on the material, indicating varying degrees of wetness.

Furthermore, the anode and cathode sheets were fragile, especially when dry, making them susceptible to breakage and shedding of their powder coating during separation. However, this represented an exceedingly small mass fraction and was considered negligible. The estimated mass loss due to electrolyte vaporisation during the tear downs was between 3-5% of the total weight of the LIB pouch cells. This estimation is consistent with previous research on the evaporation losses of the electrolyte component during the pouch cell disassembly. MEng students at the University of Birmingham conducted a study to measure the cumulative mass loss of one sheet of anode and cathode material once separated from the electrode stack. The evaporation mass loss of the electrolyte component was plotted as a function of time, as shown in **Figure 6-5**.

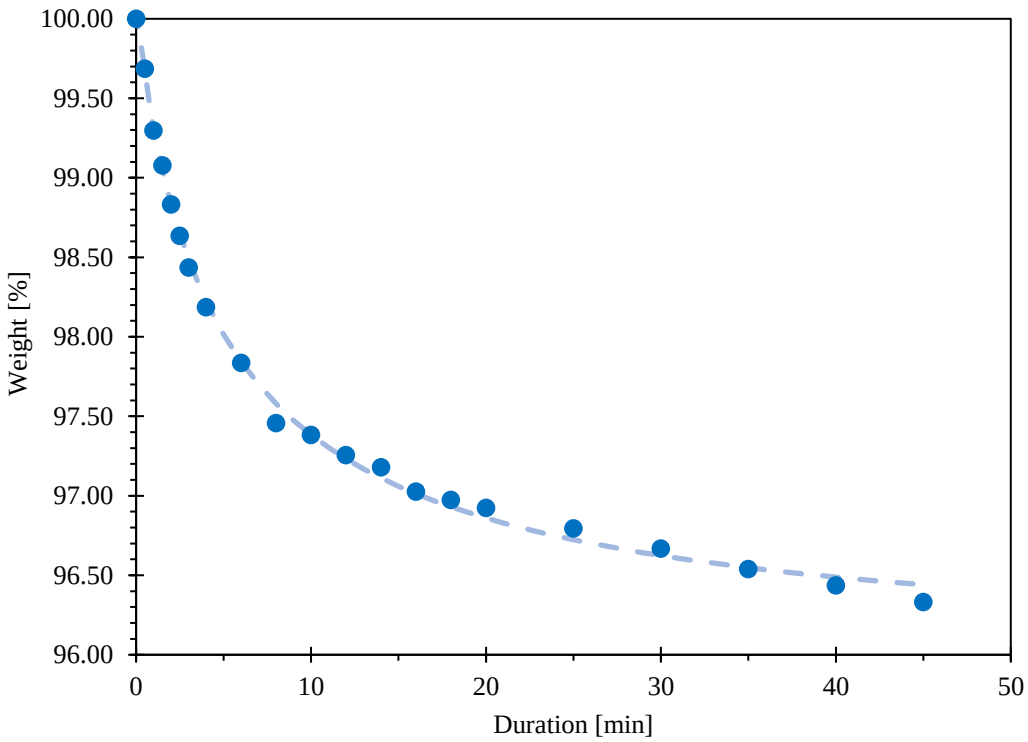

Figure 6-5:Evapouration mass loss of electrode material.

Each cathode and anode components are coated onto a current collector, typically an aluminium and copper foil, respectively. In this study, the weight of each electrode includes the mass of its respective current collector.

Magnified images of the dry anode sheet (as presented in **Figure 6-6**) were captured using a digital light microscope (Keyence, model: VHX 7000N) under partial lighting with magnifications ranging between x100-6000. The author wishes to acknowledge Miss Meera K. Jethwa for her support and contribution with the microscopy photographs.

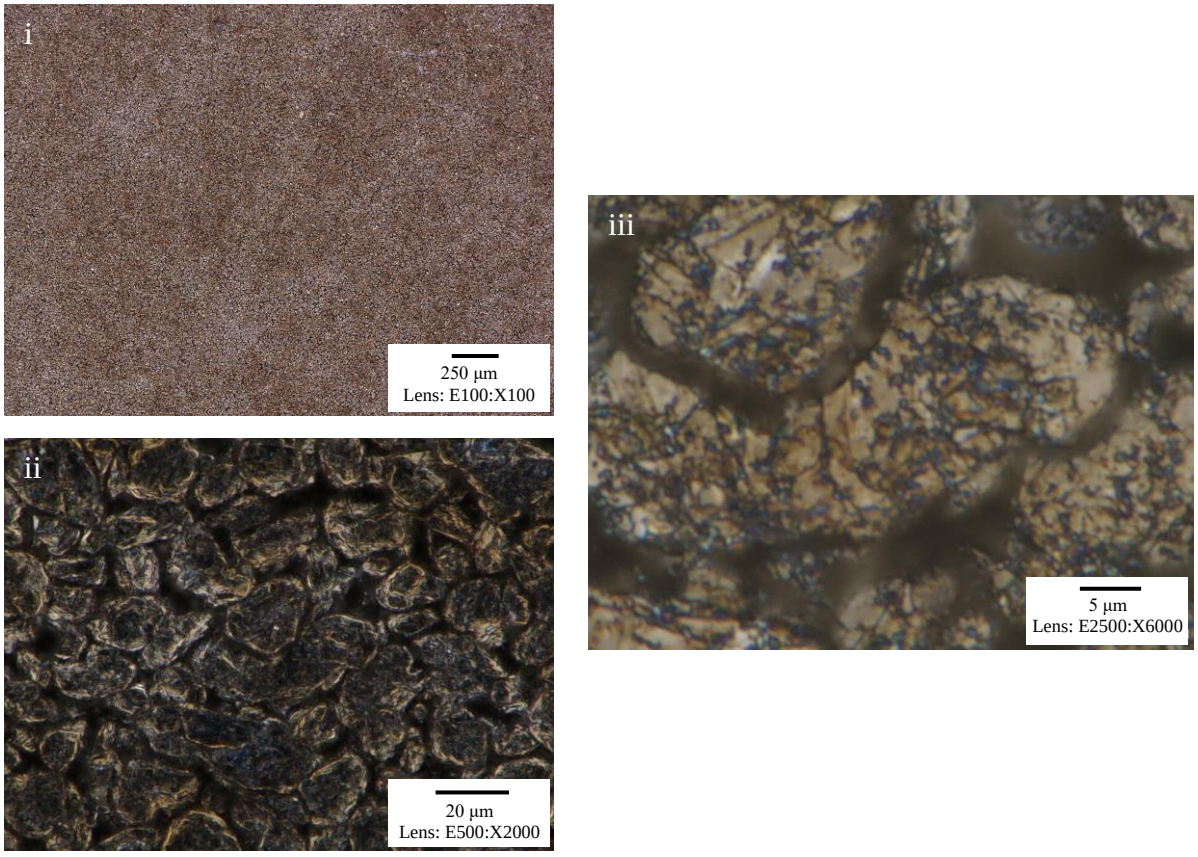

Figure 6-6: Digital microscopy photographs of the Nissan Leaf (gen 1) EV LIB pouch cell anode sheet material.

As the magnification of the solvent-free anode sheet is increased, from x100 up to x6000, as shown in **Figure 6-6**, the PTFE binder becomes evident. Fine net-like fibres can distinctly be observed, wrapping around the graphite particles. This configuration effectively holds the particles together, forming a robust network. Similar observations have been reported in various other studies related to electrode fabrication [21, 22].

6.4.4 LIB pouch cell electrolyte

Details of the mass and composition of the electrolyte used in the Nissan Leaf pouch cells were unavailable from the manufacturer. Therefore, quantification was necessary before processing the material. This step was essential for evaluating the efficacy of each extraction process and calculating the recovery yield of electrolyte per component.

6.4.4.1 Solvent quantification

Notably, only a small fraction of the electrolyte component exists in a free liquid form, as depicted in **Table 6-2**. The surface morphology of the anode and separator components was assessed using scanning electron microscopy (SEM), as presented in **Figure 6-7**. Before the analysis, each component underwent a washing process with isopropyl alcohol (IPA) and was then thoroughly dried in a ducted fume hood for at least 12 hours.

Both the anode and separator have a large surface area due to their relatively porous structure, with the separator exhibiting a particularly noticeable porousness. As a result, a significant amount of the electrolyte becomes trapped within the pores and in the subsurface of the electrode and separator materials [23, 24].

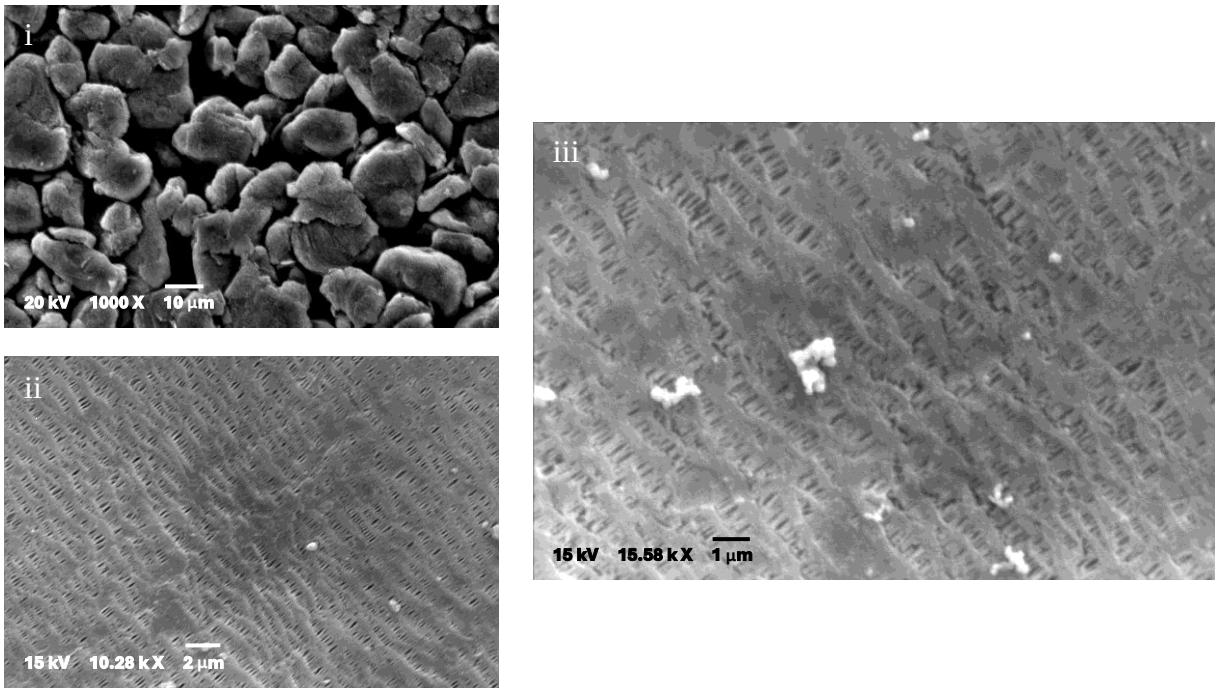

Figure 6-7: SEM images of the Nissan Leaf (gen 1) EV LIB pouch cell; i) anode (graphite), ii/iii) separator (polypropylene).

To determine the amount of electrolyte associated with each component of a LIB pouch cell, it was essential to quantify the dried mass of each component. The disassembly of a Nissan Leaf (gen 1) QCR pouch cell has previously been conducted and documented by researchers from the University of Warwick and the University of Birmingham, as outlined by *Marshall et al*. [18]. The process involved washing the components in an IPA bath and drying each component in a vacuum oven to ascertain their dried component mass.

The electrolyte component, encompassing carbonates and salt, was then recovered from the IPA solution, resulting in a total recoverable electrolyte mass of 113 g. **Table 6-3** provides a breakdown of the isolated mass of each component obtained from the literature results.

Table 6-3: Reclaimed mass of isolated cell components from a QCR Nissan Leaf EV LIB (gen 1) pouch cell [18].

$\mathbf{m_{total}}$	$\mathbf{m_{cathode}}$	$\mathbf{m_{anode}}$	$\mathbf{m_{separator}}$	$\mathbf{m_{total\ electrolyte}}$
791.0	390.1	237.0	19.0	113.0

m_i denotes the mass of each component, measured in g.

The difference in mass between the dissembled LIB pouch cell components, including the electrolyte fraction (refer to **Table 6-2**) and the dried component masses obtained from the literature (refer to **Table 6-3**) were compared.

By comparing both datasets (wet and dry LIB components), the difference allowed for estimating the mass of electrolyte in each respective component, as tabulated in **Table 6-4**.

However, results from the extraction process indicated a slightly higher proportion of electrolyte associated with the anode material. This result was investigated using thermogravimetric analysis (TGA), where it was observed that the weight of the anode material soon after disassembly deviated by more than 11%. Consequently, the estimation of electrolyte content in the anode material was adjusted accordingly.

Across all LIB pouch cells dissembled, a maximum deviation of 3.8% was noted between the total mass of electrolyte calculated in this study and the total mass of electrolyte quantified in the literature (113.0 g) [18].

Table 6-4: Estimated deposition of electrolyte in each LIB component for the Nissan Leaf EV (gen 1) LIB pouch cell.

Reference code	$m_{cathode}$	m_{anode}	$m_{separator}$	$m_{electrolyte}$	$m_{unrecovered}$	$m_{total\ electrolyte}$
PC 0203	22.1	28.1	25.3	7.4	34.6	117.5
PC 2604	22.8	28.3	23.9	8.3	32.4	115.7
PC 1406	20.3	28.5	28.6	6.3	30.3	114.0

Where m_i represents the mass of electrolyte in each component, measured in g. $m_{electrolyte}$ is the electrolyte in its free liquid form. $m_{unrecovered}$ represents the electrolyte component lost due to vaporisation.

6.4.4.2 Solvent composition

The solvent component of the electrolyte in the LIB pouch cell was quantified and characterised using GC-TCD and GC-MS analysis techniques. An initial investigation identified the primary components of the electrolyte to be diethyl carbonate (DEC) and ethylene carbonate (EC), using GC-MS (presented in **Figure 6-8**). Similar to DMC and EMC, DEC is another linear carbonate ester commonly utilised in LIB electrolytes.

However, upon closer examination of the EC peak, there were indications of peak splitting, revealing the presence of propylene carbonate (PC), an additional cyclic carbonate solvent. Initially, the identification of PC was overlooked due to GC column limitations that led to the overlapping of EC and PC components in the GC-MS chromatogram, as depicted in **Figure 6-9**. The merging of peaks is due to the isomeric and/or chemical resemblances between EC and PC.

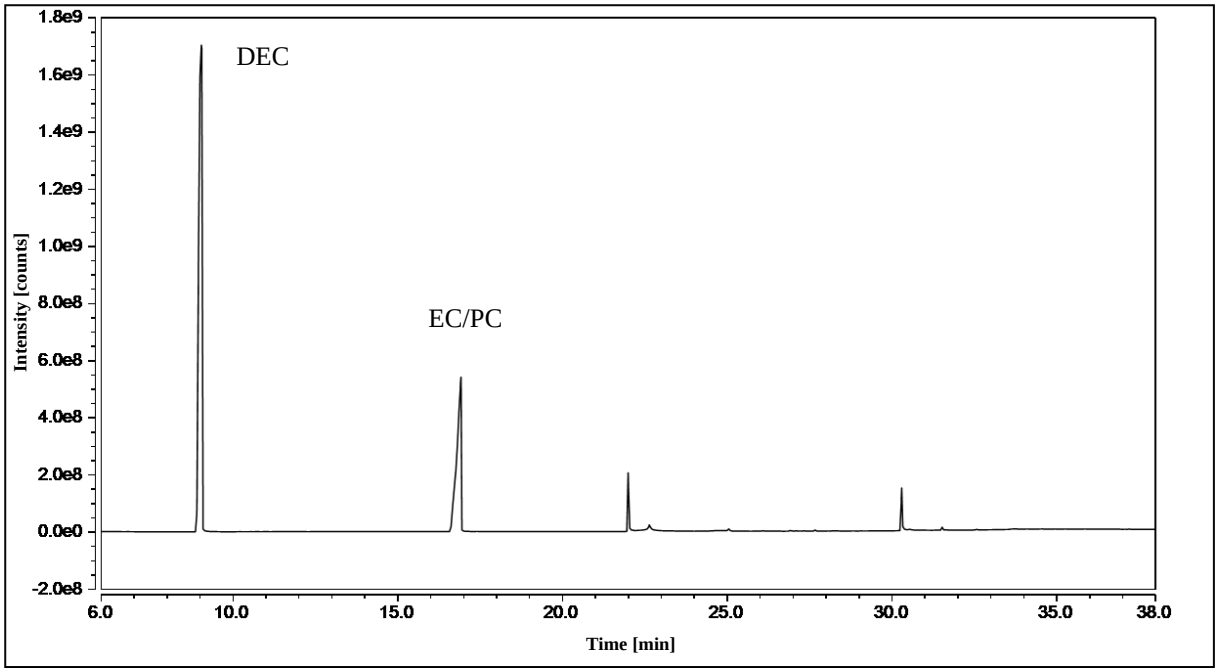

Figure 6-8: GC-MS chromatogram of Nissan Leaf (gen 1) EV LIB pouch cell electrolyte; diethyl carbonate (DEC). Ethylene carbonate (EC) and propylene carbonate (PC).

The remaining peaks detected in the chromatogram correspond to electrolyte additives, components aimed at enhancing the electrolyte's properties. Dimethylacetamide and several silicon-based compounds were identified, these components are typically stabilisers for both electrolyte and the electrodes [25, 26].

Quantification of the electrolyte composition using GC-TCD confirmed the mass ratio of linear to cyclic carbonates as 3:2 (wt.%), respectively. The chromatogram of the pouch cell electrolyte has been presented in Appendix **A7**.

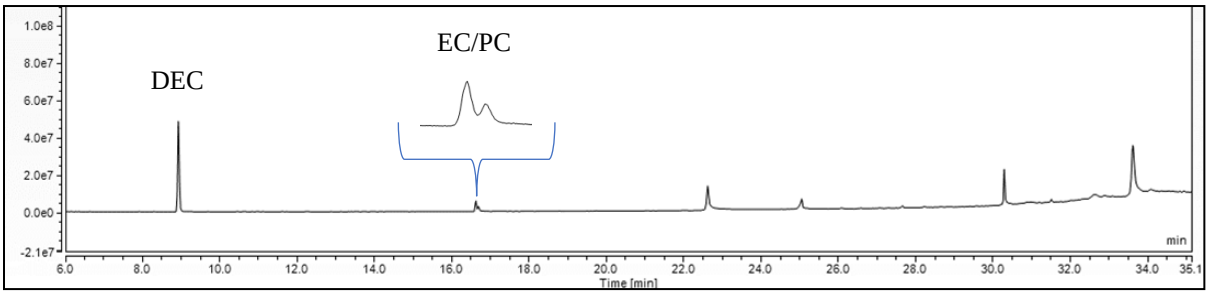

Figure 6-9: GC-MS chromatogram of Nissan Leaf (gen 1) EV LIB pouch cell electrolyte, highlighting the merged peaks of EC and PC, respectively.

6.4.4.3 Conducting salt

Various types of conducting salts are used in commercial LIBs, some notable examples include lithium hexafluorophosphate (LiPF6), lithium bis(trifluoromethanesulfonyl)imide (LiTFSI), lithium bis(fluorosulfonyl)imide (LiFSI), and lithium bis(oxalato)borate, (LiBOB) [27, 28]. Identification of the conducting salt was performed using ^{19}F and ^{31}P Nuclear Magnetic Resonance (NMR) Spectroscopy. The Bruker field strength by isotope at a frequency of 400 MHz is 376 MHz for ^{19}F and 162 MHz for ^{31}P (refer to **Table A8-1** in Appendix **A8** for the NMR frequency table). The pure liquid electrolyte retrieved from the disassembly of the pouch cell was filtered and dissolved in deuterated dimethyl sulfoxide (DMSO-d_6). **Figures 6-10** and **6-11** present the ^{19}F and ^{31}P NMR spectra of the electrolyte retrieved from the Nissan Leaf EV LIB pouch cell, respectively.

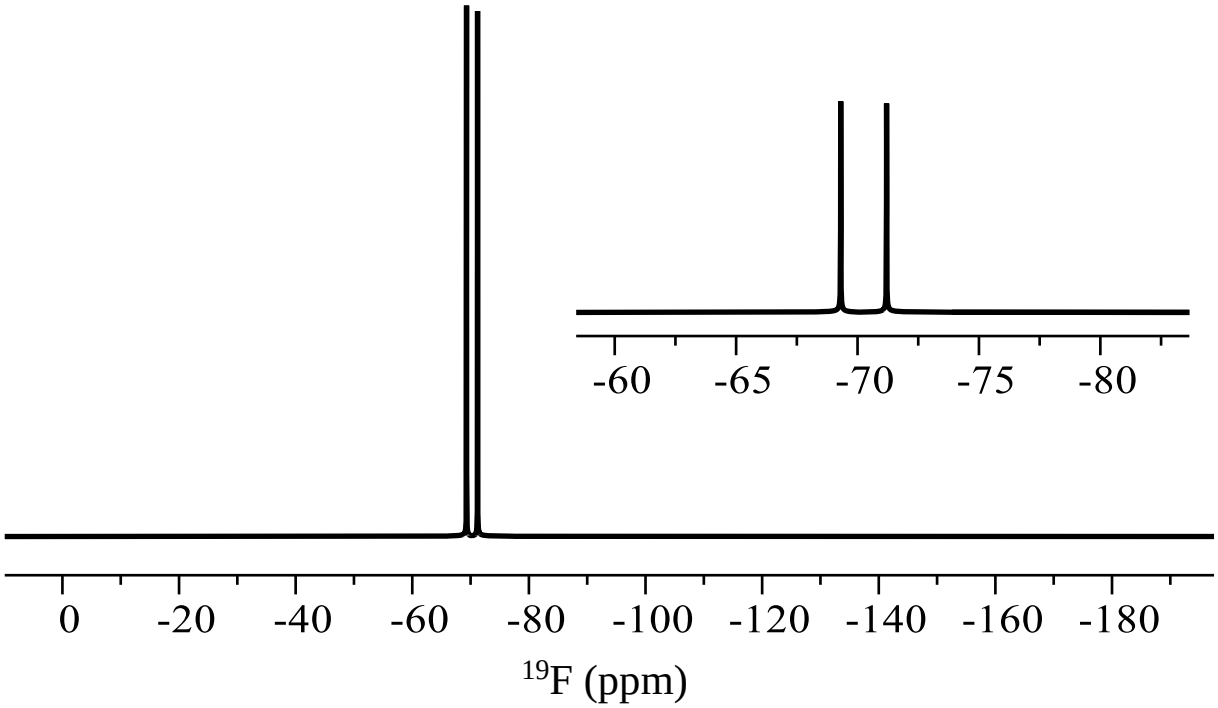

Figure 6-10: ^{19}F NMR of the Nissan Leaf (gen 1) EV LIB pouch cell electrolyte.

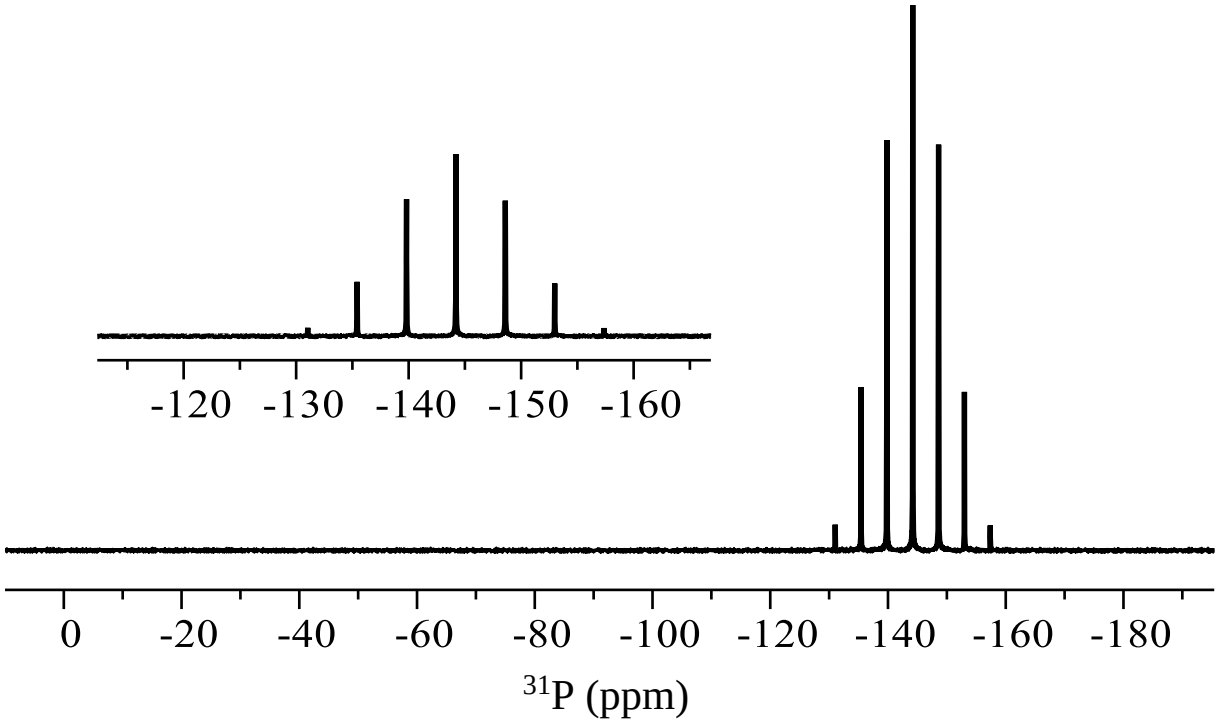

Figure 6-11: ^{31}P NMR of the Nissan Leaf (gen 1) EV LIB pouch cell electrolyte.

After examining the fluorine NMR spectrum (**Figure 6-10**), a doublet was observed at a chemical shift of -70.25 ppm. This is in good agreement with literature data by *Lu et al.* [29], where electrolyte from a lithium cobalt oxide (LCO) chemistry was dissolved in DMSO-d_6 and was characterised using fluorine NMR, confirming the presence of $LiPF_6$. To eliminate any uncertainties, a phosphorous NMR was also conducted (as shown in **Figure 6-11**), which displayed a septet at a chemical shift of -144.2 ppm. Both ^{19}F and ^{31}P NMR spectra refer to the bonds in the PF_6^- molecule, confirming the presence of $LiPF_6$ in the Nissan Leaf EV LIB pouch cell electrolyte.

The conducting salt component is dissolved in the solvent blend to form a solution with a concentration close to 1 mol L^{-1}. Using the total mass of electrolyte in the pouch cell (presented in **Table 6-4**), the average density of the electrolyte solution (1.1 g cm^{-3}) [30, 31], and considering the concentration of $LiPF_6$ (1.2 mol L^{-1}), the total mass of the conducting salt was estimated to be approximately 21 g.

6.4.4.4 Decomposition of conducting salt

The instability of the conducting salt has been previously discussed. Lithium hexafluorophosphate is prone to decomposition reactions when exposed to heat and moisture. In the presence of water, it undergoes hydrolysis via the following mechanism.

$$LiPF_6 \rightleftharpoons Li^+ + PF_5^- \quad \textbf{(6-17)}$$

$$LiPF_6 \rightleftharpoons LiF + PF_5 \quad \textbf{(6-18)}$$

$$PF_5 + H_2O \longrightarrow POF_3 + 2HF \quad \textbf{(6-19)}$$

$$POF_3 + H_2O \longrightarrow POF_2(OH) + HF \quad \textbf{(6-20)}$$

$$POF_2(OH) + H_2O \longrightarrow POF(OH)_2 + HF \quad \textbf{(6-21)}$$

Besides dissociating into Li^+ and PF_5^-, lithium hexafluorophosphate also reaches equilibrium with lithium fluoride (LiF) and phosphorus pentafluoride (PF_5). In the supercritical carbon dioxide extraction process, the neutralisation of hydrogen fluoride (HF) with sodium carbonate (Na_2CO_3) (as per **Equation 6-6)** was employed. Stoichiometric calculations were conducted to determine the required mass of Na_2CO_3 for the neutralisation reaction. It was calculated that if the hydrolysis mechanism proceeded to completion, a maximum of 0.55 g of HF would be produced from 1 g of $LiPF_6$.

$$2HF + Na_2CO_3 \rightleftharpoons 2NaF + H_2O + CO_2 \quad \textbf{(6-22)}$$

It was further determined that 2.7 g of Na_2CO_3 was required to neutralise 1 g of HF. However, to ensure complete reaction and neutralisation of the HF, an excess of 5 g of Na_2CO_3 per 1 g of HF was used.

6.5 Results and Discussion

6.5.1 Electrolyte recovery from a Nissan Leaf (gen 1) EV LIB pouch cell

In previous experimental chapters (4 and 5) the focus was on exploring the solubility behaviour and optimal extraction conditions to recover an artificial-based electrolyte using pressurised carbon dioxide. In this chapter, these findings have been applied to process genuine LIB material, specifically an LIB pouch cell designed for a Nissan Leaf (gen 1) EV. The solvent extraction method was employed to establish a benchmark against the supercritical carbon dioxide extraction process, which is not the sole technique available for extracting and recovering electrolyte components in LIBs.

To evaluate the efficiency of each process, various analytical methods were employed to assess the products recovered from the supercritical extraction technique and the solvent extraction process. The processing, characterisation, and quantification of the Nissan Leaf (gen 1) EV LIB pouch cell have been summarised in a flow diagram, as presented in **Figure 6-12**.

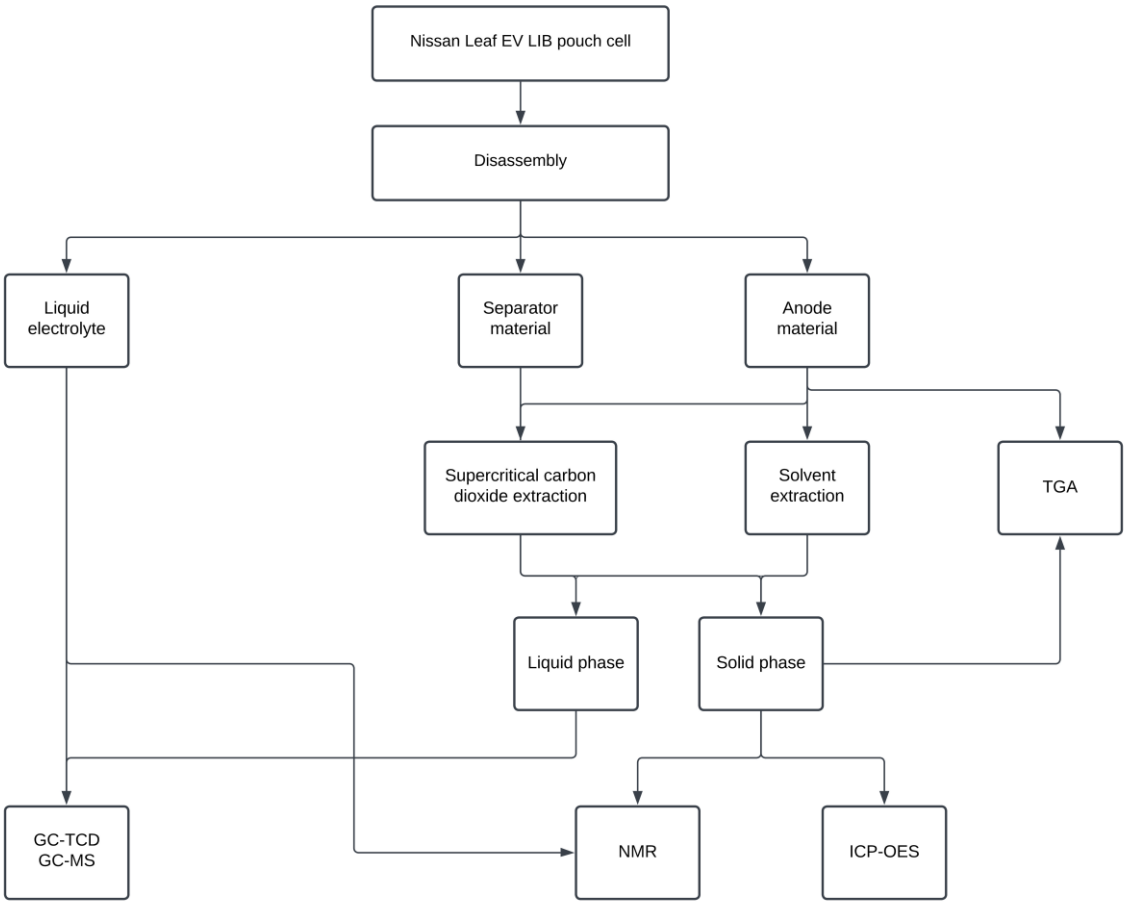

Figure 6-12: Flow diagram to show the processing and analyses performed on a Nissan Leaf (gen 1) EV LIB pouch cell.

A summary of the operational conditions for each process is provided below. For the supercritical carbon dioxide extraction technique, the optimal parameters identified in *Chapter 5* were used. The process was performed at temperature and pressure conditions of 328.2 K and 12.0 MPa, respectively. The extraction duration consisted of 45 minutes of static operation and 60 minutes of dynamic operation, with a controlled flowrate of 6 g/min. For the solvent extraction process, acetone was pumped at a flowrate of 6.5 L/min for 165 minutes, while the HPV was maintained at a temperature of 323.2 K. The experimental results of the extraction processes are presented in **Table 6-5**.

Table 6-5: Extraction of LIB components from the Nissan Leaf (gen 1) EV LIB pouch cell.

Reference code	Material	Solvent	Solvent consumption		Starting material mass (g)	Final material mass (g)	Projected electrolyte mass (g)	Recovered electrolyte mass (g)	Mass fraction of electrolyte recovered (wt.%)		Extraction yield (%)	Recovery yield (%)
			(g)	(mL)					linear	cyclic		
PC 0203	anode	acetone	-	1072	135.4	-	14.9	14.1	39.2	60.8	-	94.6
	anode	CO_2	458	-	116.3	109.1	12.8	5.7	91.4	8.6	56.3	44.5
	separator	CO_2	467	-	44.3	31.1	25.3	9.7	88.9	11.1	52.2	38.3
PC 2604	anode	acetone	-	1072	138.9	-	15.3	14.8	38.5	61.5	-	96.7
	anode	CO_2	453	-	114.3	107.0	12.6	5.8	92.1	7.9	57.9	46.0
	separator	CO_2	457	-	43.4	30.5	23.9	9.3	87.1	12.9	54.0	38.9
PC 1406	anode	acetone	-	1072	142.9	-	15.7	15.8	41.1	58.9	-	100.6*
	anode	CO_2	461	-	114.1	106.7	12.6	6.0	91.1	8.9	58.7	47.6
	separator	CO_2	458	-	47.6	29.6	28.6	12.7	92.5	7.5	62.9	44.4

Standard uncertainty, u(m) = 0.01 g, u(V) = 0.1 mL. * Values of uncertainty.

It should be noted that the extraction yield was determined by comparing the initial and final weights of the anode and separator components. After the completion of the supercritical carbon dioxide extraction process, the extracted material was weighed. While the polypropylene material from which the separator is manufactured exhibited no major visual changes, the anode material became brittle. This increased brittleness of the anode material made it challenging to weigh accurately, potentially resulting in discrepancies in the final weight of the anode processed using supercritical carbon dioxide. Regarding the solvent extraction process, the anode sheets were weighed before undergoing an acetone wash, but they were not weighed afterwards due to their weak composition and the absorption of acetone.

The recovery mass of the linear (DEC) and cyclic carbonates (EC and PC) was quantified using GC-TCD, enabling the calculation of the mass fraction of each. As observed in **Table 6-5**, the solvent extraction process proved highly efficient in recovering electrolyte components from the anode, achieving an average extraction yield of 96%, excluding the anomaly value. Notably, the last solvent extraction of the anode material (PC 1406) showcased an extraction yield of 100.6%. Despite initially believed to be an analytical discrepancy, subsequent readings confirmed this result.

The high recovery of the solvent extraction process was later corroborated by the thermogravimetric analysis (TGA) data, where the remaining mass of electrolyte in the anode material was quantified. However, the observation of this outliner suggests a possibility that the anode component may initially have contained a slightly higher mass of electrolyte than previously estimated.

All the anode and separator materials extracted from pouch cell PC 1406 exhibited slightly higher extraction and recovery yields in both extraction processes compared with the other

pouch cells (PC 0203 and PC 2604). This finding may be attributed to the timing of the extractions. In contrast, other extractions were conducted in the same week as the disassembly, these specific extractions were performed within 48 hours of disassembling the pouch cell. This observation serves as a reminder of the volatile nature of the electrolyte material and emphasises the importance of processing the materials promptly. Additionally, the weight percentage (wt.%) of the recovery of linear carbonate to cyclic carbonates showed a slight increase for all the supercritical carbon dioxide extractions of the PC 1406 material, which is consistent with expectations.

In comparison, the supercritical extraction process exhibited an average recovery yield of 46% and 41% for extracting electrolyte from the anode and separator materials, respectively. The marginally higher recovery of electrolyte from the anode material is likely due to the higher porosity of the separator material, which makes separation more challenging. As shown in the SEM images (**Figure 6-7**), the pore size required for the separator's functionality is typically less than 1 μm [32].

The mass fraction of the recovered electrolyte solvents differs significantly between the two extraction processes. In the supercritical extraction technique, the linear component, DEC, was the predominant mass fraction of the electrolyte composition, accounting for approximately 90:10 wt.%, compared to the cyclic components (EC and PC). This difference stems from the higher solubility of the linear carbonates compared to the cyclic counterparts, as determined in *Chapter 4*. The solubility behaviour of DEC appears to be similar to both DMC and EMC, based on the exceptionally greater recovery.

It is not possible to make a direct comparison of the electrolyte recovery yields between this work and that discussed in *Chapter 5*, subsection **5.6.6** due to variations in the electrolyte composition and sample matrix. However, the mass fraction of the recovered components displays a degree of similarity. Under the same extraction conditions (12.0 MPa, 328.2 K) the ratio of linear to cyclic carbonates in the electrolyte amounted to 80:20 wt.%, this outcome closely matches the findings discussed in this chapter.

In contrast, the mass fraction of electrolyte attained from the solvent extraction process is the opposite. The mass fraction of linear to cyclic electrolyte recovered was approximately 40:60 wt.%. This may seem surprising as the composition of electrolyte in the LIB pouch cell is predominantly constituted of DEC, however, this discrepancy is attributed to the significant loss of the DEC component (over 20%) during the disassembly process.

6.5.2 Nuclear Magnetic Resonance (NMR) spectroscopy of pure and recovered LIB pouch cell electrolyte

As previously discussed, lithium conducting salt is a vital part of the electrolyte, and represents about half of the total cost of commercial electrolytes [33]. As performed on pure electrolyte retrieved from the disassembly of the Nissan Leaf LIB pouch cell, both ^{19}F and ^{31}P NMR Spectroscopy were used to analyse the composition of the electrolyte recovered from both the supercritical carbon dioxide technique and the solvent extraction process. The ^{19}F NMR spectrum in **Figure 6-13** highlights the presence of the lithium salt, lithium hexafluorophosphate. Interestingly, it can be observed that the solvent extraction process is capable of recovering the lithium salt, whereas the electrolyte retrieved using supercritical carbon dioxide does not exhibit a signal. The corresponding diagram for the ^{31}P NMR spectrum has been presented in Appendix **A10**.

It is possible to extract the lithium hexafluorophosphate component using supercritical carbon dioxide extraction, but it requires a modifier. *Grützke et al.* conducted a series of liquid carbon dioxide extractions on 18650 LIB cells and initially faced challenges extracting the conducting salt. However, the author introduced a range of co-solvents, including ACN, DEC, and ACN/PC (3:1). All these modifiers proved capable of recovering the conducting salt, and the ACN/PC mixture exhibited the most efficient performance in recovering almost all of the conducting salt within the electrolyte [34].

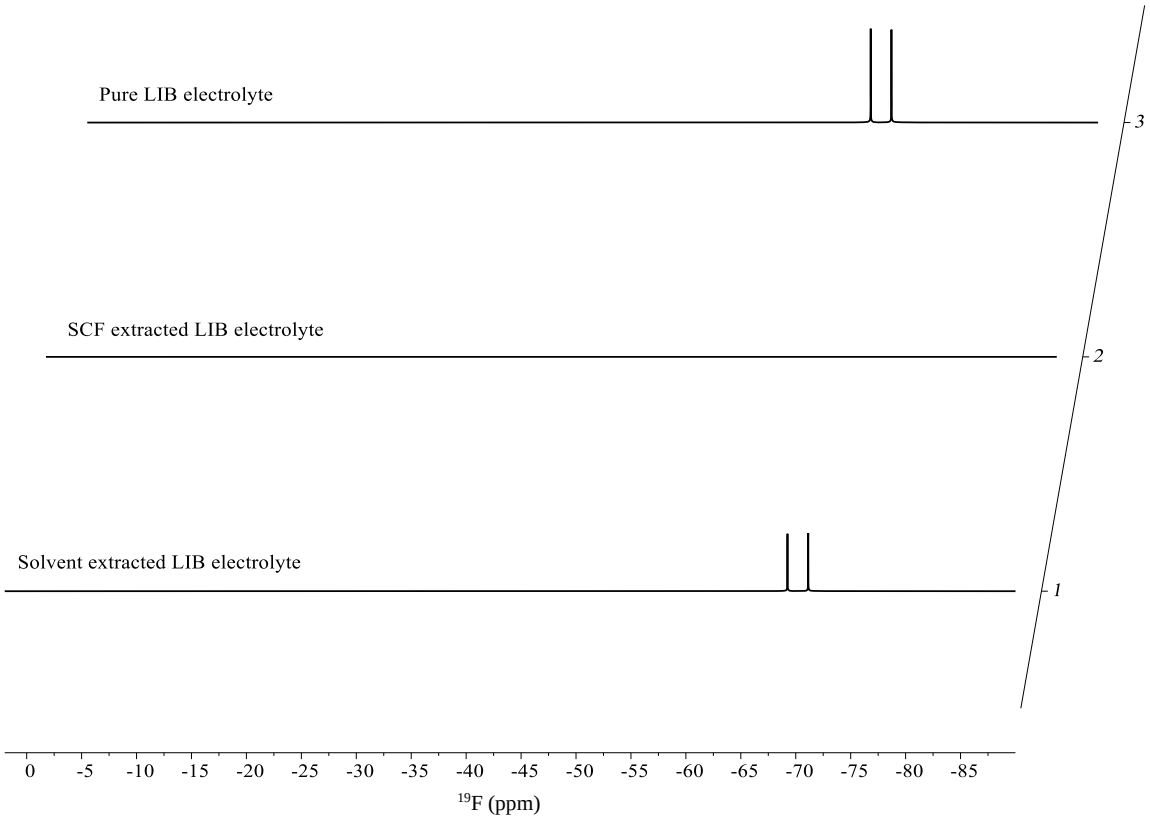

Figure 6-13: ^{19}F NMR of Nissan Leaf EV (gen 1) EV LIB pouch cell electrolyte; 1) solvent extracted LIB electrolyte, 2) SCF extracted LIB electrolyte, 3) Pure LIB electrolyte.

6.5.3 Inductive Coupled Plasma – Optical Emission Spectroscopy (ICP-OES) of pure and recovered LIB pouch cell electrolyte

Quantification of the elements present in the pure electrolyte and the electrolytes recovered from both extraction processes was conducted using Inductive Coupled Plasma – Optical Emission Spectroscopy (ICP-OES). Initial attempts using High-Performance Liquid Chromatography (HPLC) to quantify lithium concentration were successful in detection but not reliable in their quantification.

The analysis incorporated Supelco ICP multi-element standard solution IV, containing 21 elements. A four-point calibration was established in a 5% (v/v) nitric acid solution, and the calibration curves have been included in Appendix **A12**. Additional information regarding the multi-element standard and equipment used is detailed in *Chapter 3*, subsection **3.5.4**.

The solid materials were separated from the electrolytes using rotary evaporation, which effectively isolated the liquid and solid phases. The conducting salt and other solids were collected while the electrolyte solvents were evaporated. Each sample was then dissolved in a nitric acid 5% (v/v) aqueous matrix, resulting in a 1000-fold dilution. These solutions were filtered (using a Millex filter with a pore size of 0.45 μm) and transferred to 50 mL centrifuge vials (BD Falcon). The final sample volume was 20 mL, which was sufficient to determine the concentration of all 21 elements. The limit of detection (LOD) for the Perkin Elmer instrument used has been presented in Appendix **A13**.

The raw data for all samples and analysis of the 21 elements can be found in Appendix **A14**.

The primary interest of this chapter focuses on 6 elements (Al, Co, Cu, Li, Mn, and Ni), each of which is directly related to the chemistry of the Nissan Leaf EV pouch cell. **Table 6-6** provides information on the concentration of these elements in the pure LIB electrolyte as well as the electrolyte recovered from the solvent extraction process and supercritical carbon dioxide technique.

Table 6-6: The elemental concentration of pure and process recovered electrolytes from the Nissan Leaf (gen 1) EV LIB pouch cell.

Sample	Concentration (mg/L)					
	Al	**Co**	**Cu**	**Li**	**Mn**	**Ni**
Pure electrolyte	0.1278	0.0242	1.7167	5.2916	0.0347	0.0356
Solvent extracted electrolyte	0.0463	0.0034	1.8988	5.5158	0.0102	0.0079
$ScCO_2$ extracted electrolyte	0.0038	0.0032	0.8130	0.0081	0.0037	0.0045

The initial observation from **Table 6-6** indicates that the solvent extraction method captures a significantly higher proportion of elements compared to the supercritical carbon dioxide extraction process. All elements except copper in the supercritical recovered electrolyte sample were outside the LOD, rendering them statistically unreliable. However, it remains evident there is a clear divergence between both processes in terms of the recovery of solid deposits within the anode material.

Of particular interest are the concentrations of copper and lithium in each sample. The supercritical carbon dioxide extraction process failed to recover most transition metals, this is not surprising given the charge neutralisation requirements, and the absence of a co-solvent or chelating agent [35-37]. However, there is a substantial concentration of copper present in the

SFE electrolyte sample. This finding suggests that one (or more) of the electrolyte solvents may act as co-solvents.

The concentration of copper amongst the other transition metals was observed to be substantially higher in both the pure electrolyte and the solvent extracted electrolyte. Further investigation revealed that the copper from the current collector in the pouch cell tends to partially dissolve into the electrolyte during complete discharge to 0 V. This phenomenon occurs due to the high potential observed at the anode at 0 V and the oxidation of copper [18]. Studies also indicate that copper deposits can potentially accumulate on the surfaces of both electrode components during deep discharges [38, 39]. This effect might elucidate why the copper concentration in the solvent extracted electrolyte slightly exceeds that of the pure electrolyte. In addition to the electrolyte extracted, the solvent extraction process may have recovered some copper deposits on the surface of the anode material residing in the electrolyte, explaining the greater concentration of copper detected. However, it's important to note that acetone cannot dissolve copper. Instead, the smaller copper particles were likely suspended in the acetone until their dissolution in nitric acid as part of their preparation for ICP-OES [40].

Similarly, the concentration of lithium observed in the solvent extracted electrolyte exhibits a higher concentration than in the pure electrolyte. What initially seems surprising is this observation can be attributed to the behaviour of lithium ions during charging and discharging cycles. Lithium ions experience intercalation and deintercalation within the graphite layers of the battery during these cycles [41], and during the discharge of the LIB, the lithium ions are deintercalated. However, the solvent extraction process recovers the electrolyte from the pores of the anode, potentially capturing a higher concentration of lithium compared to the pure electrolyte drained from the surface of the electrodes.

6.5.4 Thermogravimetric Analysis (TGA) of LIB pouch cell anode material

To assess the efficacy of each extraction process and determine the proportion of electrolyte trapped in the material after extraction, samples were examined using thermogravimetric analysis (TGA). This involved subjecting the samples to an inert atmosphere (nitrogen) and measuring their weight as a function of temperature via a program-controlled temperature sequence. The TGA sequence was designed to consider the boiling points of the electrolyte constituents. For detailed methodology regarding the TGA, refer to *Chapter 3,* subsection **3.5.5**. Only the anode was processed under high temperatures. Polypropylene, the separator material, typically melts around 167°C [42], depending on the chemical structure. As the boiling point of cyclic components significantly exceeds this temperature, no high temperature methods were applied to the separator material. **Table 6-7** presents the results of the TGA conducted on the anode material of the Nissan Leaf (gen 1) EV LIB pouch cell, post extraction process.

Table 6-7: TGA of the Nissan Leaf (gen 1) EV LIB pouch cell anode material post-extraction.

Ref code	Source	Starting mass (µg)	Final mass (µg)	Mass deviation	
				(µg)	(%)
PC 2604	CO_2	14623	13676	947	6.476
PC 2604	SE	15043	14700	343	2.280
PC 1406	CO_2	13956	13183	773	5.539
PC 1406	SE	17748	17246	502	2.828

Where CO_2 refers to the anode material after being processed using the supercritical carbon dioxide technique, and SE corresponds to the anode material after undergoing the solvent extraction process and being left to dry in a ducted fume hood for at least 12 hours.

The anode samples subjected to supercritical carbon dioxide extraction show greater mass loss than those processed using solvent extraction. This finding aligns with the electrolyte mass recovery obtained from each extraction process using GC-TCD. **Figures 6-14** and **6-15** present the TGA and derivative thermogravimetric (DTG) curves for each LIB pouch cell anode sample following treatment with supercritical carbon dioxide and solvent extraction techniques, respectively.

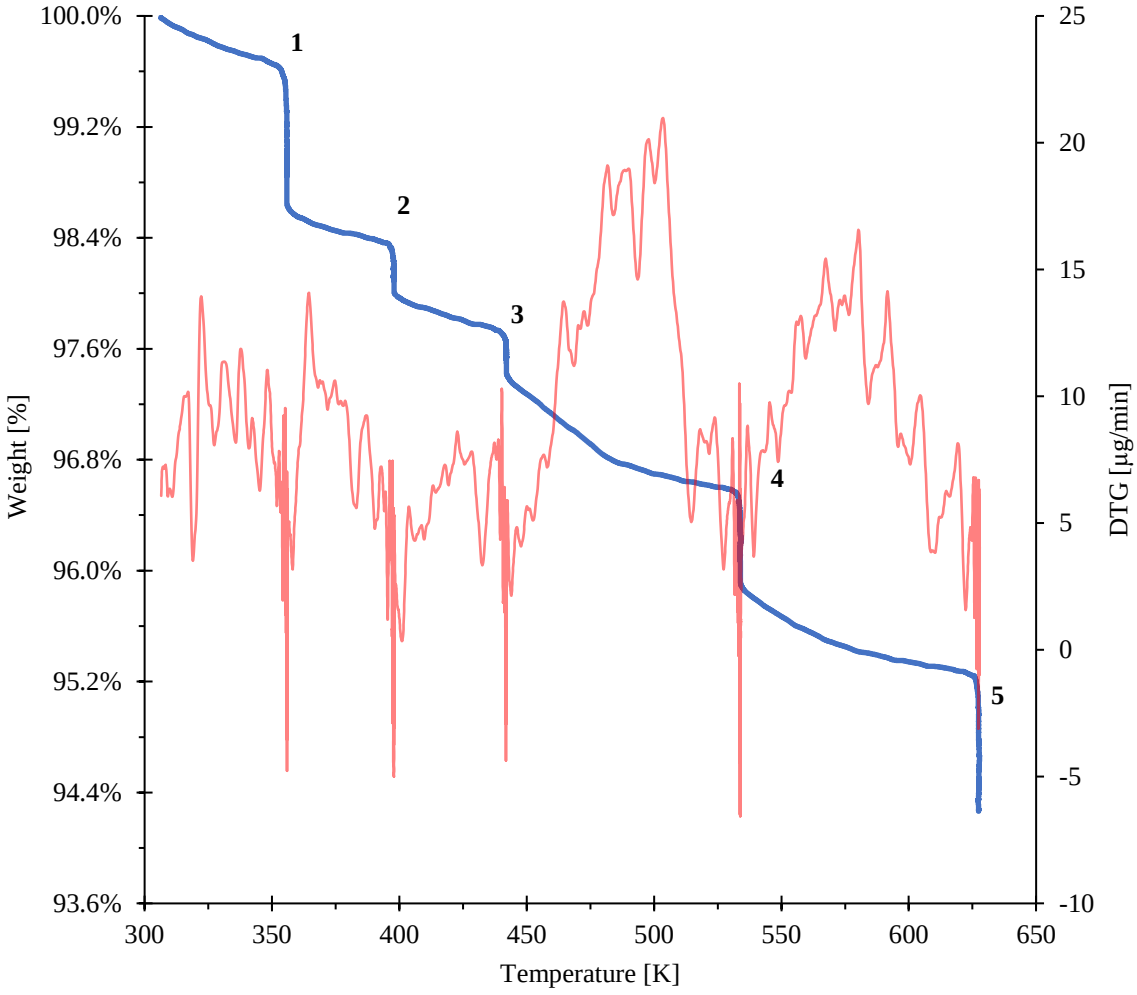

Figure 6-14: TGA-DTG plot of the Nissan Leaf (gen 1) EV LIB pouch cell anode material (PC 1406), after undergoing the supercritical carbon dioxide extraction process. TG (—), DTG (—).

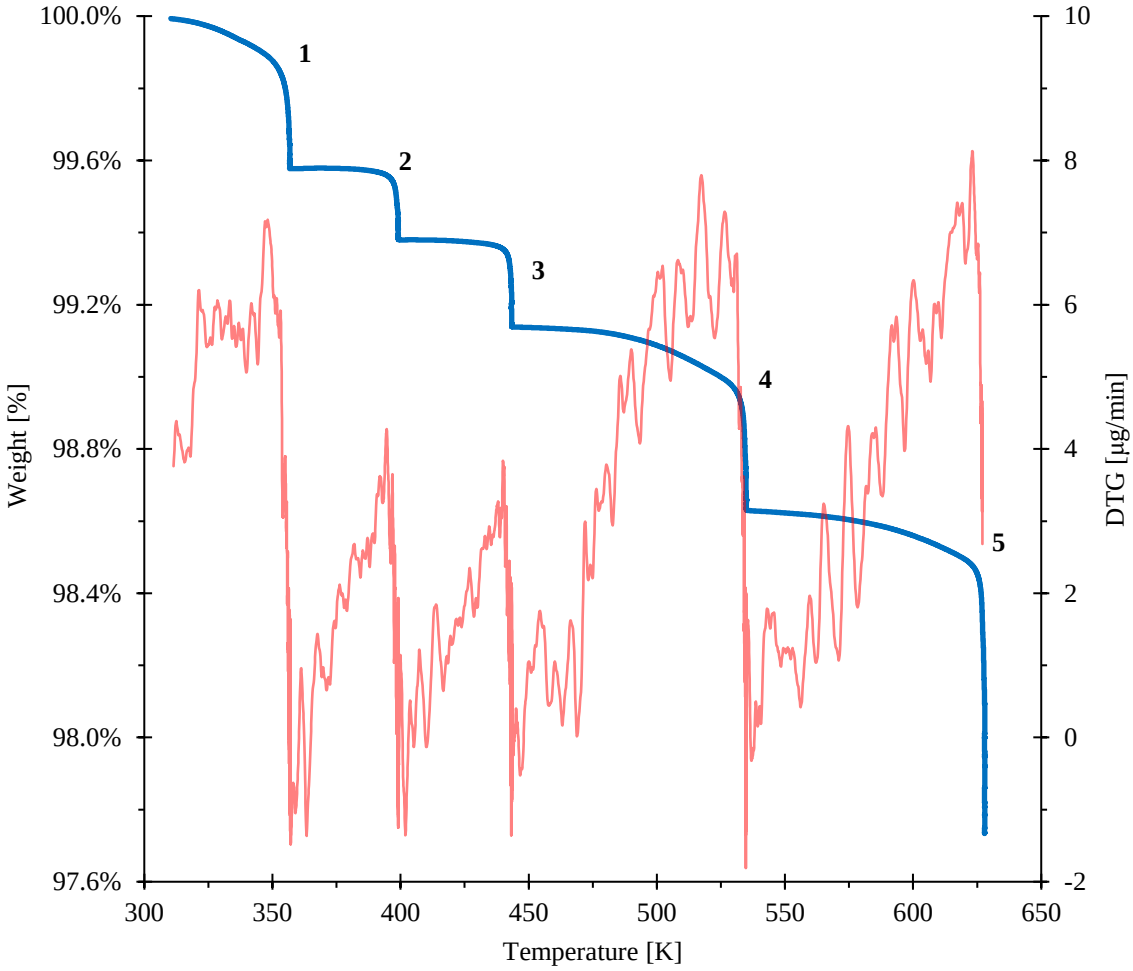

Figure 6-15: TGA-DTG plot of the Nissan Leaf (gen 1) EV LIB pouch cell anode material (PC 2604), after undergoing the solvent extraction process. TG (—), DTG (—).

The TGA-DTG curves in **Figures 6-14** and **6-15** exhibit a distinctive five-step mass loss corresponding to the different components in the anode material. The weight loss observed in the anode material processed via the supercritical carbon dioxide technique and the solvent extraction process was approximately 5.5 % and 2.3 %, respectively, between 323.15 to 625.15 K.

The initial slight weight loss up to 353 K is predominantly associated with the evaporation of the DEC close to the graphite surface. It is likely to include a small proportion of water moisture. However, this is minimal as most electrolyte solvents on the anode's surface have been

recovered during the extraction processes. The second step, between 383-403 K, is solely associated with the linear carbonate DEC, possessing a boiling point of 399 K [43]. Notably, there is a significant drop in the TGA curve with a sharp spike in the DTG curve in this temperature range.

The third decline in weight, beyond 440 K, is likely due to the decomposition of lithium hexafluorophosphate. The decomposition temperature of the conducting salt has been reported to vary significantly based on the applied measuring technique (differential scanning calorimetry (DSC) and TGA) and the presence of water moisture [44, 45]. *Gavrichev et al.* found that under ambient pressure the thermal decomposition of lithium hexafluorophosphate occurs between 450-550 K. However, in this case, the conducting salt is dissolved in the electrolyte solvent solution and subjected to a nitrogen atmosphere. Thus, its decomposition temperature may vary.

The fourth significant drop in mass corresponds well with the vaporisation of cyclic carbonates, ethylene and propylene carbonate, each possessing boiling points of 517.5 and 515.15 K, respectively [46, 47]. The sharp decrease begins at 526 K, although a gradual mass decline is also noticeable beforehand.

The final reduction in weight is attributed to the decomposition of organic oxides and the polyvinylidene fluoride (PVDF) binder, which is used to bind the active materials in both the anode and cathode. This inference is supported by a substantial drop in weight that occurs at a temperature of 628 K. This aligns with findings from *Liu et al.*, suggesting that the initial thermal decomposition of PVDF in a nitrogen atmosphere occurs at temperatures exceeding 453.15 K. Within a temperature range of 453.15 K to 653.15 K, the significant weight loss is attributed to the simultaneous decomposition of the electrolyte and binder components [48].

A limitation of TGA lies in its process capacity to handle a maximum sample weight of 200 mg, potentially introducing bias when measuring small proportions of material, particularly those of a heterogeneous nature. To mitigate this limitation, a chamber furnace, Carbolite Gero (model, ELF 1100), as shown in **Figure 6-16 (i),** was used in conjunction with the TGA instrumentation to evaluate larger sample weights, approximately 3 g in magnitude. Anode sheets were placed in ceramic crucibles, as shown in **Figure 6-16 (ii)**, and processed in batches of three to minimise potential errors in readings. These samples were exposed to a temperature of 523.15 K for at least 5 hours. Initial tests confirmed no significant mass deviations in the sample after this duration. The mass deviation data for each anode sample processed in the furnace are presented in **Table 6-8**.

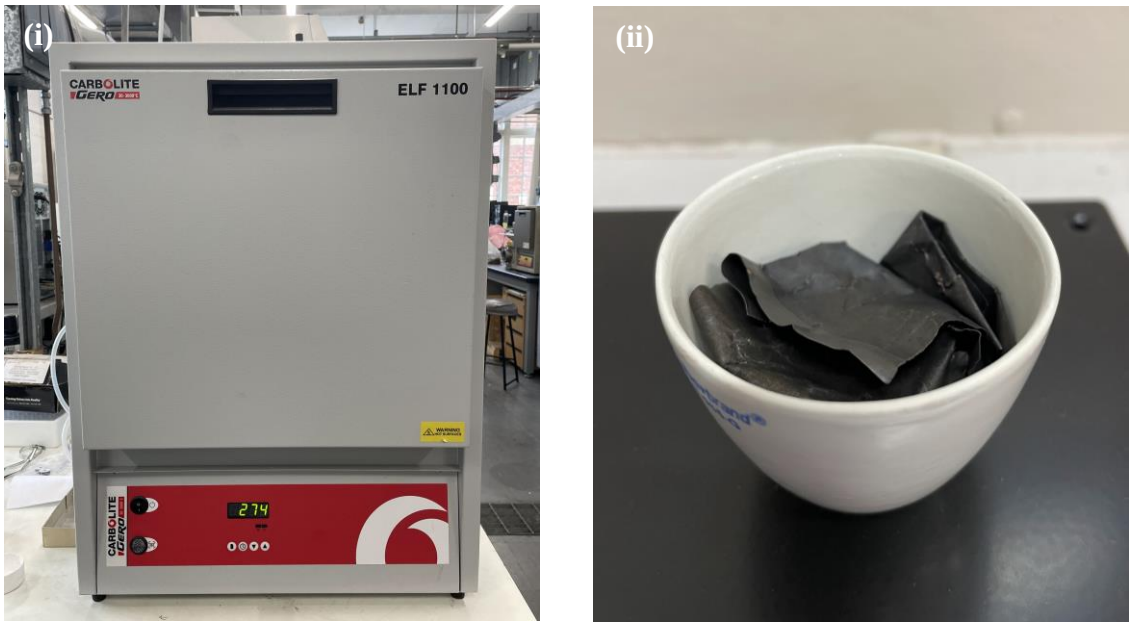

Figure 6-16: i) Carbolite Gero (model, ELF 1100) chamber furnace, ii) anode material, obtained from the Nissan Leaf (gen 1) EV LIB pouch cell.

Table 6-8: Mass deviation of Nissan Leaf (gen 1) EV LIB pouch cell anode material processed in the chamber furnace (523.15 K)

Ref code	Source	Sample mass	Starting mass	Final mass	Mass deviation	
					(g)	(%)
PC 0203	TD	3.0356	58.7635	58.4989	0.2646	8.717
		3.1327	39.8534	39.5811	0.2723	8.692
		3.0258	37.9627	37.6967	0.2660	8.791
PC 0203	CO_2	3.0211	58.3736	58.2542	0.1194	3.952
		3.0821	39.1138	38.9893	0.1245	4.039
		3.0160	37.3483	37.2098	0.1385	4.592*
PC 0203	SE	3.0491	58.8239	58.7631	0.06079	1.994
		3.1362	39.6589	39.5915	0.06737	2.148
		3.1764	37.0246	36.9744	0.05019	1.580*
PC 2604	TD	3.0239	58.79622	58.5475	0.2487	8.224
		3.0650	36.91514	36.6786	0.2366	7.719
		3.0626	39.58572	39.3437	0.2420	7.902
PC 2604	CO_2	3.3561	59.1304	59.0183	0.1121	3.340*
		3.2436	39.76642	39.6247	0.1417	4.369
		3.2126	37.0626	36.9191	0.1435	4.467
PC 2604	SE	3.1805	58.9541	58.8958	0.05834	1.834
		3.2575	39.7802	39.7186	0.06160	1.891
		3.2971	37.1453	37.0843	0.06100	1.850
PC 1406	TD	3.0463	58.80172	58.4601	0.34160	11.214
		3.0125	39.60652	39.2717	0.33486	11.116
		3.0578	36.88732	36.5361	0.35122	11.486
PC 1406	CO_2	3.0211	59.14794	59.0137	0.13424	4.443
		3.0821	39.7546	39.6079	0.14670	4.760
		3.0160	37.0699	36.9285	0.14140	4.688
PC 1406	SE	3.0096	58.78348	58.7169	0.06658	2.212
		3.0309	36.88064	36.8169	0.06376	2.104
		3.0117	39.53452	39.4689	0.06561	2.179

TD – tear down material, CO_2 - supercritical carbon dioxide processed material, SE - solvent extraction processed material.
Standard uncertainty, u(m) = 0.01 mg. The starting/final mass includes the weight of the ceramic crucible. * Values of uncertainty.

As presented in **Table 6-8**, significant mass deviations are evident in the anode materials obtained from three different sources: (i) directly retrieved from the tear down (TD), (ii) supercritical carbon dioxide processed material (CO_2), and (iii) solvent extraction processed material (SE).

Measuring the electrolyte content accurately in disassembled LIB anode material using TGA studies is challenging due to electrolyte volatility. This difficulty is observed in the deviation of mass loss exhibited between PC 0203 TD material (≈ 9%) and PC 1406 TD material (≈11 %), exceeding 2%. The reason for this discrepancy is that the PC 1406 anode material was analysed immediately within an hour of opening the pouch cell, while the PC 0203 material was analysed within 48 hours of disassembly. Similar challenges were faced in the rapid extraction of separator and anode materials from the disassembled LIB pouch cell (PC 1406), resulting in slightly higher recovery yields. This issue is discussed in the electrolyte extraction process results (refer to subsection **6.5.1**).

However, the mass deviation measurements between the processed materials via supercritical carbon dioxide extraction and solvent extraction are notably more stable and consistent between samples.

In **Table 6-8**, values of uncertainty (indicated by an asterisk) deviate as much as 25%, which is not unexpected. This variance suggests a heterogeneous distribution of lithium and electrolyte across the graphite. Research conducted by *Mühlbauer et al.* [49] mapped the lithium and electrolyte concentrations in 18650-type cells using x-ray tomography and high-resolution neutron powder diffraction. The author found noticeably higher concentrations of electrolyte in outer regions of the cell, particularly between the electrode material and cell housing. Thus, the concentration of lithium and electrolyte varies in the cylindrical cell across all orientations.

This finding applies to all the thermogravimetric experiments conducted and partially contributes to the varying mass loss among samples from the same source.

Comparison between anode samples subjected to the TGA technique and those processed using the chamber furnace demonstrated good agreement. The overall trend aligns with the extraction results, where naturally, the content of electrolyte is highest in the unprocessed anode material, directly obtained from the disassembly, followed by the supercritical carbon dioxide processed material, and lastly, the solvent-extracted material.

6.5.5 The challenges of LIB electrolyte recovery and recycling

The research and experimental work carried out in this chapter has revealed various challenges that must be addressed to recover and recycle the LIB electrolyte. The following section discusses a roadmap published on tackling these issues in the present and future [7].

These challenges can be broken down into three key areas: the dangers of EOL material, the cost of processing, and standardisation. As LIBs reach EOL, their capacity and discharge ability are reduced due to numerous ageing phenomena. Though the ageing within LIBs does not exclusively impact the degradation of LIBs' operational abilities, it also results in the formation of hazardous and corrosive compounds within the cell.

Independently, lithium hexafluorophosphate is thermally stable at temperatures under ~107°C, but once dissolved within the solvent and in contact with electrodes that can span in voltage from 0 V to over 4.3 V vs. Li/Li^+ this stability is significantly reduced. Furthermore, any exposure to moisture will cause the hydrolysis of lithium hexafluorophosphate and results in the formation of hydrogen fluoride, which imposes significant health risks if it doesn't react with other components of the cell [50]. In a 2015 research paper published by Grìtzke et al. [51], shredded NMC/graphite LIB material was transferred into storage containers and analysed

over a period of 20 months using headspace gas chromatography-mass-spectrometry. The standard compounds within the electrolyte were identified, but in addition, organo(fluoro)phosphate compounds were identified with structures that closely resembled chemical nerve agents. Dimethyl fluorophosphate (DMFP) and diethyl fluorophosphate (DEFP) were characterised in concentrations of 1.12±0.09 and 1.00±0.20 g/kg, respectively. Although these concentrations are exceptionally small, the concentration would be exponentially amplified under increased temperature, proving to be hazardous. This is more so when applied to the large volumes predicted to pass through recycling plants within the near future.

Currently, the electrolyte is not standardised, and the composition of solvent and salt fluctuates significantly amongst manufacturers, consequently it is difficult for recyclers to produce a consistent product.

For practical recycling of electrolyte to become standard practice, several challenges need to be addressed. Once the electrolyte is extracted by either a solvent based process or one incorporating supercritical carbon dioxide it then needs to be processed into a saleable product. Ideally, a process would be developed that could separate out each component of the electrolyte. However, such a process would require a large number of steps that makes it economically unfeasible. One of the main challenges to these processes is the strong coordination between the salt and the solvent coupled with the low thermal stability of the salt [50, 52]. This makes simple evaporation processes to recover the pure salt impractical. New processes that can perform this separation at lower costs than conventional processing, such as chromatography, could enable the salt to be extracted and resold.

An additional challenge is the introduction of new lithium salts into the electrolyte to improve performance [53]. Separation of these salts will be very difficult to achieve in an economically feasible manner. If these salts cannot be separated, there may be a very limited market for the mixed salts. Alternatively, this may require manufacture and possibly product-specific processing to enable the reuse of the salts by those manufacturers. However, during the lifespan of batteries, the choice of electrolytes in new batteries may change, making the recycled electrolyte obsolete. This would relegate any recovered salts to chemical feedstocks.

Apart from the issues with separation, the lack of stability of the salts in contact with moisture adds an additional challenge to recycling [50]. Performing the entire recovery process in a dry room would add significant cost and energy usage. An understanding of the breakdown kinetics is needed to design these processes at scale, so that the electrolyte with the required low acid content can be recovered. Additionally, the practical effect of the contact of the electrolyte with other components of the battery, which can effectively trap HF formed during the process, should be explored. Several alternative options can be considered for a full dry room, including inerting the process environments, or simply limiting the exposure time. Understanding the practical air stability of electrolytes can be difficult experimentally since they will be highly scale and equipment dependent.

If the ideal electrolyte cannot be directly recycled into a new battery electrolyte, new strategies are necessary to maximise its value while mitigating any environmental impacts. Processes could be developed that enable the spent electrolyte to enter the manufacturing stream for new salts at an earlier stage. This spent electrolyte would likely be concentrated to reduce volume and recover the volatile carbonate solvents before being transferred to a chemical manufacturer.

In conclusion, reclamation and recycling of the electrolyte is clearly an area that requires further development. EOL electrolyte material can introduce toxic compounds through a range of degradation pathways. Additionally, the poor thermal stability of the conducting salt makes the implementation of a commercial recycling process substantially more complicated.

The lack of standardisation of the composition of the electrolyte, and difficulties associated with separating the salt from the solvents is the key challenge behind reprocessing the EOL electrolyte directly into a new LIB. The electrolyte is typically unrecoverable within most large-scale processes, though few companies have managed to extract and reprocess it, achieving a standard that is fit for resale in the chemical industry. However, for substantial advancements, it would prove beneficial if future electrolyte blends are developed by both LIB manufacturers and recyclers, establishing a product that could be implemented into a circular economic model aimed at reducing greenhouse emissions and hazardous LIB waste.

6.6 Conclusion

This chapter pursued two primary objectives: first, to establish a standardised protocol for disassembling a commercial EV LIB pouch cell, and secondly, to recover the electrolyte component from the dissembled LIB pouch cell materials using supercritical fluid extraction (SFE) and solvent extraction techniques.

During the disassembly of the Nissan Leaf EV LIB pouch cell, the components were safely segregated, and each mass was recorded respectively. Despite the overall success of the LIB pouch cell tear down, the recovery of the electrolyte component encountered significant losses attributed to the volatility of the linear carbonates. This limitation was evident in the processing and analytical techniques undertaken, emphasising the imperative need to address this issue for minimising mass loss and optimising electrolyte retention. Prior to processing, the GC-MS technique was used to characterise the electrolyte component, revealing a solvent mixture of DEC, EC, and PC. Subsequent quantification using GC-TCD confirmed a mass ratio of linear to cyclic carbonates as 3:2 (wt.%). The lithium conducting salt was also identified as lithium hexafluorophosphate using ^{19}F and ^{31}P NMR spectroscopy.

The optimisation performed in *Chapter 5* was utilised, and the application of supercritical carbon dioxide at process conditions of 328.2 K and 12.0 MPa successfully extracted the electrolyte component from the anode and separator materials, yielding acceptable results with maximum recovery yields of 47.6% and 44.4%, respectively. The recovery composition of the electrolyte reflected the results observed in *Chapter 5*, a recovery composition of 90:10 wt.% was attained, whereby the selectivity was focused predominantly upon the linear carbonates, in this case DEC.

The main challenge encountered in the SFE ability was extracting the electrolyte component from the porous materials. To enhance the recovery yields, typically, a longer extraction duration and use of modifiers would yield a better extraction and allow a higher overall recovery of components.

Conversely, the solvent extraction technique using acetone performed exceptionally well, achieving a maximum yield of 96.7%. This process also successfully recovered the conducting salt component, lithium hexafluorophosphate, confirmed through NMR and ICP-OES techniques. Notably, higher concentrations of copper and lithium were identified in the solvent extracted electrolyte from the anode material, compared to electrolyte directly taken from the disassembled LIB pouch cell.

Analysis of the graphite anode disassembled directly from the LIB pouch cell and each post extraction process were evaluated using TGA. This technique allowed the mass loss of the residing components in the anode to be observed under high temperatures. Mass deviations between the anode samples subjected to the SFE method were found to be greater in all cases, deviating as much as 4.2% than the anode samples processed using the solvent extraction method. This finding aligned well with the quantified electrolyte mass recovery results obtained from each extraction process using GC-TCD.

Lastly, the discussion emphasised the challenges of LIB electrolyte recovery and recycling, highlighting current and future issues. The reclamation and recycling of the electrolyte component from EOL LIBs emerge as a challenging area that requires further development. The EOL electrolyte material poses a potential risk of introducing toxic compounds through various degradation pathways.

This challenge is compounded by the poor thermal stability of the conducting salt, adding complexity to the implementation of a viable commercial recycling process.

The absence of standardisation in the electrolyte composition, coupled with challenges in separating the salt from the solvents, constitutes a central obstacle to direct reprocessing of EOL electrolyte into new LIBs. Addressing these challenges requires collaborative efforts from LIB manufacturers and recyclers to develop future electrolyte blends. Substantial advancements in this direction would be instrumental in fostering a more sustainable and environmentally friendly approach to LIB recycling.

References – Chapter 6

1. Andreas Breiter ML, Thomas Schuldt, Giulia Siccardo, Nikola Vekić. Battery recycling takes the driver's seat. McKinsey's Advanced Industries Practice. 2023 https://www.mckinsey.com/industries/automotive-and-assembly/our-insights/battery-recycling-takes-the-drivers-seat.

2. Chen M, Ma X, Chen B, Arsenault R, Karlson P, Simon N, et al. Recycling End-of-Life Electric Vehicle Lithium-Ion Batteries. *Joule*. 2019; 3(11): 2622-2646. doi: https://doi.org/10.1016/j.joule.2019.09.014.

3. Islam MT, Iyer-Raniga U. Lithium-Ion Battery Recycling in the Circular Economy: A Review. *Recycling*. 2022; 7(3) https://doi/org/10.3390/recycling7030033.

4. *Concerning batteries and waste batteries amending Directive 2008/98/EC and Regulation (EU) 2019/1020 and repealing Directive 2006/66/EC.* Official Journal of the European Union; 2023.

5. *On batteries and accumulators and waste batteries and accumulators and repealing Directive 91/157/EEC.* Official Journal of the European Union; 2006.

6. Sattar A, Greenwood D, Dowson M, Unadkat P. *Automotive Lithium ion Battery Recycling in the UK*. International Manufacturing Centre (WMG). 2020.

7. Harper GDJ, Kendrick E, Anderson PA, Mrozik W, Christensen P, Lambert S, et al. Roadmap for a sustainable circular economy in lithium-ion and future battery technologies. *Journal of Physics: Energy.* 2023; 5(2): 021501. doi: 10.1088/2515-7655/acaa57.

8. Zhang R, Shi X, Esan OC, An L. Organic Electrolytes Recycling From Spent Lithium-Ion Batteries. *Global Challenges.* 2022; 6(12): 2200050. doi: https://doi.org/10.1002/gch2.202200050.

9. Bajraktarova Valjakova E, Korunoska-Stevkovska V, Georgieva S, Ivanovski K, Bajraktarova Misevska C, Mijoska A, et al. Hydrofluoric Acid: Burns and Systemic Toxicity, Protective Measures, Immediate and Hospital Medical Treatment. *Open Access Macedonian Journal of Medical Sciences.* 2018; 6: 2257-2269. doi: 10.3889/oamjms.2018.429.

10. Ghosh TK, Jasti BR. *Theory and Practice of Contemporary Pharmaceutics.* Taylor & Francis; 2004.

11. Chang Y, Lee J, Wu S, Chen C-C, Shu C. Elevated pressure and temperature effects on flammability hazard assessment for acetone and water solutions. *Journal of Thermal Analysis and Calorimetry.* 2009; 95: 525-534. doi: 10.1007/s10973-008-9460-x.

12. Jinasena A, Amarasinghe A, Amarasinghe P, Prashantha MAB. Extraction and degradation of chlorophyll a and b from Alternanthera sessilis. *Journal of the National Science Foundation of Sri Lanka.* 2016; 44: 11-21. doi: 10.4038/jnsfsr.v44i1.7977.

13. Tan M, Tan C. Effects of extraction solvent system, time and temperature on total phenolic content of henna (Lawsonia inermis) stems. *International Food Research Journal.* 2013; 20: 3117-3123.

14. Liang J, Zago E, Nandasiri R, Khattab R, Eskin NAM, Eck P, et al. Effect of Solvent, Preheating Temperature, and Time on the Ultrasonic Extraction of Phenolic Compounds from Cold-Pressed Hempseed Cake. *Journal of the American Oil Chemists' Society.* 2018; 95(10): 1319-1327. doi: https://doi.org/10.1002/aocs.12108.

15. Teutenberg T. A Brief Definition of High-Temperature Liquid Chromatography. In: *High-Temperature Liquid Chromatography: A User's Guide for Method Development*. The Royal Society of Chemistry; 2010. p. 3.

16. Yang H, Zhuang GV, Ross PN. Thermal stability of LiPF6 salt and Li-ion battery electrolytes containing LiPF6. *Journal of Power Sources.* 2006; 161(1): 573-579. doi: https://doi.org/10.1016/j.jpowsour.2006.03.058.

17. *Nissan LEAF Teardown: Lithium-ion battery pack structure* https://www.marklines.com/en/report_all/rep1786_201811 [Accessed 29/06/23].

18. Marshall J, Gastol D, Sommerville R, Middleton B, Goodship V, Kendrick E. Disassembly of Li Ion Cells—Characterization and Safety Considerations of a Recycling Scheme. *Metals.* 2020; 10(6): 773. https://www.mdpi.com/2075-4701/10/6/773.

19. Ribière P, Grugeon S, Morcrette M, Boyanov S, Laruelle S, Marlair G. Investigation on the fire-induced hazards of Li-ion battery cells by fire calorimetry. *Energy and Environmental Science.* 2012; 5(1): 5271-5280. doi: https://doi.org/10.1039/C1EE02218K.

20. Wang Q, Ping P, Zhao X, Chu G, Sun J, Chen C. Thermal runaway caused fire and explosion of lithium ion battery. *Journal of Power Sources.* 2012; 208: 210-224. doi: https://doi.org/10.1016/j.jpowsour.2012.02.038.

21. Zhang Y, Huld F, Lu S, Jektvik C, Lou F, Yu Z. Revisiting Polytetrafluorethylene Binder for Solvent-Free Lithium-Ion Battery Anode Fabrication. *Batteries*. 2022; 8(6) https://doi/org/10.3390/batteries8060057.

22. Tao R, Steinhoff B, Sun X-G, Sardo K, Skelly B, Meyer HM, et al. High-throughput and high-performance lithium-ion batteries via dry processing. *Chemical Engineering Journal.* 2023; 471: 144300. doi: https://doi.org/10.1016/j.cej.2023.144300.

23. Sauter C, Zahn R, Wood V. Understanding Electrolyte Infilling of Lithium Ion Batteries. *Journal of The Electrochemical Society.* 2020; 167(10): 100546. doi: 10.1149/1945-7111/ab9bfd.

24. Vu A, Qian Y, Stein A. Porous Electrode Materials for Lithium-Ion Batteries – How to Prepare Them and What Makes Them Special. *Advanced Energy Materials.* 2012; 2(9): 1056-1085. doi: https://doi.org/10.1002/aenm.201200320.

25. Xu M, Hao L, Liu Y, Li W, Xing L, Li B. Experimental and Theoretical Investigations of Dimethylacetamide (DMAc) as Electrolyte Stabilizing Additive for Lithium Ion Batteries. *The Journal of Physical Chemistry C.* 2011; 115(13): 6085-6094. doi: 10.1021/jp109562u.

26. Han F, Chang Z, Liu X, Li A, Wang J, Ding H, et al. Research Status of Low-Temperature Electrolyte Additives for Lithium-ion Batteries. *Journal of Physics: Conference Series.* 2021; 2009(1): 012069. doi: 10.1088/1742-6596/2009/1/012069.

27. Mauger A, Julien CM, Paolella A, Armand M, Zaghib K. A comprehensive review of lithium salts and beyond for rechargeable batteries: Progress and perspectives. *Materials Science and Engineering: R: Reports.* 2018; 134: 1-21. doi: https://doi.org/10.1016/j.mser.2018.07.001.

28. Zhang J, Wang D-W, Lv W, Qin L, Niu S, Zhang S, et al. Ethers Illume Sodium-Based Battery Chemistry: Uniqueness, Surprise, and Challenges. *Advanced Energy Materials.* 2018; 8: 1801361. doi: 10.1002/aenm.201801361.

29. Lu ZX, Mu KW, Zhang ZY, Luo Q, Yin YH, Liu XB, et al. A porous current collector cleaner enables thin cathode electrolyte interphase on LiCoO2 for stable high-voltage cycling. *Journal of Materials Chemistry A.* 2021; 9(47): 26989-26998. doi: 10.1039/D1TA07268D.

30. Yang C, Lai H, Liu Z, Ma P. Densities and Viscosities of Diethyl Carbonate + Toluene, + Methanol, and + 2-Propanol from (293.15 to 363.15) K. *Journal of Chemical and Engineering Data.* 2006; 51(2): 584-589. doi: 10.1021/je050414d.

31. Melin T, Lundström R, Berg EJ. Revisiting the Ethylene Carbonate–Propylene Carbonate Mystery with Operando Characterization. *Advanced Materials Interfaces.* 2022; 9(8): 2101258. doi: https://doi.org/10.1002/admi.202101258.

32. Rajagopalan Kannan DR, Terala PK, Moss PL, Weatherspoon MH. Analysis of the Separator Thickness and Porosity on the Performance of Lithium-Ion Batteries. *International Journal of Electrochemistry.* 2018; 2018: 1925708. doi: 10.1155/2018/1925708.

33. Pham TD, Bin Faheem A, Kim J, Kwak K, Lee K-K. Non-flammable electrolytes based on a fluorine-free salt for safe and high-voltage lithium metal batteries. *Electrochimica Acta.* 2023; 458: 142496. doi: https://doi.org/10.1016/j.electacta.2023.142496.

34. Grützke M, Mönnighoff X, Horsthemke F, Kraft V, Winter M, Nowak S. Extraction of lithium-ion battery electrolytes with liquid and supercritical carbon dioxide and additional solvents. *RSC Advances.* 2015; 5(54): 43209-43217. doi: 10.1039/c5ra04451k.

35. Lin F, Liu D, Maiti Das S, Prempeh N, Hua Y, Lu J. Recent Progress in Heavy Metal Extraction by Supercritical CO2 Fluids. *Industrial & Engineering Chemistry Research.* 2014; 53(5): 1866-1877. doi: 10.1021/ie4035708.

36. Bertuol DA, Amado FR, Cruz ED, Tanabe EH. Chapter 5 - Metal recovery using supercritical carbon dioxide. In: Inamuddin, Asiri AM, Isloor AM, (eds.) *Green Sustainable Process for Chemical and Environmental Engineering and Science*. Elsevier; 2020. p. 85-103.

37. Babel S, del Mundo Dacera D. Heavy metal removal from contaminated sludge for land application: A review. *Waste Management.* 2006; 26(9): 988-1004. doi: https://doi.org/10.1016/j.wasman.2005.09.017.

38. Langner T, Sieber T, Acker J. Studies on the deposition of copper in lithium-ion batteries during the deep discharge process. *Scientific Reports.* 2021; 11(1): 6316. doi: 10.1038/s41598-021-85575-x.

39. Guo R, Lu L, Ouyang M, Feng X. Mechanism of the entire overdischarge process and overdischarge-induced internal short circuit in lithium-ion batteries. *Scientific Reports.* 2016; 6(1): 30248. doi: 10.1038/srep30248.

40. Purdy AP, Godbey D, Buckley L. The dissolution of copper in common solvents used for low dielectric polymers. *Thin Solid Films.* 1997; 308-309: 486-489. doi: https://doi.org/10.1016/S0040-6090(97)00489-6.

41. Kim Y-O, Park S-M. Intercalation Mechanism of Lithium Ions into Graphite Layers Studied by Nuclear Magnetic Resonance and Impedance Experiments. *Journal of The Electrochemical Society.* 2001; 148(3): A194. doi: 10.1149/1.1345870.

42. Liu H, Yang F, Xiang M, Cao Y, Wu T. Development of Multilayer Polypropylene Separators for Lithium-Ion Batteries via an Industrial Process. *Industrial & Engineering Chemistry Research.* 2021; 60(30): 11611-11620. doi: 10.1021/acs.iecr.1c01577.

43. Roh N-S, Dunn BC, Eyring EM, Pugmire RJ, Meuzelaar HLC. Production of diethyl carbonate from ethanol and carbon monoxide over a heterogeneous catalytic flow reactor. *Fuel Processing Technology.* 2003; 83(1): 27-38. doi: https://doi.org/10.1016/S0378-3820(03)00079-1.

44. Kock LD, Lekgoathi MDS, Crouse PL, Vilakazi BM. Solid state vibrational spectroscopy of anhydrous lithium hexafluorophosphate (LiPF6). *Journal of Molecular Structure.* 2012; 1026: 145-149. doi: https://doi.org/10.1016/j.molstruc.2012.05.053.

45. Zinigrad E, Larush-Asraf L, Gnanaraj JS, Sprecher M, Aurbach D. On the thermal stability of LiPF6. *Thermochimica Acta.* 2005; 438(1): 184-191. doi: https://doi.org/10.1016/j.tca.2005.09.006.

46. Yaws CL. *Thermophysical Properties of Chemicals and Hydrocarbons.* Elsevier Science; 2014.

47. Wypych A, Wypych G. 3 - Solvents. In: Wypych A, Wypych G, (eds.) *Databook of Green Solvents (Second Edition)*. ChemTec Publishing; 2019. p. 19-584.

48. Liu P, Mi X, Zhao H, Cai L, Luo F, Liu C, et al. Effects of incineration and pyrolysis on removal of organics and liberation of cathode active materials derived from spent ternary lithium-ion batteries. *Waste Management.* 2023; 169: 342-350. doi: https://doi.org/10.1016/j.wasman.2023.07.025.

49. Mühlbauer MJ, Petz D, Baran V, Dolotko O, Hofmann M, Kostecki R, et al. Inhomogeneous distribution of lithium and electrolyte in aged Li-ion cylindrical cells. *Journal of Power Sources.* 2020; 475: 228690. doi: https://doi.org/10.1016/j.jpowsour.2020.228690.

50. Hui Yang GVZ, Philip N. Ross, Jr. . *Journal of Power Sources.* Thermal Stability of LiPF6 Salt and Li-ion Battery Electrolytes Containing LiPF6. 161. Berkeley, CA 94720: University of California 2006.

51. Grutzke M, Kruger S, Kraft V, Vortmann B, Rothermel S, Winter M, et al. Investigation of the Storage Behavior of Shredded Lithium-Ion Batteries from Electric Vehicles for Recycling Purposes. *Chemsuschem.* 2015; 8(20): 3433-3438. doi: 10.1002/cssc.201500920.

52. Seo DM, Reininger S, Kutcher M, Redmond K, Euler WB, Lucht BL. Role of Mixed Solvation and Ion Pairing in the Solution Structure of Lithium Ion Battery Electrolytes. *The Journal of Physical Chemistry C.* 2015; 119(25): 14038-14046. doi: 10.1021/acs.jpcc.5b03694.

53. Du Z, Wood DL, Belharouak I. Enabling fast charging of high energy density Li-ion cells with high lithium ion transport electrolytes. *Electrochemistry Communications.* 2019; 103: 109-113. doi: https://doi.org/10.1016/j.elecom.2019.04.013.

Chapter 7: Conclusions and Recommendations for Future Work

7.1 Concluding Remarks

The primary aim of this research is "*to assess and propose a viable and sustainable process for recovering the electrolyte component of LIBs used in commercial EVs through the application of pressurised carbon dioxide extraction*". A thorough investigation was carried out to achieve this objective. The concluding remarks of the research are presented below, encapsulating each experimental chapter.

Solubility measurements of LIB electrolyte components in carbon dioxide explored binary systems of CO_2 + DMC, CO_2 + EMC, and CO_2 + EC, under three different temperature conditions of 298.2, 313.2, and 328.2 K, with pressure conditions ranging between 0.12 – 14.1 MPa. Both binary systems with DMC and EMC were modelled using the PR EoS. The correlation between the experimental and modelled values was in good agreement, and the maximum deviation of the mole fraction in terms of AARD was calculated as 0.88 and 1.02% for both systems, respectively. Similarly, the DMC binary system was modelled using CPA EoS, establishing a slightly more accurate correlation than the PR EoS and producing a mole fraction AARD value of 0.75% between model and experimental values. Finally, the validation of the EC binary system was assessed using two semi-empirical equations, namely, Chrastil, and Méndez-Santiago and Teja (MST) models. The MST model exhibited a marginally better fit than the Chrastil model, resulting in an AARD of 12.7%, compared with 14.5%.

DMC exhibited the highest solubility in carbon dioxide in both binary and quaternary systems. This property was attributed to its high vapour pressure and symmetrical structure. EC exhibited the lowest solubility in carbon dioxide, possessing a considerably lower vapour pressure and high polarity due to its asymmetric structure. Within the constraints of the system parameters explored, the linear carbonates required low pressure and high temperature conditions to promote their solubility. In contrast, EC required high pressure and low temperature to enhance

its dissolution. As the electrolyte incorporates a blend of solvents, a multicomponent system (CO_2 + DMC + EMC + EC) was introduced in a gravimetric ratio of 1:1:1. The quaternary system was measured under the identical temperature points of the binary systems at a pressure ranging from 2.1 to 10.0 MPa. The established quaternary system generally exhibited the same behaviour as observed in the binary systems. However, an interesting finding was the enhancement of EC's solubility. This was attributed to DMC and EMC, whereby both linear carbonates were discovered to act as co-solvent under all isotherms.

The findings acquired from the phase equilibria studies were utilised in a pressurised fluid extraction process. Pressurised carbon dioxide was employed to extract an artificially created LIB electrolyte incorporating a homogeneous mixture comprising DMC, EMC, and EC in a mass ratio of 1:1:1 and weighing 1.5 g. The initial optimisation focused on the process flowrate and extraction duration. A dynamic flowrate was identified to be most effective between 2.4 – 2.6 L/min, essentially where the solute saturation in carbon dioxide reaches its maximum threshold.

Following the flowrate optimisation, extraction durations from 30 to 480 minutes were conducted to assess the extraction kinetics between subcritical (313.2 K, 6.0 MPa) and supercritical (328.2 K, 12.0 MPa) carbon dioxide. Subcritical fluid (SBCF) conditions proved significantly more effective for recovering linear carbonates than the supercritical fluid (SCF) condition. However, the subcritical fluid extraction (SFE) failed to recover the EC component in its entirety and eventually plateaued at 80% after 480 minutes; in contrast, the SFE process performed a complete extraction of all components under an identical time frame.

Central composite design (CCD), a response surface methodology (RSM), was used to optimise and evaluate the combined effects of pressure and temperature to determine their impact on the

overall extraction yield and individual component recovery. The extractions were performed at 298.2, 313.2, and 328.2 K, with system pressures ranging from 3.0 – 12.0 MPa. The overall recovery by component revealed that linear carbonates were more responsive to temperature enhancements across all pressure conditions. This finding was also observed in the phase equilibria studies in the binary systems of each linear carbonate investigated. This outcome emphasises the importance of vapour pressure and confirms that fluid density is not the sole determinant controlling the extraction yield. In comparison, EC demonstrated a strong association with fluid density, consistently appearing in higher concentrations with increasing pressure across all isotherms. Overall, the optimal extraction yield attained from the artificial LIB electrolyte was 70.2%, achieved at a system pressure of 12.0 MPa and a temperature of 328.2 K.

Despite the overall success of the QCR Nissan Leaf (gen 1) EV LIB pouch cell disassembly, the electrolyte segregation and collection of each respective component introduced significant challenges. Firstly, at least 60% of the total electrolyte by mass is trapped in the electrode and separator components, which makes the separation and recovery process complex. Additionally, a large fraction of the electrolyte component vaporises instantly once the aluminium casing of the LIB pouch cell is breached, and the electrode sheets are separated and exposed to air. This is due to the volatility of linear carbonates. Early analysis of the electrolyte solvents in the LIB pouch cell revealed a mix of linear (DEC) and cyclic (EC and PC) carbonates in a mass ratio of 3:2, respectively. This composition was confirmed using GC-MS and GC-TCD techniques. The lithium conducting salt was also identified as lithium hexafluorophosphate using ^{19}F and ^{31}P NMR spectroscopy.

Supercritical carbon dioxide extraction was performed at 328.2 K and 12.0 MPa under a flowrate of 6 g/min for 60 minutes of dynamic and 45 minutes of static operation. The extraction

generated satisfactory results, where a maximum recovery yield of 47.6% and 44.4% from the anode and separator materials was achieved, respectively. Although the linear carbonate was DEC, the solubility behaviour of this component was very similar to both DMC and EMC.

A fundamental challenge experienced with this technique was the difficulty in extracting the electrolyte component from the subsurface of each porous material. However, implementing a longer extraction duration and the application of modifiers can overcome this limitation and enhance the recovery yields. In contrast, the solvent extraction technique using acetone demonstrated an exceptional performance. Under an HPV temperature of 323.2 K and pump flowrate of 6.5 L/min for 165 minutes, the process achieved a maximum yield of 96.7%. This method also proved successful in recovering lithium, confirmed using the ICP-OES technique. Trace amounts of lithium were detected in the SCF extracted electrolyte. In contrast, in the solvent extracted electrolyte, the lithium concentration was found to be as high as in the electrolyte obtained from the disassembled LIB pouch cell. However, additional research is required to determine whether this method is practical and if the separation from the electrolyte component is feasible. Additionally, high concentrations of the transition metals, in particular, copper, were discovered in the solvent extracted electrolyte. This observation is likely to be a consequence of the oxidation of copper once the LIB pouch cell is completely discharged to 0 V. As acetone is incapable of dissolving copper, the smaller copper particles were likely suspended in the solution and then dissolved in the nitric acid solution as part of their preparation for ICP-OES.

Finally, TGA studies were performed to determine the proportion of electrolyte components residing in the graphite anode. Anode samples obtained directly from the dissembled LIB pouch cell and the post-extraction process were subjected to high temperatures to observe their mass deviations. The results aligned well with the findings from the extraction processes. As

expected, the anode samples subjected to the supercritical extraction process exhibited larger mass loss, up to 4.2%, than samples subjected to the solvent extraction process.

7.2 Recommendations for Future Work

Based on the key findings established in this research, several areas are identified for improvement and further investigation.

Regarding process improvements, the analytical solubility measurements were performed using an offline quantification technique. However, employing an on-line sampling method can improve the phase equilibria measurements. This can be achieved by installing a six-port sampling valve connected between the high-pressure vessel (HPV) and the GC-TCD, allowing a more prompt and reliable analysis [1, 2]. Additionally, the control of the flowrate of carbon dioxide in both experimental rigs was regulated manually using micro metering valves. This proved challenging when simultaneously attempting to control the dynamic flowrate at 6 g/min, under a system pressure of 12.0 MPa, and holding the internal pressure of the minor pressure vessel (MPV) at 0.5 MPa. Therefore, although comparatively more expensive, implementing an automated flow control pump or process control valves would alleviate this issue.

The solvent extraction process demonstrated the capability to recover a wide range of LIB electrolyte components. *Grützke et al.* extracted the lithium conducting salt using liquid carbon dioxide and modifiers of an 18650 LIB cell [3]. Expanding upon this principle, it would be interesting to explore the combination of pressurised carbon dioxide with a range of chelating agents to target and recover the metal components in the LIB material.

The bridge to commercialisation lies in the economics behind the process. Two MEng students under the authors supervision assessed the feasibility of “recycling EV LIB electrolyte” using a techno-economic assessment (TEA). The underlying findings of the research revealed the

SFE process using carbon dioxide to be economically infeasible, based solely on the recovery of the electrolyte solvent component. When accounting for the high capital costs associated with the SFE process, the technique needs to guarantee the recovery of the lithium conducting salt element to be marginally profitable. In the experimental research, the solvent extraction method proved effective in recovering the lithium component, whereas the SCF extraction technique was incapable. However, the application of a co-solvent in conjunction with the SCF extraction technique may prove to be a viable method.

Further, research is required to validate the economic viability of the three leading electrolyte recovery techniques: solvent extraction, supercritical carbon dioxide extraction, and vacuum extraction. Additional research in this domain would prove extremely useful, particularly with governmental organisations, regulators, and private investors.

Various difficulties were encountered when disassembling the Nissan Leaf (gen 1) EV LIB pouch cell. The most significant was the loss of linear carbonates due to vaporisation. Preliminary work was initiated to create a process enabling the LIB pouch cell to be exposed to the supercritical carbon dioxide technique in its entirety. In theory, this would enable the extraction of the electrolyte component from the LIB pouch cell without encountering the mass losses associated with the vaporisation of linear carbonates. Initial thoughts suggest that the application of a larger vessel and an internal cutting mechanism to expose the pouch cell before pressurising the HPV could potentially offer a viable solution.

The recycling of spent LIBs has been widely studied and implemented; substantial progress has been accomplished in recycling of the electrodes and current collectors. However, the attention and interest in EOL LIB electrolyte recovery falls short at both research and industrial levels.

Improper disposal of spent LIBs, especially the aged organic electrolyte, can cause severe environmental pollution and threats to human health [4].

The following phase of research must address the recovery of end-of-life LIB electrolyte material. It is hoped that the findings from this research thesis have made an informative and valuable contribution towards achieving this critical objective.

References – Chapter 7

1. Sim Yeoh H, Hean Chong G, Mohd Azahan N, Abdul Rahman R, Yaw Choong TS. Solubility Measurement Method and Mathematical Modeling in Supercritical Fluids. *Engineering Journal.* 2013; 17(3): 67-78. doi: 10.4186/ej.2013.17.3.67.

2. Raal JD, Mühlbauer AL. *Phase equilibria : measurement and computation.* Series in chemical and mechanical engineering. Washington, D.C.: Taylor & Francis Washington, D.C.; 1998.

3. Grützke M, Mönnighoff X, Horsthemke F, Kraft V, Winter M, Nowak S. Extraction of lithium-ion battery electrolytes with liquid and supercritical carbon dioxide and additional solvents. *RSC Advances.* 2015; 5(54): 43209-43217. doi: 10.1039/c5ra04451k.

4. Zhang R, Shi X, Esan OC, An L. Organic Electrolytes Recycling From Spent Lithium-Ion Batteries. *Global Challenges.* 2022; 6(12): 2200050. doi: https://doi.org/10.1002/gch2.202200050.

Appendices

List of Appendices

A1: Databank of Compounds

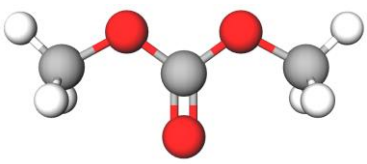

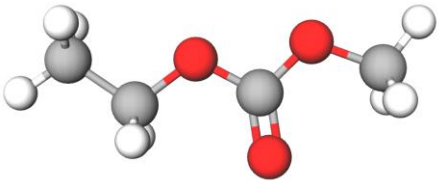

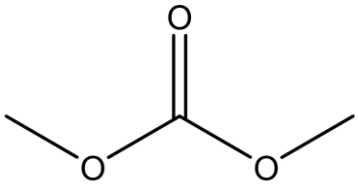

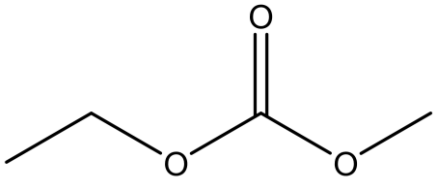

Name	Dimethyl carbonate (DMC)	Ethyl methyl carbonate (EMC)
Common name	Carbonic acid dimethyl ester	Carbonic acid ethyl methyl ester
CAS number	616-38-6	623-53-0
Molecular formula	$C_3H_6O_3$	$C_4H_8O_3$
Molecular weight (g/mol)	90.08	104.11
Density (g/cm^3)	1.279	1.012
Boiling point (K)	363.11	380.65
Melting point (K)	277.06	259.15
Flash point (K)	335.25	297.05
Vapour pressure (Kpa)	5.3 (293.15 K)	3.9 (298.15)

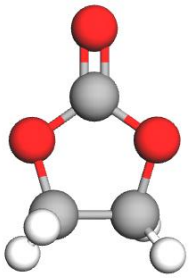

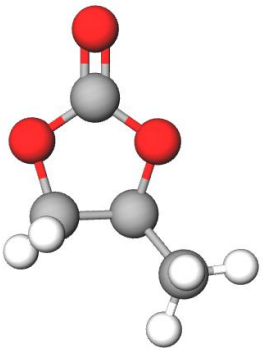

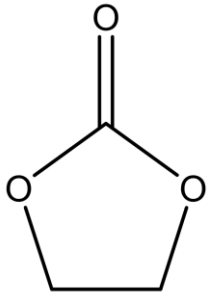

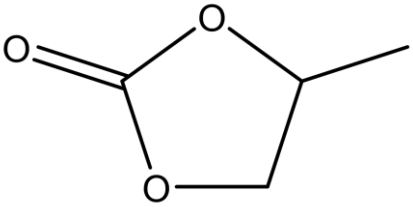

Name	Ethylene carbonate (EC)	Propylene carbonate (PC)
Common name	1,3-dioxolane-2-one	4-methyl-1,3-dioxolan-2-one
CAS number	96-49-1	108-32-7
Molecular formula	$C_3H_4O_3$	$C_4H_6O_3$
Molecular weight (g/mol)	88.06	102.09
Density (g/cm^3)	1.321	1.205
Boiling point (K)	521.35	514.85
Melting point (K)	309.55	223.95
Flash point (K)	425.0	405.0
Vapour pressure (Kpa)	0.0013 (293.15 K)	0.0027 (293.15 K)

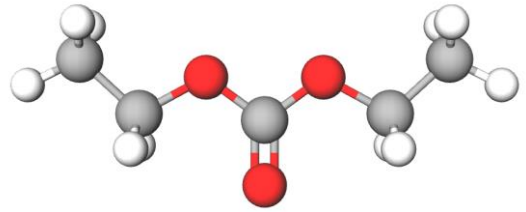

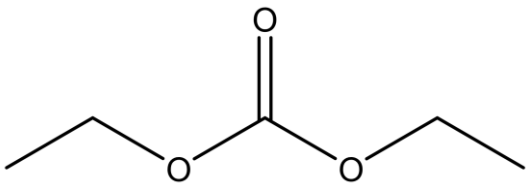

Name	Diethyl carbonate (DEC)
Common name	Carbonic acid diethyl ester
CAS number	105-58-8
Molecular formula	$C_5H_{10}O_3$
Molecular weight (g/mol)	118.13
Density (g/cm^3)	1.217
Boiling point (K)	398.15
Melting point (K)	230.15
Flash point (K)	298.15
Vapour pressure (Kpa)	1.066 (293.15 K)

References (A1)

[1] S. Hess, M. Wohlfahrt-Mehrens, M. Wachtler. Flammability of Li-Ion Battery Electrolytes: Flash Point and Self-Extinguishing Time Measurements. Journal of The Electrochemical Society. (2015).162(2):A3084. Doi:10.1149/2.0121502jes.

[2] A. Wypych, G. Wypych. 3 - Solvents. In: A. Wypych, G. Wypych, editors. Databook of Green Solvents (Second Edition): ChemTec Publishing; (2019). p. 19-584.

[3] Critical Properties and Acentric Factor - Organic Compounds. Yaws' Critical Property Data for Chemical Engineers and Chemists: Knovel (2012). https://app.knovel.com/hotlink/toc/id:kpYCPDCECD/yaws-critical-property/yaws-critical-property.

[4] V. Pokorný, V. Štejfa, M. Fulem, C. Červinka, K. Růžička. Vapor Pressures and Thermophysical Properties of Dimethyl Carbonate, Diethyl Carbonate, and Dipropyl Carbonate. J Chem Eng Data. (2017).62(10):3206-3215. Doi:10.1021/acs.jced.7b00295.

A2: Calibration of Thermocouples

The thermocouples installed in the various experimental rigs were calibrated over a range of temperatures, between -5°C – 60°C. Thermocouples were placed in a circulating water bath and a recirculating glycol chiller (temperature dependent). The temperature was measured using an RS Pro RS51 wired digital thermometer capable of measuring temperatures between -30°C to 250°C. The calibration results for each thermocouple are tabulated below in **Table A.2-1**.

Table A.2-1: Calibration of thermocouples

Chapter	Thermocouple	Calibration Temperature (°C)	Recorded Temperature (°C)	Deviation (°C)	Deviation (%)
4/6	TI-01	-10	-10.3	-0.3	3.0
		30	29.9	-0.1	0.3
		70	69.9	-0.1	0.1
4/6	HE-01	-10	-10.4	-0.4	4.0
		30	30.1	+0.1	0.3
		70	70.2	+0.2	0.3
4/6	HE-02	-10	-9.8	+0.2	2.0
		30	29.8	-0.2	0.7
		70	70.1	+0.1	0.1
5	TI-01	-10	-10.3	-0.3	3.0
		30	30.1	+0.1	0.3
		70	70.1	+0.1	0.1

[a]Standard uncertainties are u(T) = 0.1 K

A3: Determination of the Equilibrium Duration

An investigation was conducted to determine the equilibrium time of the EC component in carbon dioxide. The experiment was carried out at an operational temperature of 328.2 K and a system pressure of 11.7 MPa. The vapour phase was sampled as detailed in *Chapter 4: Solubility Measurements of LIB Electrolyte Components in Carbon Dioxide*, **4.3.2.5** *Solute collection and depressurisation*. The solubility was determined across several time intervals to establish the duration at which the CO_2 + EC system reaches equilibrium.

Solubility data has been tabulated and plotted in **Table A.3-1** and **Figure A.3-1**, respectively, as a function of time.

Table A.3-1: Determination of equilibrium time for the binary system, CO_2 + EC[a].

Temperature (K)	Pressure (MPa)	Time interval (hours)	Solubility (g/g)
328.3	11.7	1	0.001214
328.2	11.6	2	0.002453
328.3	11.6	4	0.003538
328.3	11.7	8	0.003972
328.1	11.6	16	0.004021

[a]Standard uncertainties are u(T) = 0.1 K, u(P) = 0.01 MPa

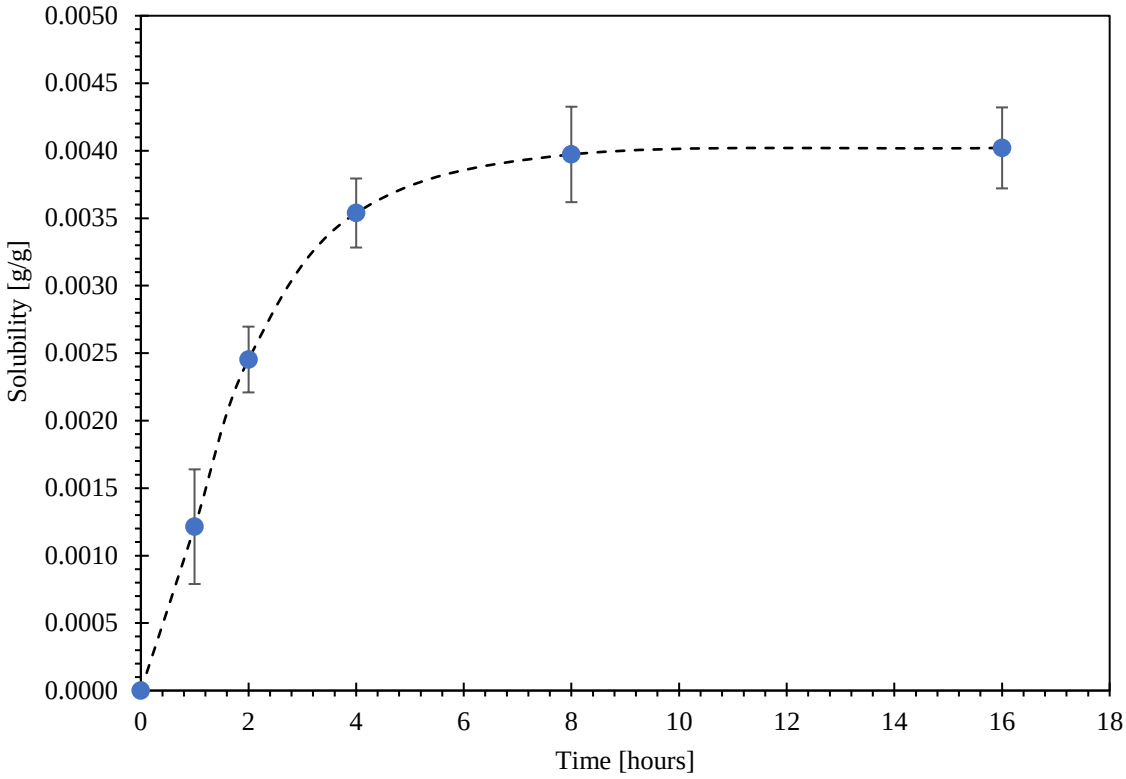

Figure A.3-1: Solubility of CO_2 + EC binary system as a function of time.

In **Figure A.3-1** it can be observed that the solubility of EC in carbon dioxide starts to stabilise between 6-10 hours. Based on this preliminary investigation, the equilibrium was allowed to equalise for at least 10 hours. However, due to the long time required for equilibrium, the system was left overnight, allowing for a total of 16 hours for equilibrium. Since, EC is a solid at room temperature, its dissolution is less than that of DMC and EMC. Therefore, the same time interval was given to all systems to ensure that they reached equilibrium.

A4: System Pressure Drop Between Samplings

After the system reached an equilibrium state, vapour samples were taken through the sampling loop. It was observed that the associated pressure drops caused by the sampling were minimal and did not exceed 1.2% of the total system pressure. In most cases, the samples did not noticeably affect the system pressure, and the depressurisation observed was less than 0.01 MPa, which is the smallest denomination of the HPV internal pressure indicator. However, all samples that did exceed this pressure were recorded. **Figure A4-1** shows the recorded pressure drops caused by the sampling, plotted against the system pressure.

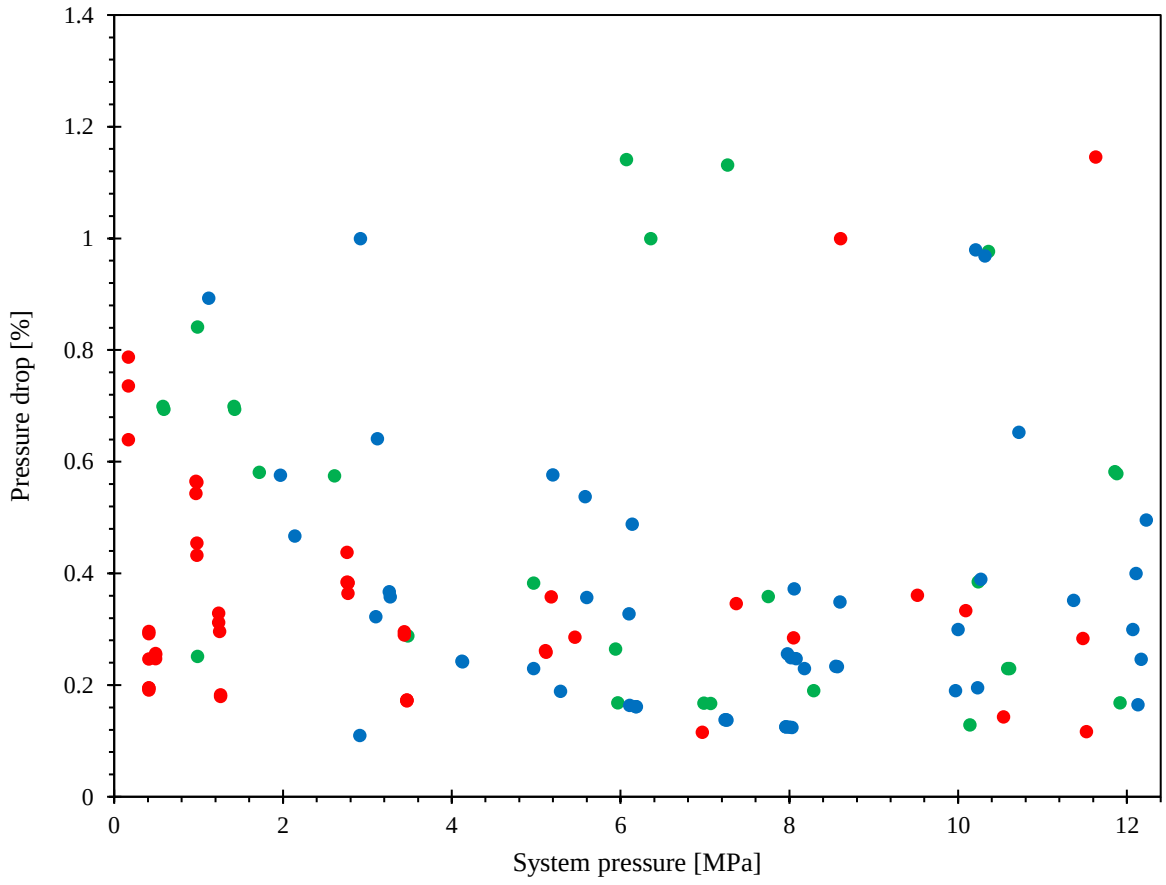

Figure A4-1: Sampling pressure drop as a function of system pressure.
(●) 298.2 K, (●) 313.2 K, (●) 328.2 K.

A5: Optimisation of Flowrate

Table A5-1: The influence of dynamic flowrate of carbon dioxide on the extraction yield of artificial LIB electrolyte. From 1.5 g of sample at conditions of 6.0 MPa and 313.2 K.

Flowrate (L/min)				V (L)	e_{inital} (g)	e_{final} (g)	Extraction yield (%)	S (g/ml)
1	2	3	Avg					
0.55	0.57	0.55	0.56	19.7	1.564	0.126	8.1	6.40
0.54	0.58	0.55	0.56	19.1	1.514	0.097	6.4	5.08
1.03	1.04	1.04	1.04	32.8	1.669	0.194	11.6	5.91
1.04	1.03	0.99	1.02	32.9	1.536	0.226	14.7	6.85
2.01	2.03	2.05	2.03	63.1	1.524	0.337	22.1	6.42
2.03	2.10	2.07	2.07	64.5	1.513	0.309	20.4	4.79
2.52	2.55	2.53	2.53	80.1	1.538	0.387	25.2	4.83
2.47	2.51	2.51	2.50	77.4	1.515	0.415	27.4	5.36
3.06	3.04	3.07	3.06	95.0	1.517	0.332	21.9	3.49
3.04	3.10	3.07	3.07	96.6	1.522	0.370	24.3	3.83
3.52	3.54	3.59	3.55	107.0	1.523	0.334	21.9	3.12
3.52	3.50	3.48	3.50	105.2	1.543	0.302	19.6	2.87
4.45	4.53	4.51	4.50	137.1	1.527	0.283	18.5	2.07
4.52	4.38	4.42	4.44	138.8	1.518	0.319	21.0	2.30

Standard uncertainties are u($\dot{Q}$) = 0.01 L, u(m) = 0.01 mg. t = 30 minutes.

A6: Design of Experiments (DOE)

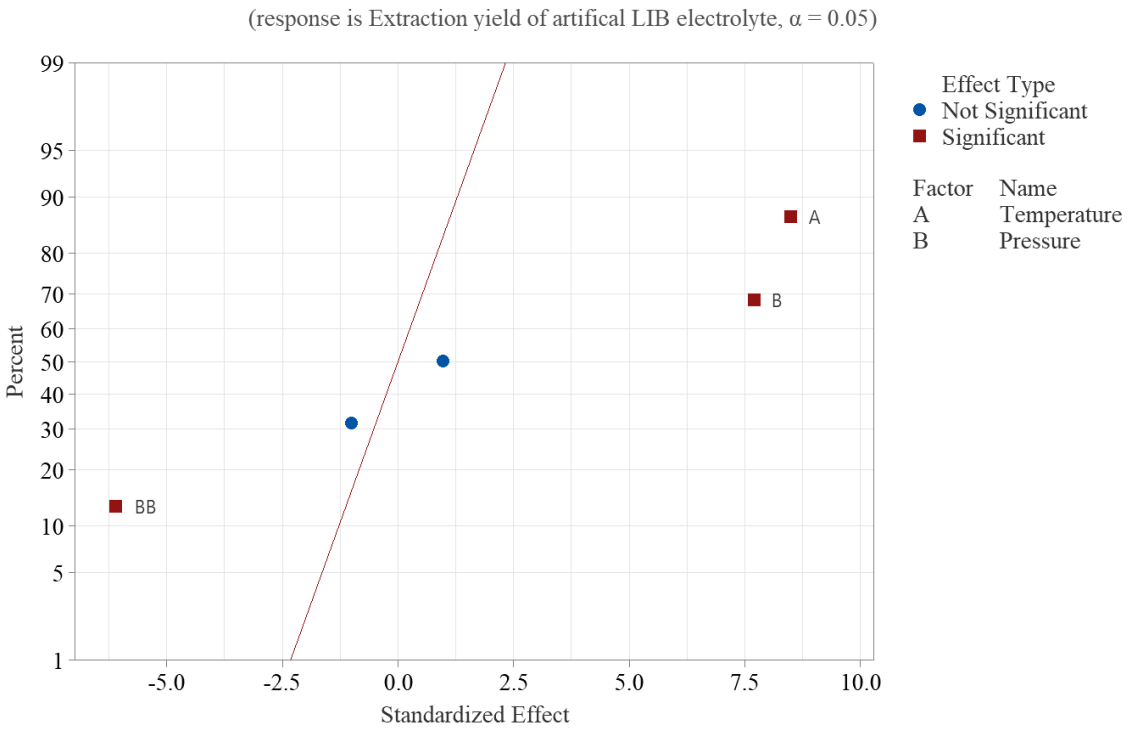

Figure A6-1: Normal plot of effects from the DOE of the extraction of artificial LIB electrolyte, as presented in **Table 5-4**.

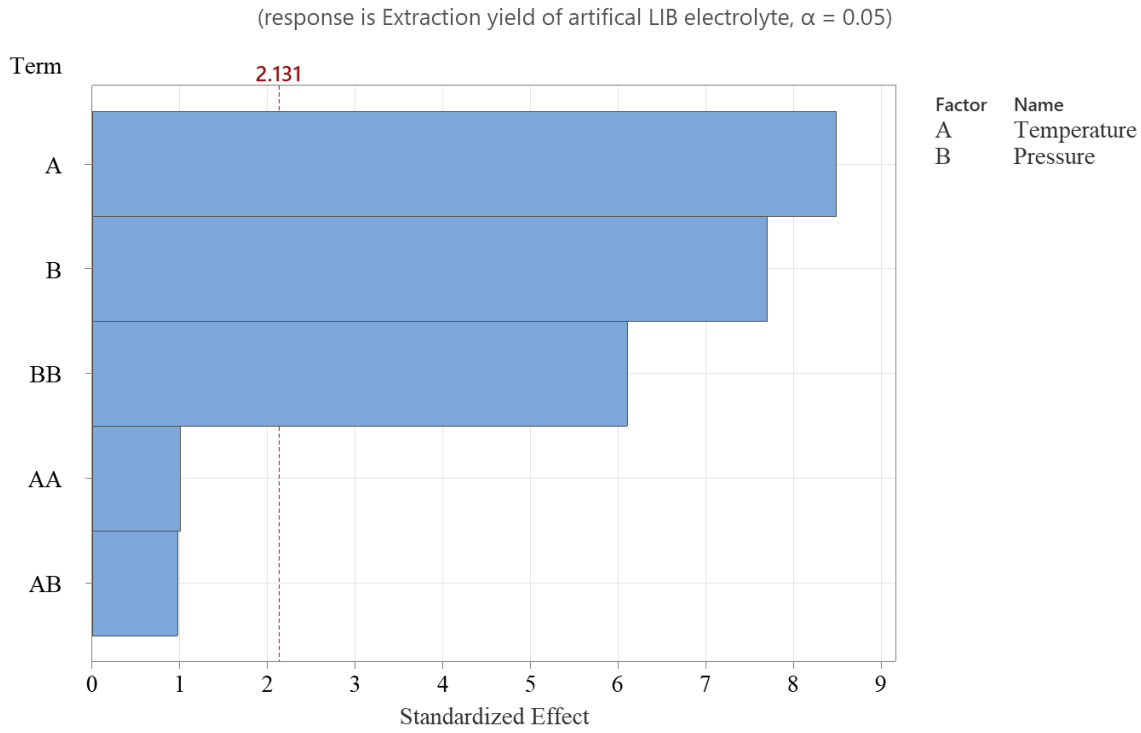

Figure A6-2: Pareto chart of effects from the DOE of the extraction of artificial LIB electrolyte, as presented in **Table 5-4**.

A7: GC-TCD Chromatogram of Nissan Leaf LIB Pouch Cell

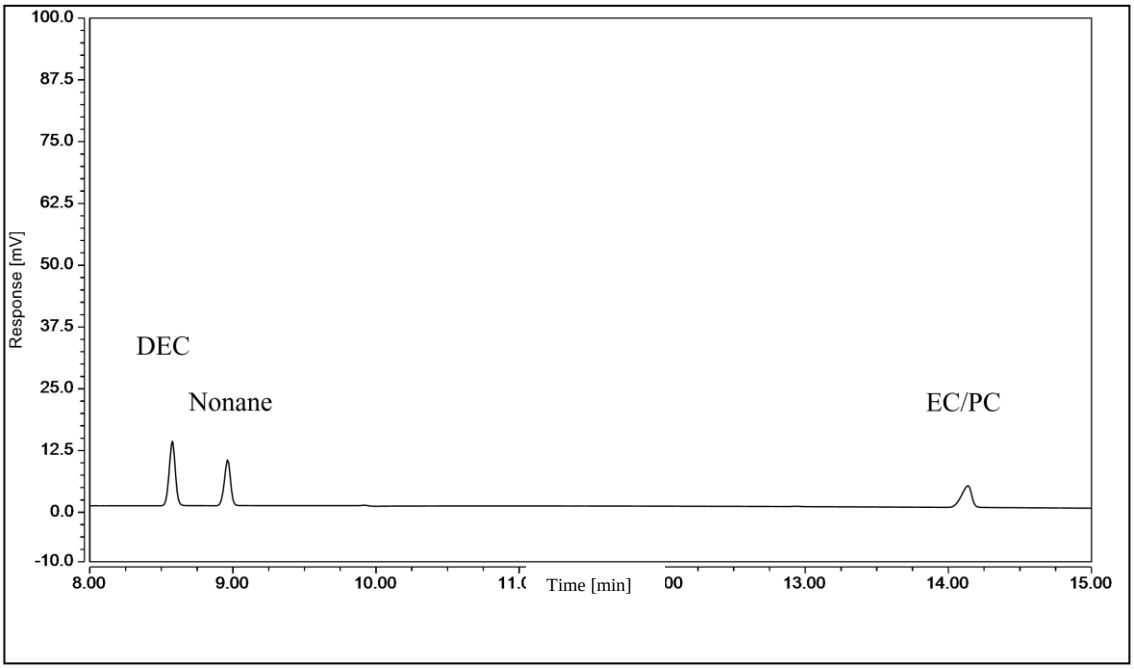

Figure A7-1: GC-TCD chromatogram of Nissan Leaf EV LIB pouch cell electrolyte.

A8: NMR Frequency Table

Table A8-1: NMR Frequencies vs. Bruker Field Strengths.

Isotope		Spin	Nat. Abund. (%)	Receptivity		Larmor Frequencies (MHz) vs. Bruker Field Strengths (Tesla) Freq. to 3 decimals are experimental for IUPAC Standards; freq. to 2 dec. are calculated from magn. moments										
				Natural rel. ^{13}C	Molar rel. ^{1}H	7.04925	9.39798	11.7467	14.0954	16.4442	17.6185	18.7929	19.9673	21.1416	22.3160	23.4904
1	H	1/2	99.9885	5.87E+03	**1.00E+00**	**300.130**	**400.130**	**500.130**	**600.130**	**700.130**	**750.130**	**800.130**	**850.130**	**900.130**	**950.130**	**1000.130**
2	H	1	0.0115	6.52E−03	9.65E−03	46.072	61.422	76.773	92.124	107.474	115.150	122.825	130.500	138.175	145.851	153.526
3	H	1/2		-	1.21E+00	320.131	426.795	533.459	640.123	746.786	800.118	853.450	906.782	960.114	1013.446	1066.778
3	He	1/2	1.34E-04	3.48E−03	4.42E−01	228.636	304.815	380.994	457.173	533.352	571.441	609.531	647.620	685.710	723.799	761.889
6	Li	1	7.59	3.79E+00	8.50E−03	44.167	58.883	73.600	88.316	103.032	110.390	117.748	125.106	132.464	139.822	147.180
7	Li	3/2	92.41	1.59E+03	2.94E−01	116.642	155.506	194.370	233.233	272.097	291.529	310.961	330.393	349.825	369.257	388.688
9	Be	3/2	100.0	8.15E+01	1.39E−02	42.174	56.226	70.277	84.329	98.381	105.407	112.433	119.459	126.485	133.510	140.536
10	B	3	19.9	2.32E+01	1.99E−02	32.245	42.989	53.732	64.476	75.220	80.591	85.963	91.335	96.707	102.079	107.451
11	B	3/2	80.1	7.77E+02	1.65E−01	96.294	128.378	160.462	192.546	224.630	240.672	256.714	272.755	288.797	304.839	320.881
13	C	1/2	1.07	**1.00E+00**	1.59E−02	75.468	100.613	125.758	150.903	176.048	188.620	201.193	213.765	226.338	238.910	251.483
14	N	1	99.636	5.90E+00	1.01E−03	21.688	28.915	36.141	43.367	50.594	54.207	57.820	61.433	65.046	68.659	72.273
15	N	1/2	0.364	2.23E−02	1.04E−03	30.423	40.560	50.697	60.834	70.971	76.039	81.107	86.176	91.244	96.312	101.381
17	O	5/2	0.038	6.50E−02	2.91E−02	40.687	54.243	67.800	81.356	94.913	101.691	108.469	115.248	122.026	128.804	135.582
19	F	1/2	100.0	4.89E+03	8.32E−01	282.404	376.498	470.592	564.686	658.780	705.827	752.874	799.921	846.968	894.015	941.062
21	Ne	3/2	0.27	3.91E−02	2.46E−03	23.693	31.587	39.482	47.376	55.270	59.217	63.165	67.112	71.059	75.006	78.953
23	Na	3/2	100.0	5.45E+02	9.27E−02	79.390	105.842	132.294	158.746	185.198	198.424	211.650	224.876	238.101	251.327	264.553
25	Mg	5/2	10.00	1.58E+00	2.68E−03	18.373	24.494	30.616	36.738	42.859	45.920	48.981	52.042	55.103	58.163	61.224
27	Al	5/2	100.0	1.22E+03	2.07E−01	78.204	104.261	130.318	156.375	182.432	195.460	208.489	221.517	234.546	247.574	260.602
29	Si	1/2	4.685	2.16E+00	7.86E−03	59.627	79.495	99.362	119.229	139.096	149.030	158.963	168.897	178.831	188.764	198.698
31	P	1/2	100.0	3.91E+02	6.65E−02	121.495	161.976	202.457	242.938	283.419	303.659	323.900	344.140	364.380	384.621	404.861
33	S	3/2	0.75	1.00E−01	2.27E−03	23.038	30.714	38.390	46.066	53.742	57.580	61.418	65.256	69.094	72.932	76.770
35	Cl	3/2	75.76	2.10E+01	4.72E−03	29.406	39.204	49.002	58.800	68.598	73.497	78.396	83.295	88.194	93.093	97.992
37	Cl	3/2	24.24	3.88E+00	2.72E−03	24.478	32.634	40.789	48.945	57.101	61.179	65.256	69.334	73.412	77.490	81.568
39	K	3/2	93.258	2.79E+00	5.10E−04	14.005	18.672	23.338	28.004	32.671	35.004	37.337	39.670	42.003	44.337	46.670
41	K	3/2	6.730	3.34E−02	8.44E−05	7.687	10.249	12.810	15.371	17.932	19.213	20.494	21.774	23.055	24.336	25.616
43	Ca	7/2	0.135	5.10E−02	6.43E−03	20.199	26.929	33.659	40.389	47.119	50.484	53.849	57.214	60.579	63.944	67.309
45	Sc	7/2	100.0	1.78E+03	3.02E−01	72.907	97.199	121.490	145.782	170.074	182.220	194.366	206.511	218.657	230.803	242.949
47	Ti	5/2	7.44	9.18E−01	2.10E−03	16.920	22.557	28.195	33.833	39.470	42.289	45.108	47.926	50.745	53.564	56.383
49	Ti	7/2	5.41	1.20E+00	3.78E−03	16.924	22.563	28.203	33.842	39.481	42.300	45.120	47.939	50.759	53.578	56.398
50	V	6	0.250	8.18E−01	5.57E−02	29.924	39.894	49.865	59.835	69.805	74.790	79.775	84.761	89.746	94.731	99.716
51	V	7/2	99.750	2.25E+03	3.84E−01	78.943	105.246	131.549	157.852	184.155	197.306	210.458	223.609	236.761	249.912	263.064
53	Cr	3/2	9.501	5.07E−01	9.08E−04	16.965	22.617	28.270	33.922	39.575	42.401	45.227	48.054	50.880	53.706	56.532
55	Mn	5/2	100.0	1.05E+03	1.79E−01	74.400	99.189	123.978	148.768	173.557	185.951	198.346	210.741	223.135	235.530	247.924
57	Fe	1/2	2.119	4.25E−03	3.42E−05	9.718	12.955	16.193	19.431	22.669	24.288	25.906	27.525	29.144	30.763	32.382
59	Co	7/2	100.0	1.64E+03	2.78E−01	71.212	94.939	118.666	142.393	166.120	177.984	189.847	201.711	213.575	225.438	237.302
61	Ni	3/2	1.1399	2.40E−01	3.59E−03	26.820	35.756	44.692	53.628	62.564	67.032	71.500	75.968	80.436	84.904	89.372
63	Cu	3/2	69.15	3.82E+02	9.39E−02	79.581	106.096	132.612	159.127	185.643	198.901	212.158	225.416	238.674	251.931	265.189
65	Cu	3/2	30.85	2.08E+02	1.15E−01	85.248	113.652	142.055	170.459	198.863	213.065	227.266	241.468	255.670	269.872	284.074
67	Zn	5/2	4.102	6.92E−01	2.87E−03	18.779	25.035	31.292	37.549	43.806	46.934	50.063	53.191	56.319	59.448	62.576
69	Ga	3/2	60.108	2.46E+02	6.97E−02	72.035	96.037	120.038	144.039	168.041	180.041	192.042	204.043	216.043	228.044	240.045
71	Ga	3/2	39.892	3.35E+02	1.43E−01	91.530	122.026	152.523	183.020	213.517	228.765	244.013	259.262	274.510	289.758	305.007

A9: NMR Field Blank Spectra

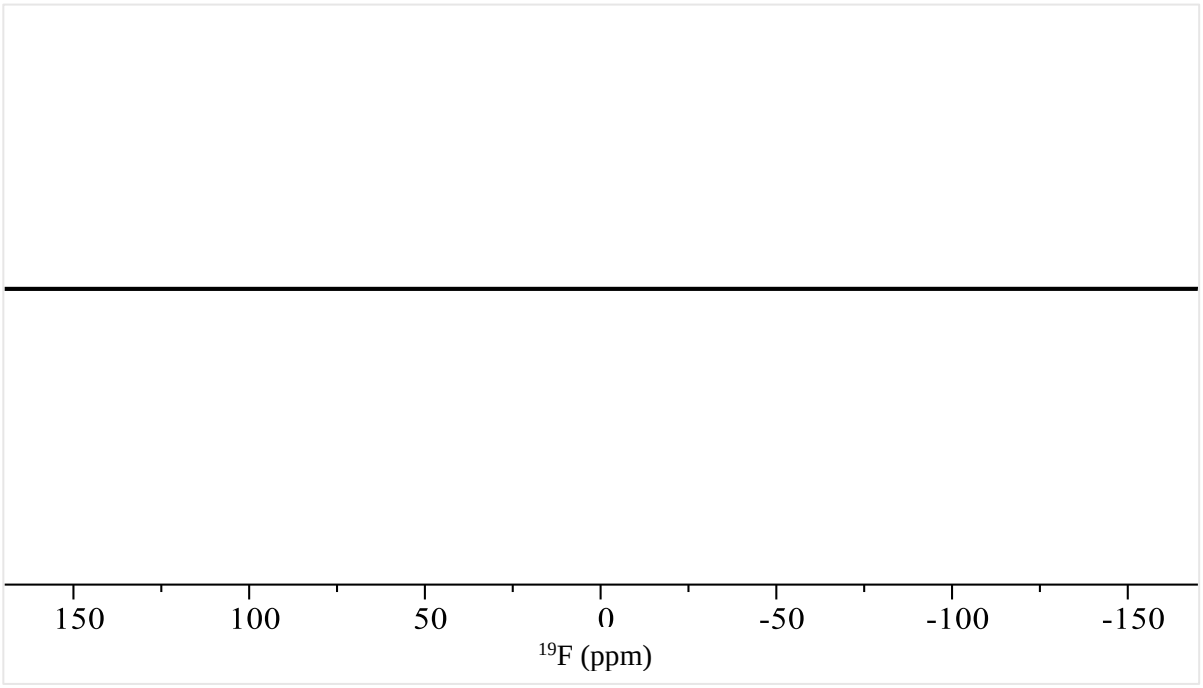

Figure A9-1: ^{19}F NMR field blank spectrum.

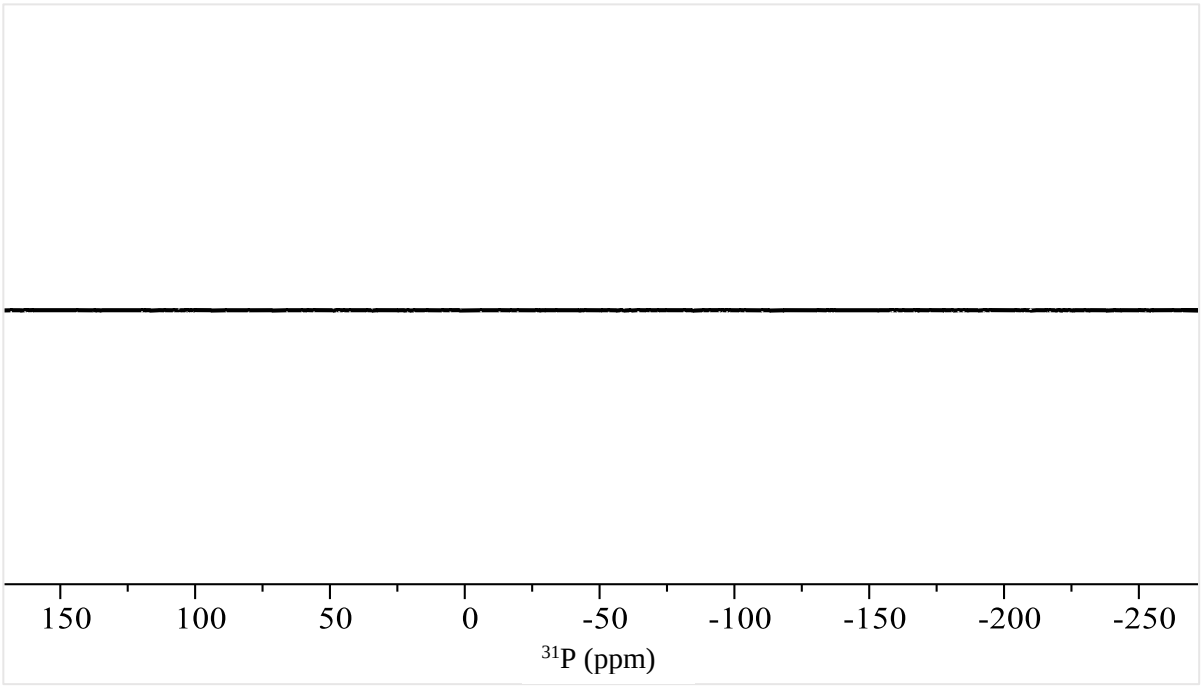

Figure A9-2: ^{31}P NMR field blank spectrum.

A10: NMR Spectroscopy of Pure and Recovered LIB Pouch Cell Electrolyte

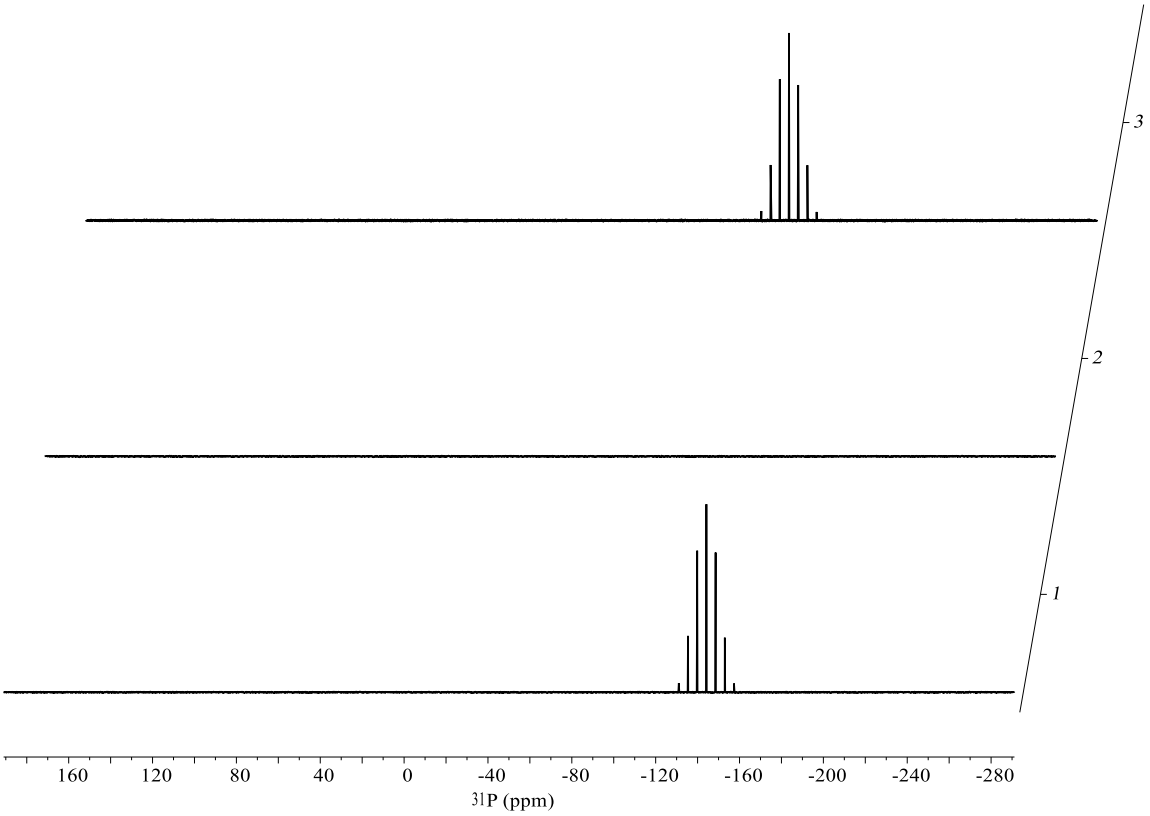

Figure A10-1: ^{31}P NMR of Nissan Leaf EV LIB pouch cell electrolyte; 1) solvent extracted LIB electrolyte, 2) SCF extracted LIB electrolyte, 3) Pure LIB electrolyte.

A11: Supelco ICP Multi-Element Standard Solution IV Certificate of Analysis

Supelco®

www.sigmaaldrich.com

Certificate of Analysis – Reference Material

Producer:	Merck KGaA, Frankfurter Str. 250, 64293 Darmstadt, Germany
Description of CRM:	**ICP multi-element standard solution IV**
Ord. No.:	1.11355.0100
Lot No.:	HC15457555
Composition:	23 elements in HNO_3 Suprapur® 6.5%
Density:	The density of the standard solution is 1.0896 g/cm³ at 20°C.
Method of Analysis:	Inductively coupled plasma optical emission spectrometry (ICP-OES).
Traceability:	This reference material has been measured applying high precision ICP-OES and is traceable to the corresponding **NIST SRM®** as mentioned on page 2. *NIST: National Institute of Standards and Technology, Gaithersburg, USA.*
Storage:	Store at +15°C to +25°C tightly closed in the original container.
Application and correct use:	This reference material is intended for use as **calibration standard** for atomic absorption spectrometry, spectrophotometry and other analytical techniques. Shake well before use and never pipet directly from the original container.
Date of release:	2021/07/27
Minimum shelf life:	2024/04/30
Certificate Version:	1 issued on 2021/07/27

Mass concentration (w/v) ± expanded measurement uncertainty

1.11355.0100
HC15457555

Element	Analysed value mg/l	Uncertainty mg/l	Traceable to SRM®	Batch Code
Ag	1000	± 20	SRM 3151	160729
Al	998	± 10	SRM 3101a	140903
B	997	± 10	SRM 3107	190605
Ba	1000	± 10	SRM 3104a	140909
Bi	1001	± 10	SRM 3106	180815
Ca	999	± 10	SRM 3109a	130213
Cd	999	± 10	SRM 3108	130116
Co	1008	± 10	SRM 3113	190630
Cr	995	± 10	SRM 3112a	170630
Cu	1009	± 10	SRM 3114	120618
Fe	994	± 10	SRM 3126a	140812
Ga	998	± 10	SRM 3119a	140124
In	996	± 10	SRM 3124a	110516
K	1008	± 10	SRM 3141a	140813
Li	998	± 10	SRM 3129a	100714
Mg	999	± 10	SRM 3131a	140110
Mn	999	± 10	SRM 3132	050429
Na	1000	± 10	SRM 3152a	120715
Ni	999	± 10	SRM 3136	120619
Pb	1001	± 10	SRM 3128	101026
Sr	999	± 10	SRM 3153a	990906
Tl	997	± 10	SRM 3158	151215
Zn	998	± 10	SRM 3168a	120629

The expanded measurement uncertainty U is calculated as $U = k \cdot u_{characterisation}$, where $k = 2$ is the coverage factor for a 95% coverage probability and $u_{characterisation}$ is the combined measurement uncertainty in accordance to DIN EN ISO/IEC 17025.

Analytical standard released by
Approving Officer

A. Yildirim

Dipl.-Ing. Ayfer Yildirim
Responsible Manager of LS-OII-QS3

A12: ICP-OES Calibration Plots

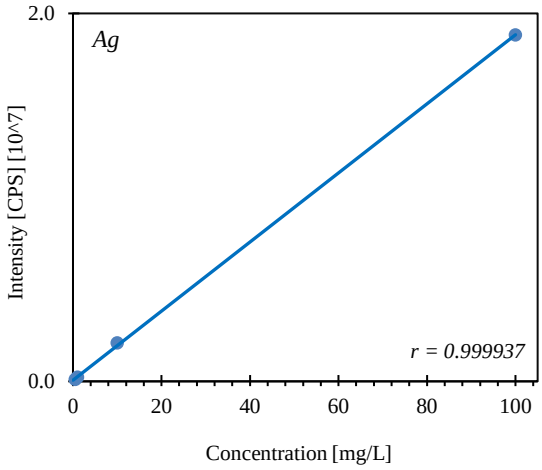

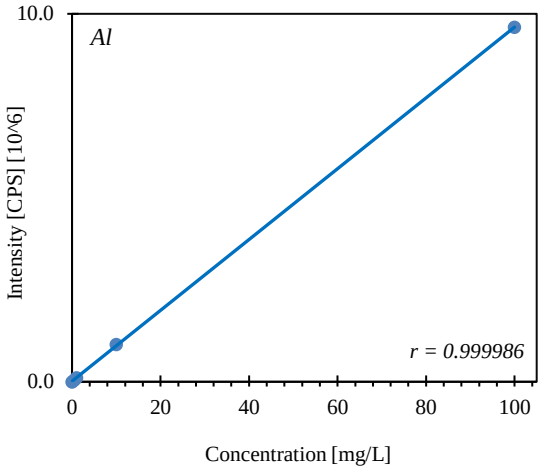

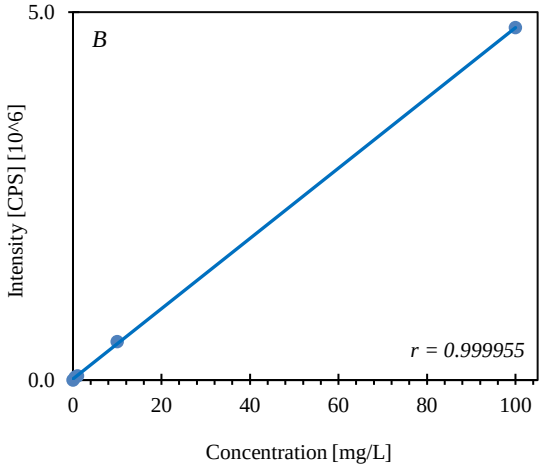

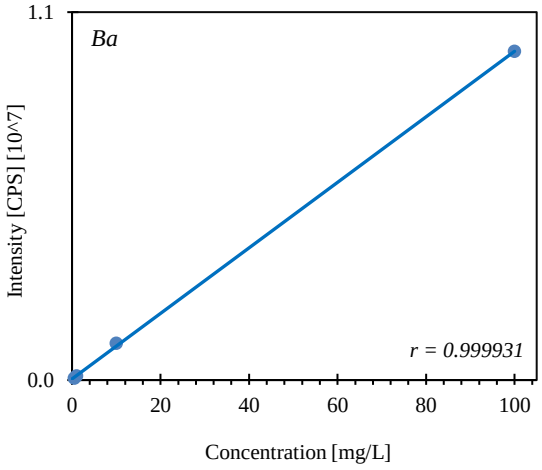

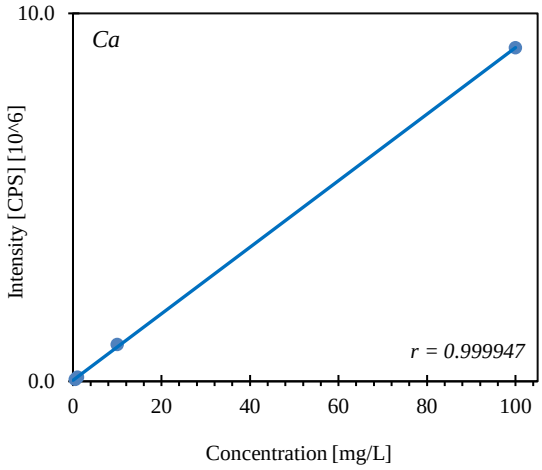
Ca
r = 0.999947
10.0
0.0
Intensity [CPS] [10^6]
0
20
40
60
80
100
Concentration [mg/L]

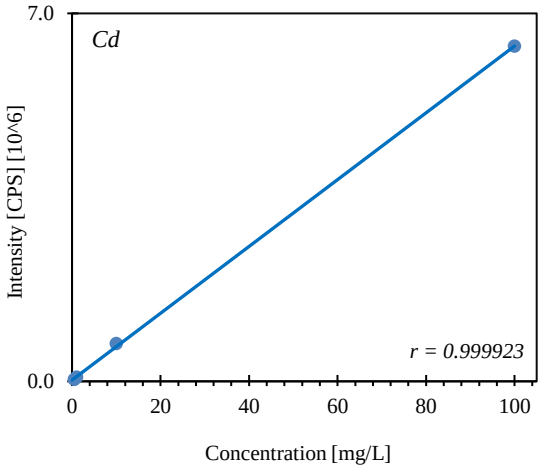
Cd
r = 0.999923
7.0
0.0
Intensity [CPS] [10^6]
0
20
40
60
80
100
Concentration [mg/L]

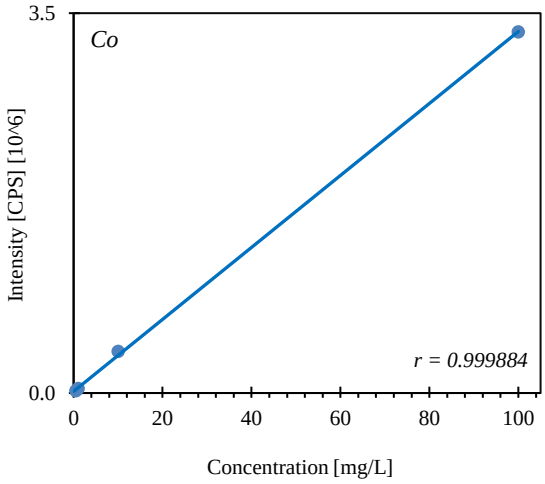
Co
r = 0.999884
3.5
0.0
Intensity [CPS] [10^6]
0
20
40
60
80
100
Concentration [mg/L]

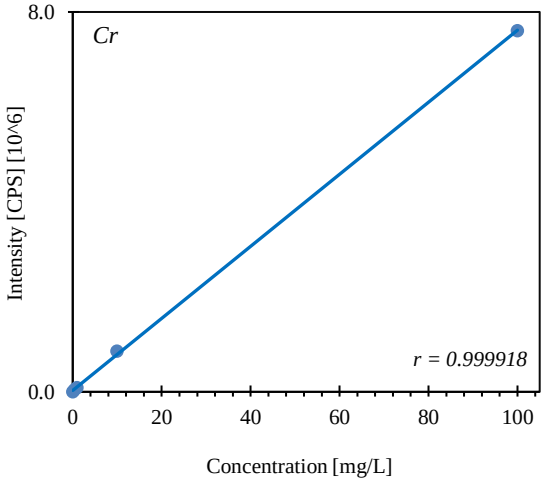
Cr
r = 0.999918
8.0
0.0
Intensity [CPS] [10^6]
0
20
40
60
80
100
Concentration [mg/L]

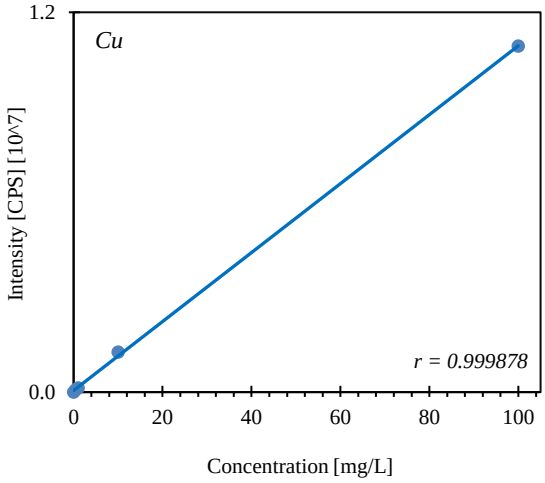
Cu
r = 0.999878
1.2
0.0
Intensity [CPS] [10^7]
0
20
40
60
80
100
Concentration [mg/L]

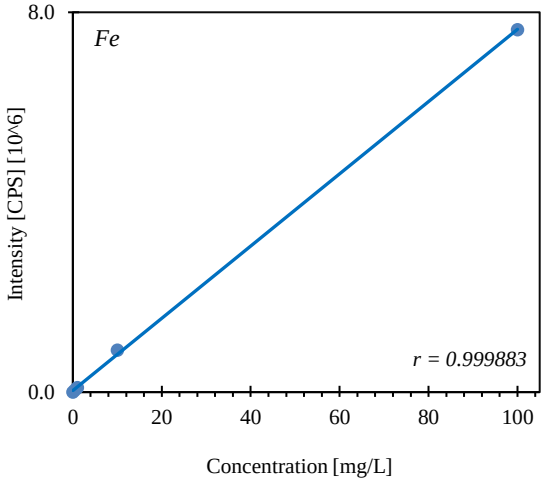
Fe
r = 0.999883
8.0
0.0
Intensity [CPS] [10^6]
0
20
40
60
80
100
Concentration [mg/L]

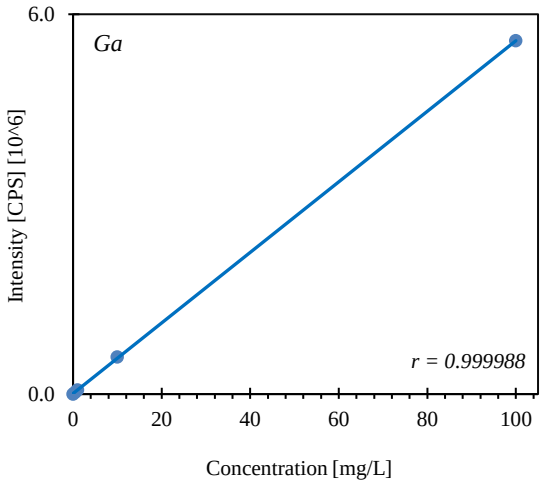
Ga
r = 0.999988
6.0
0.0
Intensity [CPS] [10^6]
0
20
40
60
80
100
Concentration [mg/L]

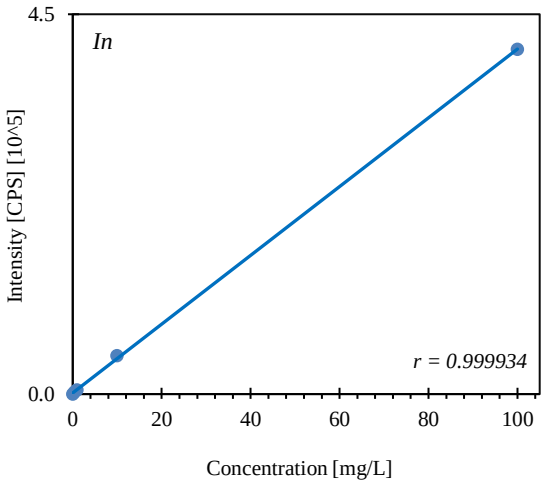
In
r = 0.999934
4.5
0.0
Intensity [CPS] [10^5]
0
20
40
60
80
100
Concentration [mg/L]

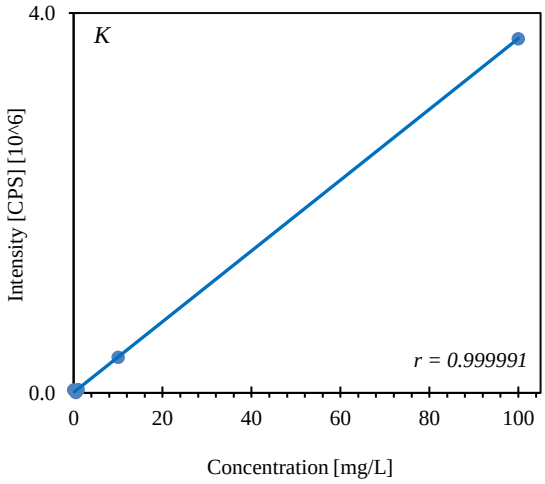
K
r = 0.999991
4.0
0.0
Intensity [CPS] [10^6]
0
20
40
60
80
100
Concentration [mg/L]

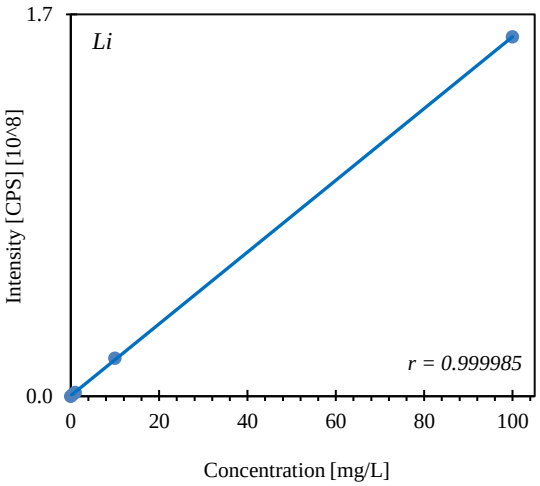
Li
r = 0.999985
1.7
0.0
Intensity [CPS] [10^8]
0
20
40
60
80
100
Concentration [mg/L]

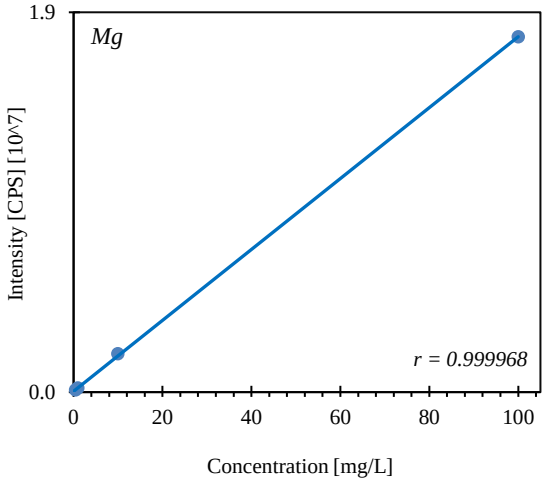
Mg
r = 0.999968
1.9
0.0
Intensity [CPS] [10^7]
0
20
40
60
80
100
Concentration [mg/L]

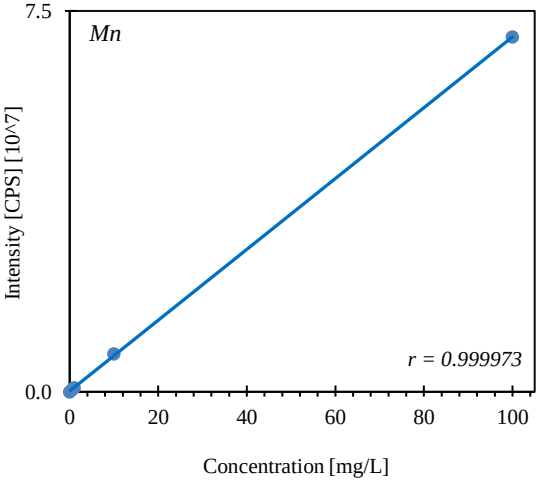
Mn
r = 0.999973
7.5
0.0
Intensity [CPS] [10^7]
0
20
40
60
80
100
Concentration [mg/L]

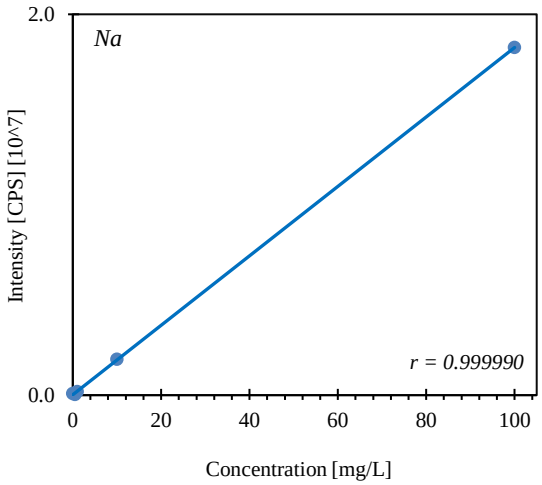
Na
r = 0.999990
Intensity [CPS] [10^7]
2.0
0.0
0
20
40
60
80
100
Concentration [mg/L]

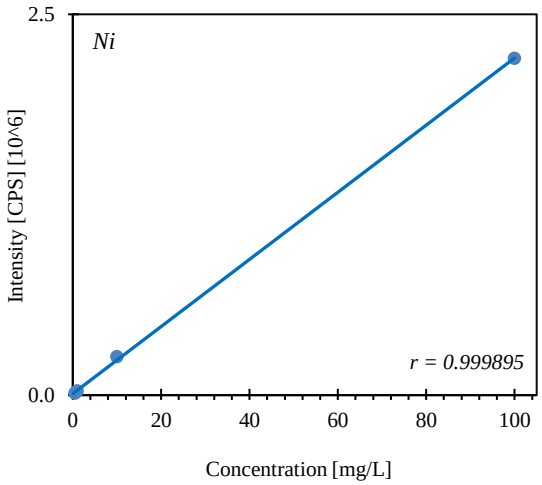
Ni
r = 0.999895
Intensity [CPS] [10^6]
2.5
0.0
0
20
40
60
80
100
Concentration [mg/L]

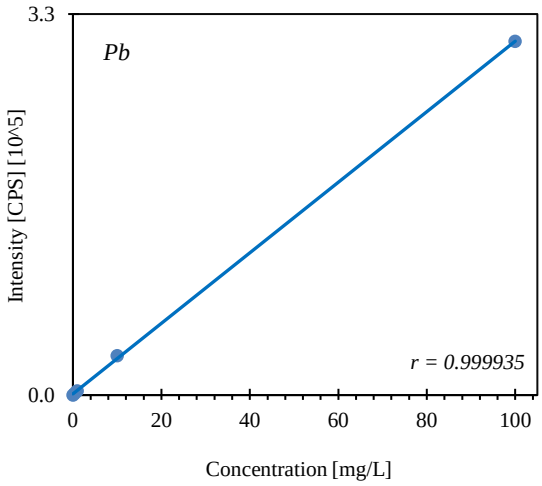
Pb
r = 0.999935
Intensity [CPS] [10^5]
3.3
0.0
0
20
40
60
80
100
Concentration [mg/L]

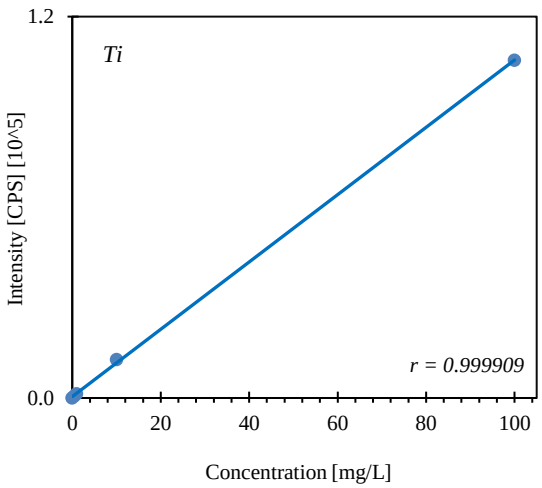
Ti
r = 0.999909
Intensity [CPS] [10^5]
1.2
0.0
0
20
40
60
80
100
Concentration [mg/L]

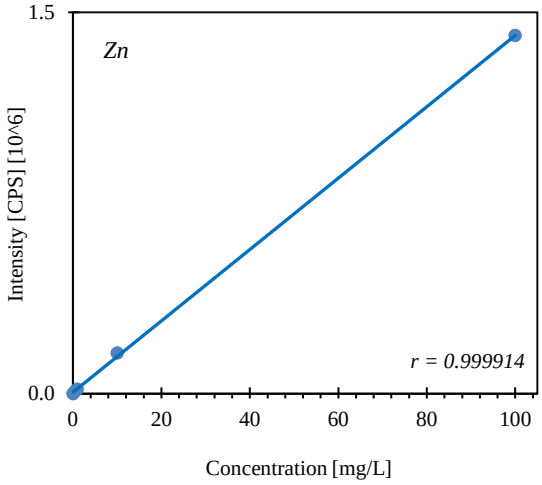
Zn
r = 0.999914
Intensity [CPS] [10^6]
1.5
0.0
0
20
40
60
80
100
Concentration [mg/L]

A13: Perkin Elmer ICP-OES Limit of Detection (LOD)

ATOMIC SPECTROSCOPY DETECTION LIMITS

Element	Flame AA	Hg/Hydride	GFAA	ICP-OES	ICP-MS
Ag	1.5		0.005	0.6	0.00003
Al	45		0.1	1	0.00001*
As	150	0.03	0.05	1	0.0003
Au	9		0.15	1	0.00005
B	1000		20	1	0.0002
Ba	15		0.35	0.03	0.00002
Be	1.5		0.008	0.09	0.00009
Bi	30	0.03	0.05	1	0.000004
Br					0.04
C					
Ca	1.5		0.01	0.05	0.00005*
Cd	0.8		0.002	0.1	0.00006
Ce				1.5	0.00005
Cl					2
Co	9		0.15	0.2	0.000006*
Cr	3		0.004	0.2	0.00005*
Cs	15				0.00005
Cu	1.5		0.014	0.4	0.00003*
Dy	50			0.5	0.0002
Er	60			0.5	0.0001
Eu	30			0.2	0.00007
F					
Fe	5		0.06	0.1	0.0001*
Ga	75			1.5	0.00004
Gd	1800			0.9	0.0003
Ge	300			1	0.0004*
Hf	300			0.5	0.0003
Hg	300	0.006	0.6	1	0.001
Ho	60			0.4	0.00004
I					0.003
In	30			1	0.000003
Ir	900		3.0	1	0.00009
K	3		0.005	1	0.00004
La	3000			0.4	0.00004
Li	0.8		0.06	0.3	0.0000004
Lu	1000			0.1	0.00004
Mg	0.15		0.004	0.04	0.00001
Mn	1.5		0.005	0.1	0.00005*

Element	Flame AA	Hg/Hydride	GFAA	ICP-OES	ICP-MS
Mo	45		0.03	0.5	0.00003
Na	0.3		0.005	0.5	0.00001
Nb	1500			1	0.000009
Nd	1500			2	0.0003
Ni	6		0.07	0.5	0.00006*
Os				6	0.00006
P	75000		130	4	0.6*
Pb	15		0.05	1	0.00001*
Pd	30		0.09	2	0.00008
Pr	7500			2	0.00003
Pt	60		2.0	1	0.00007
Rb	3		0.03	5	0.0002
Re	750			0.5	0.0003
Rh	6			5	0.00003
Ru	100		1.0	1	0.00002
S				10	0.5*
Sb	45	0.15	0.05	2	0.00003
Sc	30			0.1	0.001
Se	100	0.03	0.05	2	0.0003*
Si	90		1.0	10	0.1
Sm	3000			2	0.0002
Sn	150		0.1	2	0.00003
Sr	3		0.025	0.05	0.00002
Ta	1500			1	0.000006
Tb	900			2	0.00003
Te	30	0.03	0.1	2	0.0003*
Th				2	0.00005
Ti	75		0.35	0.4	0.00003*
Tl	15		0.1	2	0.000004
Tm	15			0.6	0.00003
U	15000			10	0.000005
V	60		0.1	0.5	0.00001*
W	1500			1	0.00002
Y	75			0.2	0.00002
Yb	8			0.1	0.0001
Zn	1.5		0.02	0.2	0.0001*
Zr	450			0.5	0.00002

All detection limits are given in micrograms per liter and were determined using elemental standards in dilute aqueous solution. All detection limits are based on a 98% confidence level (3 standard deviations).

Actual detection limits may vary depending on system configuration, matrices, and laboratory conditions.

All atomic absorption detection limits were determined using instrumental parameters optimized for the individual element, including the use of System 2 electrodeless discharge lamps where available. Data shown were determined on a PerkinElmer AA.

Cold-vapor mercury detection limits were determined with dedicated FIMS 100 and FIMS 400 mercury analyzer. The detection limit of FIAS 100 and FIAS 400 is 0.2 µg/L with a hollow cathode lamp, 0.05 µg/L with a System 2 electrodeless discharge lamp.

Hydride detection limits shown were determined using an MHS-15 Mercury/Hydride system.

GFAA detection limits were determined on a PerkinElmer AA using 50 µL sample volumes, an integrated platform and full STPF conditions. Graphite-furnace detection limits can be further enhanced by the use of replicate injections.

All ICP-OES detection limits were obtained under simultaneous multi-element conditions with the axial view of a dual-view plasma using a cyclonic spray chamber and a concentric nebulizer.

All ICP-MS measurements were performed on a NexION ICP-MS with a quartz sample introduction system using a 1-second integration time and ten replicates in de-ionized water. Detection limits were measured under multi-element conditions in Standard mode, except where denoted by an asterisk (*). Detection limits denoted by * were performed in a Class 1000 Cleanroom using Reaction mode with the most appropriate cell gas and conditions for that element.

A14: ICP-OES of Pure and Recovered LIB Pouch Cell Electrolyte

Table A12-1: Elemental concentration (mg/L).

	Ag	Al	B	Ba	Ca	Cd	Co	Cr	Cu	Fe	Ga
1	0.1990181	0.1278049	1.4246769	0.0273678	0.0688632	0.0157243	0.0242203	0.0520638	1.7166750	0.2401982	0.0205235
2	0.0061845	0.0462646	0.3782112	0.0014401	0.0226899	0.0012160	0.0034268	0.0061696	1.8988342	0.0315477	0.0039482
3	0.0025406	0.0038319	0.1736579	0.0008172	0.0143714	0.0006427	0.0031764	0.0027126	0.0812953	0.0170646	0.0039421

Table A12-2: Elemental concentration (mg/L).

	In	K	Li	Mg	Mn	Na	Ni	Pb	Ti	Zn
1	0.0254059	-0.0084281	5.2915574	0.0090752	0.0347456	0.1591895	0.0355660	0.0166489	0.0008604	0.0184658
2	0.0014008	0.0213580	5.5157461	0.0026860	0.0101792	0.1781034	0.0079070	0.0064896	-0.0001155	0.0099762
3	0.0008509	-0.1436312	0.0081444	0.0008043	0.0037492	-0.1061499	0.0044952	0.0037892	-0.0005172	0.0070432

Where; **1** – represents pure LIB electrolyte taken from the Nissan Leaf (gen 1) pouch cell during disassembly, **2** – represents pure LIB electrolyte recovered from the Nissan Leaf (gen 1) pouch cell anode using the solvent extraction technique, **3** – represents pure LIB electrolyte taken from the Nissan Leaf (gen 1) pouch cell anode using the pressurised carbon dioxide extraction technique.